Designing photocatalytic materials by merging macromolecules with small molecular photocatalysts

Dissertation

zur Erlangung des akademischen Grades
„Doktor der Naturwissenschaften (Dr. rer. nat.)“
im Promotionsfach Chemie
des Fachbereichs Chemie, Pharmazie und Geowissenschaften
der Johannes Gutenberg-Universität Mainz

Thomas Kuckhoff

Geboren in Koblenz

Mainz, 2023

Dekan:

1. Berichterstatter: Prof. Landfester
2. Berichterstatter: Prof. Besenius
   Mündliche Prüfung: 31.01.2024

Erklärung

Die Dissertation wurde im Arbeitskreis von Prof. Dr. Landfester am Max-Planck-Institut für Polymerforschung angefertigt.
Ich bestätige hiermit, dass die vorliegende Arbeit selbständig angefertigt wurde und nur unter Verwendung der angegebenen Hilfsmittel. Alle verwendeten Hilfsmittel und Quellen wurden eindeutig gekennzeichnet. Ich versichere weiter, dass diese Arbeit bisher noch nicht veröffentlicht wurde oder Teil einer anderen Dissertation ist.

Ampfing, den

Thomas Kuckhoff

Acknowledgment

I would like to express my sincere gratitude for the people who have contributed to the realization of this thesis. Their help, support and guidance, have been critical in achieving this work.

Firstly, I want to thank Prof. Landfester for granting me the incredible opportunity to work at the Max Planck Institute. Her guidance and support have been invaluable over the last four years. Particularly, during the challenging times of the Corona pandemic and subsequent lockdowns, Prof. Landfester provided the stability and encouragement needed. I further want to thank Prof. Besenius and Prof. Frey for attending my defense and participating as my examiner.
I also want to express my gratitude towards Calum Ferguson for his scientific guidance and mentorship throughout this thesis and over the years. His input, suggestions and encouragement have been crucial for the success of my projects, and I am grateful for the discussions and project meetings we have had.

Further, I would like to acknowledge Amanda Jarvis mentorship and guidance during my research stay at the University of Edinburgh. Her willingness to accommodate me in her group, and the support for the collaboration were greatly appreciated.

With great sadness, I want to acknowledge Kai Zhang who untimely passed away. He introduced me to the world of photocatalysis and enabled me to take my first step towards my PhD for which I am thankful.
My gratitude is also extended to the members of the photocatalysis group, namely Rong, Julian, Seunghyeon as well as my former colleagues Niklas and Wenxin. I am thankful for the fellowship we build over many hours together. As well as our projects discussions which significantly improved my scientific understanding.
In this context, I also want to thank Evelina and Katherine for helping me adjust to a new research group.

Furthermore, I want to acknowledge the contributions of the polymer analysis group for their expertise and measurements regarding GPC, HPLC, and DLS. I would also like to express my gratitude to Robert Graf for his assistance in ssNMR analysis, Angela for performing repeated synthesis.
I want to take a moment to appreciate my friends at the Max Planck Institute for the enjoyable moments we shared, both inside and outside the institute.

Lastly, my deepest and most profound thanks go to my family. Their unwavering support and encouragement have been the bedrock of my journey. Their love, understanding, and sacrifices have been nothing short of extraordinary. I am forever grateful for their presence in my life.

Therefore, I want to thank all my colleagues, supervisors, friends and my family from the bottom of my heart for their support, guidance and contributions, without their effort this thesis would not exist.

Zusammenfassung

Photokatalyse ist eine umweltfreundliche und nachhaltige Methode, bei der sichtbares Licht zur Katalyse chemischer Reaktionen eingesetzt wird. Moderne Photokatalysatoren sind jedoch in ihrer Anwendung durch intrinsische Nachteile eingeschränkt. Homogene Katalysatoren sind oft schlecht zu recyceln, leiden unter Photobleaching und sind auf seltene Erdmetalle angewiesen. Heterogene Photokatalysatoren hingegen haben im Vergleich aufgrund einer schlechten Lichtdurchdringung und einem begrenzten Substrattransport einen geringeren Wirkungsgrad.

Die Kombination von makromolekularen Strukturen mit niedermolekularen Photokatalysatoren ist ein Ansatz, um vorteilhafte Materialeigenschaften mit photokatalytischer Aktivität zu verbinden und die vorteilhaften Aspekte der homogenen und heterogenen Photokatalyse zu vereinen.

Das übergeordnete Ziel dieser Arbeit war es, die Kombination von niedermolekularen Photokatalysatoren mit makromolekularen Strukturen zu untersuchen, um die vielseitige Anwendbarkeit der modernen Photokatalyse mit vorteilhaften Materialeigenschaften zu kombinieren.

In dieser Arbeit wurden funktionalisierte metallfreie Photokatalysatoren, auf Grundlage von π-erweiterten Benzothiadiazol, kovalent mit makromolekulare Trägerstrukturen verbunden, um einen effizienten Photokatalysator zu entwickeln und die Auswirkungen des Materials auf die photokatalytischen Fähigkeiten zu analysieren.

Insgesamt wurden drei Projekte durchgeführt, in denen zum einen ein Hydrogel mit hoher Lichtdurchlässigkeit sowie linearen Polymeren und Proteine mit niedermolekularen Photokatalysatoren kombiniert wurden, um neuartige makromolekulare Photokatalysatoren zu entwickeln.

Polymere bieten eine ideale Trägerstruktur für Photokatalysatoren, da sie aufgrund der gewählten Monomere und Polymerisationsart eine große Bandbreite von Materialeigenschaften und möglicher Strukturen ermöglichen. Funktionalisierte Photokatalysatoren können mittels Copolymerisation in die gewünschten Polymere integriert werden, umso Materialeigenschaften mit Photokatalyse zu verbinden.

Deswegen ist die Copolymerisation von Photokatalysatoren mit Trägermaterialien mittels RAFT, ATRP oder radikalische Polymerisation als neue Entwicklungsplattform für heterogene Photokatalysatoren von großem Interesse. Dennoch ist wenig über die Wechselwirkung und den Einfluss des Comonomer auf die photokatalytische Effizienz bekannt. Im ersten Projekt wurde ein Vinyl-funktionalisierter Photokatalysator basierend auf Benzothiadiazol mit sieben verschiedenen Monomeren Methylmethacrylat (MMA), Styrol (S), Acrylnitril (AN), sowie Benzylmethacrylat (BMA), Hydroxyethylmethacrylat (HEMA), *N,N*-Dimethylaminoethylmethacrylat (DMAEMA) und *N,N*-Dimethylacrylamid (DMA) durch radikalische Polymerisation copolymerisiert. Die Copolymere Polymethylmethacrylat (PMMA-BT), Polystyrol (PS-BT), Polyacrylnitril (PAN-BT) zeigten signifikante

Verschiebungen in Absorption- und Emissionsspektra und wurden im Folgenden auf ihre Auswirkung auf die photokatalytische Effizienz und die photophysikalischen Eigenschaften zu untersuchen. Die Copolymere wurden mittels UV/Vis- und Fluoreszenzspektroskopie analysiert sowie die Fluoreszenzlebensdauer und Quantenausbeute ermittelt. Darüber hinaus wurden die optische Bandlücke und die HOMO/LUMO-Niveaus bestimmt und drei photokatalytische Reaktionen mittels kinetischer Messungen analysiert, wobei die photokatalytische Effizienz eine Abhängigkeit von dem gewählten Comonomer aufwies. Im direkten Vergleich zu MMA und AN besitzt Styrol als Comonomer einen positiven Effekt auf photophysikalische und photokatalytische Eigenschaften. Die Copolymerisation des Photokatalysators mit Styrol führt zu einer höheren Lebensdauer des angeregten Zustands, eine geringere Blauverschiebung und einer besseren photokatalytischen Aktivität.

Die Effizienz von heterogene Photokatalysatoren ist in der Regel durch eine geringe Eindringtiefe des Lichts in das heterogene Material sowie durch Lichtstreuung an der Materialoberfläche begrenzt. Darüber hinaus verringert die begrenzte Substratdiffusion die Effizienz der photokatalytischen Materialien weiter. In einem zweiten Projekt wurde daher ein photokatalytisches Hydrogel auf der Grundlage eines lichtdurchlässigen Polymernetzwerks entwickelt. Das Hydrogel besaß eine hohe Durchlässigkeit für sichtbares Licht und quoll gleichzeitig in Wasser, wodurch die Eindringtiefe des Lichts in das Material verbessert wurde, während gleichzeitig die Substratdiffusion durch das gequollene Polymernetzwerk verbessert wird. Aufgrund der Materialeigenschaften wurde das Hydrogel zum Schadstoffabbau unter sichtbarem Licht eingesetzt, wobei die Substrate in das Hydrogel aufgenommen werden können bevor sie abgebaut werden. Die Funktionsfähigkeit und der mögliche Anwendungsbereich wurden durch die Photooxidation von Farbstoffen, organischen Sulfiden sowie die Reduktion von $Chrom^{VI}$ und den Photoabbau von Glyphosat bewiesen. Darüber hinaus wurde in einem groß angelegten Experiment das Potenzial des Hydrogels durch den Photoabbau von Glyphosat im Halblitermaßstab bewiesen.

Das letzte Projekt wurde in Zusammenarbeit mit der Gruppe von Dr. Jarvis an der Universität von Edinburgh durchgeführt. Das Design und die Entwicklung künstlicher metallfreier Photoenzyme zielt darauf ab, die Selektivität enzymatischer Reaktionen mit den Vorteilen moderner synthetischer Photokatalysatoren zu kombinieren. Dadurch wird die Abhängigkeit von Seltenerdmetallen verringert und gleichzeitig mildere Reaktionsbedingungen ermöglicht, was zu einem nachhaltigeren katalytischen System führt. Im letzten Kapitel wurde ein neuartiges künstliches Photoenzym erschaffen. Ein Photokatalysator basierend auf einem Iodoacetamid funktionalisierten Benzothiadiazol wurde in ein Steroidträgerprotein (SCP-2L) integriert. SCP-2L ist ein idealer Kandidat für den Einbau eines niedermolekularen Photokatalysatoren, da es über einen hydrophoben Tunnel verfügt, der die Substratbindung in wässrigen Medien erleichtert. Durch ortsspezifische Mutagenese wurden nicht-

natives Cystein strategisch um den hydrophoben Tunnel herum platziert, wodurch drei SCP-2L-Varianten entstanden. Der Photokatalysator wurde selektiv an drei Varianten gebunden und drei Photoenzyme wurden synthetisiert. Die Analyse des photophysikalischen Verhaltens mittels UV/Vis- und Fluoreszenzspektroskopie sowie die kinetischen Messungen einer photokatalytischen Reaktion zeigten Unterschiede in der Reaktivität in Abhängigkeit von der Bindungsposition auf.

Abstract

Photocatalysis is an environmentally friendly, sustainable method that uses visible light irradiation to catalyze chemical reactions. However, the application of modern photocatalysts is often limited by their intrinsic drawbacks. Homogeneous catalysts often possess poor recyclability, suffer from photobleaching, and often rely on rare earth metals. At the same time, heterogeneous photocatalysts typically have lower efficiencies than their homogeneous counterparts due to poor light penetration and limited substrate mass transport.

The combination of macromolecular structures with small photocatalytic moieties is an approach to combine beneficial material properties with photocatalytic activity. Merging the beneficial aspects of homogeneous and heterogeneous photocatalysis.

This thesis aimed to investigate the combination of small molecular photocatalysts with macromolecular structures, combining the versatility of modern photocatalysis with beneficial material properties.

In this work, functionalized metal-free photocatalytic moieties based on π-extended benzothiadiazole were covalently incorporated into macromolecular support structures to design efficient photocatalysts and analyze the effect of the material on the photocatalytic capabilities.

Overall, three projects were carried out combining macromolecular structures comprising of linear polymers, a high transmittance hydrogel, and protein scaffolds with photocatalytic moieties. Designing novel macromolecular photocatalysts.

Polymers are an ideal support for photocatalytic moieties because they allow for a wide range of possible material properties and structures due to the chosen monomer and type of polymerization. Functionalized photocatalytic moieties enable the copolymerization and integration into polymer supports, combining material properties with the photocatalyst.

Due to this, the copolymerization of photocatalytic moieties into support material via RAFT, ATRP, or free radical polymerization has emerged as a new development platform for heterogeneous photocatalysts. Nevertheless, little is known about the interaction and influence of the comonomer on the photocatalytic efficiency. In the first project, a vinyl functionalized benzothiadiazole-based photocatalytic moiety was copolymerized with seven different monomers, methyl methacrylate(MMA), styrene (S), acrylonitrile (AN) as well as benzyl methacrylate (BMA), hydroxyethyl methacrylate (HEMA), *N,N*-dimethylaminoethyl methacrylate (DMAEMA), and *N,N*-dimethylacrylamid (DMA) via free radical polymerization. The copolymers poly(methyl methacrylate) (PMMA), polystyrene (PS), and polyacrylonitrile (PAN) had a significant effect on the on the absorption and emission spectra. In consequence, these three copolymers were used to investigate the comonomer effect on the photocatalytic efficiency and photophysical properties. The copolymer was analyzed via

UV/Vis- and fluorescence spectroscopy, fluorescence lifetime, and quantum yield measurements. In addition, the optical band gap and HOMO/LUMO levels were determined. Further, three photocatalytic reactions were analyzed via kinetic measurements showing evidence of an impact on the photocatalytic efficiency depending on the chosen comonomer. In direct comparison to methyl methacrylate and acrylonitrile, the usage of styrene as a comonomer has a positive effect on the photophysical properties and photocatalytic efficiency. The copolymerization of the photocatalytic moiety with styrene leads to an increased lifetime of the excited state, lower blue shift, and better photocatalytic activity.

Heterogeneous photocatalysts are typically limited by low light penetration into the heterogeneous material, as well as light scattering on the material surface. In addition, limited substrate diffusion into heterogeneous photocatalysts reduces the overall efficiency of the photocatalytic materials. In a second project, a photocatalytic hydrogel based on a high-transmittance polymer network was created. The hydrogel possessed a high transmittance under visible light while also being swellable in water. Improving the light penetration depth into the material while also improving the substrate diffusion due to the swollen polymer network. Due to the material properties, the hydrogel was used for pollutant remediation under visible light, allowing for the uptake of substrates into the hydrogel before being degraded. The viability and possible application range were demonstrated by the photooxidation of dyes, organic sulfides, as well as the reduction of chromium^{VI} and the photodegradation of glyphosate. Furthermore, a large-scale experiment proved the hydrogel's potential by photodegrading glyphosate on a half-liter scale.

The final project was undertaken in cooperation with the Jarvis group at the University of Edinburgh. The design and development of artificial metal-free photoenzymes aim to combine the selectivity of enzymatic reactions with the benefits of modern synthetic photocatalysts. Removing the need for rare earth metals and allowing for milder reaction conditions, leading to a more sustainable catalytic system. In the last chapter, a novel artificial photoenzyme was created. Integrating photocatalytic iodoacetamide functionalized benzothiadiazole moiety into a steroid carrier protein (SCP-2L). SCP-2L is an ideal candidate for incorporating a photocatalytic moiety due to the possession of a hydrophobic tunnel facilitating substrate uptake in aqueous media. Through site-selective mutagenesis, non-native cysteine residues were strategically placed around the hydrophobic tunnel, introducing three SCP-2L variants. The photocatalyst was site-selectively bound to three variants and yielded three photoenzymes. Analysis of the photophysical behavior via UV/Vis and fluorescence spectroscopy, as well as monitoring of a photocatalytic reaction, highlighted differences in the reactivity depending on the binding site.

Table of Content

Acknowledgment 1
Zusammenfassung 2
Abstract 5
1 Introduction 9
2 Theoretical Background 13
3 Homogeneous and Heterogeneous Photocatalysts 15
3.1 Homogeneous Photocatalysts 15
3.1.1 Homogeneous Photocatalysts Based on Transition Metal Complexes 15
3.1.2 Homogeneous Photocatalysts Based on Organic Dyes 16
3.1.3 Homogeneous Photocatalysts based on Benzothiadiazole 18
3.2 Heterogeneous Photocatalysis 20
3.3 Photocatalytic Small Molecules Incorporated into Classical Polymers 23
3.3.1 Particles 25
3.3.2 Microgels 27
3.3.3 Star Shaped Polymers and Dendrimers 29
3.3.4 Porous Three-Dimensional Networks 31
3.3.5 Macrogels 33
3.3.6 Conclusion 33
3.4 Combining Photocatalysis with Proteins 34
3.4.1 Artificial Photoenzymes 36
4 Characterization Techniques 43
4.1 Gas Chromatography–Mass Spectrometry 43
4.2 Liquid Chromatography–Mass Spectrometry 44
4.3 Gel Permeation Chromatography 44
4.4 UV/Vis-Spectroscopy 44
4.5 Photoluminescence Spectroscopy 45
4.6 Fourier-Transform Infrared Spectroscopy 46
4.7 Cyclic Voltammetry 46
4.8 Nuclear Magnetic Resonance Spectroscopy 47
5 Data and Results 49
5.1 Comonomer Effects in Photocatalytic Classical Polymers 50
5.1.1 Motivation: Missing Link Between Classical Polymers and Photocatalysis 50
5.1.2 Results and Discussion: Comonomer Influence on the Photocatalytic Efficiency 54

5.1.3 Conclusion: Copolymers Impact the Photocatalytic Efficiency and Photophysical Properties 67
5.2 Photocatalytic Hydrogels with a High Transmission Polymer Network for Pollutant Remediation 69
5.2.1 Motivation: Photocatalysis for Environmental Friendly Wastewater Remediation 69
5.2.2 Results and Discussion: Design of a Highly Transmittance Photocatalytic Hydrogel 71
5.2.3 Conclusion: Novel Photocatalytic Material for Wastewater Treatment 88
5.3 Reactivity Tuning of Metal-Free Artificial Photoenzymes through Binding Sites Specific Bioconjugation 89
5.3.1 Motivation: The Design of Artificial Photoenzymes 89
5.3.2 Results and Discussion: Comparison of Three Novel Metal-Free Artificial Photoenzymes 91
5.3.3 Conclusion: Position Depending Optical Properties and Photocatalytic Efficiency 101
6 Experimental section 103
6.1 Comonomer Effects in Photocatalytic Classical Polymers 103
6.1.1 Material and Characterization: 103
6.1.2 Synthesis Method 107
6.1.3 Photocatalytic Reactions 110
6.2 Photocatalytic Hydrogels with a High Transmission Polymer Network for Pollutant Remediation 116
6.2.1 General Information and Methods Characterization 116
6.2.2 Synthesis Methods 117
6.2.3 Photocatalytic Reactions 120
6.3 Reactivity Tuning of Metal-Free Artificial Photoenzyme through Binding Sites Specific Bioconjugation 129
6.3.1 General Information and Characterization: 129
6.3.2 Synthesis Methods 130
6.3.3 Photocatalytic Reaction 139
7 Summary and Outlook 143
8 References 144
9 List of Figures 166
10 List of Tables 173
11 List of Acronyms 174
12 Scientific Contribution 176

1 Introduction

Light is a renewable and abundant energy source, possessing the potential answer to our increasing energy demand and reliance on fossil resources. On average, 1.36 kW/m^2 of solar irradiation reaches the earth's surface, of which approximately 40% is in the visible light spectrum.[1,2] Nature uses this resource and converts solar energy via photosynthesis. In contrast, global CO_2-emission reached an all-time high of 36.8 GT in 2022, caused by an increasing energy demand and over-reliance on fossil fuels.[3] To overcome this dependence on limited resources and reduce our environmental impact, the utilization of light for photocatalysis has soared in popularity. (Figure 1.1) Inspired by nature, photocatalysis offers an alternative to conventional thermal catalysts, being researched for the synthesis of high-value chemicals as well as H_2 evolution, CO_2-reduction, and wastewater remediation.

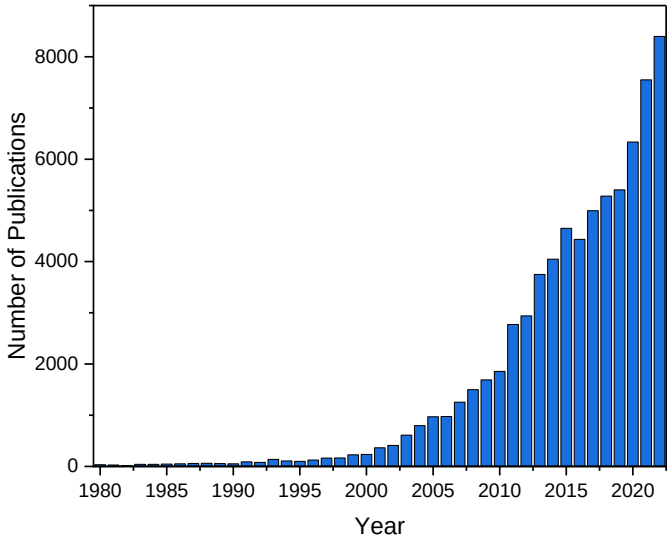

Figure 1.1 Number of publications between 1980 and 2022. Search term "photocatalysis" CAS SciFinder^n. www.scifinder-n.cas.org. Accessed 22 May, 2023.

Although its significant increase in popularity, first reports about light usage for chemical transformation reach back to the early 20th century. Neiber reported the bleaching of Prussian blue in the presence of ZnO under light irradiation and introduced the term "photocatalysis".[4] Giacomo Ciamician became an advocate for the usage of light in chemistry, highlighting the limited availability of fossil fuels as early as 1912.[5,6] Nevertheless, photocatalysis remained a footnote in chemical research until Fujishima and Honda reported the photocatalytic hydrogen evolution via TiO_2 in 1972.[7] Further Nicewicz and Macmillan's publication highlighting the possible application of photocatalysis in organic synthesis in 2008.[8] Over the last decades, research efforts focused on the design of novel homogeneous and heterogeneous photocatalysts, as well as photocatalytic reactions.

Metal-free dyes emerged as alternatives to transition metal catalysts. Dyes like rhodamine B and eosin Y, as well as specifically designed photocatalytic moieties, have been investigated to remove the

dependence on rare elements like ruthenium and iridium. On the other hand, heterogeneous photocatalysts are being investigated as a recyclable alternative to homogeneous photocatalysts and are based on various organic and inorganic materials covering a wide range of structural designs.
However, so far, photocatalysts still possess significant limitations, which restrict their widespread applicability. Homogeneous photocatalysts are often hard to recycle and can contaminate the product, rely on rare earth metals, and can be toxic, while fully organic photocatalytic dyes suffer from photobleaching. On the other hand, heterogeneous photocatalysts face issues such as limited light penetration into the photocatalytic material, light scattering on the surface, as well as limitations in diffusion and mass transfer.
Therefore, novel design strategies are needed to negate these drawbacks. The ideal photocatalyst would combine the benefits of homogeneous and heterogeneous photocatalysis. These photocatalysts should be easy to recycle and stable under irradiation while also being highly efficient. Therefore, an emerging field is the incorporation and fixation of small molecular photocatalysts into macromolecular structures like polymers and proteins. Polymers and proteins are macromolecular structures possessing advantageous material properties that could make them favorable support structures for small molecular photocatalysts.
Polymers are an ideal support for photocatalytic moieties because they allow for a wide range of possible material properties and structures due to the chosen monomer and type of polymerization. The ability to recycle polymers and the easy fixation of small molecular photocatalysts through copolymerization make them interesting candidates for the next generation of heterogeneous photocatalysts. Furthermore, copolymerization allows high control over the position and concertation of photocatalysts in the polymer backbone, allowing the fine-tuning of material and photocatalytic properties.
Enzymes, on the other hand, are used in nature as highly specific and efficient catalytic systems under mild and benign conditions. Proteins possess a three-dimensional leading to steric hindrance near the active center, leading to highly selective and substrate-specific catalytic processes. These properties have a potential synergy with photocatalysis and make proteins a promising development platform for a novel class of photocatalytic enzymes. Embedding small molecular photocatalysts within a protein structure can lead to the development of novel artificial photoenzymes, combining the benefits of enzymatic precision with the capabilities of photocatalysis. This photocatalytic material is highly sustainable, benefits from milder reaction conditions, and can use water as a sustainable solvent, leading to an overall highly environmentally friendly system.
Therefore, combining small molecular photocatalysts with macromolecular structures is a path to link advantageous material properties with photocatalytic activity and merge the favorable aspects of homogeneous and heterogeneous photocatalysis.
In this context, the aim of this thesis was to incorporate small molecular photocatalysts into macromolecular structures with beneficial material properties to develop macromolecular materials

with photocatalytic capabilities. In addition, this thesis aimed to gain insights into the effect of the material on the photocatalyst and its photocatalytic capabilities. Three projects were realized, integrating a π-extended benzothiadiazole photocatalyst into linear polymers, a hydrogel, and protein scaffolds to contribute to a more sustainable and environmentally friendly future.

The performed research projects can be divided into three main stages: identifying and designing suitable material, incorporating the photocatalyst, and analyzing the photocatalytic behavior. In the first step, macromolecular support with suitable material properties was identified and accordingly synthesized. In the case of this thesis, three different structures were investigated. The first research chapter (5.1) is used to analyze the effect of comonomers on photocatalytic efficiency and photophysical properties. The second chapter (5.2) introduces a high transmittance hydrogel as material support, allowing for wastewater remediation. Lastly, the third chapter (5.3) is based on using a protein scaffold as macromolecular support. In the second step, the adequate photocatalyst was synthesized and incorporated into the macromolecule. In this Ph.D. thesis, the photocatalytic moiety is based on a π-extended benzothiadiazole. This fully organic photocatalyst possesses a donor-acceptor design, and can be modified to allow the incorporation into macromolecules, either through copolymerization (chapter 5.1 & 5.2) or bioconjugation (chapter 5.3).

In the last step of these projects, the developed photocatalytic macromolecules were used for photocatalytic testing, and the material and photophysical properties were analyzed. Aiming to evaluate the capabilities and properties of these photocatalysts under light irradiation.

In the first chapter 5.1, three monomers, methyl methacrylate, styrene, and acrylonitrile, were copolymerized with the photocatalytic moiety. The copolymerization of photocatalytic moieties into polymers is a powerful tool for designing photocatalysts with beneficial morphologies. However, little is known about the effect of the comonomer on the photocatalytic capabilities. Therefore, a systematic study is undertaken to analyze the influence of three monomers on the photophysical properties of a π-extended benzothiadiazole photocatalyst.

In the second chapter 5.2, a high transmittance photocatalytic hydrogel was developed. Heterogeneous photocatalysts are limited in application due to low light penetration depth, light scattering on the material surface, and limited substrate diffusion. Therefore, a high transmittance hydrogel based on *N,N*-dimethylacrylamide was designed, allowing for better light penetration into the material. Negating the drawback of heterogeneous photocatalysts. The material was used for pollutant degradation in water, and an upscaled photodegradation was performed.

Enzymes perform highly specific and selective reactions under benign conditions but are often cofactor-dependent, limiting their possible application. In chapter 5.3, an artificial photoenzyme was designed by incorporating a single photocatalytic moiety into protein scaffolds. Three variants with varying binding sites were synthesized, and the effect of the position on the photocatalytic efficiency was investigated, leading to a stable artificial photoenzyme that requires no cofactors for photocatalytic reactions under visible light irradiation.

This thesis is divided into seven chapters, including the theoretical background of photocatalysis and an overview of homogeneous and heterogeneous photocatalysis, before introducing current research on polymer-based photocatalysts and artificial photoenzymes. After describing the applied characterization techniques, chapter five reports the data and results of three conducted projects. Proceeded to the experimental section and a summary of this thesis.

2 Theoretical Background

In the following chapter, the theory of photocatalysis is shortly explained, utilizing a small molecular photocatalyst under visible light irradiation as an example.

The working mechanism of a photocatalyst is unlike that of a conventional catalyst and has been intensively researched in order to find greener and more environmental friendly alternatives to existing synthetic strategies.[9-12] Thermal catalysts reduce the energy of the transition state to catalyze reactions, while the photocatalysts absorb light and use the absorbed photon energy to catalyze electron or energy-transfer reaction.[9,12]

The first step of this mechanism is the absorption of visible light to transfer the molecule from the ground state into the excited state. In this process, the light energy must be equal to or higher than the existing bandgap (ΔE_{gap}) between the highest occupied molecular orbital (HOMO) and the lowest unoccupied molecular orbital (LUMO). The light absorption excites an electron from the HOMO to the LUMO, leaving a vacancy in the HOMO and creating an electron-hole pair.

Due to the vacancy hole in the HOMO and an electron in the LUMO, the photocatalyst in the excited state possesses better oxidative and reductive properties than in the ground state. Through light absorbance, the photocatalyst becomes a better reductant and oxidant, enabling the catalysis of chemical reactions. Next to the bandgap and potential of the HOMO/LUMO levels, the lifetime of the excited state is of key importance for designing an efficient photocatalyst. As every system desires to reach the lowest potential energy state, the excited state is unstable and returns to the ground state via radiative or non-radiative transitions. Therefore, charge separation and diffusion prolong the excited state lifetimes by preventing electron–hole recombination and are essential for efficient electron transfer reactions.

The photoinduced electron transfer reaction can proceed via two pathways, either a reductive quenching cycle or an oxidative quenching cycle. (Figure 2.1) In the reductive cycle, an electron is transferred from an electron donor to the photocatalyst, resulting in the oxidation of the substrate and reduction of the photocatalyst. Consequently, in the oxidative cycle, the electron is transferred from the LUMO to an electron acceptor, oxidizing the photocatalyst. Through a second electron transfer, the photocatalytic cycle is completed.

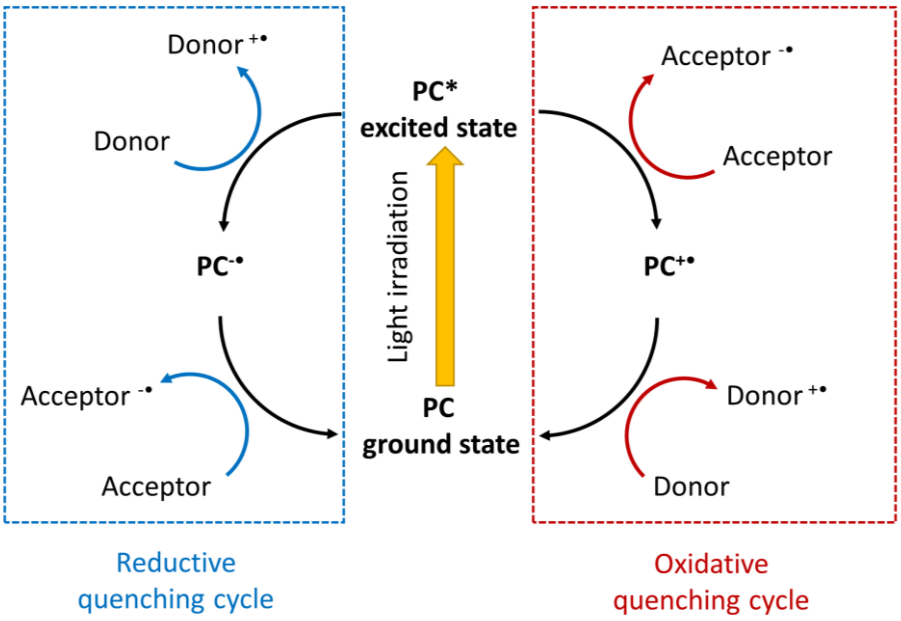

Figure 2.1 Depiction of the photocatalytic mechanism involving an oxidative or reductive quenching cycle.

Alternative to an electron transfer, a photocatalyst can also partake in an energy transfer reaction. This reaction is most commonly observed in the presence of oxygen, leading to the formation of singlet oxygen via a Dexter energy transfer mechanism. As energy transfer and electron transfer can be competing reactions, electron transfer reactions are often performed in the absence of oxygen.

Visible light offers the possibility to catalyze a wide variety of redox reactions, usually requiring thermal energy and/or conventional catalysts. By harnessing light energy, photocatalysis facilitates sustainable catalytic reactions without reliance on limited fossil fuels and without producing environmentally harmful side products.

In the following chapter, homogeneous and heterogeneous photocatalysts are summarized, and design strategies based on the incorporation of small molecular photocatalysts into macromolecular structures are introduced.

3 Homogeneous and Heterogeneous Photocatalysts

3.1 Homogeneous Photocatalysts

3.1.1 Homogeneous Photocatalysts Based on Transition Metal Complexes

Within the field of homogeneous photocatalysis, transition metal complexes like $[Ru(bpy)_3]^{2+}$ are the most commonly employed photocatalysts, with a vast library of reports, reviews, and books dedicated to their characterization and capabilities. Prominent reviews by the research group of MacMillan[9,13] highlight the photocatalytic capabilities of transition metal complexes, while the book chapter of Arias-Rotondo and McCusker[14] gives a comprehensive overview of the photophysical properties of $[Ru(bpy)_3]^{2+}$.

Although the first reports of $[Ru(bpy)_3]^{2+}$ reach back to 1936, its usage for organo-photocatalysis was rarely reported.[15] The group around Kellogg used $[Ru(bpy)_3]^{2+}$ for the reduction of sulfonium ion in the presence of Hantzsch ester as a sacrificing agent.[16,17] Cano-Yelo and Deronzier reported the photocatalytic Pschorr cyclization, yielding phenanthrene derivatives.[18] Only in the last decades the usage of transition metal photocatalysts has become the focus of intensive research after the report of MacMillan and Nicewicz in 2008.[8] In their research, MacMillan and Nicewicz combined an organo-catalyst with a ruthenium photocatalyst for the enantioselective α-alkylation of aldehydes. In the same year, the group of Yoon reported the [2+2]-enone cycloaddition.[19] Since then, a variety of reactions and conditions have been reported. Examples include the hydroxylation of boronic acids with $[Ru(bpy)_3]^{2+}$.[20] On the other hand, the borylation of aryl halides was reported by Jiang *et al.* and required the utilization of *fac*-$Ir(ppy)_3$. Under the right conditions, the synthesis could be directly followed by photocatalytic hydroxylation of the synthesized boronic esters.[21] The stereoselective synthesis of z-alkenyl thioethers from 1,2,3-thiadiazoles was achieved through the combination of $[Ru(bpy)_3]^{2+}$ and $Cu(OAc)_2$ as co-catalyst.[22] It was observed that the reaction also proceeded in the absence of the co-catalyst but with lower stereoselectivity. $[Ru(bpy)_3]^{2+}$ was further successfully used for the chlorination of aromatic compounds in the presence of NaCl and $Na_2S_2O_8$.[23] The group of Bolm reported the photocatalytic synthesis of β-keto sulfoximines from phenylacetylene,[24] while Trieu *et al.* reported the photocatalytic synthesis of isoxazolidines with high diastereomer selectivity.[25]

The efficiency of transition metal photocatalysts is based on the desirable photophysical properties of polypyridine complexes. This includes their near 100% efficiency for forming the excited state upon photon absorption while also possessing lifetimes between 300 ns and 6 µs.[26-28] Under visible light irradiation, the absorbance of $[Ru(bpy)_3]^{2+}$ is attributed to a metal-to-ligand charge transfer (MLCT) leading to a charge separation. Transferring an electron from the metal center to the ligand.[29] Upon irradiation, the complex undergoes a rapid intersystem crossing (ISC) within ~100 fs from ^{1}MLCT to the triplet state ^{3}MLCT.[30] Due to electron transfer from the metal center to the ligand, the ligand can be

used as a reducing agent, with the transition metal being an oxidizing agent. Accordingly, the photoexcited molecule becomes a better oxidant and reductant. In the excited state, the photocatalyst can be used in reductive and oxidative cycles through single electron transfer (SET), with the redox potential and bandgap being influenced by the choice and functionalization of ligands.[31] (Figure 3.1)
In a study by Lin et al., various polypyridine ruthenium complexes were compared in regards to their photophysical properties and reduction potential. Significant differences in the redox potential and bandgap were observed depending on the chosen ligand.[31]

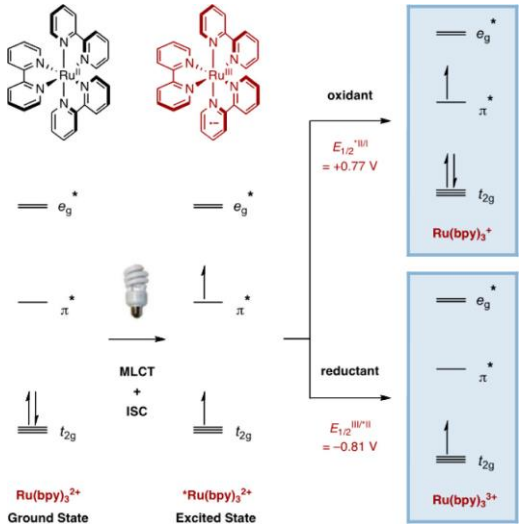

Figure 3.1: Depiction of molecular orbitals of $[Ru(bpy)_3]^{2+}$ and the creation of an electron-hole pair upon irradiation. Followed by the possible SET in an oxidative or reductive quenching process.[9] Reproduced with permission of ACS Copyright © 2013.

In addition to the photocatalytic electron transfer, the excited state of $[Ru(bpy)_3]^{2+}$ can be used for energy transfer, with the ^{3}MLCT state being efficiently quenched in the presence of oxygen, generating single oxygen. Already in 1973, Demas et al. analyzed the deactivation of singlet oxygen by ruthenium (II) complexes.[32] More recent, reviews by the Glorius and Xiao research groups have summarized the energy transfer pathways of photocatalysts and the possible use in photochemistry.[11,12]
Although their high efficiency, transition metal photocatalysts require the utilization of rare earth elements like ruthenium and iridium, which reduces their applicability due to high costs and possible toxicity, as a result, homogeneous organic dyes were investigated as a possible alternative.

3.1.2 Homogeneous Photocatalysts Based on Organic Dyes

In addition to transition metal-based photocatalysts, a wide variety of fully organic dyes can be applied as photocatalysts, as highlighted in a comprehensive book chapter by Zeitler as well as a review by Romero and Nicewicz.[33,34] The usage of fully organic small molecule photocatalyst allows for a more environmentally friendly and economical approach due to the removal of expensive and rare earth metals. Dyes based on benzophenone,[35-37] acridinium,[38-40] thiazine,[41-43] or xanthene[44-47] have been

reported for a range of photocatalytic reactions. (Figure 3.2) Organic photocatalytic dyes require an extended conjugated π-system to enable visible light absorption, with smaller molecules like benzophenones, quinones, or quinoliniums only being active under UV-irradiation. Prominent fully organic photocatalysts are based on acridinium and xanthene derivatives, including Mes-Acr$^+$,[38] eosin Y, and rose bengal. These organic photocatalysts are readily available and have been well studied for applications in photocatalysis due to their beneficial HOMO/LUMO levels and bandgap allowing for visible light absorption. The optical and photophysical properties of fluorescein and its derivatives have been extensively studied over the last decades.

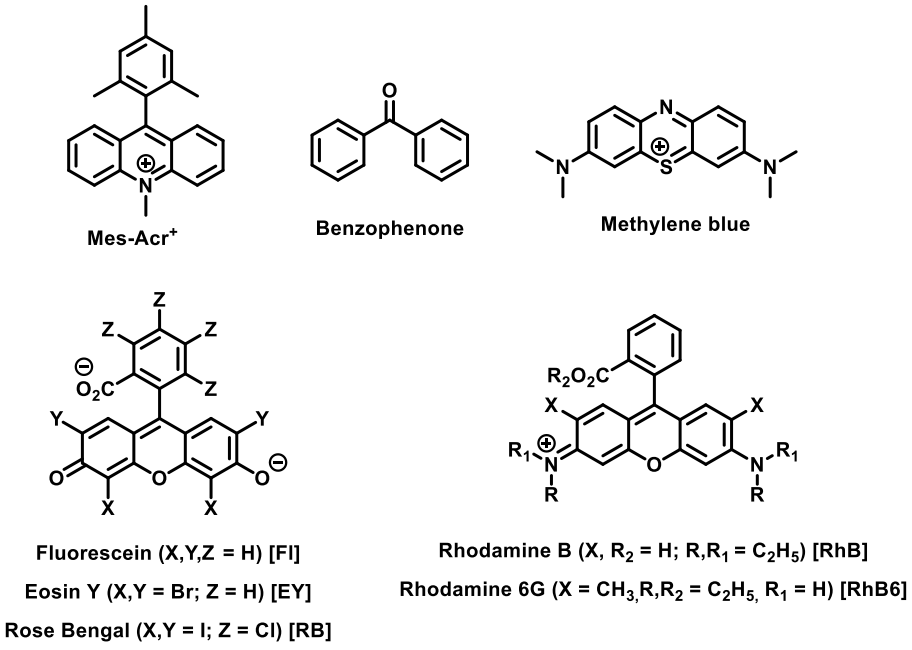

Figure 3.2 Common fully organic dyes used as photocatalysts based on acridinium, fluorescein, rhodamine thiazine.

Due to their functional groups, xanthene dyes possess different equilibrium forms as well as protonated and deprotonated forms. Different photophysical properties can be observed depending on protonation, leading to changes in the photocatalytic capabilities dependent on the solvent and protonation of the used dye. As an example, the neutral species of fluorescein possesses three tautomers, of which one disrupts the fully conjugated π-system and consequently does not absorb visible light. Slyusareva and Gerasimova highlighted the absorbance and fluorescence dependence of fluorescein, eosin Y and erythrosine B in regards to the pH, displaying lower absorbance at lower pH values.[48]

Majek *et al.* investigated the photocatalytic substitution of arene diazonium salts with bis(pinacolato) diboron using eosin Y as a photocatalyst. It was observed that under basic conditions or through the usage of DMSO as a solvent, a better photocatalytic efficiency could be achieved.[49]

Of the xanthene-based photocatalyst, eosin Y and rose bengal are commonly used due to fast occurring ISC and higher yield of the excited triplet state.[50,51] This effect can be explained through the degree of

halogenation and the corresponding heavy atom effect.[52,53] Fully deprotonated fluorescein possesses a high fluorescence quantum yield ϕ_f (FL = 0.93) but suffers from shorter fluorescence lifetimes (τ_f~4 ns) and low ϕ_{ISC} (FL = 0.03). In contrast, eosin Y and rose bengal undergo fast ISC, with ϕ_{ISC} increasing to ϕ_{ISC} (EY = 0.32) and ϕ_{ISC} (RB = 0.77). In turn, the higher amount of ISC generation of triplet states reduces the fluorescence lifetime and quantum yield accordingly.

The degree of halogenation further affects the photophysical properties, leading to changes in the redox potentials and red shifting the absorption and emission spectra.[54] Zhang et al. compared fluorescein with its halogenated derivatives. In the line of fluorescein, eosin y, and erythrosine, the required energy to reach the excited state S_1 decreases from 2.42 eV to 2.31 eV and 2.29 eV, showcasing the effect of halogenation.[54] Due to the high amount of ISC, halogenated xanthenes derivatives are efficient for triplet energy transfer reactions, like the formation of singlet oxygen,[55,56] which can oppose electron transfer reactions.[57] Further self-quenching has been observed between the semiconductors' ground state and the excited state.[58-60]

The efficient singlet oxygen generation and SET are used for photocatalytic reactions, and photodegradation of wastewater pollutants.[61,62] Rose bengal was reported for the photooxidation of organic sulfides.[63] A commonly reported photocatalytic reaction for FL-derivatives is the coupling of tetrahydroisoquinolines derivatives with a variety of nucleophilic substrates, including nitromethane, dialkyl malonates, malononitrile, and dialkyl phosphonates using eosin y or rose bengal under visible light irradiation.[64-66] Further photocatalytic reactions of tertiary alkyl amines include the [3+2] cycloaddition with alkynes or *N*-methyl maleimide, which was reported for the synthesis of pyrroloisoquinoline.[46] Reductive intramolecular cyclisation of bisenones was further reported by Neumann and Zeitler using eosin Y and Hantzsch ester or *N,N*-diisopropylethylamine (DIPEA) as a sacrificing agent.[67] The photocatalytic bromination of sp^3 C-H was successfully performed by Kee *et al.* in moderate yields.[47] Further, photoreaction examples include the hydrogenation of nitroarenes yielding the corresponding aniline derivative in good yields,[68] as well as the commonly reported aryl radical formation utilizing aryl diazonium salts.[69]

3.1.3 Homogeneous Photocatalysts based on Benzothiadiazole

Besides the usage of transition-metal complexes and organic dyes, π-extended benzothiadiazoles have been investigated as homogeneous photocatalysts.[70,71] Benzothiadiazole photocatalysts are based on a donor-acceptor design (D-A), allowing for systematic control over the bandgap, and HOMO/LUMO levels, with tunable absorption of visible light. D-A design combines electron-acceptor groups like benzothiadiazole with electron-rich donors in a small organic semiconductor. Upon light irradiation, an electron is excited into the LUMO, creating an electron-hole pair. The D-A design promotes charge separation and enables a longer excited state lifetime by preventing the electron-hole pair's recombination. By varying the electron-donor and – acceptor moieties in the molecule, the HOMO and

LUMO levels of the photocatalyst can be controlled. This allows for defined band gaps and absorption of visible light, regulating the optical and photophysical properties. The first extensive analysis of π-extended 2,1,3-benzothiadiazole derivatives was conducted by DaSilveira Neto *et al.* in 2005.[72] (Figure 3.3) The optical and electronic properties of the benzothiadiazole derivatives were characterized as possible candidates in OLED applications, including fluorescent lifetime and quantum yield measurements as well as determinations of band gaps and absorbance and emission spectra.
The D-A design was further developed by the group of Zhang in 2016 and applied for photocatalytic purposes as an alternative to traditional metal-based photocatalysts.[70] It was theorized that the D-A design would increase the photocatalytic moiety's reactivity due to the excited state's extended lifetime and control over the band gap and HOMO/LUMO levels.

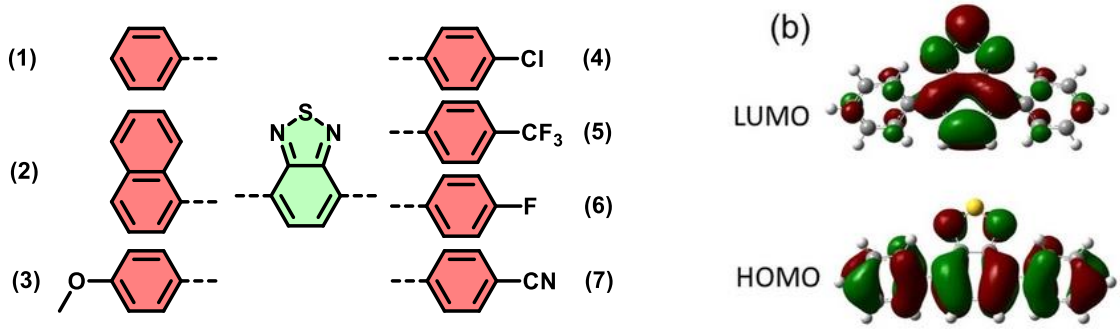

Figure 3.3 π-extended benzothiadiazole investigated by DaSilveira Neto *et al.*[72] (left). Calculated molecular orbitals of the HOMO/LUMO-level of diphenyl benzothiadiazole (1) indicating a shift in electron density upon irradiation.[73] (right) Reproduced with permission of Wiley-VCH Copyright © 2019.

Overall, five photocatalytic moieties were synthesized, combining electron-rich phenyl and thiophene groups with benzothiadiazole, benzoxadiazole, and benzoselendiazole as electron-acceptor moieties. Density functional theory (DFT) calculations were used to visualize the frontier orbitals, showcasing a significant shift in the electron density from the electron-rich donor moieties in the HOMO to the electron acceptor moiety in the LUMO. The D-A design proved to be efficient for a range of photocatalytic reactions, including dehalogenations, indole couplings, C-C couplings of aryl iodides with furan and pyrrole, bromation of alcohols as well as photoinitiator of polymerizations.[71,73-75]

Homogeneous photocatalysts have proven their efficiency and photoredox capabilities, synthesizing various products. Highlighting the possibility of photocatalysis to have an environmentally friendly impact on the chemical industry. Despite that, homogeneous photocatalysts possess a list of intrinsic drawbacks that hinder their implementation.[76,77] As mentioned, transition metal complexes require rare earth metals, which can lead to increased costs. Further, the environmental impact of mining these metals must also be considered. Fully organic dyes, while being more environmentally friendly, suffer from photobleaching and are, just like their counterparts, hard to recycle, potentially contaminating the desired product.[78] To account for these downsides, the development of heterogeneous photocatalysts offers a potential solution due to higher stability and easy recycling.

3.2 Heterogeneous Photocatalysis

In the following chapter, heterogeneous photocatalysts are introduced with a focus on fully organic photocatalysts.

In heterogeneous photocatalysis, the reaction medium and catalyst are phase-separated, allowing easy separation of the usually solid photocatalyst from the liquid reaction medium, leading to a simplified recycling and purification process. Therefore, heterogeneous photocatalysts improve upon the existing limitations of small molecular photocatalysts, which suffer from a lack of recyclability and are dependent on rare earth metals, while also suffering from photobleaching.[10,79]

Heterogeneous photocatalysts possess a band structure emerging from overlapping orbitals, broadening the discrete energy levels and forming energy bands based on the linear combination of the molecular orbitals.[80] Otherwise, heterogeneous photocatalysts work like their homogeneous counterparts by light absorption, which transfers the photocatalyst into the excited state. An exciton is created with an electron being transferred from the valence band (VB) to the conduction band (CB), leaving an electron hole in the VB. Lastly, the photocatalyst interacts with the substrate through energy- or electron-transfer. (Figure 3.4)

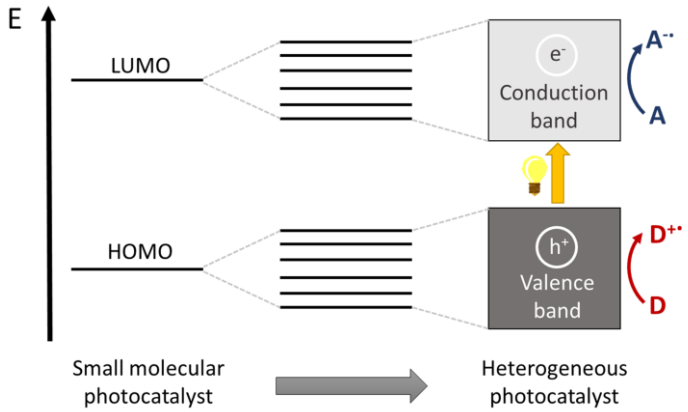

Figure 3.4: Formation of the band structure in heterogeneous photocatalyst, based on molecular orbital of a small molecular photocatalyst. Depictured mechanism of heterogeneous photocatalysis through light absorption followed by electron transfer from the photocatalyst towards an electron acceptor (A) or from an electron donor (D) into the valence band.

Therefore, creating an efficient heterogeneous photocatalyst is bound to specific requirements and an ideal combination of morphology, optical- and photophysical properties. (i) The energy level of the valence and conductive band must be chosen to increase the likelihood of an electron being excited to the CB, with the energy of the bandgap being in the visible light spectrum to increase quantum efficiency. (ii) The material must possess a high charge mobility to reduce the chance of recombination and a quick charge transfer to the surface.[81,82] (iii) The material must possess a high surface-to-volume ratio to increase substrate diffusion and photocatalyst-substrate interaction[83-85] while also possessing the necessary wettability.[86] (iV) Lastly, high light penetration depth with long excited lifetimes are required to reduce light scattering and catalyst loading. Due to this, various inorganic and organic heterogeneous photocatalysts have been created, covering a variety of structures and possible

applications. Inorganic photocatalysts are often based on TiO_2.[87-90] Unfortunately, TiO_2 only absorbs light in the high energy and low abundant UV-range. Therefore, other inorganic materials like Bi_2O_3,[91-93] CdS/CdSe,[94-97] lead halide perovskites,[98-100] and metal-organic frameworks (MOFs)[101-104] have been investigated as possible photocatalytic material to improve on this limitation and allow the adjustment of absorbance as well as HOMO/LUMO levels and the resulting bandgap.

In addition to inorganic photocatalysts, fully organic conjugated polymers have emerged as efficient photocatalysts based on conjugated mesoporous polymers (CMP), covalent organic frameworks (COFs) and covalent triazine framework (CTF). As a metal-free alternative, these systems are designed from readily available elements, possessing a chemically robust structure, while their conjugated design allows for an increased charge transfer.[105-108]

CMPs possess a fully organic amorphous structure with a fully conjugated π-system synthesized by metal-catalyzed coupling reactions. The polymerization of CMPs was first reported by Cooper and coworkers in 2007 through a Sonogashira–Hagihara coupling[109] but can also be achieved via different metal-catalyzed C-C-coupling reactions. In addition to the mentioned Sonogashira–Hagihara coupling,[110-112] the Suzuki-Miyaura coupling[113,114] is the most commonly used method, using halogenated aromatic monomers in combination with organoboron monomers to achieve a carbon-carbon formation in the presence of a palladium catalyst. Further possible methods include Yamamoto couplings between aryl halides using a nickel complex as the catalyst as well as Heck,[115] Glaser,[116] Schiff,[117,118] or oxidative[119] coupling. (Figure 3.5) The formed polymers possess exceptionally high chemical stability and tolerate a wide range of conditions and solvents while also reducing photobleaching. The conjugated π-system allows for an exciton diffusion and charge separation, increasing the excited state's lifetime. The mesoporous structure further increases the surface area, allowing for better substrate diffusion and photocatalyst-substrate interaction. The choice of monomer allows tuning of the conjugated structures and gives control UV/VIS-absorbance, optical and electronic bandgap. Therefore CMPs have been explored as heterogeneous photocatalysts for a variety of reactions, including hydrogen evolution,[120] CO_2 reduction,[121,122] amine coupling,[123,124] sulfide oxidation,[125,126] boronic acid hydroxylation,[127] aza-henry reaction,[111,128] dehalogenation,[129] C-C cleavage,[130] C-C formation,[131-133] dye degradations,[134,135] as well as cycloadditions.[136]

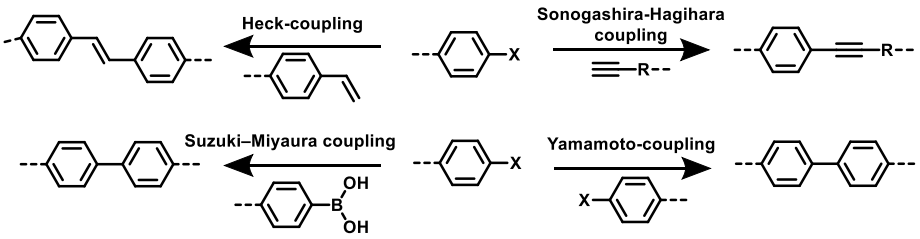

Figure 3.5: Methods utilized in coupling reactions to synthesis conjugated mesoporous polymers.

Compared to CMPs, covalent organic frameworks (COFs) possess a highly porous crystalline network based on covalent bonds between building blocks and linking groups.[137] Yahi reported the first COF in

2005 by synthesizing a porous material composed of rigid organic building blocks linked through boroxine anhydride formation.[138,139] Since then, numerous types of COFs have been designed based on a wide range of building blocks and linking groups utilizing imine,[140,141] azine,[142,143] heptazin,[144] boronic,[139,145,146] squaraine,[147] double bonds,[148,149] benzoxazole,[150] borosilicate,[151] and boranhydrid[146] and others possible linking groups.

The material properties of COFs are appealing for a range of possible applications,[152,153] including gas adsorption,[151,154,155] semiconductors,[105,156] wastewater remediation,[157,158] as well as photocatalysis.[105,108,144,148] COFs possess high chemical and thermal stability, preventing degradation and allowing for possible material recycling.[157,159] The crystallinity, in combination with an extended π-system, accelerates charge diffusion and electron-hole separation, increasing the lifetime of the excited state while simultaneously transporting the charge carriers to the surface.[105,137,138,148,159,160] They further possess a high surface area and high porosity, enhancing substrate diffusion, while the possibility to tune optical and photophysical properties enables visible-light absorption.[105,108,161] First usage of COFs for photocatalytic hydrogen evolution was reported in 2014 by Lotsch and coworkers.[161] A usage of 1,3,5-tris-(4-formyl-phenyl)triazine and 2,5-diethoxy-terephthalohydrazide as building blocks leads to hydrazone formation and a mesoporous 2D honeycomb-network.

Covalent triazine frameworks were introduced in 2008 by Kuhn *et al.* through trimerization of aromatic nitriles in molten $ZnCl_2$.[162] The resulting CTFs showed promising properties and high stability. The polymer consisted of a three-dimensional crystalline triazine-based organic framework, which possessed a highly porous structure with a high surface area. Since then, new synthesis strategies have been developed, allowing for milder reaction conditions.[163-167] This enabled the synthesis of various CTFs with tunable photophysical properties and three-dimensional mesoporous structure, which have been reported for photocatalysis, especially for hydrogen evolution,[168-171] CO_2 storage and reduction[172,173] or organic synthesis.[141]

Fully organic heterogeneous photocatalysts negate the intrinsic drawbacks of homogeneous photocatalysts, including toxicity, high production cost, photobleaching, and a lack of sufficient recyclability. The efficiency of heterogeneous photocatalysis depends on a high surface-to-volume ratio, substrate diffusion, and high light penetration.[174] To maximize these properties, the synthesis of CTFs was recently combined with silica templates, allowing the formation of nanoparticles, hollow shells, and nanoporous CTFs.[175-178] Further COFs with different morphologies, including sheets,[148,179] nanoparticles,[180] spheres,[181] hollow nanotubes,[182] nanofibers[183] have also been reported.

However, the material properties are dictated by the need for a fully conjugated polymer network, which leads to a variety of downsides. Heterogeneous photocatalysts are often hard to modify, and the design of specific structural designs depends on the usage of templates. They further possess poor wettability and are difficult to disperse in water.[184] Additionally, light scattering and low penetration depth, in combination with a slower mass diffusion, lead to a lower activity than their homogeneous counterparts.[174]

3.3 Photocatalytic Small Molecules Incorporated into Classical Polymers

In addition to CMP and COF, classical polymers have emerged as versatile support for incorporating photocatalytic moieties by combining the versatility and application range of polymers with the photocatalytic capabilities of homogeneous photocatalysts.[185,186] Classical polymers are based on small repeating units, which are covalently bound through a variety of possible polymerization techniques, including radical, controlled radical, or anionic polymerization, as well as polyaddition or polycondensation. Polymers are easy to synthesize and allow for various structural designs, morphologies, and tunable material properties. Depending on the desired structure and material properties, changes can easily be achieved by altering monomer choice and ratio, molecular weight, the addition of crosslinker, or the chosen polymerization method.

CMPs, COFS, and CTFs, on the other hand, require templates to design different structures, lack necessary control, or require difficult reaction conditions unsuited for upscaling.[176,187] Additionally, the photophysical and material properties depend on the conjugated π-system. Therefore, changes in the monomer or morphology can lead to changes in fully conjugated materials' optical properties.[120,187]

Combining the small molecular photocatalyst with classical polymers can, therefore, be used to introduce beneficial structures and material properties to heterogeneous photocatalysts. By doing so, certain disadvantages of heterogeneous photocatalysts, like limited mass transfer, poor wettability, low light penetration depth, and light scattering, are negated while simultaneously reducing the amount of required photocatalytically active material.

So far, the combination of polymers with photocatalysis has led to a broad range of achieved morphologies and methods, including particles,[188-194] capsules,[195] and dendrimers.[196,197] Further examples include linear,[198-202] crosslinked,[188,189,192,194,203-207] temperature and pH-responsive,[195,208-215]thermophore,[216,217] and graft-from polymers.[218] In addition, self-assembly-polymerization,[201,202,219-222] self-promoted polymerization,[74,223] and high internal phase emulsion polymerization (HIPE),[224] have been reported.

Homogeneous small molecule photocatalysts have been well studied, and their photocatalytic process has been well documented.[13,225-227] Through functionalization, these photocatalytic moieties can be incorporated into classical polymers. So far, free radical polymerization,[203,205] ATRP,[213,214] RAFT,[189,209,221] NMP,[218] and anionic polymerization[215] have been reported to incorporate photocatalytic moieties into classical polymers. At the same time, post modifications include click chemistry and non-covalent binding as well as nucleophilic substitution.[193,206,207]

Depending on the required photocatalytic capabilities, various photocatalytic moieties have been combined with classical polymers, including dyes like rose bengal[218,219] or BODIPY,[206] fully organic diphenyl benzothiadiazole,[186] porphyrin derivatives,[197] as well as rare earth metal complexes including

$Ir(ppy)_3$[217] and $Ru(bpy)_3$.[216] (Figure 3.6) Due to their incorporation into classical polymers the downside of homogeneous photocatalysis like poor recyclability and photobleaching can be addressed.

Therefore, the aim of the first two chapters of this thesis was to incorporate photocatalytic moieties into classical polymers to study the influence of the comonomer on the photocatalytic moiety and design heterogeneous photocatalysts with beneficial material properties.

So far, little is known about the influence of the comonomer choice on the photocatalytic efficiency, and monomers are chosen with specific structural designs in mind. Therefore, in the first chapter we investigate the influence of monomers on the photocatalytic efficiency. A further downside of heterogeneous photocatalysts can be the low light penetration into the material, reducing the overall efficiency. In the second chapter, a high transmittance hydrogel was designed, allowing light to penetrate the support material and only being absorbed by the photocatalytic moiety.

In the following chapter, we highlight the current state of research on the design strategies for incorporating small molecular photocatalysts into classical polymers and their morphologies. (Figure 3.6) These structural designs include particles, capsules, star-shaped polymers, dendrimers, microgels, and crosslinked porous structures.

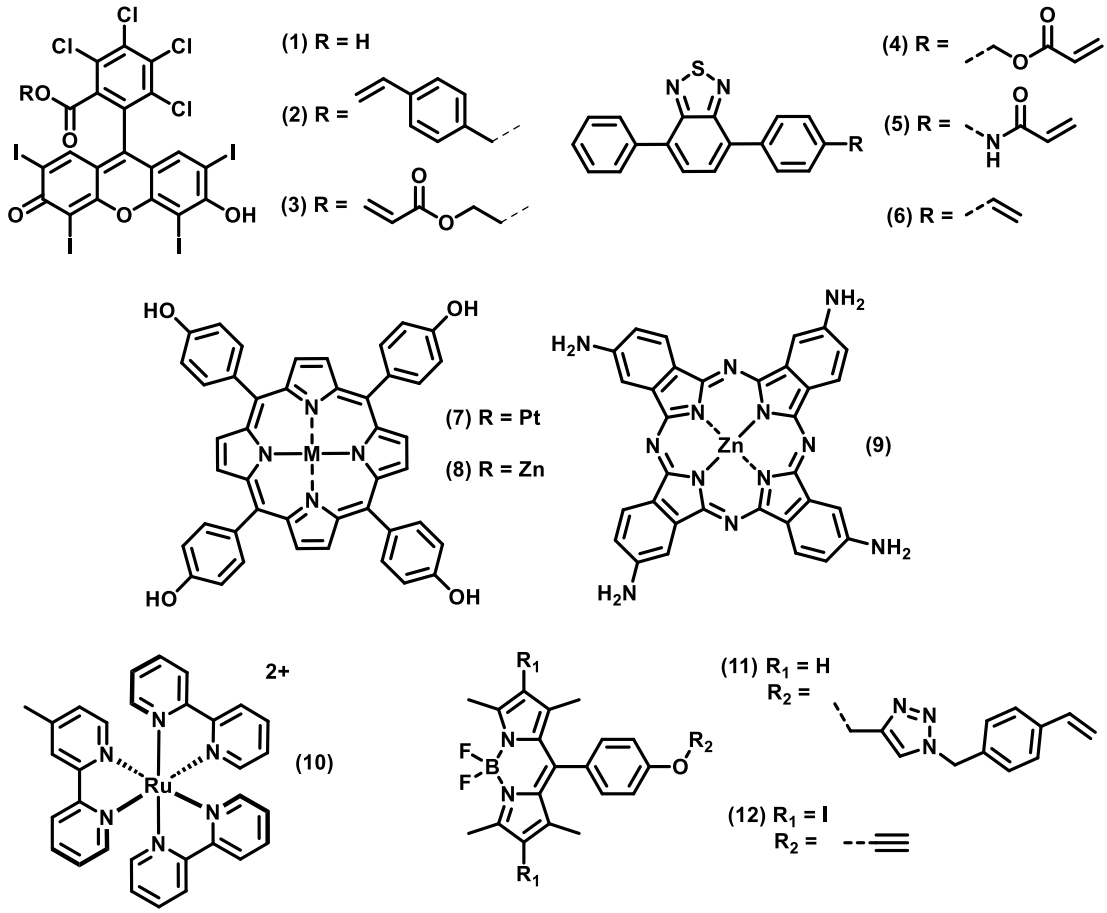

Figure 3.6 Small molecular photocatalyst incorporated into classical polymers.

3.3.1 Particles

Some of the first reports of incorporating photocatalytic moieties in classical polymers were published by Neckers` group in 1975, combining photocatalytic dyes with a Merrifield resin.[193] Merrifield resin consists of a crosslinked styrene-divinylbenzene copolymer with a chloromethylated surface functionalization and was used as a heterogeneous polymer support. Five dyes were covalently bound to the particle surface and used for the photooxidation of double bonds. These photocatalytic dyes, possessing a carboxyl group, including rose bengal, were used for surface functionalization through simple nucleophilic substitution. (Figure 3.6 **(1)**) Neckers` group achieved a surface modification of 20% using rose bengal and used the heterogeneous photocatalyst for the production of singlet oxygen and the photooxidation of electron-rich alkenes in dichloromethane. The bound photocatalyst could outperform the homogeneous dye due to its low solubility in the solvent and better dispersion of the heterogeneous photocatalyst.

The surface modification of Merrifield resin was further developed by Burguete *et al*.[228] After surface modification of Merrifield resin with rose bengal, the remaining chloromethyl-groups were reacted with pyridine, resulting in a positively charged and more hydrophilic surface. (Figure 3.6 **(1)**) The photocatalyst was used to oxidize furoic acid via singlet oxygen in methanol. Compared to the previous report by Neckers and coworkers,[193] the free dye was fully dissolved. However, it was still outperformed by the charged resin, while the resin only modified with rose bengal could not outperform the free dye. Lastly, the recyclability was showcased over 11 cycles, reaching complete conversion in all cases. Although the post-modification of synthesized particles is a well-established procedure, the design of photocatalysts, which can be easily copolymerized into polymers, allows for higher flexibility over synthesis approach, concentration, position, and monomer choice.

The group of Save reported the combination of RAFT-mediated polymerization-induced self-assembly (RAFT-PISA) with photocatalytic moieties in two different publications.[201,219] Rose bengal was functionalized and copolymerized with acrylic acid via RAFT polymerization, followed by chain extension with a second block using n-butyl acrylate as a monomer, which led to the formation of water-stabilized latex nanoparticles with narrow dispersion and a diameter of 85 nm.[201] (Figure 3.6 **(2&3)**) Further investigation of the RAFT polymerization showed that rose bengal did not hinder polymerization or particle formation. The formed particles could further be used to cast a film on glass surfaces. The photocatalytic efficiency was demonstrated through the photo-oxygenation of furfuryl alcohol under visible light irradiation at 515 nm. Quantum yield calculations showed that the nanoparticles were highly efficient in producing singlet oxygen but were still slightly outperformed by the free RB.

In a follow-up study, the effect on $^1O_2$ production was investigated by altering the position of the photocatalytic moiety, placing the photocatalyst either in the hydrophilic shell or the hydrophobic core.[219] (Figure 3.6 **(2&3)**) The formed latex-NP had comparable diameters close to 100 nm. Again, high

quantum yields for the formation of singlet oxygen were observed without any apparent dependence on the position within the NP.

Li *et al*. also reported the usage of RAFT-PISA for the design of a pH-responsive photocatalytic nanoparticle.[209] Responsive systems allow the introduction of external triggers to activate and deactivate the photocatalytic capabilities of the heterogeneous photocatalyst, enabling controlled activation and easy recovery of the photocatalysts under constant light irradiation.
In the first step, a di-block copolymer was synthesized from diisopropylamine ethyl methacrylate (DPA) and a functionalized photocatalytic moiety. (Figure 3.6 **(4)**) Chain extension with hydrophobic benzyl methacrylate led to the self-assembly of the polymer, creating a core–shell polymer nanoparticle. (Figure 3.7) Upon protonation, the PDPA was protonated, stabilizing the nanoparticle in water and giving access to the photocatalytic moiety. The PDPA chains were deprotonated at high pH values, and the nanoparticles aggregated, deactivating the photocatalytic nanoparticles. The system was used for four photocatalytic reactions and recycling tests, including the reduction of Cr^{VI} and C-C coupling of 3-methyl indole with β-nitrostyrene.

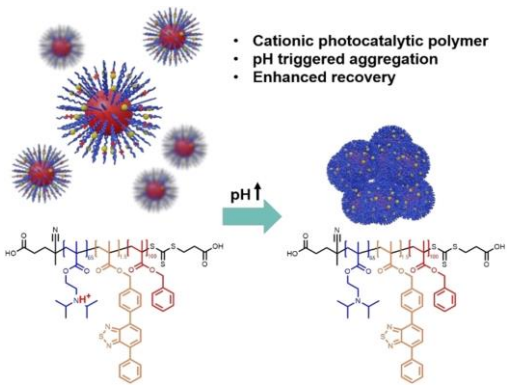

Figure 3.7 Schematic aggregation of pH-responsive RAFT-PISA photocatalytic nanoparticle[209] Reproduced with permission of the author. (CC BY 4.0)

Besides the combination of nanoparticles and small molecule photocatalysts, Shiraishi *et al*. demonstrated the usage of a SiO_2-NP template for the encapsulation of a single photocatalytic dye into a thermoresponsive crosslinked poly(*N*-isopropylacrylamide) shell.[195] PNIPAM possesses an advantageous lower critical solution temperature (LCST) in water, leading to the precipitation of the polymer at elevated temperatures.
The encapsulation of the photocatalytic dye in a thermoresponsive PNIPAM was performed in four steps. First, SiO_2-NP were synthesized through hydrolysis in the presence of methylene blue (MB), trapping the dye. The NP were then surface-functionalized, and through radical polymerization of NIPAM and crosslinker, PNIPAM was grown on the NP-surface. Lastly, the etching of the template

yielded the encapsulated homogeneous photocatalyst (TH@PC). (Figure 3.8) At room temperature, the capsule possesses a diameter of 550 nm. Under heating, the PNIPAM collapses, reaching a capsule diameter of 365 nm at 31 °C before aggregating. The singlet oxygen production was measured at increasing temperatures and compared to the free dye, and a copolymer of PNIPAM and the photocatalyst. Using TH@PC led to a complete suppression of singlet oxygen formation at elevated temperatures, outperforming the copolymer and highlighting an efficient on-off switchable heterogeneous photocatalyst.

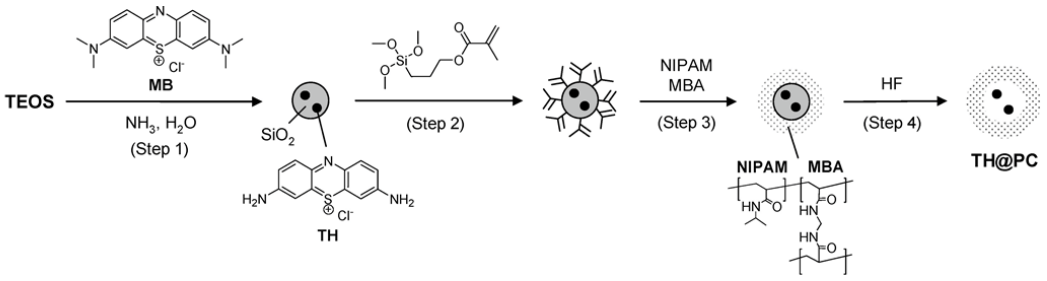

Figure 3.8 Synthesis route for encapsulated homogeneous methylene blue in thermoresponsive crosslinked PNIPAM shell.[195] Reproduced with permission of the American Chemical Society Copyright © 2008.

3.3.2 Microgels

The formation of microgels allows for the swelling of colloids in solvents. Ideal support for photocatalytic moieties allows for larger pore sizes and better substrate diffusion.

Save and coworkers reported the first photocatalytic microgel based on vinyl acetate, *N*-vinyl caprolactam, and divinyl adipate as crosslinker.[188] The colloids were formed through miniemulsion polymerization, including functionalized rose bengal as a photocatalyst. (Figure 3.6 **(2),** Figure 3.9) The resulting microgel was designed to swell in ethanol and reached a hydrodynamic radius of 260-285 nm, depending on crosslinker concentration. The photocatalytic capabilities of the microgel were analyzed via singlet oxygen quenching with furfuryl alcohol and diphenylisobenofuran performed in water or ethanol, respectively. Measured singlet oxygen quantum yields show a lower performance for the microgel than the free dye. The microgel collapses in water, and the singlet oxygen quantum yield is significantly reduced. Nevertheless, even in ethanol, the free dye outperforms the microgel, although the gap is reduced. However, the microgel could be repeatedly used for up to five cycles without significant loss in efficiency. Further, the stability of the microgel was highlighted, showcasing reduced photobleaching under irradiation compared to the free dye.

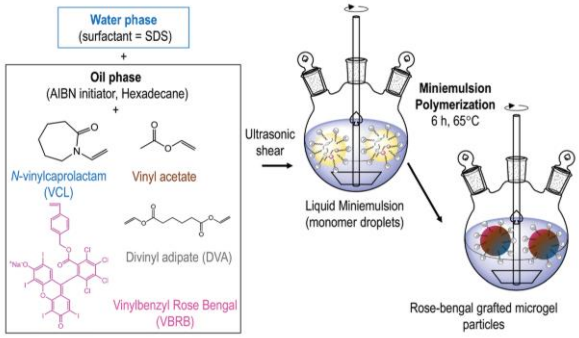

Figure 3.9 Schematic miniemulsion polymerization for the synthesis of photocatalytic microgels.[188] Reproduced with permission from the Royal Society of Chemistry.

In further work, the microgel was applied for heterogeneous photocatalysis in flow.[222] The microgel was used in a gas-liquid-solid setup for the in-flow photocatalytic conversion of α-terpinene to ascaridole in ethanol. Through the usage of a flow setup, light penetration could be significantly increased, leading to a fast conversion. The authors assume that the gas-liquid-solid setup leads to an effective mixing of substrates and more efficient oxygen transport. The usage of a microgel allowed the recycling of the heterogeneous material and reduced the amount of photobleaching compared to the free dye. Highlighting the application of a heterogeneous photocatalytic system over its homogeneous counterparts and supporting the previous findings.[188]

A temperature-responsive photocatalytic microgel was reported by Ferguson *et al.*[208] Comparable to Shiraishi *et al.* work,[195] the LCST of P(NIPAM) was exploited to exercise control over the photocatalytic activity. Emulsion polymerization of NIPAM, crosslinker, and a diphenyl-benzothiadiazole-based photocatalyst yielded a microgel with a diameter of 190 nm. (Figure 3.6 **(5)**) However, the microgel diameter decreased sharply to 70 nm upon heating, hindering the photocatalytic activity. The system was used for four photoreactions, including the oxidation of NADH to NAD^+. The controllable on-and-off switching of the photocatalytic microgel was proven through two kinetic measurements. The NADH conversion was monitored at 25 and 40 °C, reaching 70% conversion at 25 °C, while no significant conversion was observed at 40 °C.

3.3.3 Star Shaped Polymers and Dendrimers

Star-shaped polymers possess a single central core with multiple extending polymer chains. The polymer chains can be used to increase the solubility of the core in various solvents and introduce thermo- or pH-responsive behavior. The introduction of a small molecule photocatalyst into a star shape polymer could lead to an accessible photocatalytic center stabilized by the polymer chains.

Zuo *et al.* synthesized a star-shaped polymer based on a porphyrin core (THPP) and poly(2-(dimethylamino)ethyl methacrylate (PDMAEMA) chains.[215] (Figure 3.6 **(7)**) The amphiphilic star-shaped polymer possessed a hydrophobic core, complexing platinum and hydrophilic polymer chains creating unimolecular micelles (UMs). At low pH, PDMAEMA is protonated and increases the solubility of the UMs in water. Upon deprotonation, the polymer chains became hydrophobic, and the UMs aggregated. (Figure 3.10) The system was used for photocatalytic H_2 evolution using ascorbic acid as a sacrificing agent. Under low pH, the star polymers self-assembled into ultra-small Nanoparticles with a high hydrogen generation rate of 2028 µmol $g^{-1}h^{-1}$. A high pH-value led to aggregation and precipitation, hindering the mass transfer and reduced the catalytic activity to 172 µmol $g^{-1}h^{-1}$. In comparison, combining Pt-loaded THPP with linear PDMAEMA leads to the aggregation of the photocatalyst and a low H_2 generation of 26.3 µmol $g^{-1}h^{-1}$.

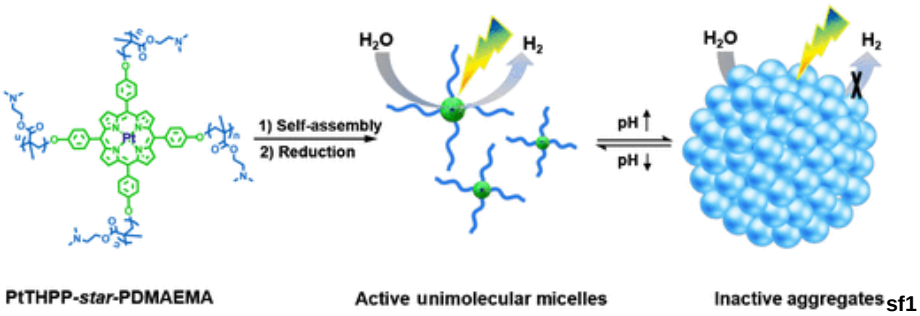

Figure 3.10: Working mechanism of pH-responsive star-shaped polymer with hydrophobic porphyrin core.[215] Reproduced with permission of the Chinese Chemical Society © 2020.

Further thermoresponsive photocatalytic designs were reported by Duan and coworkers utilizing ATRP to synthesize a series of thermoresponsive photocatalytic star-shaped copolymers. Combining PNIPAM chains with porphyrin or phthalocyanine derivatives as photocatalysts and hydrophobic cores.[212-214] (Figure 3.6 **8&9**) The synthesized photocatalysts were used to photodegrade organic dyes and could be recycled by precipitation at higher temperatures.

Dendrimers

Over the years, dendrimers have attracted attention for possible use in drug delivery, biomedical or industrial applications.[229,230] Dendrimers have a highly symmetric, branched structure consisting of three parts. A core, branches called generations, and terminal functional groups give dendrimers their tree-like three-dimensional network. Their highly branched structure with accessible, functional groups makes them possible support material for the fixation of small molecular photocatalysts.

Guerra *et al.* reported the combination of a second-generation polyamidoamine (PAMAM) dendrimer with a fixated ruthenium-based photocatalyst for continuous flow photocatalysis.[196] (Figure 3.6 **(10)**) In the first step, PAMAM was functionalized with a bipyridine group to allow the complexation of $Ru(bpy)_2Cl_2$, leading to a recyclable heterogeneous photocatalyst. (Figure 3.11) It was reported that from 16 terminal groups per dendrimer, on average, 14.7 could be functionalized. The photocatalyst was then used in a continuous flow to catalyze three photoreactions and compared to the homogeneous equivalent. Using the dendrimer for the halogenation of alcohols showed near-complete conversion. Additionally, the halogenation of alcohols, a reductive ring opening of chalcone-α,β-epoxide, and an azide reduction were performed, achieving comparable results to the homogeneous photocatalyst. The material could be recycled with the benefit of little to no ruthenium leaching but required nanofiltration.

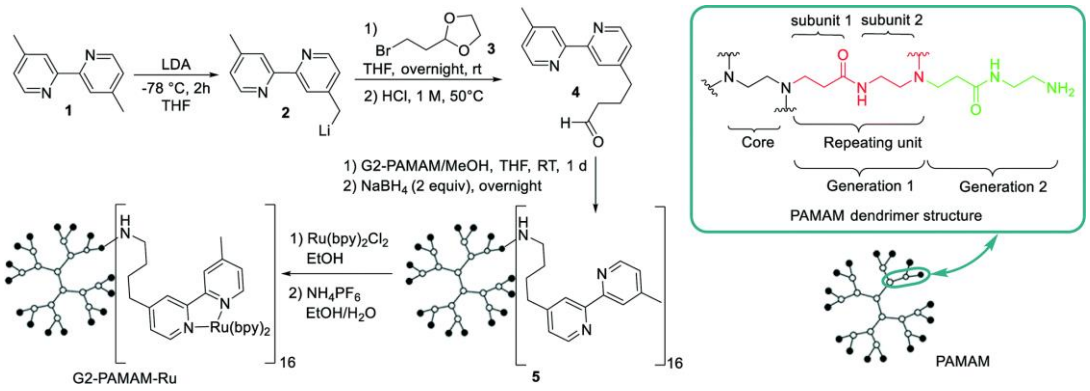

Figure 3.11 Synthesis route for photocatalytic dendrimer. Based on second generation PAMAM dendrimer.[196] Reproduced with permissions from the Royal Society of Chemistry.

Other examples of the possible combination of photocatalytic moieties and dendrimers were reported by Chavan *et al.* synthesizing porphyrin-functionalized dendrimers.[197] The dendrimers were based on halogenated pyrimidine derivatives, functionalized with phenolic porphyrin via nucleophilic aromatic substitution. The yielded dendrimers were used for the photooxidation of six olefins via singlet oxygen, yielding the corresponding allylic hydroperoxides. Although near-complete conversions were achieved, all olefins formed regioisomers upon oxidation. The dendrimers could further be recycled

via nanofiltration, but the recycling test showed significant photodegradation of the porphyrin. Further photodegradation experiments over 20 h at 0 °C showed a decrease in absorbance by 75%.

3.3.4 Porous Three-Dimensional Networks

In addition to the formation of particles, microgels, and dendrimers, polymers can also be used to synthesize highly porous three-dimensional networks. These structures can have a high surface area and chemical stability, making them ideal substrates for incorporating photocatalytic moieties. Depending on the chosen monomers, crosslinker concentrations, and polymerization methods, rigid structures, as well as organo- or hydrogels, can be synthesized.

Save and coworkers prepared a heterogeneous honeycomb structured photocatalyst via NMP of styrene and 4-vinylbenzyl chloride followed by breath figure self-assembly.[218] The breath figure process utilizes small water droplets as templates, while the more polar functional groups of the polymer position at the water surface area. The honeycomb structure self-assembles during evaporation of the solvent under highly humid airflow. A statistical copolymer was synthesized via NMP, and the photocatalytic moiety rose bengal was grafted on the polymer. (Figure 3.6 **(1)**) Through nucleophilic substitution, approximately 1/6 of copolymer chains were functionalized. The heterogeneous photocatalyst consisted of three layers and pore sizes of 2-2.5 µm. In contrast, using non-grafted rose bengal in combination with the statistic copolymer led to a disruption of the self-assembling and a non-porous film. Further leaking of RB was observed in the non-covalently bound version. The heterogeneous photocatalyst was used for the photooxidation of 1,5-dihydroxy naphthalene and α-terpinene in ethanol under visible light irradiation. The honeycombed structured photocatalyst outperformed the non-porous film in both cases. Nevertheless, a significant amount of photobleaching was observed for the covalently bound photocatalyst, reducing its adaptability. Over a span of eight hours, 75% of the grafted rose bengal was degraded, which was attributed to the general low photostability of rose bengal.

A non-covalent surface modification was reported by Li *et al.*, modifying polydimethylsiloxane (PDMS) with rose bengal for cross-dehydrogenative coupling reactions of tetrahydroisoquinoline.[207] (Figure 3.6 **(1)**) A highly porous sponge-like PDMS structure was created using a sugar template method.[231] (Figure 3.12)

The PDMS sponge was then functionalized over three steps with 2-(methacryloyloxy) ethyl trimethylammonium chloride yielding ammonium groups on the surface. Through ion exchange, the disodium salt of rose bengal was non-covalently attached to the surface, yielding a heterogeneous PDMS-based photocatalyst. SEM and EDS mapping show a highly porous 3-dimensional structure with homogeneous photocatalyst distribution. As photoreactions, a scope of 16 cross-dehydrogenative coupling reactions was performed, reaching high conversions and highlighting the recyclability over 15

cycles. The sponge was further used for an upscaled one-gram reaction using a continuous flow reactor, reaching 88% conversion over 48 h under green light irradiation.

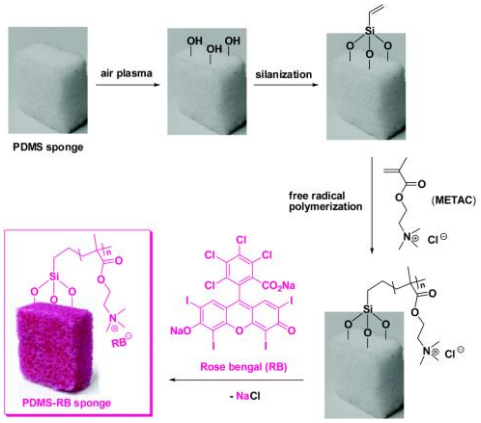

Figure 3.12: Non-covalent surface modification of a heterogeneous PDMS sponge with rose bengal.[207] Reproduced with permission from the Royal Society of Chemistry.

Li *et al.* reported the usage of high internal phase emulsion (HIPE) polymerization to synthesize a highly porous photocatalytic polymer.[206,224] HIPE polymerization allows the synthesis of porous and tunable polymer networks and is a promising support for photocatalysts. Five heterogeneous photocatalysts were synthesized based on styrene and divinylbenzene and using a functionalized boron-dipyrromethene (BODIPY) as a photocatalyst (BODIPY)-HIPE). (Figure 3.6 **(11)**) The created material possessed up to 6.5 wt.% of photocatalyst and had an average cavity size of 10 µm diameter, reaching up to 40 µm. The fluorescence peak could be observed at 509 nm, giving a high quantum yield of 0.72. The heterogeneous photocatalyst was used for the photooxidation of five organic sulfides in methanol using visible light (400 to 700 nm). The material could be recycled and was used up to nine times, reducing the overall conversion from 99% to 90%.

Even though (BODIPY)-HIPE showed photocatalytic activity, the incorporated photocatalytic moiety was distributed evenly in the material and not only on the surface, reducing the efficiency. For this reason, Li *et al.* improved this work by functionalizing the heterogeneous support after polymerization instead of through direct copolymerization.[206] Styrene, divinyl benzene, and 4-vinylbenzyl chloride were copolymerized via HIPE, and the resulting porous material was functionalized using sodium azide. (Figure 3.13) Through a click reaction, a functionalized iodo-BODIPY photocatalytic moiety was covalently attached to the surface of the heterogeneous support material. (Figure 3.6 **(12)**) The material had a lower cavity diameter of approximately 4.5 µm than its predecessor, a surface area of 230 m^2g^{-1}, and a photocatalyst loading of 15.32 wt.%. The smaller pore size was attributed to a possible collapse during the surface modification. The photooxidation of five organic sulfides was performed and compared to the previously reported (BODIPY)-HIPE.[196] It was shown that the heterogeneous photocatalyst using an iodo-BODIPY possessed a higher photocatalyst loading concentrated on the polymer surface and achieved a higher conversion rate.

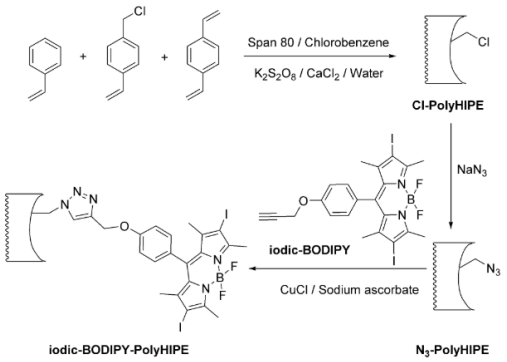

Figure 3.13 Synthesis of the heterogeneous support via HIPE followed by surface modification through azide-alkyne cycloaddition.[206] Reproduced with permission of Wiley-VCH © 2017.

3.3.5 Macrogels

The formation of a macrogel allows for the usage of flexible polymer networks as support. Allowing for swelling in solvents and increasing diffusion of substrates, allowing for better photocatalyst-substrate interaction.

A further organogel was recently reported by the group of Zhang.[203] A photocatalytic moiety based on a donor-acceptor design was randomly copolymerized with a PEG-crosslinker and methyl methacrylate. The resulting organogel readily swelled in nitromethane and was correspondingly used for [4+2]-cycloadditions under blue light irradiation. Vinyl-functionalized diphenyl benzothiadiazole was used as a photocatalytic moiety, allowing quick cycloaddition of trans-anethole and isoprene. (Figure 3.6 **(6)**) A substrate scope of eleven substrates was demonstrated, achieving high conversion and allowing the recycling of the heterogeneous photocatalyst.

In further work, the crosslinked organogel was modified through an additional monomer.[232] Through additional sodium 4-vinyl benzenesulfonate, the hydrophilicity of the gel could be tuned to allow swelling in water. The network could be used under visible light irradiation for pollutant degradation in water. Four pollutants in the form of 2,4-dichlorophenol, diethyl phthalate, acetophenone, and bisphenol-A could be degraded under an oxygen atmosphere.

3.3.6 Conclusion

The combination of small molecular photocatalysts with classical polymers allows the design of novel photocatalytic materials with control over morphology and material properties, which addresses the drawbacks of heterogeneous photocatalysts while also stabilizing small molecular photocatalysts. In this work, chapters 5.1 and 5.2 combine a fully organic small molecular photocatalyst with classical polymers. In chapter 5.1, linear copolymers were synthesized to analyze the effect of the comonomer on the photocatalytic efficiency and photophysical properties, while in chapter 5.2, a high transmittance photocatalytic hydrogel was created, allowing for efficient pollutant remediation under visible light irradiation.

3.4 Combining Photocatalysis with Proteins

In nature, enzymes perform a critical role by catalyzing a wide variety of essential reactions under mild and benign conditions. As biological catalysts, enzymes are complex biomolecules based on a polypeptide amino acid sequence, which gives enzymes their three-dimensional structure. This protein scaffold, in combination with an often-required cofactor, allows the efficient and highly effective catalysis of stereo- and regioselective reactions. These reactions are often substrate-specific and can target non-reactive parts of the substrates, which are often not achievable with a common catalyst. An example being the Flavin-dependent halogenase RebH enabling the regioselective C-7 halogenation of tryptophan.[233,234]

Although used for fermentation since ancient times, the actual discovery of enzymes is contributed to Anselme Payen in 1833.[235,236] Kühne in 1877 introduced the now commonly used term “enzyme”, but only by 1894 the now famous lock and key model was introduced by Emil Fischer.[237,238]

Nevertheless, only over the last decades has enzyme usage in industrial processes been explored as an alternative to classical catalysts. In recent history, two prominent figures contributed to the now rapid development and continuous research into protein engineering. Smith received the Nobel Prize in Chemistry in 1993 for his work on site-directed mutagenesis in 1978.[239] Further, Arnold and Stemmer were bestowed with the Nobel Prize in 2018 for their work on directed evolution.[237,240-242] Since then, usage of public databases in combination with computational analysis of sequence homology has led to a stark increase and access to modified enzymes, allowing for a wider range of possible applications.[243-246]

Due to their abilities, enzymes have recently attracted a lot of attention as a more environment-friendly and efficient approach to catalyze reactions in industrial applications like the synthesis of drugs or high-value chemicals.[247-249] Enzymes possess several advantages over regular chemical catalysts, including the previously mentioned capabilities to catalyze highly selective and specific reactions while considering stereo and regioselectivity, resulting in fewer side products and reducing the amount of undesired site products. Further advantages are the mild reaction conditions in which proteins operate. Lower temperature and pressure are required, reducing energy consumption while also using water as a green solvent. These benefits, combined with a fully biodegradable catalyst, lead to a highly sustainable approach, reducing their carbon footprint and the environmental impact of industrial processes.

Additionally, replacing classical catalysts can remove the requirement for rare earth metals like ruthenium and iridium, often used in asymmetric catalysis. Substituting them with renewable resources prevents further mining and competition with other resource-demanding industries. Therefore, enzymes can be produced from less expensive resources, leading to further economic

benefits and a more independent industry and improving planning securities from the global supply of precious metal and possible cost fluctuations.[250-252]
Nevertheless, significant hurdles still need to be overcome for a wider adaptation of biochemistry. First and foremost, the adaptation of enzymes is hindered by their own unique features. Enzymes substrate specificity is of significant importance in organisms but also limits their application range. As a result, changes in the peptide structure are often required to allow the combination with unnatural substrates. Due to their peptide structure and three-dimensional protein scaffold, enzymes are often incompatible with industrial processes as they can be sensitive to pH value, temperature, and solvent changes, leading to the denaturation of the biocatalyst.[249,253,254] This low stability severely limits the compatibility with existing processes. The greatest challenge, however, is the dependence on costly cofactors in stoichiometric quantities, reducing the economic validations of enzymes over less efficient chemical procedures.[255] In nature, these cofactors like nicotinamide adenine dinucleotide (phosphate) (NAD(P)) or flavin adenine dinucleotide (FAD) are constantly recycled and play a crucial role in their activity.

The combination of photocatalysis with biocatalysis is a beneficial method to negate the dependence on expensive cofactors.[255] Photocatalysis is a promising approach that meets the necessary requirements and offers an efficient synergetic effect. It is a gentle and environmentally friendly method, which allows for benign reaction conditions by utilizing visible light. Currently, two pathways are investigated to combine the benefits of these environmentally friendly catalytic methods, by either using the photocatalyst in solution for cofactor recycling or covalently binding the photocatalytic moiety to a modified protein. The need for stoichiometric usage of expensive cofactors can be negated by constant *in situ* recycling of these cofactors. Therefore, heterogeneous[256,257] as well as homogeneous[258-261] photocatalysts have been employed to regenerate the cofactor. In combination with an enzyme, these photocatalysts have been used to catalyze a variety of reactions, including reduction of α,β-unsaturated alkenes,[259,262-264] reduction of aldehydes,[256] oxidation of alcohols,[257] halogenations aromatic compounds.[260,261]
This method requires no enzyme modification and allows one to choose a specific enzyme to catalyze a desired reaction, while the photocatalyst is chosen depending on the used cofactor.
The downside of this method is that they are hard to optimize, as the used photocatalyst and enzyme possess different reactivity, leading to undesired side reactions or degradation of the enzyme.[256,257] Furthermore, these setups still require the presence of cofactors, are dependent on the efficiency of the enzyme, and can be outperformed by the enzymatic regeneration of cofactors.[261] Another downside is the often required usage of mediators, complicating the systems further.[262,264,265]
The preferable approach is, therefore, the development of a complete artificial photo-enzyme by covalently binding the photocatalytic moiety to the enzyme. This approach, in particular, is a highly

desirable aim as it pairs the benefits of enzymatic precision with the substrate range and capabilities of state-of-the-art chemical photocatalysts.

3.4.1 Artificial Photoenzymes

Artificial photoenzymes combine the benefits of photocatalysis with bioengineering by covalently binding a photocatalytic moiety to a protein. Compared to the free photocatalyst in solution, this improves the interaction between the protein scaffold and the photocatalytic moieties.[266] These artificial photoenzymes are not dependent on a mediator or cofactors, or they are limited by diffusion. The photocatalyst can be used in combination with an actual cofactor for electron or energy transfer to the catalytic center.[267,268] Further, through protein engineering, a photocatalytic moiety can be introduced as an active center while the protein scaffold is modified to increase reactivity, substrate- or stereoselectivity.[266,269,270]

In 2010 Cheruzel and coworkers incorporated a photocatalytic moiety into the monooxygenases Cytochrome P450-BM3 from Bacillus megaterium for mechanistic investigation of the P450 catalytic cycle.[268] The enzyme possesses a prosthetic Heme group, which catalyzes the hydroxylation of fatty acids. Through site-directed mutagenesis, three residues were replaced. Two native cysteine residues (C62A, C156S) were removed, while a non-native cysteine was introduced (K97C). After expression, the variant was bioconjugated with a functionalized ruthenium photocatalytic moiety $[Ru(bpy)_2(IA\text{-}phen)]^{2+}$ (5-iodoacetamido-1;10-phenanthroline = IA-phen). The photoenzyme was used for transient absorption measurements with ruthenium(III)-hexamine trichloride as a quencher. Cheruzel and coworkers observed an electron transfer from the photosensitizer to the prosthetic Heme.

Following these first findings, the group around Cheruzel used the photoenzyme for the hydroxylation of lauric acid in $\omega_{1\text{-}3}$-position under visible light irradiation, using sodium diethyldithiocarbamate (DTC) as sacrificing agent and removing the need for NAD(P)H as cofactor completely.[271]

It could be shown that in comparison to the wild-type domain using H_2O_2 as an electron and oxygen donor, the two artificial photoenzymes Ru-Q397C-BM3 and Ru-K97C-BM3 had a higher TON. Further, using a photosensitizer in combination with DTC did not affect the regioisomer ratio.

In further work, the stability and efficiency of the artificial photoenzyme could be significantly improved. By experimenting with the position of the photosensitizer, optimizing the proximity to the active Heme catalyst, and altering the photocatalytic moiety by functionalizing the bipyridine ligands with methoxy groups, the overall turnover number could be increased significantly. Outperforming previous publications in the same field, highlighting the impact of the moiety's positioning and combining photo- and biocatalysis capabilities.[267] (Figure 3.14)

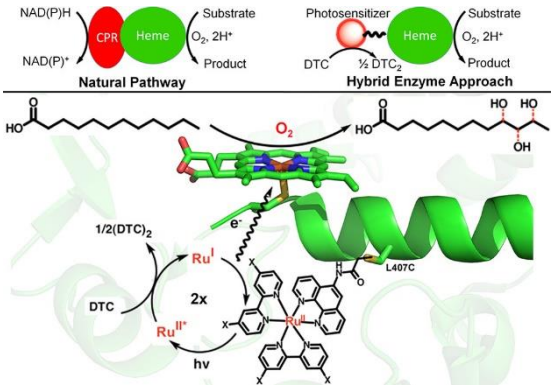

Figure 3.14. Comparison of the natural redox reaction and the pathway using the artificial photoenzyme. (top) Detailed interaction between the photocatalyst and the active center.[267] Reproduced with permission from the American Chemical Society Copyright © 2013.

Similarly to Cheruzel, Wang and coworkers mutated superfolder yellow fluorescent protein to create an artificial photoenzyme capable of reducing CO_2.[272] Introducing a photosensitizer in the form of benzophenone and a terpyridine nickel complexes as the active center to achieve an electron transfer under light irradiation. As the naturally occurring enzyme has an insufficient excited state lifetime, which would be too short for an efficient electron transfer, Tyr66 was replaced using genetically encoded benzophenone–alanine. Further mutating the enzyme by replacing Tyr203 with Phenylalanine yielded PSP1, and the photochemical reduction of PSP1 under irradiation in the presence of dithionite as a sacrificing agent was observed. Unfortunately, no biological sacrificial reduction agent was applicable due to the too-high reduction potential of benzophenone. Therefore, two further modifications were required (Tyr203Asp, His148Glu) to yield PSP2 by introducing charged residues in the area around the photosensitizer, the reduction potential could be modulated, and ascorbic acid could be used as sacrificing agent. X-ray crystallography further indicated a change in the confirmation of PSP2 with a rotation of the benzene ring upon irradiation and reduction.

Three further mutations were performed to allow an efficient reduction of CO_2, followed by the bioconjugation of a modified terpyridine ligand to an unnatural cysteine residue. Mechanistic investigations showed that a distance between the photosensitizer and catalyst is required to allow a two-electron transfer. The excited-state lifetime of the photosensitizer was determined in the presence and absence of ascorbic acid, yielding 123 µs and 34 µs.

Based on this success, Wang and coworkers increased the possible application range of the artificial photoenzyme.[273] In further work, superfolder yellow fluorescent protein was again mutated to possess an unnatural benzophenone photosensitizer replacing Tyr66 and an unnatural cysteine residue. Through bioconjugation, an iodofunctionalized bipyridine ligand was covalently attached to the protein. Further complexation of Ni^{2+} yielded PSP-95-Ni^{2+}(bpy). The resulting artificial photoenzyme was then used for the hydroxylation of aryl halides and C-N cross-coupling between pyrrolidine/imidazole and para-bromobenzylaldehyd reactions. The reactions were irradiated at 380 nm and performed in DMF/Tris-HCl buffer (pH 8.8) under argon using DIPEA as a sacrificing agent. The photoenzyme allowed the hydroxylation of 21 substrates, including chloro-, bromo-, and iodo- aryl halides. (Figure 3.15) Further characterization and mechanistic investigation highlighted a long lifetime of the excited state of 158 µs. It could also be shown that the efficiency was altered by altering the distance between the photosensitizer and the nickel complex. The optimal distance between benzophenone and the metal catalyst was 1.19 nm, with shorter and longer distances reducing the conversion.

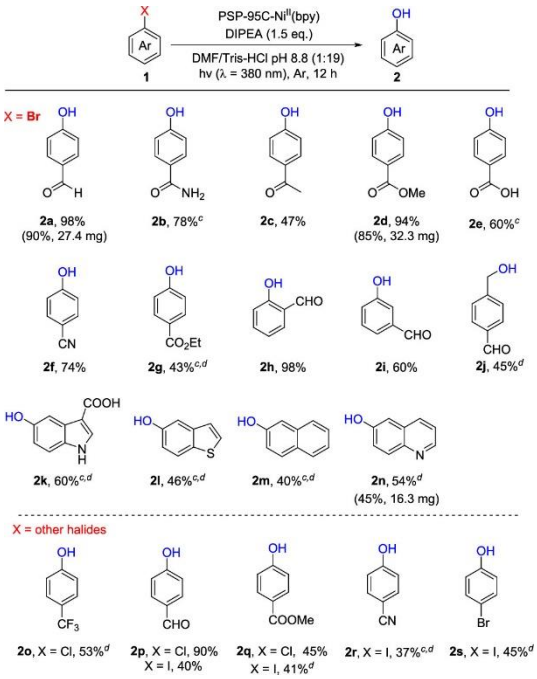

Figure 3.15 Reaction scope for the hydroxylation of aryl halides using the synthesized artificial photoenzyme.[273] Reproduced with permission from the American Chemical Society Copyright © 2021.

In 2015, the group around Lewis created the first artificial photoenzyme in which the photocatalytic moiety was not used as a mediator for an existing cofactor but to directly act on a substrate.[274] For this purpose, an oligopeptidase (POP) (from Pyrococcus furiosus) was first modified to possess four non-natural alanine mutations (E104A, F146A, K199A, D202A) to form a small opening in the protein scaffold. Further, a non-natural azide-modified amino acid was introduced, replacing the catalytic active amino acid (S477Z). The 4-azido-phenyl alanine mutation (Z477) could then be bioconjugated with a bicyclo[6,1,0]nonyne functionalized 9-mesityl-10-methylacridinium (Mes-Acr$^+$) perchlorate yielding the artificial photoenzyme (POP-ZA$_4$-5). (Figure 3.16) Unfortunately, the overall bioconjugation only yielded a conversion of 50% in part due to the decomposition of the required azide functionalized amino acid. Regardless, the photoenzyme was then used for the photooxidation of five organic sulfides, achieving moderate conversion with five mol% catalysts under blue light irradiation.

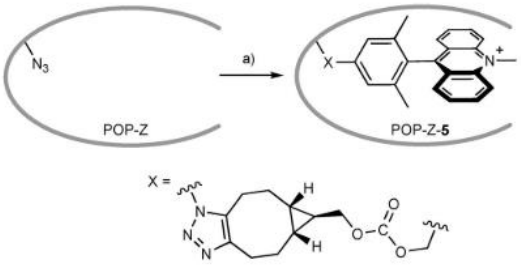

Scheme 2. Formation of artificial enzyme POP-ZA$_4$-5. a) 5, 5% ACN/Tris.

Figure 3.16 Synthesis of artificial photoenzyme through bioconjugation using azide-alkyne cycloaddition.[274] Reproduced with permission of WILEY-VCH © 2015.

In a similar approach, Schwochert *et al.* selected three protein scaffolds: aspartate dehydrogenase (AspDH), phosphoribosylamine-glycine ligase (GARS), and folylpolyglutamate synthase (FPGS) from Thermotoga maritima (TM) for the incorporation of iodoacetamide functionalized Mes-Acr$^+$ photocatalytic moieties.[266] (Figure 3.17) The proteins were chosen due to their comparable high thermostability and protein scaffold, which allowed the uptake of the moiety in a protein pocket. The proteins were mutated to include non-natural cysteine residue within the protein cavity, yielding two explicit variants per protein and six in total. The protein variations were then bioconjugated with two Mes-Acr$^+$ derivatives, yielding 12 artificial photoenzymes. The photoenzymes were analyzed via fluorescence lifetime and quantum yield measurements. The protein scaffold and positioning of the photocatalytic moiety within the enzyme significantly impacted the photophysical properties. For example, in the case of Tm(AspDH)T223C-1b, the quantum yield compared to the pure photocatalyst (1a) increased by 2.45 times. All twelve variants were used for the photocatalytic oxidation of organic sulfides. Ten of the twelve variants showed an increase in conversion compared to the pure photocatalytic moieties for the oxidation of thioanisole to phenyl methyl sulfoxide. The most efficient photoenzymes were used to oxidize ten organic sulfides, with at least one variant outperforming the free catalyst in eight cases.

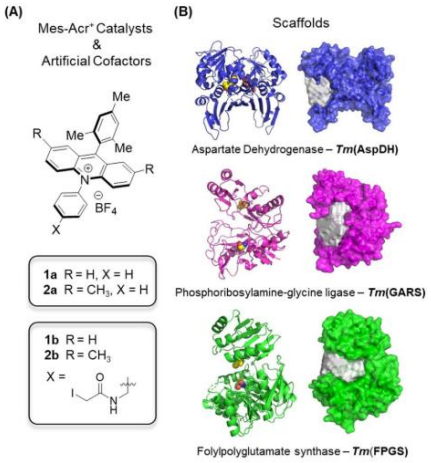

Figure 3.17 Functionalized Mes-Acr$^+$ photocatalytic moieties (left) and the protein scaffolds for the bioconjugation (right) used for the photooxidation of thioanisole derivatives.[266] Reproduced with permission of WILEY-VCH © 2020.

Lewis[275] further incorporated covalently and non-covalently bound $Ru(bpy)_3^{2+}$ derivatives into prolyl oligopeptidase (POP) from Pyrococcus furiosus (Pfu). This work aimed to catalyze the [2+2] photocycloaddition of 4-methoxystyrene and cinnamoyl imidazole and intramolecular cyclization dienones. Further, the photophysical and binding properties were intensively investigated.

Overall, eight $Ru(bpy)_3^{2+}$ derivatives with different functionalities like $–CO_2$, –tBu, $–NH_2$ $–CH_2NH_3$ were non-covalently attached to three variants while analyzing the dissociation constant. Further, six derivatives, including endo/L, endo/D, exo/L, and exo/D, were functionalized with an endo-[6.1.0]-bicyclononyne (BCN) group and bioconjugated with five different variants possessing a non-natural genetically encoded azido phenylalanine. All variants were bioconjugated with a high conversion of over 99%, significantly improving the yield of artificial photoenzymes compared to his previous work.

The fluorescence lifetime significantly differed depending on the used photocatalyst and the incorporation position. In the case of the covalently bound photocatalyst, all variants showed increased lifetimes compared to the free catalyst in water.

Only covalently bound photocatalysts could be tested as the buffer salt and sacrificing agent quickly replaced non-covalently bound moieties. The photoenzymes showed higher conversions than the free dye, but unfortunately, no control over the enantioselectivity was observed.

In 2022, the research groups of Green and Yuzhou Wu, independent of each other, developed artificial photoenzymes for intramolecular 2+2 cycloadditions, using direct evolution in combination with encoded benzophenone as photocatalyst. In both cases, the photocatalytic moiety was used for a triplet energy transfer to the substrate, requiring no further cofactors and allowing for high stereo- and regioselectivity.

The research groups of Green used direct evolution of a computationally designed Diels-Alderase DA_20_00 combined with a genetically encoded benzophenone for the intramolecular [2+2] cycloaddition of 2-quinolone derivatives.[269] Diels-Alderase DA_20_00 was originally designed to

catalyze thermally allowed [4+2] cycloadditions, and it was assumed that the active pocket of the scaffold could also support [2+2] cycloadditions. Benzophenone was chosen as a photocatalyst as its reactivity allowed the photocatalytic cyclization of 2-quinolone derivatives without selectivity. After incorporating the genetically encoded photocatalyst (BpA173), the artificial photoenzyme (EnT1.0) showed an increased reactivity and region- and enantioselectivity. Testing eight variants by introducing unnatural alanine residue in proximity to the photocatalyst yielded EnT1.1. EnT1.1 showed a significant increase in conversion as well as selectivity by introducing mutation M90A. In the following, a directed-evolution workflow using saturation mutagenesis substituted residues in the active site and second coordination sphere. Testing of around 3.500 library members leads to the variant EnT1.3 with five further mutations. EnT1.3 increase the conversion for the intramolecular cycloaddition of 4-(but-3-en-1-yloxy)quinoline-2 (1H)-one, from 12% with low region and enantioselectivity for variant EnT1.0, to 100% (9:1r:r, <99% ee). With these results and high reactivity, a substrate scope with 13 derivatives was conducted. Interestingly, it was observed that EnT1.3 was not the superior photoenzyme for all substrates, and other variants were more efficient in four instances. Lastly, two bimolecular [2+2] cycloadditions were performed using 2-quinolone and methyl/ethyl vinyl ketone, reaching over 70% conversion and high enantioselectivity.

Wu and coworkers used multidrug resistance regulator LmrR as a protein scaffold for intramolecular [2+2] cycloaddition of indole derivatives.[270] Due to its high triplet state energy and lifetime of the excited state, 4-benzoyl phenylalanine was chosen as a photocatalytic moiety. The photocatalyst could catalyze the model reaction but without enantioselectivity. The substrate docking mechanism was predicted to optimize the protein scaffold and the photocatalyst's position. Residues assumed to be in close proximity to the protein pocket were reserved to increase substrate enzyme binding. At the same time, the genetically encoded photocatalyst was introduced to allow an efficient energy transfer. Four rounds of direct evolution were needed from the wild-type to optimize the artificial photoenzyme. The first generation of artificial photoenzymes introduced only the photocatalyst and showed a lower conversion than the free photocatalyst and no enantioselectivity (TPe1.0). In the second round, the previously calculated docking mechanism was proven right, and a previously reserved residue was mutated (W96L) to allow a significant increase in enantioselectivity. After the third round, the photoenzyme (TPe3.0) achieved 54% conversion (77% ee) within one hour compared to 89% for the free photocatalyst in 12 h. Unfortunately, the artificial photoenzyme showed a highly substrate-specific behavior, and testing further indole derivative led to a significant drop in enantioselectivity while achieving high conversions

Therefore, further mutations were performed, and the photocatalyst 4-benzoyl phenylalanine was replaced through 3’-fluoro-4-benzoyl phenylalanine. The additional fluoro group proved beneficial for conversion and stereoselectivity, as it further stabilized the substrate in the scaffold through additional H···F bridges.

The optimized photoenzyme achieved between 80% and 97% conversion with high enantioselectivity for 15 substrates. Comparable to the results of Green's work, not one specific enzyme variation could outperform the others, and depending on the substrate, different enzymes showed a higher conversion or enantioselectivity.

To this day, the stereoselectivity and substrate-specific reactivity of enzymes surpass conventional catalysts, and especially the design of stereo- and or regioselective photocatalysts is a challenging field due to limited interaction between the photocatalyst and substrates.[226] The design of artificial photoenzyme possesses the potential to combine enzymatic precision with photocatalytic prowess under benign reaction conditions while removing the dependency on cofactors.[255] However, the design of artificial photoenzyme is a novel field requiring further research to design efficient systems comparable to existing alternatives.
In chapter 5.3, a fully organic artificial photoenzyme was created through bioconjugation of a small molecular photocatalyst into a human steroid carrier protein. (SCP-2L)
In total, three variants with differing binding positions were created, and the influence of the positioning was studied.

4 Characterization Techniques

The following chapter provides an overview about the characterization methods and techniques utilized in this work. Small molecular photocatalysts were synthesized and incorporated into macromolecular structures, including linear polymers, crosslinked hydrogels, and protein scaffolds. These materials were characterized and consequently used for photocatalytic reactions. Therefore, all projects use overlapping techniques like gas chromatography–mass spectrometry or UV/Vis- and fluorescence spectroscopy, while other characterization methods were specifically used in a single project.

4.1 Gas Chromatography–Mass Spectrometry

A gas chromatography-mass spectrometer (GCMS) combines the separation capabilities of a gas chromatograph with the sample analysis of a mass spectrometer. A GCMS consists of an injector, a column located within a temperature-controlled oven, as well as a mass spectrometer. (
Figure 4.1) A gas chromatograph uses an inert gas as mobile phase, which carries the sample through the column. The retention time of the sample depends on the volatility of the sample as well as its interaction with the stationary phase and the used temperature gradient.

During a measurement, a sample is placed in the injector and vaporized. In combination with the carrier gas, the sample is then injected on the column where the molecules separate and enter the mass spectrometer. In the MS, molecules are ionized and fragmented, yielding the corresponding mass spectrum. The GCMS is an efficient analysis tool used for the analysis of volatile samples up to 300 °C. In combination with a standard, it can further be used for concentration determination. Larger molecules, on the other hand, like proteins, polymers as well as salts, cannot be analyzed with this method.

In this work, GCMS measurements were performed to analyze the products of photocatalytic reactions, and kinetic experiments were monitored. The conversion and yield can be determined in two ways. A standard of known concentration can be measured against the substrates as a calibration curve, or the conversion can be determined through the ratios of substrates.

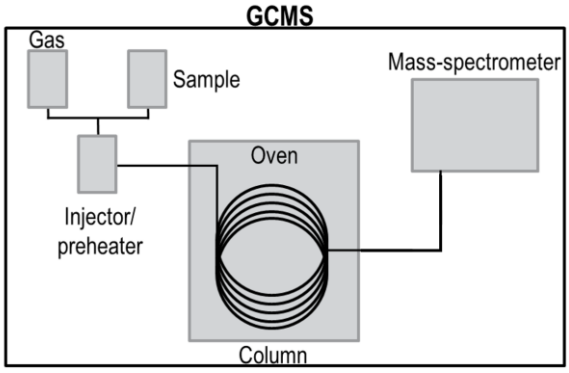

Figure 4.1: GCMS set up consisting of the injector and preheater, oven with column as well as the mass-spectrometer.

4.2 Liquid Chromatography–Mass Spectrometry

Similar to a GCMS, liquid chromatography–mass spectrometry (LCMS) combines a liquid chromatograph for the separation of molecules with the analysis methods of a mass spectrometer. In comparison to a GCMS, a LCMS uses a liquid mobile phase in combination with an immobilized stationary phase. Ultrahigh liquid chromatograph uses pressures of up to 120 mPa and allows for the separation of larger non-volatile molecules like proteins or peptides using solvent mixtures as mobile phase.

In the last project, (chapter 5.3) LCMS measurements were used to characterize purified proteins and bioconjugated artificial photoenzymes.

4.3 Gel Permeation Chromatography

Gel permeation chromatography (GPC) is one of the most commonly used analytic tools to determine the molecular weight of polymers. GPC is a form of size exclusion chromatography and uses differences in the hydrodynamic radii to achieve separation. Like other chromatography methods, GPC consists of a mobile and stationary phase, with the stationary phase consisting of a porous material. With no direct interaction between the polymer and stationary phase, the separation solely depends on the hydrodynamic radius, with larger molecules eluting before smaller ones. Due to the porous material, smaller molecules can enter into more caveats, increasing the retention time.

Compared to static light scattering or NMR spectroscopy, GPC is not an absolute method, requiring a measured standard with known molecular weight and distribution to which a measured sample can be compared. GPC was used in chapter (5.1) to determine the molecular weight of synthesized polymers and their dispersity.

4.4 UV/Vis-Spectroscopy

UV/Vis-spectroscopy is an analytic method to measure wavelength-dependent transmission and absorption of a molecule in visible and ultraviolet light. In a UV/Vis spectrometer, a sample, most often dissolved and placed in a cuvette, is irradiated with monochrome light. (Figure 4.2)

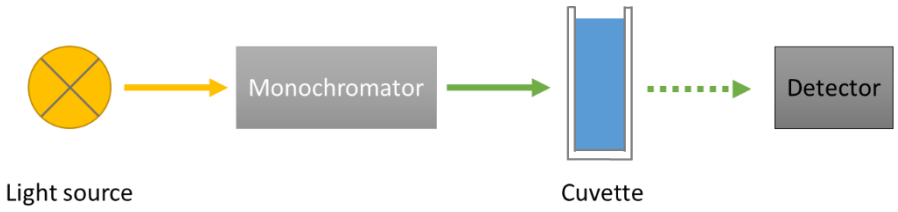

Figure 4.2 UV/Vis-spectrometer. Consisting of a light source, monochromator, cuvette and detector.

The absorption of light occurs when the photon energy is sufficient to excite an electron from the HOMO to the LUMO. Due to this process, the overall light intensity (I_0) is reduced while transitioning

the sample. Comparing the light intensity to a blank measurement gives the absorbance of the molecule at a specific wavelength. The absorbance *A* follows the Lambert Beer law (eq.1) and depends on the concentration *c*, the molar extinction coefficient *ε,* and the diameter of sample *d*.

$$\mathrm{A} = \log\left(\frac{I_0}{I}\right) = \varepsilon * \mathrm{c} * \mathrm{d} \qquad (1)$$

UV/Vis-spectroscopy was used to analyze the synthesized photocatalyst and determine concentrations and kinetic measurements.

4.5 Photoluminescence Spectroscopy

Photoluminescence spectroscopy is an analytic method to measure the photon emission of molecules upon light irradiation. Upon light irradiation, a photoluminescence molecule is excited from the ground state S_0 into an excited state S_n. As the excited state is unstable, a transition to the back to the ground state via radiative or non-radiative transitions occurs. Radiative transitions include fluorescence or phosphorescence after inter-system-crossing (ISC). Compared to the absorbance, photoluminescence is shifted to a higher wavelength due to vibration relaxation, which is called Stokes shift. In a photoluminescence spectrometer, the detector is angled to the excitation beam to prevent interference with the detection. Through the usage of monochromators, the photoluminescence can be analyzed without interference of the excitation wavelength. (Figure 4.3)

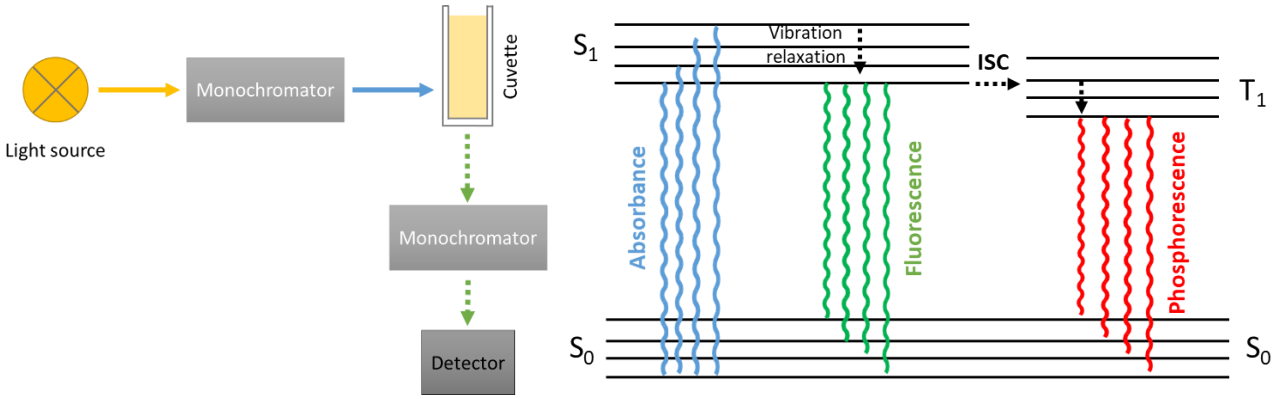

Figure 4.3: Fluorescence spectrometer setup (left); Jablonski-Diagram with absorbance and possible radiative transitions fluorescence, and phosphorescence (right).

In combination with a standard, photoluminescence spectroscopy can be used to determine the quantum yield of a sample. (eq.2) The quantum yield of a molecule is defined as the ratio of emitted photons to the number of absorbed photons.

$$\phi = \frac{number\ of\ emitted\ photons}{number\ of\ absorbed\ photons} \qquad (2)$$

As photoluminescence is readily quenched by a variety of molecules, including oxygen, all samples need to be measured in the absence of air. Nevertheless, this effect can also be used to analyze the interactions between quenchers and photoluminescence molecules by controlled addition of known quencher concentrations.
Lastly, time-resolved photoluminescence (TRPL) is an analysis method to determine the lifetime of the excited state (τ_0) of a molecule. After irradiation of a photoluminescence molecule, the molecule relaxes back to the ground state depending on the form of relaxation and stability of the excited state. This process can range from pico- to nanoseconds for fluorescence and up to milliseconds for phosphorescence. Long lifetimes are an essential requirement of efficient photocatalysts, involving energy- and electron transfers but can be influenced by a variety of factors including solvents or quenchers.
Photoluminescence spectroscopy was used to determine changes in the emission depending on the photocatalyst's surrounding. Further, TRPL and quantum yield measurements were performed in chapter 5.1 to investigate the comonomer impact on the photocatalytic moiety.

4.6 Fourier-Transform Infrared Spectroscopy

Fourier-transform infrared spectroscopy (FTIR) is an analytic method to characterize molecules via infrared absorption. In contrast to UV/Vis spectroscopy, FTIR uses wavenumbers in the range of 4000 cm^{-1} to 700 cm^{-1}. It can be used to identify specific functional groups within a molecule based on their vibration. A molecule can vibrate in different modes, including stretching or bending of chemical bonds. If these vibrations induce a dipole moment, IR irradiation can be absorbed by the molecule, leading to the absorption of IR light at specific wavelengths, which are characteristic for the functional group. The resulting IR spectrum can be used to identify the functional groups present in the molecule, while the region between 1200-700cm^{-1} is referred to as fingerprint region due to its unique nature depending on the molecule.
FTIR spectroscopy was used to characterize polymers and copolymers and identify specific functional groups.

4.7 Cyclic Voltammetry

Cyclic voltammetry is an analytic method designed to measure the reduction and oxidation potential of molecules.[276] The measurement apparatus consists of three electrodes within an electrolyte solution (Figure 4.4). The three electrodes include a working electrode out of graphene or gold, a counter electrode out of platinum, as well as a reference electrode. As the redox potential is measured against the reference electrode, the electrode potential needs to be well established. Nevertheless, a

variety of different reference electrodes, including saturated calomel or silver chloride electrodes, exist.

Measurements are either performed with the sample being fully dissolved in an electrolyte solution or in cases of insufficient solubility as a membrane, directly formed on the working electrode. The electrolyte solution further requires a large enough potential window as well as the absence of oxygen and water to prevent interference. During the measurement, a potentiostat is used to apply a voltage on the working electrode while measuring the current. Upon reaching the oxidation or reduction potential of the sample, a current can be detected between the working and counter electrode. (Figure 4.4) By plotting the applied current against the measured current, cyclic voltammetry measurements were performed to determine the reduction onset of the photocatalytic moieties.

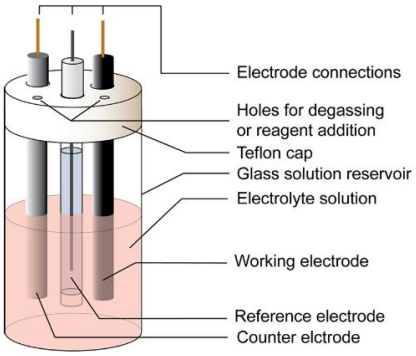

Figure 4.4 Depicturing of an electrochemical cell.[276] Reproduced with permission of The American Chemical Society and Division of Chemical Education, Copyright © 2017.

4.8 Nuclear Magnetic Resonance Spectroscopy

Nuclear magnetic resonance spectroscopy (NMR) is used to determine the molecular structure of a chemical and is additionally used to determine the purity of a synthesized material or measure reaction kinetics. Nuclei can possess a nuclear spin (*I*), with common isotopes like ^{1}H, ^{13}C, and ^{31}P possessing a nuclear spin of $I = ½$. Due to this spin, nuclei have a magnetic momentum, which is proportional to the intrinsic gyromagnetic ratio (γ) and the angular momentum (L).

$$\mu = \gamma * L \tag{4}$$

In the absence of an external magnetic field, the spin states are degenerated. Upon being placed in an external magnetic field (B_0), a spin alignment occurs, leading to distinct energy levels. (Figure 4.5) In the case of $I = ½$ the spin can align as $m_s = + ½$ and $– ½$ with the energy difference depending on the magnetic field strength as well as the magnetic momentum. Through irradiation of the sample with radio frequency, the spin state of the nuclei can be excited, leading to the absorbance of specific frequencies.

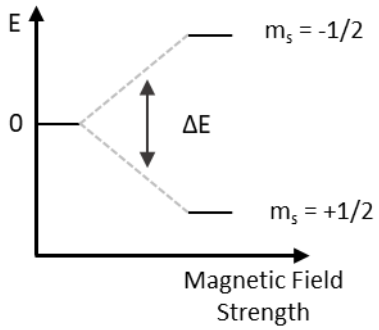

Figure 4.5 Energy splitting of a nucleus in an applied magnetic field with a spin of ½.

Due to the natural abundance and intrinsic gyromagnetic ratio of different isotopes NMR spectroscopy, possess large differences in sensitivity, which can be counteracted by stronger magnets and corresponding magnetic fields as well as longer measurement times and increased sample concentration. (Table 4.1),

Table 4.1: Isotopes and their intrinsic properties.[277]

Isotope	Spin	Gyromagnetic ratio (10^7 rad·s^{-1}·T^{-1})	Natural abundance (%)	Relative sensitivity
^{1}H	1/2	26.752	99.9	1.000
^{13}C	1/2	6.728	1.1	0.016
^{31}P	1/2	10.841	100.0	0.066

Solid state NMR (ssNMR) is a particular form of NMR using crystalline or amorphous samples without solvent and is commonly used for insoluble samples. The lack of mobility and anisotropic interactions leads to a broadening of the signals in NMR spectra. Magic angle spinning (MAS) is used to offset this effect; therefore, the sample is spun at high frequency in the kHz region around its one axis, while angled in 54.7° degree to the applied external magnetic field.

In this work ^{1}H-, ^{13}C-, ^{31}P-NMR spectroscopy was conducted in solution to characterize synthesis products and conducted kinetic experiments. ^{13}C-ssNMR spectroscopy was conducted to characterize synthesized photocatalytic hydrogel.

5 Data and Results

In the following chapter, a single photocatalytic moiety, diphenyl-benzothiadiazole, is functionalized and incorporated into three support materials to introduce beneficial material properties and analyze the support influence on the photocatalyst. Therefore, the photocatalytic moiety was introduced into linear copolymers, a hydrogel, and a protein scaffold through radical copolymerization or bioconjugation.
The following data and results section is separated into three chapters, with the first two chapters combining the photocatalyst with linear polymers and a hydrogel, while the last chapter covered the synthesis of artificial photoenzymes.

In the first chapter, a vinyl-functionalized photocatalytic moiety was copolymerized with styrene, methyl methacrylate, and acrylonitrile to analyze the effect of the copolymer on the photocatalyst. Therefore, the photophysical properties of the comonomer were analyzed via UV/Vis-Absorbance, emission, and excitation spectroscopy, as well as fluorescence lifetime and quantum yield measurements. Additionally, kinetic studies of three photocatalytic reactions were performed, highlighting the copolymer influence on the photocatalytic process.

In the second chapter, an acrylamide-functionalized photocatalytic moiety was copolymerized with *N*,*N*-dimethylacrylamide and *N*,*N*'-methylenebis(acrylamide) to create a high transmittance hydrogel. The hydrogel support readily swells in water, allowing for high light penetration and substrate diffusion while reducing light scattering. The photocatalytic hydrogel required only a low photocatalyst concentration (2 mol%) and was used for the photodegradation of wastewater pollutants. The benefits of the high transmittance were highlighted by upscaling the photodegradation of glyphosate to a gram scale.

In the last chapter, an iodoacetamide-functionalized photocatalyst was bioconjugated to three steroid carrier protein (SCP-2L) variants, creating artificial photoenzymes. The three variants possessed non-natural cysteine residues within the protein scaffold and enabled the covalent binding of the photocatalyst. The influence of the photocatalyst position was analyzed via UV/Vis absorbance and emission spectra and kinetic measurements of the photooxidation of an organic sulfide.

5.1 Comonomer Effects in Photocatalytic Classical Polymers

This chapter is based on the article "Comonomer effects in photocatalytic classical polymers", which is currently submitted and positively reviewed by RSC Applied Polymers. I synthesized and characterized the material and performed the photocatalytic reactions. DFT calculations were performed by Julian Heuer.

The copolymerization of photocatalytic moieties into polymeric material has emerged as a new development platform for heterogeneous photocatalysts. Classical polymers enable a variety of different structural designs like hydrogels and nanoparticles to be produced. Incorporating small molecule photocatalysts into polymeric structures has created a new class of heterogeneous photocatalysts. However, little is known about the interaction and influence of the classical polymer composition on photocatalytic efficiency. Here, a vinyl functionalized benzothiadiazole photocatalyst was copolymerized with three dramatically different monomers, methyl methacrylate, styrene, and acrylonitrile, via free radical polymerization, and the effect of the comonomer choice on the photocatalytic efficiency was investigated.

5.1.1 Motivation: Missing Link Between Classical Polymers and Photocatalysis

Photocatalysis uses visible light to facilitate chemical reactions and can remove the need for thermal energy, establishing itself as a more environmentally friendly alternative to classic catalysis.[186,278,279] Rapid development over the last decade has provided access to a wide range of reactions previously only achieved through classic catalysts.[13,33,226,280] At the same time, as the range of possible applications increases, new photocatalytic systems are developed to improve upon existing limitations, such as photobleaching, limited light penetration, or substrate scope. Homogeneous photocatalysts based on rare earth metals or organic dyes are by now well established, with examples like eosin y or ruthenium-based photocatalysts proving their capability and wide range of possible applications.[281-283] Due to their homogeneous nature, these dyes are exceptionally efficient but suffer from a range of downsides. Photobleaching, poor recyclability, and the usage of precious earth metals hinder their adaptation.[77,78] Heterogeneous metal-free photocatalysts built from conjugated frameworks emerged to negate these traits,[184,284-287] allowing for easy tuning of the band gap while being easy to recycle and cost-efficient. Unfortunately, metal-based or metal-free heterogeneous systems are hampered by diffusion limitations of the substrate and low light penetration, rendering large amounts of catalyst inactive during a reaction.[288-290] Further, their morphology and material properties are often directly dictated by their need for a conjugated π-system. As a result, it is hard to modify these systems or alter their material properties for specific applications.

An ideal photocatalyst would possess the benefits of both homogeneous and heterogeneous systems, achieving high efficiency while allowing the altering of material properties.[209] A recent development is, therefore, the fixation of photocatalytic moieties on support material to combine the versatility and application range of single photocatalytic moieties with the material properties of the support. Allowing for a wide variety of possible structures while material properties can be easily adjusted. One of the easiest and most efficient ways to incorporate single photocatalytic moieties into the support material is their copolymerization via free or controlled radical polymerization.[199,223] Polymers are an ideal platform as support material possessing a variety of classic monomers, giving control over material properties and structural design. Allowing for a covalent integration of the photocatalyst into a wide variety of structures like hydrogels, microgels, or responsive nanoparticles.[188] These structures can be optimized for specific needs like solvent compatibility, light transmittance, or position of the photocatalyst, with the comonomer determining the material properties, which are chosen for a desired outcome, leading to a highly flexible platform. Interestingly, while it is well known that the structure design and solvent can directly influence the photocatalytic efficiency, the monomer used in the copolymerization is chosen due to the desired material properties of the polymer. The interaction between the photocatalyst and the comonomer is often an afterthought. Assuming negligible interaction between the photocatalyst and surrounding polymer, having minimal influence on the photocatalytic efficiency.

Kobayashi and Yoo reported the usage of a polymer-immobilized Iridium catalyst for the phosphorylation of *N*-aryl tetrahydroisoquinolines. The catalyst was functionalized to allow copolymerization into a support material. Three heterogeneous polymers based on a combination of ethyl methacrylate with styrene, *N*-isopropyl acrylamide, or benzyl methacrylate were synthesized, leading to different efficiencies depending on the chosen comonomer.[192] Our group recently reported the copolymerization of a benzothiadiazole-based photocatalyst into a self-assembled di-block copolymer. By intentionally positioning the photocatalytic unit in the hydrophobic core or the more hydrophilic shell, differences in the efficiency depending on the polarity of the substrate could be observed. Highlighting the effect of the photocatalyst positioning in a polymer backbone on the reactivity.[221]

Similar effects are reported in the emerging field of artificial photoenzymes, where the microenvironment of the protein scaffold can affect the photocatalytic efficiency depending on the placement of the photocatalytic moiety.[291]

So far, we assume that the choice of the monomer and the resulting polymer backbone have an insignificant influence on the photocatalytic moiety and the overall photocatalytic efficiency. Aiming to increase efficiency through changes in structural design and morphology. However, an actual systematic study still needs to be included. Electron-withdrawing effects, steric hindrance, and charge density could affect the photocatalytic moiety. Therefore, using monomers with a stabilizing effect could be beneficial for photocatalytic efficiency.

In this chapter, the effects and influences on the photocatalytic capabilities and photophysical properties of diphenyl benzothiadiazole were investigated. In a first step, various photocatalytic moieties with different functional groups were analyzed via UV/Vis-absorbance before a possible solvent effect was investigated. Consequently, a metal-free organic vinyl functionalized benzothiadiazole moiety was copolymerized with seven monomers, and the influence of three commonly used monomers, styrene, methyl methacrylate, and acrylonitrile, to analyze the comonomer effect on the photocatalytic behavior. (Figure 5.1)

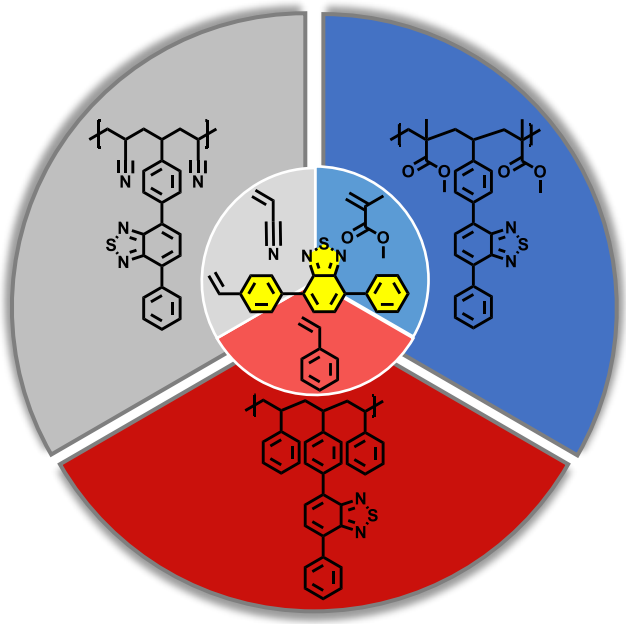

Figure 5.1: Photocatalytic moiety is copolymerized with three distinct monomers, styrene, methyl methacrylate and acrylonitrile to investigate the effect of the comonomer on the photocatalytic efficiency and photophysical properties.

In a first step, the effect of modifying small molecule photocatalysts with different functional groups and possible solvent effects were investigated. Vinyl-based functional groups are required to allow the copolymerization and covalent incorporation of a photocatalytic moiety into macromolecular structures. Different functional groups on the photocatalyst can increase the corresponding reactivity or copolymerization rate. However, so far, nobody investigated if different functional groups influence the photocatalytic efficiency and photophysical properties. Therefore, seven different functional groups were investigated via UV/Vis absorbance spectroscopy. (Figure 5.2) Non-functionalized diphenyl benzothiadiazole possesses a peak absorbance at 381 nm. The most basic functionalization with a vinyl group to allow incorporation into copolymer leads to a red shift of 392 nm to a peak of 11 nm. It can be explained through an increase in the fully conjugated system. ± Inductive (± I) and mesomeric (± M) effects are known to have a significant impact on the reactivity and absorbance of conjugated systems. The most significant effect can be observed by the addition of an amine, leading to a red shift to 442 nm. This effect is reduced by the further functionalization to an acrylamide group,

leading to a peak at 399 nm. The incorporation of hydroxyl groups leads to a similar effect but in a lower magnitude (399 nm). In contrast, adding a hydroxyl methyl group leads to a blue shift due to an –I-effect (375 nm).

Therefore, the absorbance of the photocatalytic moiety depends on the functional group and can be used to tune the photophysical properties. Nevertheless, the vinyl-based groups are required to allow copolymerization and possess different incorporation rates and need to be considered, leading to a possible compromise between incorporation rate and desirable absorbance wavelength.

In the following, the vinyl-functionalized group was used as it minimized the possible influence of the functional group after incorporation.

In the following step, the solvatochromism of vinyl-functionalized photocatalytic moiety was investigated in five solvents. (Figure 5.4) The small molecular photocatalyst is a non-polar photocatalyst. It possesses no functional groups compared to rose bengal or eosin y, leading to the assumption that different solvents would only have a small effect on the photocatalytic moiety. In DMF, Toluene, and THF, the photocatalyst shows similar absorbance, peaking at 391 to 393 nm, which is surprising, as toluene (393 nm), DMF (391nm), and THF (391 nm) possess differences in their polarity and dielectric constant. On the other hand, ACN and $MeNO_2$ lead to a strong blue shift compared to the previous solvents, peaking at 386 nm ($MeNO_2$) and 384 nm. In the following, all experiments were performed in DMF to dissolve all synthesized copolymers. After investigating the influence of the functional group and solvent, a possible influence of the comonomers was investigated. Therefore, seven different monomers, methyl methacrylate(MMA), styrene (S), acrylonitrile (AN), benzyl methacrylate (BMA), hydroxyethyl methacrylate (HEMA), *N,N*-dimethylaminoethyl methacrylate (DMAEMA) and *N,N*-dimethylacrylamide (DMAA) were copolymerized with the vinyl functionalized photocatalytic moiety via free radical polymerization. The corresponding copolymers were analyzed via UV/Vis-spectroscopy. (Figure 5.3, Figure 5.4) The non-optimized copolymerization led to comonomers with different molecular weights between 7500 g/mol and 24200 g/mol but a comparable amount of incorporated photocatalyst between 0.72-1.3 wt.%. The absorbance of all seven copolymers was investigated, leading to absorbance peaks between 384 nm for PAN-BT and 392 nm for PS-BT. Most Copolymers possessed only a negligible effect on the absorbance, with PMMA, PBMA, PHEMA, and PDMA being separated by two nm. PAN, PS, and PMMA showed significant variations in the absorbance and emission peaks, assumingly based on their significant differences in polarity and stabilization of the photocatalyst. Consequently, these three copolymers were used for further investigation.

The resulting copolymers were first analyzed via GPC, IR, UV/Vis-absorbance, fluorescence lifetime, quantum yield, and DLS measurements. In addition, DFT and Tauc-Plot calculations and cyclic voltammetry were used to determine the HOMO/LUMO levels and the resulting bandgap. Lastly, the photocatalytic efficiency was investigated via kinetic studies of three model reactions: the hydroxylation of boronic acids, the C-C coupling of benzyl bromide as well as an electron-rich indole

coupling reaction. Displaying significant discrepancies in the performance based on the chosen comonomer. The photocatalytic unit is based on a donor-acceptor design using a benzothiadiazole unit as an electron acceptor. Further, the photocatalytic moiety possesses no functional groups and eliminates any possible interference with the polymer or substrate. Making it an ideal candidate for investigating possible influences of the surrounding polymer. This metal-free photocatalyst has shown high stability in various photocatalytic reactions and can easily be functionalized to allow incorporation in various structures like hydrogels or responsive polymer particles. The photocatalyst was modified with a vinyl functionalization to allow easy copolymerization. (see Figure 6.4) The functional vinyl-group was chosen to replicate the unmodified homogeneous photocatalyst incorporated into a polymer backbone while preventing changes in the optical properties and photocatalytic activity. The polymers were chosen based on their possible interaction with the photocatalytic moiety. Considering their different polarities, dielectric constant, and possible interaction with the photocatalyst, styrene, methyl methacrylate, and acrylonitrile were investigated as possible monomers. Polystyrene could enable possible π-π-Interactions between the photocatalyst and the polymer backbone.[292,293] Due to its highly polar backbone, polyacrylonitrile, on the other hand, could have a beneficial charge stabilization affecting the efficiency of the photocatalytic moiety.[294,295]

5.1.2 Results and Discussion: Comonomer Influence on the Photocatalytic Efficiency

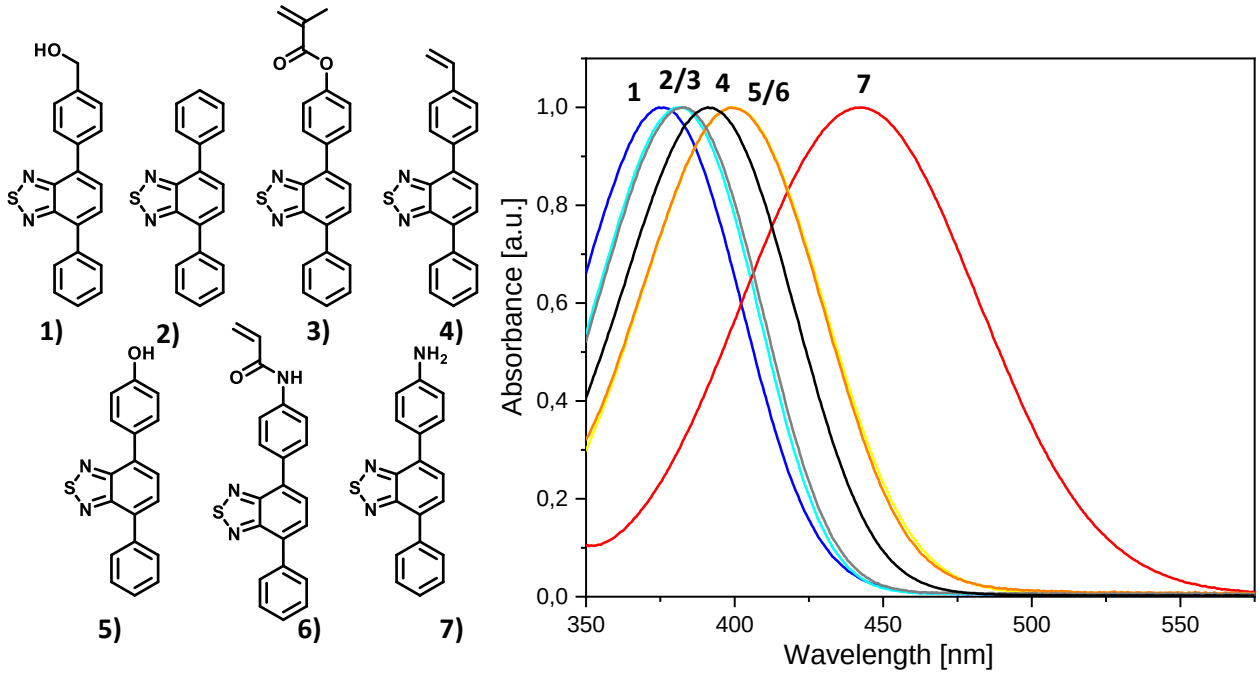

Figure 5.2: The chosen functionality effects the absorbance of the diphenyl benzothiadiazole core based on the ± inductive and mesomeric effect of the functionality. Measurement performed in DMF.

Due to the low reactivity and propagation rate of styrene, the polymers were synthesized via free radical polymerization. Opting for an incorporation of 5 wt.% of photocatalyst leading to good

photocatalytic performance while maximizing the possible comonomer influence. Yielding three distinct copolymers based on polystyrene (PS-BT), poly(methyl methacrylate) (PMMA-BT), and polyacrylonitrile (PAN-BT). The copolymers were analyzed, and the incorporation of photocatalysts was confirmed by GPC, ^{1}H NMR, UV/Vis, and FTIR spectroscopy. The copolymers possessed molecular weights between 15,000 and 20,000 g/mol and dispersities of 2.4-3 Đ with an incorporation of 5.3 to 6.3 wt.% of photocatalyst. (Figure 5.5) All three polymers readily dissolve in DMF. Therefore, DMF was chosen as the solvent system for all analytic purposes and as reaction medium for photocatalytic testing.

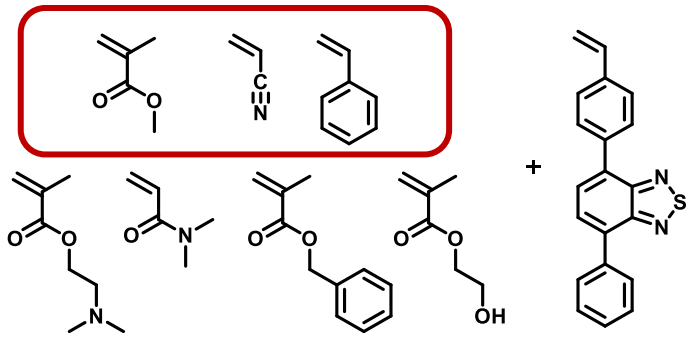

Figure 5.3: Used monomers for the copolymerization with the photocatalytic moiety. Methyl methacrylate, styrene and acrylonitrile were chosen for further analysis.

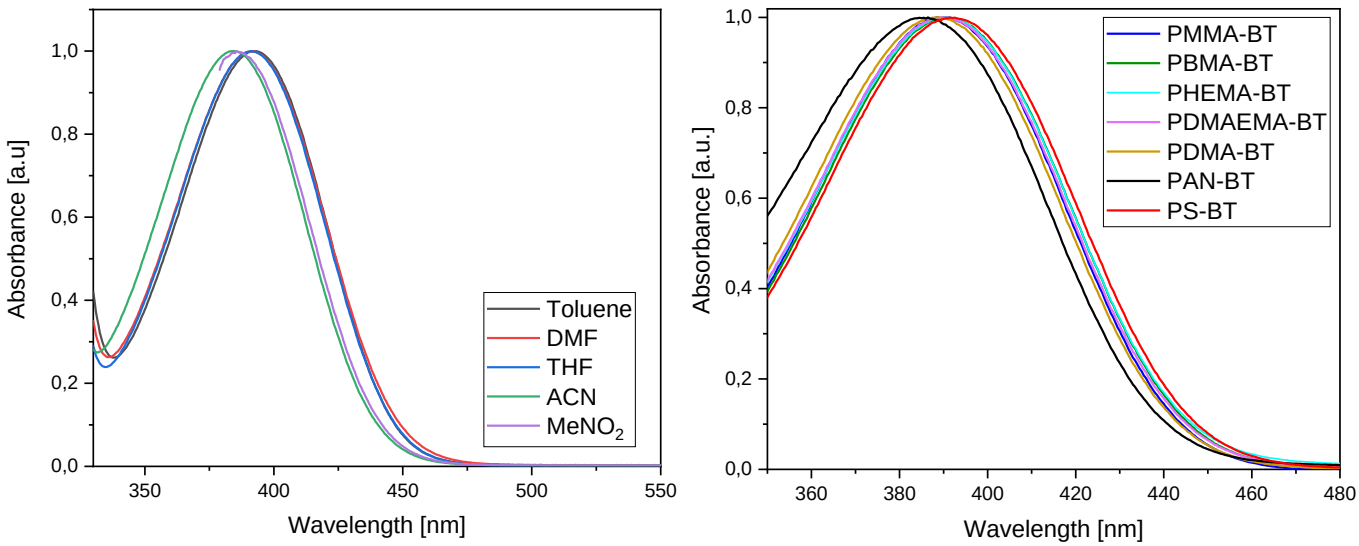

Figure 5.4: Influence of different solvents on the absorbance of the photocatalytic moiety. (left) Influence of comonomer choice on the absorbance of the photocatalytic moiety. Measurements were performed in DMF. PDMAEMA measured in water. (right)

As the polymer's swelling behavior and structure could impact the photocatalytic efficiency, the hydrodynamic radii were determined. The copolymers have comparable hydrodynamic radii between 6-8 nm, allowing a direct comparison of the photocatalytic efficiency. (see Figure 6.2) FTIR allows easy identification of the polymers showing specific bands at 1700-1800 cm^{-1} and 700 cm^{-1} for aromatic -C-

H bending in PS-BT. 2250 cm^{-1} for C≡N stretching in PAN-BT and ester-C=O stretching in PMMA-BT at 1700 cm^{-1}. (Figure 5.5) As previously reported, the low concentration of incorporated photocatalyst makes detection over FTIR difficult. Even with higher weight percentages of photocatalysts, the IR-bands at 700 cm^{-1} are the only indication of incorporation.

The ^{1}H-NMR spectroscopy analysis highlights the photocatalytic moiety between 8.3 – 7 ppm for PMMA-BT and PAN-BT, while in the case of PS-BT the styrene overlaps with the photocatalytic moiety. The polymer backbone can be observed at 2.4 – 1.9 and 3.6 – 3.1 ppm for PAN-BT, 3.8 – 3.3, 2.0 – 1.7 and 1.1 – 0.5 ppm for PMMA-BT, PMMA-BT, and 2.4 – 1.0 ppm PS-BT. (see Figure 6.5-6.7) The incorporation of the photocatalyst was determined via UV/Vis-absorbance. (Figure 5.6)

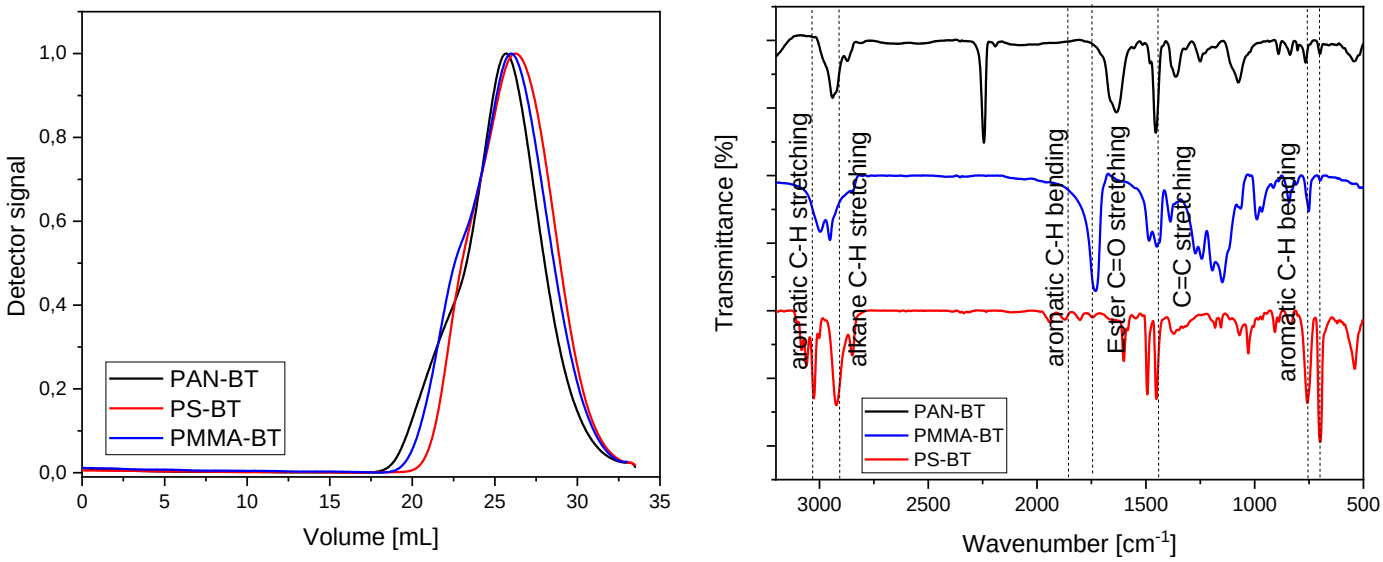

Figure 5.5: GPC of PAN-BT, PS-BT and PMMA-BT in DMF against a PMMA standard (left). FTIR spectra of PAN-BT, PS-BT and PMMA-BT as dry powder in KBr pellets (right).

The solvent affects the UV/Vis-absorbance spectrum of the non-functionalized homogeneous photocatalyst 4,7-diphenyl-benzo-[2,1,3]thiadiazole (Ph-Bt-Ph), displaying a hypsochromic shift depending on the solvent, shifting from 392 in toluene to 384 nm in acetonitrile. (Figure 5.4)

Indicating the stabilization of a slightly more polarized ground state. This effect can be observed and replicated in polymers. Incorporated in a polymer backbone, we observed shifts in the absorbance spectra depending on the comonomer. Incorporated in PMMA-BT and PS-BT, the main absorbance peak shifts slightly, while in combination with PAN-BT, the peak blue-shifted by 7 nm. PS absorbance peaks at 392 nm in DMF, followed by PMMA-BT at 390 nm. (Table 5.1, Figure 5.6) The significant deviant is found in polyacrylonitrile (PAN-BT), where a shift to 385 nm can be observed. These values are similar to the homogeneous photocatalyst in toluene and ACN, respectively. Showcasing that the immediate environment of the polymer has an impact on the stabilization of the catalyst, similar to a change in the solvent. PAN is a highly polar polymer with high dielectric values, leading to a blue shift

compared to PS. It could be argued that the polymer backbone replicates the solvent effect to some extent. Similar trends can be observed in the emission and excitation spectra. The emission peaks indicate the same blue shift, with PS-BT having the highest emission peak at 509 nm followed by PMMA-BT and PAN-BT at 503 nm, with all three copolymers possessing the same stokes shift of stokes shift of 117 nm. (Table 5.1, Figure 5.6)

Along with the absorbance and emission spectra, the polymers were compared through excitation spectra, which replicated the results given by the absorbance and emission spectra. The excitation maximum at 507 nm is blue-shifted by 7 nm compared to the absorbance for all copolymers. (Table 5.1, Figure 5.9) PS-BT has the highest maximum at 385 nm, leading to the absorbance of higher wavelengths of over 460 nm. PAN-BT in comparison, has an excitation maximum at 379 nm leading to a maximum absorbance wavelength of 460 nm. (Figure 5.9)

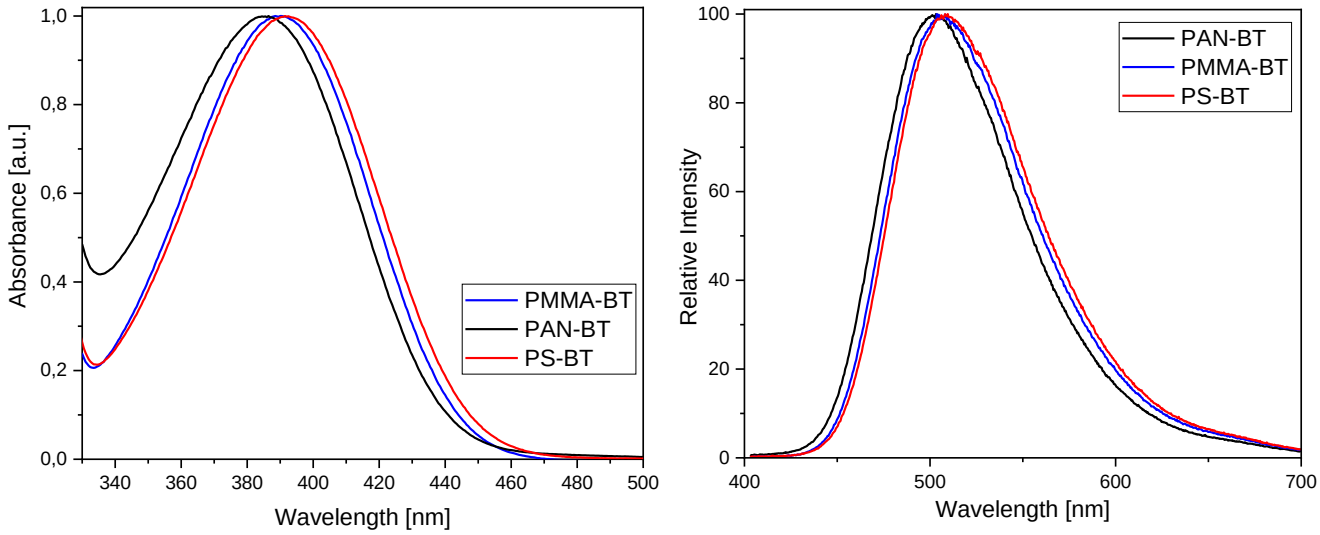

Figure 5.6: Absorbance spectra (left) of PMMA-BT, PAN-BT and PS-BT in DMF indicating a change in absorbance depending on the comonomer. Fluorescence spectra (right) of PAN-BT, PMMA-BT and PS-BT showing a blue shift in PAN-BT indicating the influence of the comonomer.

The fluorescence lifetimes for all three polymers are shown to be between 10-11 ns, indicating similar results, with PS-BT having the highest and PAN-BT having the lowest fluorescence lifetime. (Table 5.1, Figure 5.7) The lifetime measurements for PS-BT and PMMA-BT show neglectable differences of 11.1 and 11.0 ns. In comparison, the lifetime of the excited state of the photocatalytic moiety in PAN-BT is reduced to 10.2 ns.

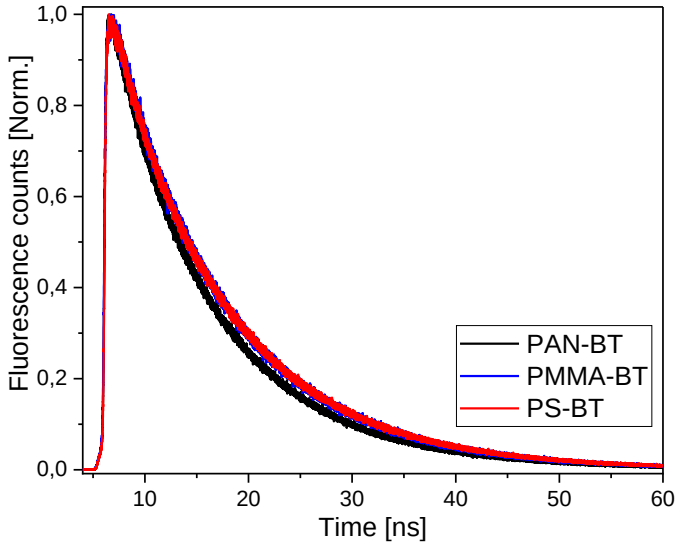

Figure 5.7: Normalized average of three fluorescence lifetime measurements of PAN-BT, PMMA-BT, PS-BT.

The quantum yield of the unmodified 4,7-diphenyl-2,1,3-benzothiadiazol ($\Phi_{Photocatalyst}$=80) was previously reported by DaSilveira Neto *et al.* who measured against quinine sulfate (1 M H_2SO_4).[72] The QY was determined after a known procedure by plotting the integral of the fluorescence spectra against the intensity of the absorbance for different concentrations. The calculated gradients can then be used in combination with the gradient of the standard to calculate the quantum yield via the shown equation (3).

$$\phi_x = \phi_{st}\left(\frac{Grad_x}{Grad_{ST}}\right)\left(\frac{\eta_x^2}{\eta_{st}^2}\right) \quad (3)$$

ϕ_{st} = quantum yield standard; $Grad_{ST}$ = calculated gradient of the standard;
η_{st}^2 = squared value of the refraction index of the solvent standard

The photocatalytic moiety is again influenced by the comonomer.[72,296] PS-BT and PMMA-BT again only show minor differences and a comparable high quantum yield to the unmodified 4,7-diphenyl-2,1,3-benzothiadiazol. (Table 5.1, Figure 5.8) PAN-BT, on the other side, shows a much lower quantum yield of 0.82 compared to the free photocatalyst, which can be attributed to the increasing absorbance of the polymer backbone at a lower wavelength, leading to non-radiant relaxation playing a more prominent role in PAN-BT.

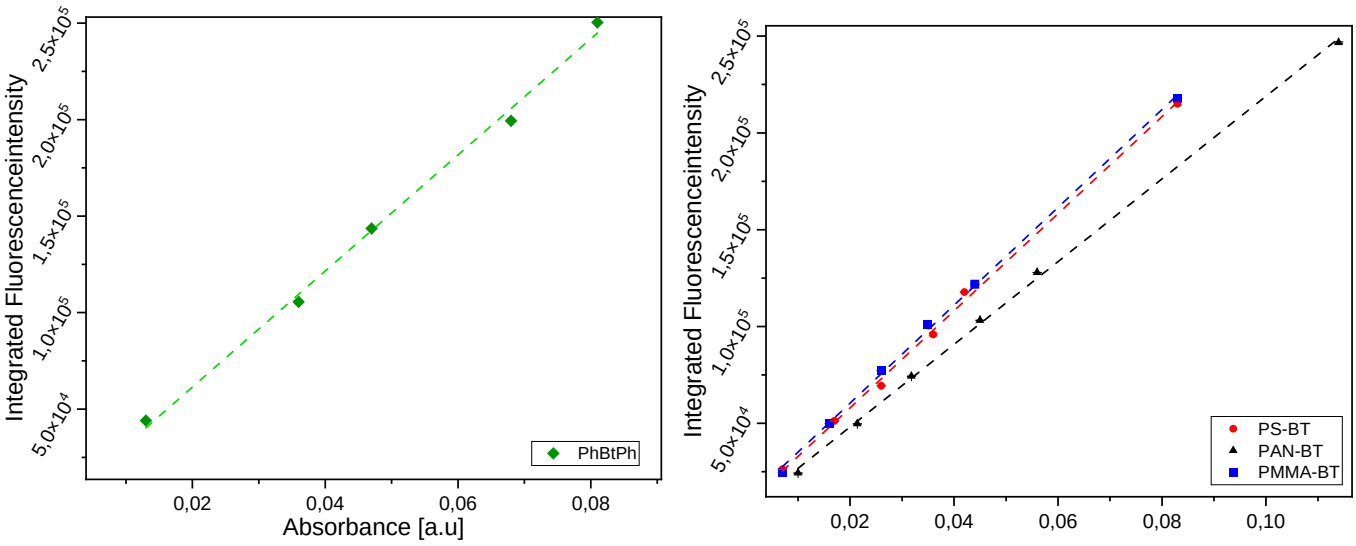

Figure 5.8: Quantum yield calculation of PAN-BT, PMMA-BT and PS-BT using 4,7-diphenyl-2,1,3-benzothiadiazole at 366 nm in ACN as reference.

The band gap and energy value of the orbitals are crucial for the photocatalytic prowess and determine the reductive and oxidative capabilities of the photocatalyst. Through copolymerization, Huber *et al.* incorporated a benzothiadiazole photocatalyst in a heterogeneous organogel based on crosslinked PMMA. Through cyclic voltammetry and density functional theory calculations (DFT) DFT calculations of the pure photocatalyst and the copolymer, changes in the bandgap, as well as the HOMO and LUMO levels, could be observed.[203] Therefore, in the next step, the HOMO/LUMO levels of the copolymers and the electron gap were calculated and analyzed using DFT calculations, cyclic voltammetry, and Tauc-Plot. The theoretic orbital energies were determined for trimers using B3LYP with basis set 6-31+g(d).[297-300] Depending on the comonomer, the calculation indicates different values for HOMO/LUMO levels for PS-BT, PAN-BT, and PMMA-BT. (Figure 5.9) PS-BT and PMMA-BT show only minor differences in the band gap with 3.29 and 3.30 eV.

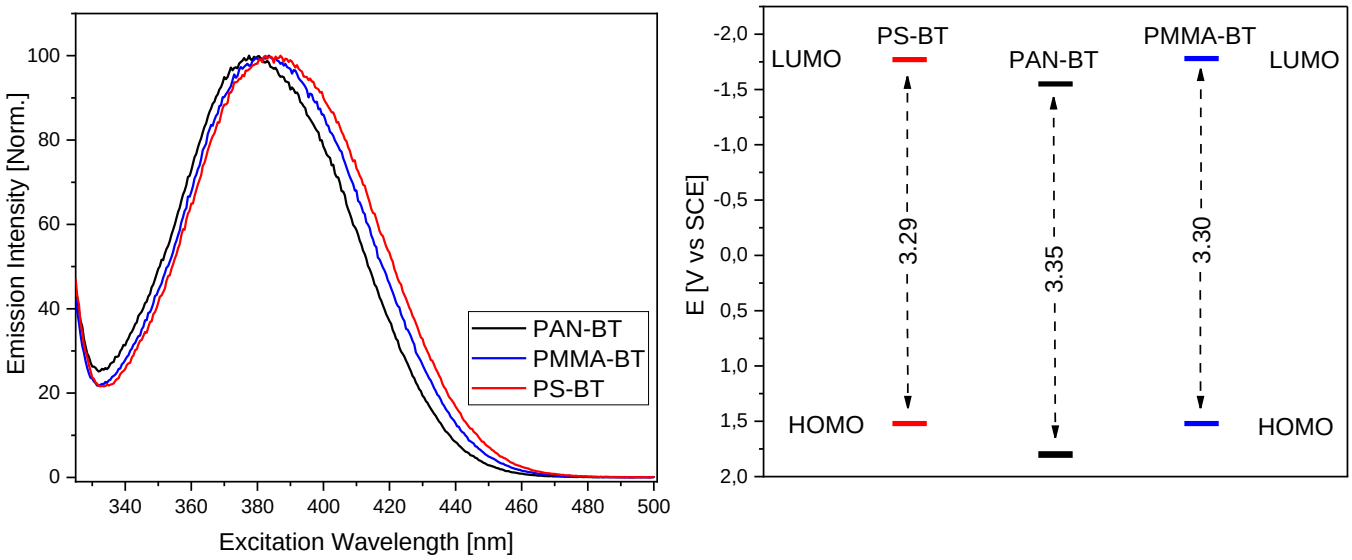

Figure 5.9: Three copolymers were analyzed via excitation spectra (left) and DFT calculations (right). The copolymers show a blue shift from PS-BT to polar PAN-BT. DFT calculations confirm a higher bandgap for PAN-BT, while PMMA-BT and PS-BT lie closer together.

The LUMO and HOMO levels for both polymers are comparable at -1.77 and -1.78 V vs. SCE (LUMO) and 1.52 V vs. SCE for the HOMO, respectively. PAN shows the largest electron gap with 3.35 V vs. SCE and the lowest LUMO and highest HOMO level energies with -1.53/1.80 V vs. SCE. The calculations further highlight the electron density shift during excitation. In the ground state, the electrons are located within the phenyl groups, while the LUMO highlights a high electron density within the benzothiadiazole unit. (Figure 5.10) Cyclic voltammetry measurements indicate only small differences between the polymers and are smaller compared to the theoretical values. The reduction onset was determined to be between -1.35 V vs SCE for PMMA-BT, -1.3 for PS-BT, and -1.29 for PAN-BT. (see Figure 6.3) These values are comparable to previous cyclic voltammetry measurements of PMMA and poly(*N*,*N*-dimethylacrylamide) with copolymerized benzothiadiazole-based photocatalyst.[203,301]

In addition to DFT calculations and CV measurements, the optical electron bandgap was determined.[302,303] (Table 5.1: Measured and calculated values for PMMA-BT, PAN-BT and PAN-BT (5 wt%). Absorbance, Emission, Excitation maxima and fluorescence lifetime were measured in DMF. Quantum yield measured in DMF against 4,7-Diphenyl-2,1,3-benzothiadiazol in ACN at 366 nm. DFT calculations performed using B3LYP 6-31+g(d). Optical bandgap calculation based on UV/Vis-measurements in DMF.Table 5.1, Figure 6.1) The values were used to determine the HOMO levels of all polymers. The values are smaller than predicted by the DFT calculation, with around 2.9 eV, and lie closer together. It can be observed again that PAN-BT has a larger electron gap (2.92 eV) compared to PS-BT (2.89 eV) and PMMA-BT (2.87 eV). After observing changes in the optical properties as well as a possible influence on bandgap depending on the chosen comonomer, we decided to further investigate the comonomer influences on the photocatalytic efficiency through kinetic studies of three

model reactions. Further, Stern-Vollmer Plots were used to investigate the interaction between the sacrificing agents and the copolymers.[304] The model reactions were chosen to include the hydroxylation of boronic acids as well as the C-C coupling of benzyl bromide as well as an electron-rich heterocyclic indole coupling reaction. The photocatalytic reaction covers a variety of conditions under nitrogen, oxygen, and the usage of different sacrificing agents. First, the hydroxylation of diphenyl boronic acid was investigated. This reaction is well established, and various publications cover mechanistic investigations, possible conditions, and usable photocatalysts.[20]

Table 5.1: Measured and calculated values for PMMA-BT, PAN-BT and PAN-BT (5 wt%). Absorbance, Emission, Excitation maxima and fluorescence lifetime were measured in DMF. Quantum yield measured in DMF against 4,7-Diphenyl-2,1,3-benzothiadiazol in ACN at 366 nm. DFT calculations performed using B3LYP 6-31+g(d). Optical bandgap calculation based on UV/Vis-measurements in DMF.

Entry	Polymer	Absorbance peak	Emission peak	Excitation	$\Phi_{Polymer}$ /$\Phi_{Photocatalyst}$	τ_o	Eg_{opt}	HOMO /LUMO(DFT)
1	PMMA-BT	390	507	383	1.0	11.0	2.87	1.52/-1.78
2	PS-BT	392	509	385	1.0	11.1	2.89	1.52/-1.77
3	PAN-BT	385	503	379	0.8	10.2	2.92	1,80/-1.55

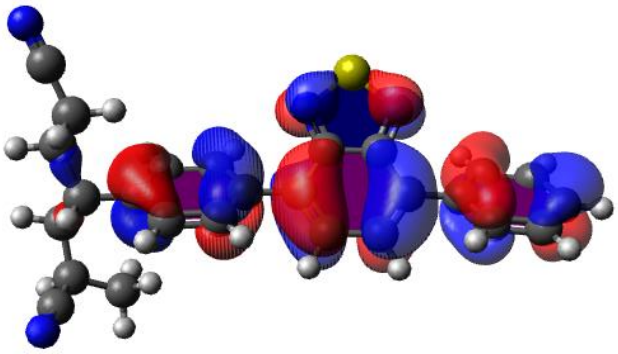

PAN-BT HOMO: 1.8 V vs SCE

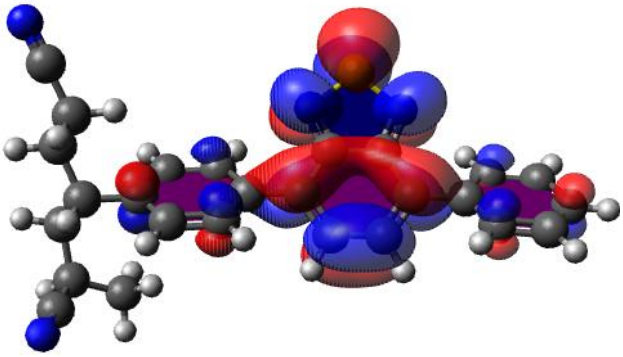

PAN-BT LUMO: -1.55 V vs SCE

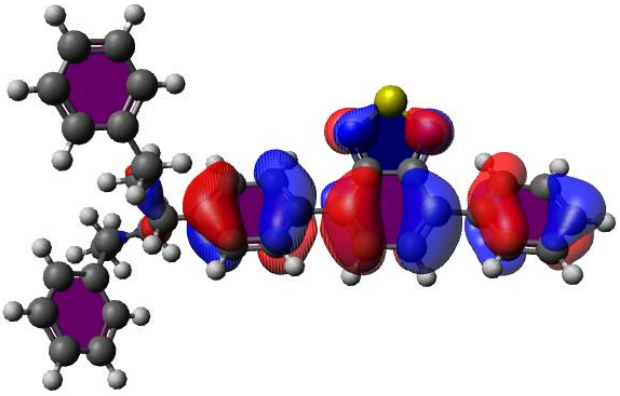

PS-BT HOMO: 1.52 V vs SCE

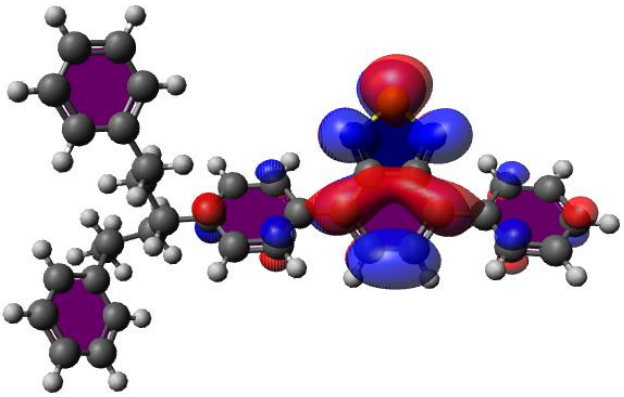

PS-BT LUMO: -1.77 V vs SCE

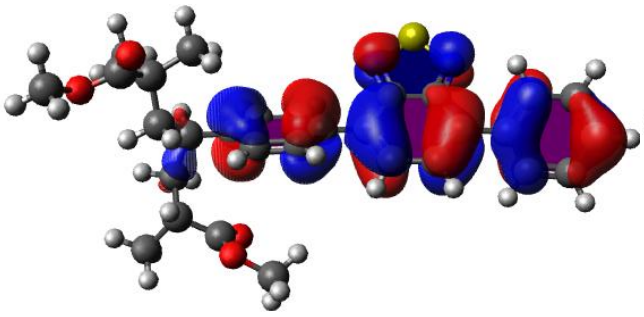

PMMA-BT HOMO: 1.52 V vs SCE

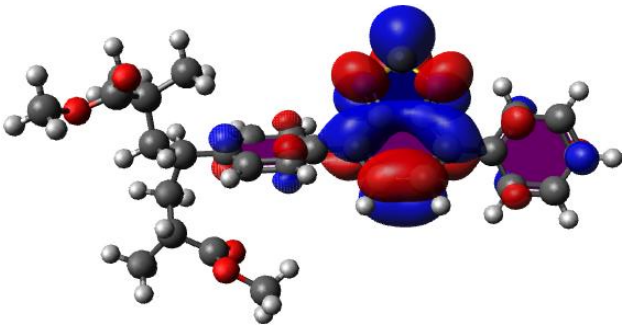

PMMA-BT LUMO: -1.78 V vs SCE

Figure 5.10: HOMO (left) and LUMO (right) of PAN-BT, PS-BT and PMMA-BT Indicating electron density shift in excited state compared to ground state.

The reaction was conducted with all three copolymers under blue light irradiation at room temperature. The copolymers successfully catalyzed the hydroxylation, leading to high conversion in all three cases. (Figure 5.11, Figure 6.14-6.16) The kinetic study was analyzed over a time span of 6 h, reaching over 90% conversion for PS-BT, PMMA-BT, and PAN-BT. PAN-BT showed the lowest conversion of 90%. Nevertheless, all three polymers reach high turnover numbers of 900-960. Interestingly, the kinetic study indicates that PS-BT has a higher conversion rate, reaching 87% after 4 h compared to 74% and 82% for PAN-BT and PMMA-BT. Showcasing a slightly higher efficiency for PS-BT over PMMA-BT or PAN-BT. Mechanistic investigations by Pitre *et al.* highlight the necessity of superoxide for the hydroxylation of boronic acids.[305] Therefore, the reaction was conducted under oxygen atmosphere, in DMF, in the presence of DIPEA as a sacrificing agent. The role of the sacrificing agent was investigated through a Stern Vollmer Plot, indicating a similar quenching rate for all three polymers, with PAN-BT slightly elevated compared to PMMA-BT and PS-BT. (Figure 5.12)

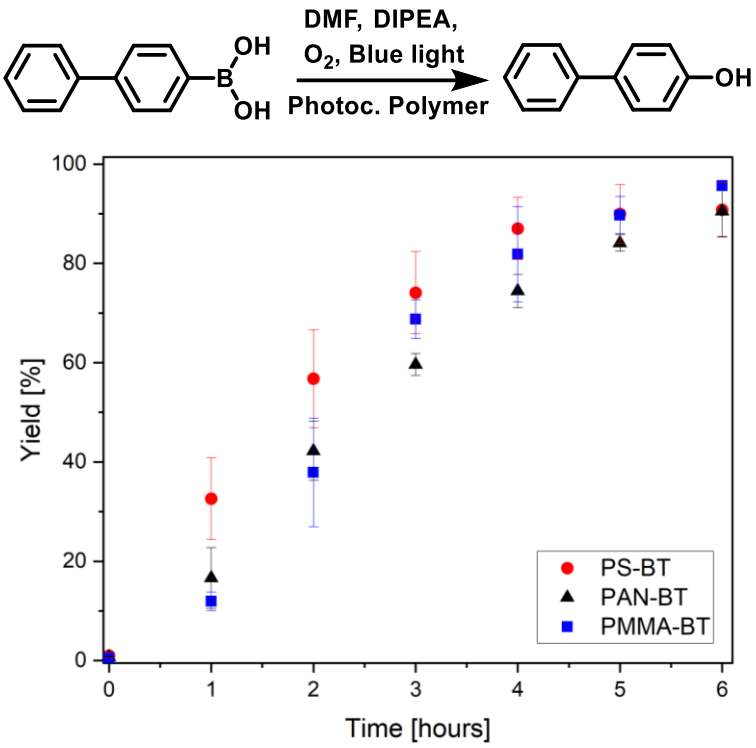

Figure 5.11: Photocatalytic hydroxylation of 4-biphenyl boronic acid measured over time using PS-BT, PMMA-BT and PAN-BT. 4-biphenylboronic acid (19.8 mg, 100 µmol) *N*,*N*-diisopropylethylamine (52 µL, 300 µmol) and photocatalytic polymer (100 nmol photoactive unit) in DMF (2mL), O_2-Atm. blue light irradiation.

This may be explained by the mechanism of the reaction where the electron is transferred from the photocatalyst to oxygen, which then interacts with the substrate. As oxygen is small and can quickly diffuse to the photocatalyst, the polymer has only a limited effect on the reactivity.

As a second photocatalytic reaction, the C-C coupling reaction of 4-chlorobenzylbromid was investigated, which was previously not reported for this photocatalyst to the best of our knowledge.[306] (Figure 5.13, Figure 6.11-6.13) Li *et al.* reported the usage of a Cu-modified TiO_2 photocatalyst for the C-C coupling under UV-irradiation.[307] The reaction was performed under blue light in the presence of DIPEA. The coupling again indicates a comonomer effect on the efficiency of the photocatalytic moiety. The photocatalytic reaction was analyzed via a kinetic study over a time span of eight hours, in which a conversion of 61 to 83% was achieved. The highest conversion of 83% and a TON of 277 was again yielded by PS-BT, followed by PAN-BT and PMMA-BT with 68 and 61% conversion and TON 227 and 203, respectively. Interestingly, the reaction was first attempted with triphenylamine (TPA) instead of DIPEA to prevent a hydrogen transfer and the formation of 4-chlorobenzylbromid as a side product. Interestingly, the reaction shows a slower reaction rate in the presence of TPA. Nevertheless, it was observed that the formation of 4-chlorotoluene is also unfavored in the presence of DIPEA, and only traces of 4-chlorotoluene are observed. (see Figure 6.11: GCMS trail of 1,2-bis(4-chlorophenyl)ethane using 1-bromo-octane as standard.Figure 6.11) Lastly, the C-C coupling between diethyl bromomalonate and 3-methyl indole was investigated. (Figure 5.14)

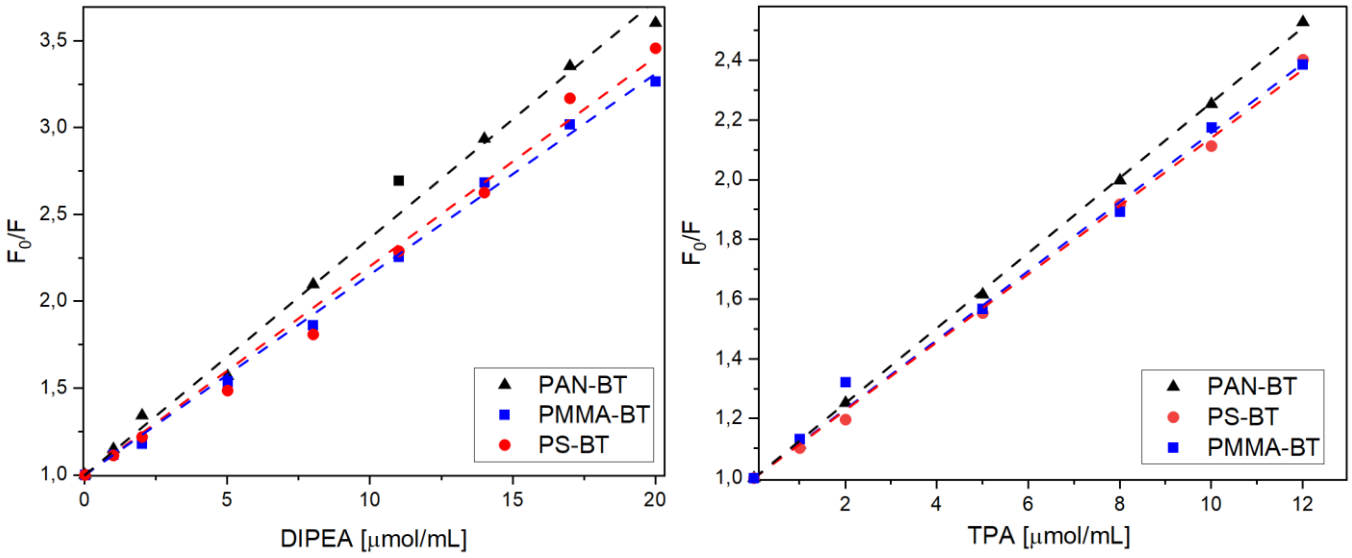

Figure 5.12: Stern-Volmer Plot of PAN-BT, PS-BT and PMMA-BT using DIPEA (left) and TPA (right) as quenching agent.

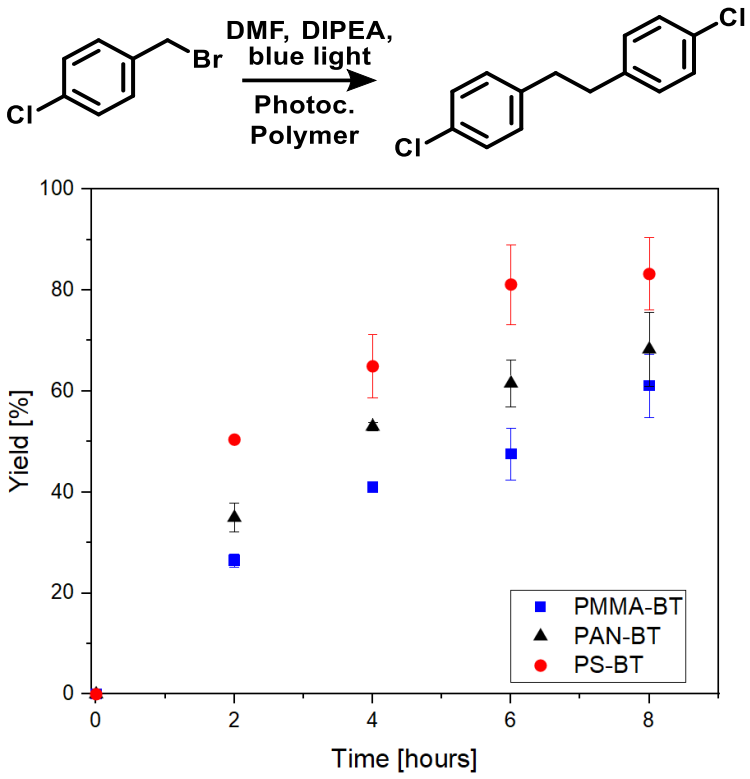

Figure 5.13: Photocatalytic C-C coupling of 4-Chlorobenzylbromide over eight hours using PS-BT, PMMA-BT and PAN-BT indicating a comonomer on the overall efficiency. 4-chlorobenzyl bromide (20.5 mg, 100 µmol) *N*,*N*-diisopropylethylamine (175 µL, 1 mmol) and photocatalytic polymer (300 nmol photocatalytic moiety) in DMF (2 mL), N_2-Atm. blue light irradiation.

The reaction was performed quickly in under 90 min., requiring the usage of TPA to reduce the favored dehalogenation of diethyl bromomalonate. GCMS analysis, in combination with a kinetic study, highlights the total conversion of the indole to the desired product. (Figure 5.14**,** Figure 6.8-6.10) Using PS-BT, a complete conversion of the indole is observed in 80 min (600 TON). PMMA-BT, in comparison reaches a TON of 360 in 80 min, indicating a 40% decrease in efficiency. Lastly, PAN-BT again shows the lowest photocatalytic efficiency, reaching a conversion of 20% (120 TON), which highlights the most significant drop in performance in all tested reactions. Although the contrast in the capability of the copolymers is significant, the trend is comparable to the previous reaction, where PS-BT outperformed PMMA-BT or PAN-BT. Further, the quenching behavior of TPA was analyzed, showing comparable quenching results and a decrease in fluorescence to DIPEA. The general trend is repeated, with all three copolymers showing only slight variation and PAN-BT being slightly elevated compared to PS-BT and PMMA-BT. (Figure 5.12)

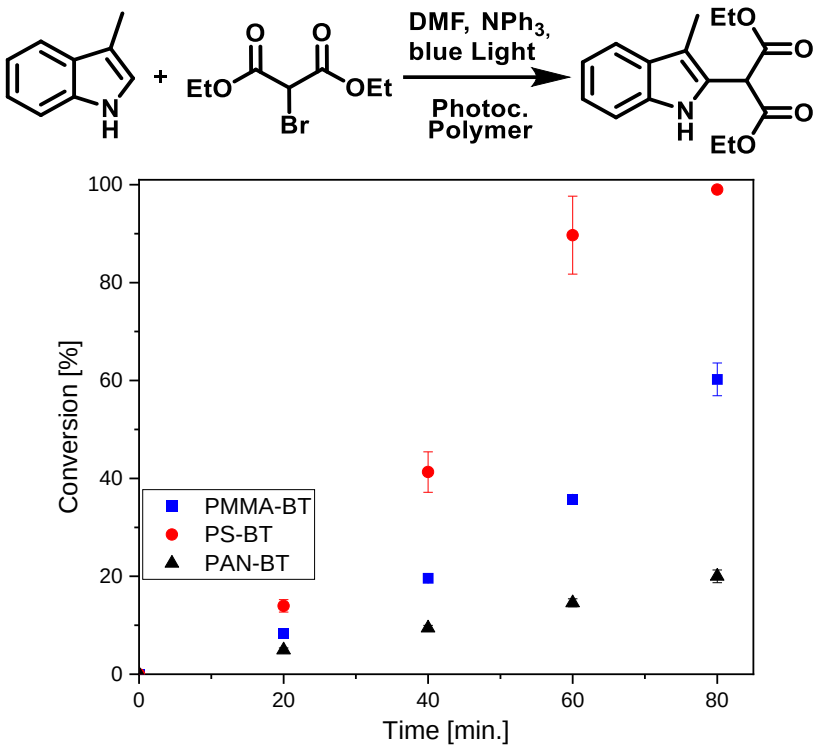

Figure 5.14: Kinetic investigation of the C-C coupling of 3-methyl indole measured over 80 min showing full conversion for PS-BT. 3-methyl indole (19.7 mg, 150 µmol), diethyl bromomalonate (71.7 mg, 300 µmol) and triphenylamine (73.6 mg, 300 µmol) and photocatalytic polymer (250 nmol photoactive unit) in DMF (2 mL) Ar-Atm. blue light irradiation.

5.1.3 Conclusion: Copolymers Impact the Photocatalytic Efficiency and Photophysical Properties

In summary, we copolymerized three common monomers with a donor-acceptor-based photocatalyst and investigated the impact of the comonomer on the photocatalytic activity. In a first step, seven functionalized benzothiadiazole moieties were investigated via UV/Vis absorbance. As expected, the chosen functionalization has a significant effect on the absorbance wavelength. Based on these findings, a vinyl-functionalized photocatalytic moiety was chosen to allow maximizing any comonomer effect and minimizing any effect of the functional group. The solvent effect was also investigated with DMF, toluene, and THF possessing an absorbance peak between 391-393 nm, while $MeNO_2$ and ACN led to a significant blue shift. For the analysis of the comonomer effect, DMF was chosen based on the necessity to dissolve the copolymers. Seven monomers were copolymerized with vinyl benzothiadiazole and investigated via UV/Vis absorbance and fluorescence spectroscopy. The comonomers based on PMMA, PBMA, PHEMA, and PDMA showed little effect on absorbance and emission, while PAN-BT and PS-BT had the highest blue and redshift.

Therefore, in the next step, the photophysical properties of the comonomers PS-BT, PAN-BT, and PMMA-BT were analyzed. UV/Vis spectra show a dependence based on the monomer choice, with PAN-BT possessing a blue shift compared to PS-BT and PMMA-BT. Quantum yield and fluorescence lifetime measurements also indicate a correlation with the polymer backbone. The differences between PMMA-BT and PS-BT are negligible. At the same time, PAN-BT shows deviating values indicating a lower lifetime of the excited state as well as a reduced quantum yield and a blue shift of the absorption and emission spectra. DFT calculations and cyclic voltammetry were used to determine the HOMO and LUMO levels, and the optical bandgap was determined. Showing only marginal differences between the three polymers.

In the next step, the photocatalytic performance of the three copolymers was analyzed in three photocatalytic kinetic studies. As model reactions, the hydroxylation of boronic acids and two C-C coupling reactions were successfully performed, and the conversion and TON were determined. Through this catalytic testing, it could be shown that the comonomer choice impacts the photocatalytic efficiency. The hydroxylation of boronic acid was not significantly impacted by the comonomer choice, which can be explained by the diffusion of oxygen, which is not hindered by the polymer structure in the solution. The C-C coupling reactions, on the contrary, need closer proximity between the photocatalyst and the substrate to proceed, and therefore more significant differences can be observed.

Interestingly, a trend could also be observed over all tested reactions, which lay in accordance with the measured optical properties. PS-BT possessed the highest absorbance wavelength paired with the longest lifetime of the excited state and could outperform the other two copolymers. It could be argued that the π-π interaction affects the photocatalytic efficiency by stabilizing the excited state of the photocatalyst. PAN-BT, on the other hand, possessed a higher blue shift in the absorbance spectra

and a lower lifetime, leading to a lower performance under visible light irradiation. Indicating that depending on the photocatalytic reaction, the chosen polymer can impact the performance, and an adequate and suitable copolymer must be chosen.

Nevertheless, polymers as support for photocatalytic moieties are useful due to the vast possible material properties and morphologies that the right monomer combinations can achieve. It is, therefore, vital to find the most efficient compromise between the possible impact of the comonomer on the photocatalytic efficiency and possible benefits due to the designed material. In this study, linear polymers were investigated, removing the structural design of heterogeneous photocatalysts. Further, the effect of the chosen functional group of the benzothiadiazole was explored via UV/Vis-absorbance, and a systematic study has yet to be performed. The chosen functional group could have a significant impact on the copolymerization parameter as well as the photocatalytic activity.

5.2 Photocatalytic Hydrogels with a High Transmission Polymer Network for Pollutant Remediation

This chapter is based on an article, "Photocatalytic hydrogels with a high transmission polymer network for pollutant remediation" published in *Chem. Mater.* 2021, **33**, 9131-9138. I synthesized and characterized the material and performed the photocatalytic reaction. Here, a classical photocatalytic polymer hydrogel composed of a high transmittance polymer network and small conjugated photocatalytic moieties is present. Radical copolymerization of a photocatalytically active benzothiadiazole acrylamide monomer with water-compatible *N*,*N*-dimethylacrylamide produced a photocatalytic hydrogel where only the photocatalytic moiety absorbs visible light. The photocatalytic hydrogel network enables easy partitioning of pollutants into the gel network, where they are photocatalytically degraded. The versatility and reusability of the photocatalytic material were demonstrated for the degradation of both inorganic metal and organic contaminants, including *N*-(phosphonomethyl)glycine (glyphosate), the most commonly used herbicide. Furthermore, the potential of this material was explored in large-scale experiments, where glyphosate could be readily photodegraded at a half-liter scale.

5.2.1 Motivation: Photocatalysis for Environmental Friendly Wastewater Remediation

Sunlight is an abundant and renewable energy source that can be utilized to facilitate a broad range of chemical reactions. Inspiration can be taken from nature, where sunlight is used as a clean energy source in photosynthesis. Numerous heterogeneous photocatalytic materials have been produced to mimic this natural process, and were implemented into a wide-range of chemical applications, including water splitting,[308-314] photoredox reactions,[79,124,136,285,315,316] CO_2 reduction,[317-320] photo-dynamic therapy[321-324] and wastewater purification.[62,325-328]

Wastewater treatment is an important part of a sustainable water management and integral for an ever-increasing global population. The recycling of water by purification through separation or degradation of pollutants is, therefore, essential. Unfortunately, conventional sewage treatment systems are not able to efficiently remove new emerging molecular pollutants.[329,330] Photocatalysis has therefore received increasing attention for water contaminant degradation.[62,326-328] Photocatalysis enables ecologically friendly wastewater purification by photodegradation, facilitated by the generation of highly oxidizing species. Previously, heterogeneous photocatalysts have been used for wastewater treatment based on different materials ranging from inorganic materials, such as TiO_2, to nanodots and conjugated polymers.[134,331-334]

Nevertheless, one of the most prominent drawbacks of heterogeneous photocatalytic materials is the low photon penetration depth into the photocatalytic material. A low and uneven irradiation is often

observed in bulk applications, lowering overall irradiation efficiency and, therefore, photodegradation.[335-338] This can be due to light incident on the heterogeneous material being scattered. Furthermore, light penetration into heterogeneous photocatalytic materials is often limited, leading to inefficient usage of the photocatalytic material, especially in large-scale applications. This poor penetration may be due to the absorption of light by non-photocatalytically active materials.

Ideally, a heterogeneous photocatalytic system for water purification would be created that could be easily recovered and reused. Furthermore, visible light incident on the material, should be homogeneously absorbed across the photocatalytic material, and not be obstructed by the supporting material. Additionally, the photocatalytic material must be compatible with aqueous environments, allowing for easy partitioning of reagents into and out of the photocatalytic material. Therefore, the synthesis of a high transmittance, hydrophilic, porous substrate in combination with a homogeneous distributed photocatalytic moiety may yield more efficient photocatalysts.[287,339-342]

Hydrogels are hydrophilic networks, which contain over 90% water, have a high biocompatibility, and allow easy substrate diffusion into the material. As a result, hydrogels have been widely studied for biomedical applications, including drug delivery.[343-345] Moreover, transparent hydrogels have been use in soft contact lenses.[344,346,347] Compared to rigid porous structures, hydrogels possess a more flexible framework, which allows for swelling in water. This behavior leads to a highly swollen structure, which aids an easy diffusion of molecules into the gel. Due to this, hydrogels are studied with great interest for possible applications in wastewater remediation as their properties allow for the absorbance of dyes and org. pollutants.[348,349] Hydrogels can easily be synthesized through radical polymerization without the need for exceedingly toxic materials, or heavy metals. Therefore, transparent hydrogels would be a desirable polymer matrix for the incorporation of photocatalysts. Recently, our group has described the synthesis of a new class of photocatalytic classical polymers.[189,203,208] The copolymerization of photocatalytic small molecules, modified with vinyl functionality and classical monomers, combines the versatility of classical polymers with photocatalytic activity. This combination produces a new hybrid material class of photocatalytically active polymers.[185] Here, we have designed photocatalytic hydrogels, where only the photocatalytic moieties absorb visible light, as illustrated in Figure 5.15. The copolymerization of photocatalytic small molecules with classical monomers produces highly efficient photocatalytic gels. A *N*,*N*-dimethylacrylamide (DMAA), based gel was selected due to the high transmittance of visible light through the gel, allowing more energy to be available for the photocatalytic units. A donor-acceptor type photocatalytic unit containing benzothiadiazole (~2 mol%) was copolymerized into the gel material, with leaching of the photocatalytic unit inhibited.

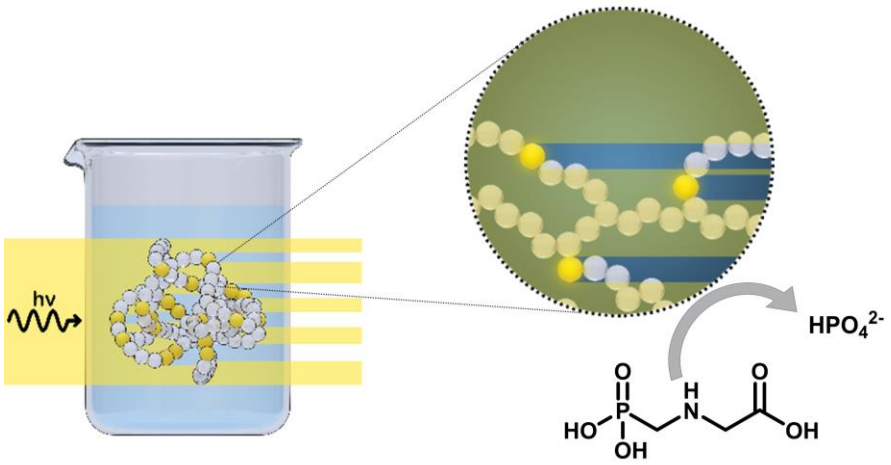

Figure 5.15 High transmittance photocatalytic hydrogels allow for easy light penetration into the photocatalytic system for efficient water remediation. Light is not reflected or absorbed by the polymer network and is, therefore, available for photocatalytic reactions.

Due to its intrinsic properties, the hydrogel allows for a high substrate diffusion into the substrate, while the high transmittance of the polymer network does not interfere with the absorbance properties of the photocatalytic units. The photocatalytic hydrogel was used for the photodegradation of model wastewater pollutants. The broad application range and versatility of the photocatalytic hydrogel was investigated for the photooxidation of *N*-(phosphonomethyl)glycine (glyphosate), rhodamine B, organic sulfurs, as well as the photoreduction of inorganic pollutants, namely heavy metal contaminants in the form of chromium (VI). Furthermore, the scalability of the material was investigated for a gram-scale photodegradation of glyphosate.

5.2.2 Results and Discussion: Design of a Highly Transmittance Photocatalytic Hydrogel

In the first step, three suitable hydrophilic monomers were investigated to design a high-transmittance hydrogel. *N,N*-dimethylacrylamide (DMAA), acrylamide (AA), and hydroxyethyl methacrylate (HEMA) were combined with poly(ethylene glycol)diacrylate (PEG-DA) to synthesize hydrogels via radical polymerization in water. (Figure 5.16) The polymerizations were performed in degassed cuvettes, allowing for direct analysis of the designed materials via transmittance measurements. Photocatalytic hydrogels were synthesized using radical polymerization, allowing quick and cost-efficient synthesis. Comparing the resulting crosslinked polymers PDMAA-PEG, PAA-PEG, and PHEMA-PEG showed, in all cases, a high transmittance at higher wavelengths, reaching 98% at 565 nm. (Figure 5.17)
Nevertheless, at lower wavelengths, significant differences between the polymers were observed, with PHEMA-PEG possessing the overall lowest transmittance at lower wavelengths, reaching 95% transmittance at 460 nm. PDMAA-PEG, on the other hand, possessed the highest transmittance,

reaching 95% at 402 nm. PDMAA possessed the highest transmittance at lower wavelengths, and was selected as the support polymer. In the next step, the concentration of the crosslinker on the transmittance was investigated. Three concentrations of one, two, and five equivalents of crosslinker were synthesized. Although the differences between one and two equivalents were neglectable on the transmittance, the hydrogel possessed a honey-like consistency with only one Eq. of crosslinker. Adding 5 Eq., on the other hand, led to a significant decrease in transmittance, reaching only 84% at 402 nm. In the last step, the PEG crosslinker was replaced with *N*,*N*-dimethylacrylamide to allow comparable propagation rates between the monomer crosslinker and photocatalytic moiety, leading to a high transmittance hydrogel reaching up to 95% transmittance at 400 nm.

The hydrogel matrix was therefore constructed from DMAA and crosslinked using *N*,*N*'-methylenebis(acrylamide). (Figure 5.18) This gel network was selected due to its high transmittance of visible light. Preventing energy loss due to light scattering and absorption of non-photocatalytically active portions of the hydrogel. The absorbance of the polymer matrix was analyzed via transmittance measurement displaying high transmittance of 95 to 99% between 400-800 nm, while in the UV-region below 400 nm, the hydrogels absorbance increases. (Figure 5.19)

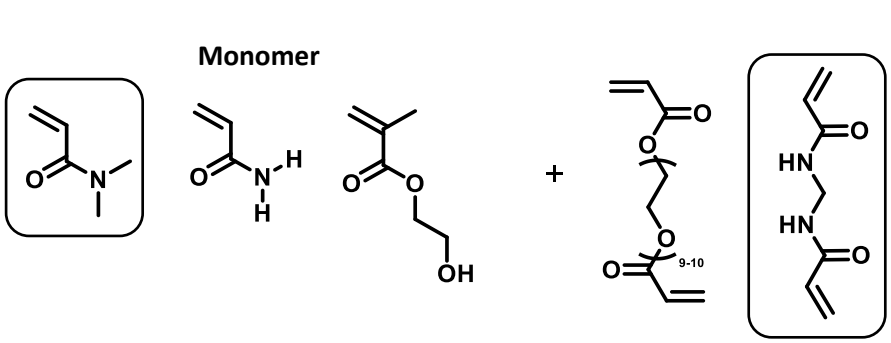

Figure 5.16: Analyzed monomers and used crosslinker to synthesis a highly transmittance hydrogel. Highlighted are *N*,*N*-dimethylacrylamide and *N*,*N*'-methylenebis(acrylamide) which were chosen for the hydrogel.

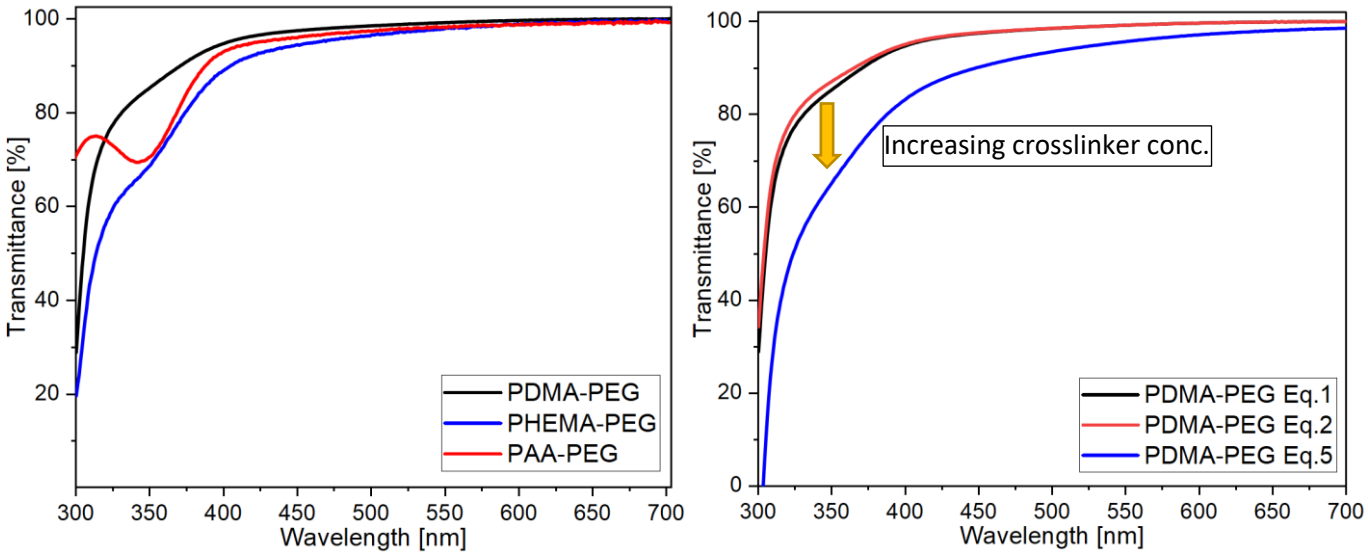

Figure 5.17: Transmittance values of PDMA, PAA and PHEMA crosslinked with PEG. PDMA possesses the highest transmittance compared to the other monomers. (left) Influence of crosslinker concentration on the transmittance of the synthesized hydrogel. (right)

N-(4-(7-Phenylbenzo[c][1,2,5]thiadiazol-4-yl)phenyl)acrylamide photocatalytic monomer was copolymerized into the hydrogel network, leading to a high transmittance photocatalytic hydrogel, a high transmittance photocatalytic hydrogel. (Figure 5.18, Figure 6.17-6.18) The photocatalytic monomer displayed a peak absorption at 400 nm, with the absorption extended to 470 nm. (Figure 5.19) The photocatalytic monomer was designed and synthesized to include acrylamide functionality to ensure that the propagation rate of the polymerization for each monomer was in the same order of magnitude, which is integral to producing a homogenous photocatalytic hydrogel. Density functional theory (DFT) calculations of the photocatalytic monomer were used to predict the energy and electron density of the highest occupied molecule orbital (HOMO) and lowest unoccupied molecule orbital (LUMO). (Figure 5.20) The HOMO and LUMO-levels were 1.42 V and -1.75 V vs SCE, respectively.

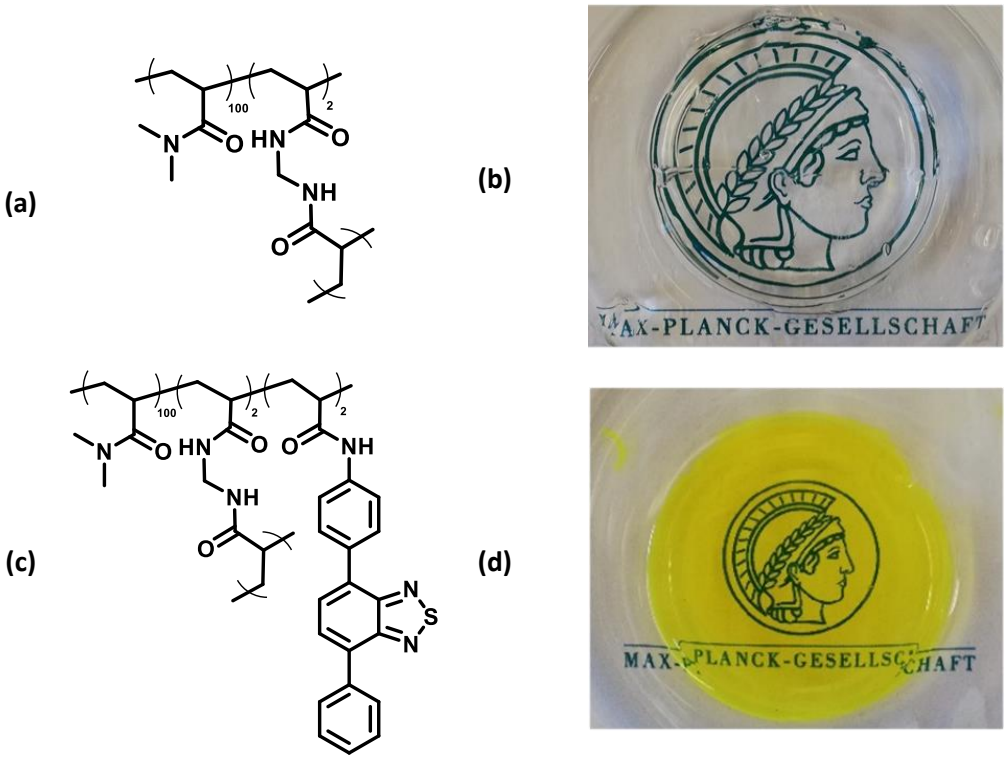

Figure 5.18 High transmittance hydrogel (a) molecular structure of designed hydrogel, (b) synthesized high transmittance hydrogel, (c) molecular structure of designed photocatalytic hydrogel, (d) synthesized photocatalytic.

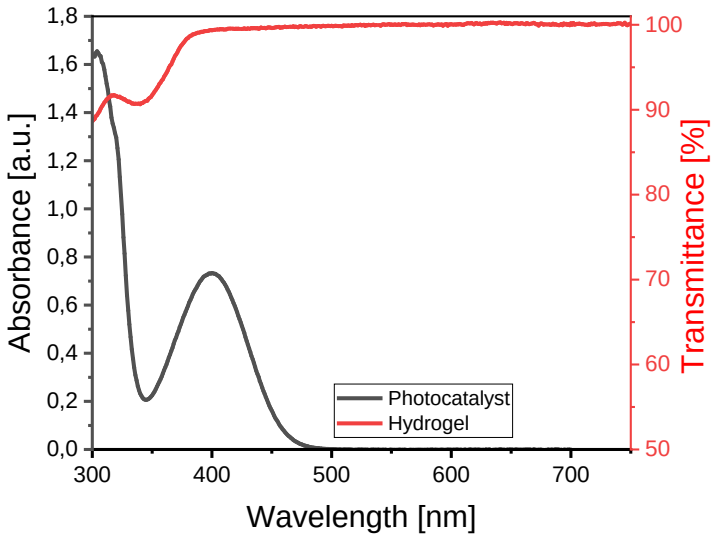

Figure 5.19 Transmittance spectra of the hydrogel without photocatalyst (red), absorbance spectra of the photocatalyst (black).

From cycle voltammetry, the LUMO-level of the photocatalytically hydrogel was determined to be -1.30 vs SCE, similar to the calculated value. (Figure 5.20) The difference in measured and calculated LUMO levels is believed to be due to the calculated value being for the monomer, not the polymerized form. Previously published DTF calculations and CV-measurements of vinyl functionalized benzothiadiazole monomers display comparable HOMO/LUMO energies, indicating stable energy levels regardless of the chosen functionalization.[203] This enables different functionalities to be incorporated and copolymerization with various monomers with differing propagation rates to be achieved.

Solid-state-NMR (ssNMR) and Fourier transform infrared (FTIR) spectroscopy were used to verify the inclusion of the photocatalytic monomer within the polymer. ^{13}C-ssNMR spectroscopy shows a peak at 37 ppm corresponding to the polymer backbone and the methylamine groups. A strong peak was observed at 175 ppm due to the carbonyl group of each monomer. Aromatic peaks are observed between 125-160 ppm, which correspond to the photocatalytic monomer, showing that the active unit is indeed within the polymer hydrogel. (Figure 5.21) FTIR analysis of the photocatalytic hydrogel and the photocatalytic monomer was undertaken. (Figure 5.22) The FTIR shows peaks at 2930 cm^{-1} for the $-CH_2$ and $-CH_3$ stretch vibration. The peak at 1620 cm^{-1} can be assigned to the stretching of the carboxamide. Signals at around 1500 cm^{-1} are attributed to the $-CH_3$ deformation, while the band at around 1260 cm^{-1} is due to C-N stretching. Due to the low concentration of photocatalytic moiety within the hydrogel (1.9 mol%), the peaks corresponding to the conjugated photocatalytic monomer are not easily discerned.

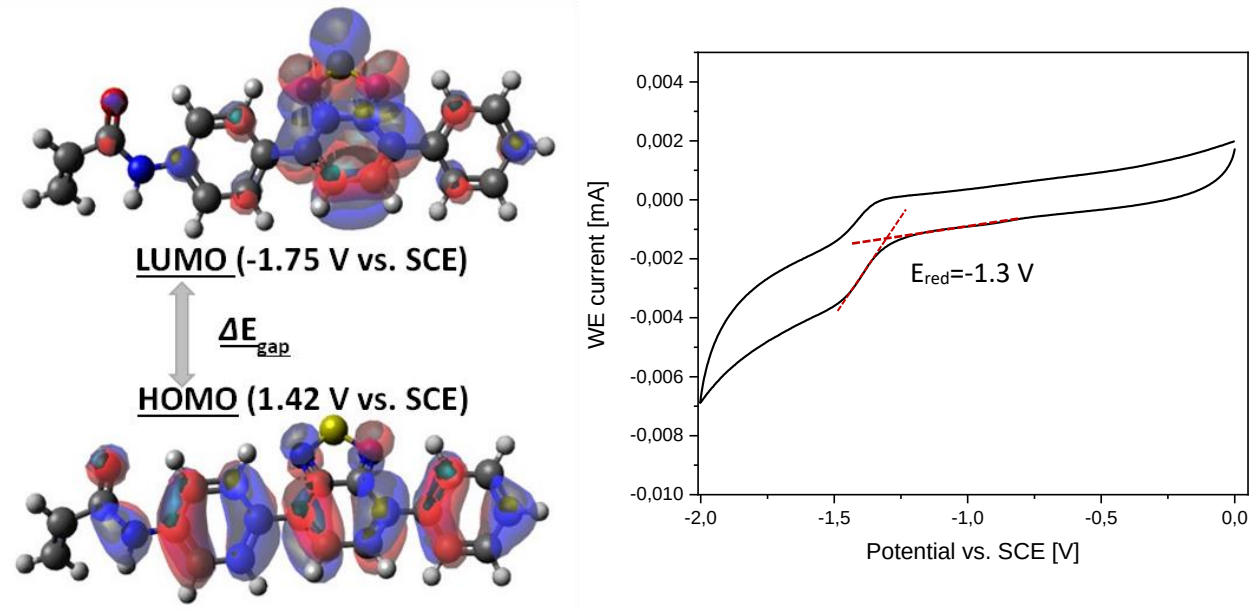

Figure 5.20 (left) DFT-Calculated electron structure and HOMO/LUMO-level of *N*-(4-(7-phenylbenzo[c][1,2,5]thiadiazol-4-yl)phenyl)acrylamide vs SCE. (right) Cyclic voltammetry of photocatalytic hydrogel (100 mV/S).

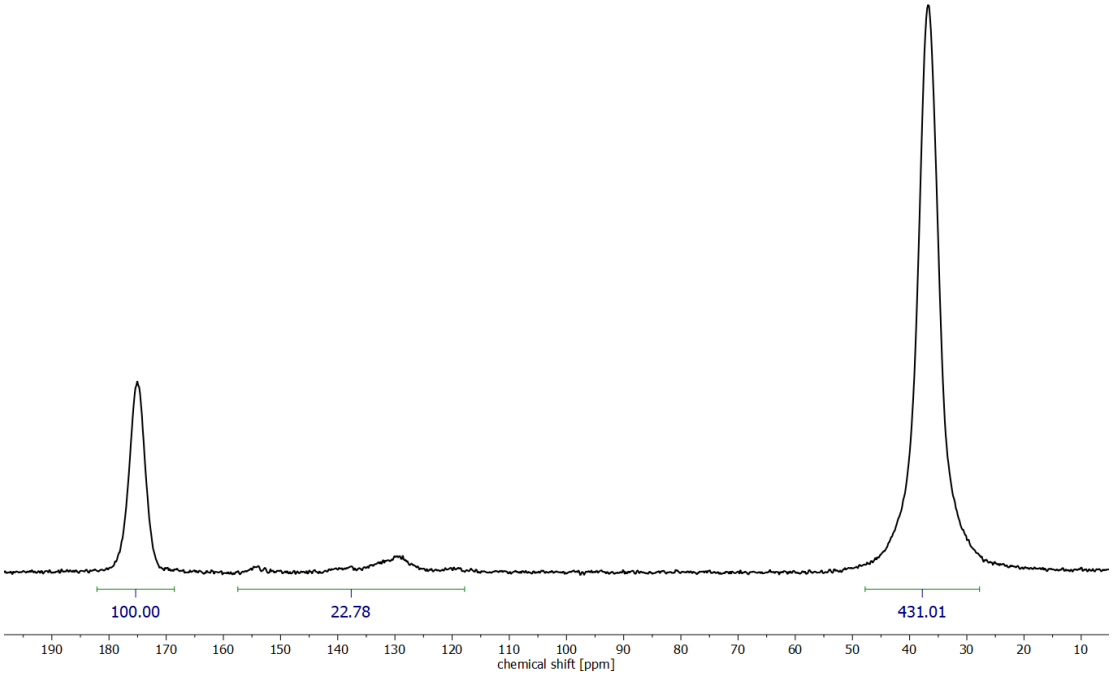

Figure 5.21: Solid state NMR spectroscopy: ^{13}C-CP-MAS NMR spectrum of photocatalytic hydrogel.

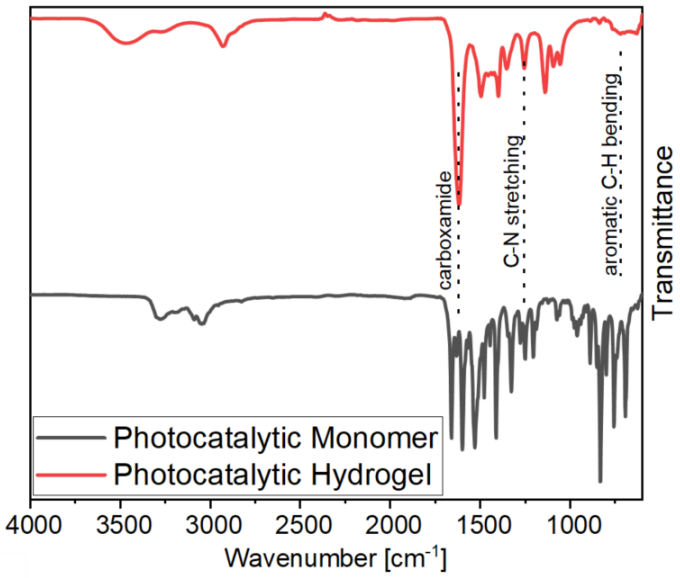

Figure 5.22 FTIR of photocatalytic hydrogel (red) and the synthesized photocatalytic monomer (black).

UV/Vis-absorbance spectra of the dried hydrogel showed peak absorption at 420 nm extending to 510 nm, indicating a red shift compared to the pure photocatalytic monomer in DMSO. (Figure 5.23) The photocatalytic behavior of the synthesized hydrogel was further analyze through photocurrent

measurements. (Figure 5.23) In five repeating cycles, a photoinduced conductivity was measured, presenting a clear photoresponsive behavior.

The dried photocatalytic hydrogel readily swells in water. The degree of swelling was determined by fluorescence spectroscopy. Here, the photocatalytic units incorporated into the gel network enable easy monitoring of the swelling process. The photocatalytic hydrogel swelled in water by a factor of 2.5 within 30 sec., and as expected, we see an even distribution of the photocatalyst across the gel network. (Figure 5.24) Furthermore, no leaching of the photocatalytic moiety was observed during the swelling process. The degree of swelling of the hydrogel was obtained over three swelling cycles, where the weight gain was measured and the water content determined. Showing that the fully swollen gel reaches a water content of 92%. (Figure 5.25)

Water pollutants can be classified into two categories: organic and inorganic. Here, we have determined the potential of the high transmittance photocatalytic hydrogel for remediation of both pollutant classes. Initially, we investigated the degradation of organic pollutants, including small molecule pollutants and industrially relevant agrochemical-based water pollutants. The photocatalytic degradation of an organic dye molecule, rhodamine B, was undertaken. Here, over 95% of the aqueous organic dye was removed within four hours in the presence of photocatalytic hydrogel. (Figure 5.26) Following the successful degradation of simple dye molecules, the remediation of organosulfur containing compounds was targeted.

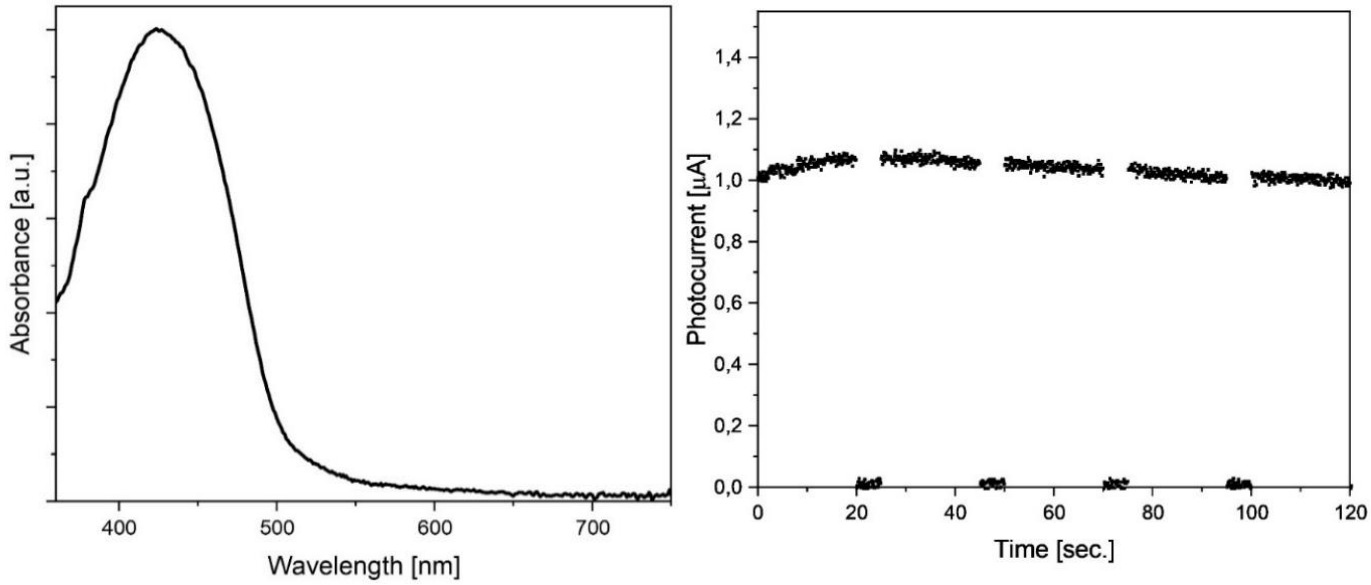

Figure 5.23 a) UV/Vis-Absorbance spectra of dried photocatalytic hydrogel. b) Photocurrent measurements under blue light (power: 0.16 W cm^2, λ = 460 nm) with 20 sec. irradiation intervals.

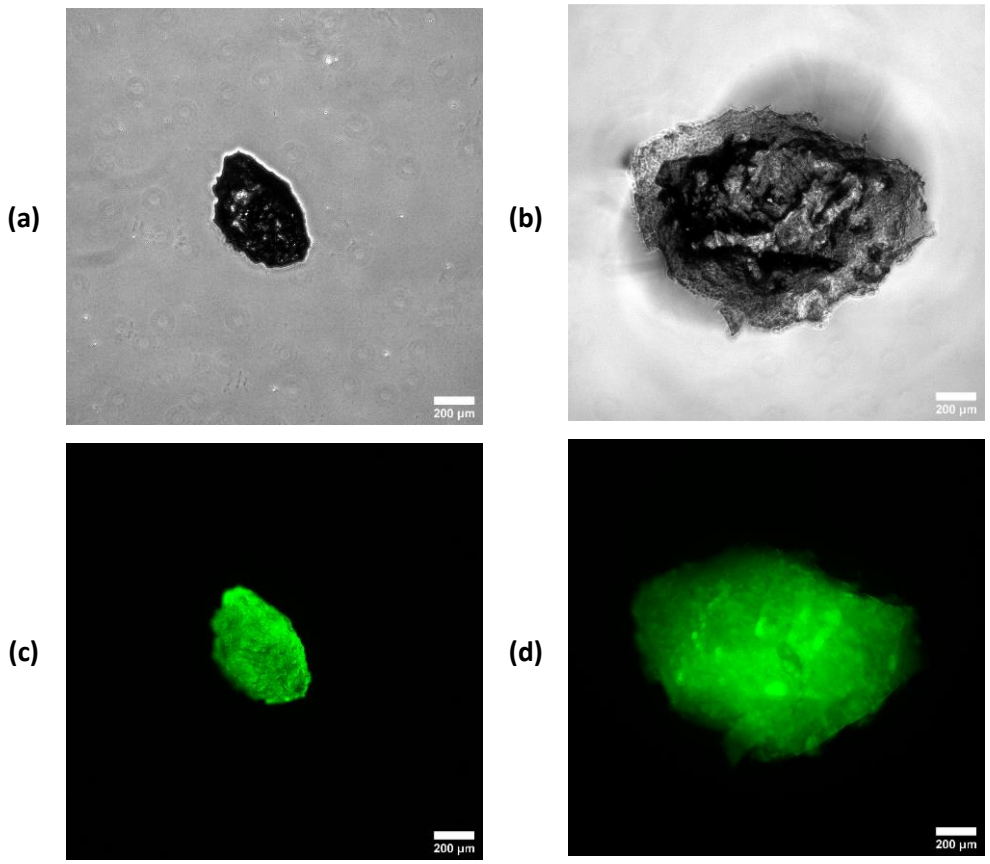

Figure 5.24 Swelling behavior of the photocatalytic hydrogel. Dry hydrogel in the absence of water. (a and c) Photocatalytic hydrogel after 30 sec. in the presence of water (b and d).

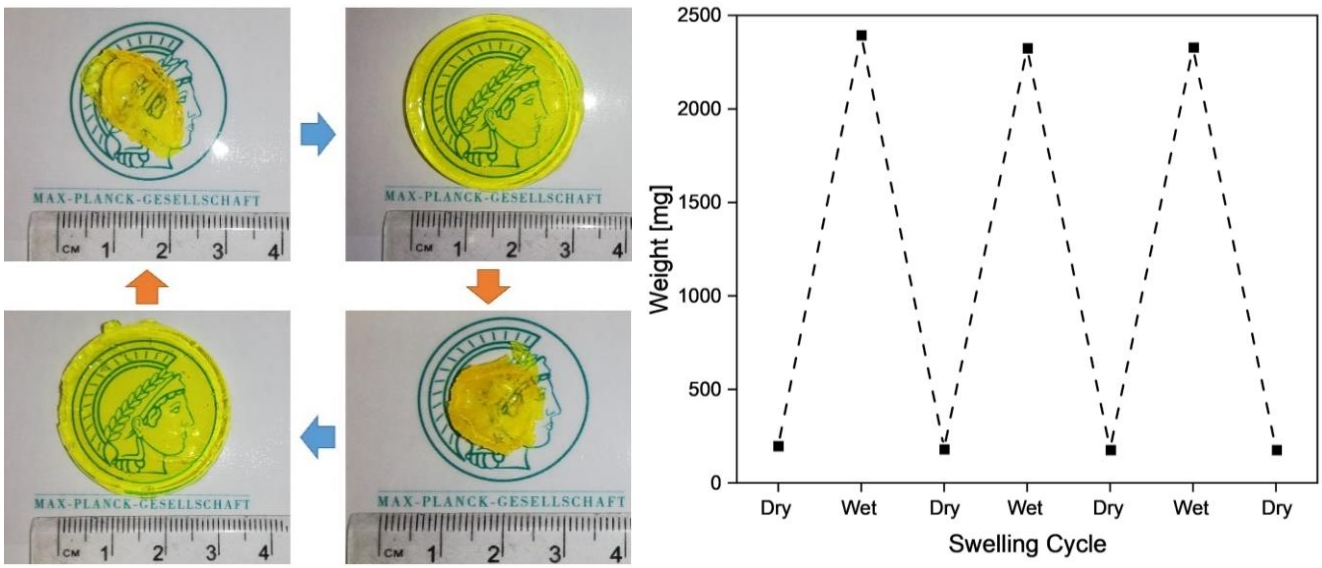

Figure 5.25 Reversible swelling and drying of the photocatalytic polymer hydrogel (left); weight gain during swelling circle (right).

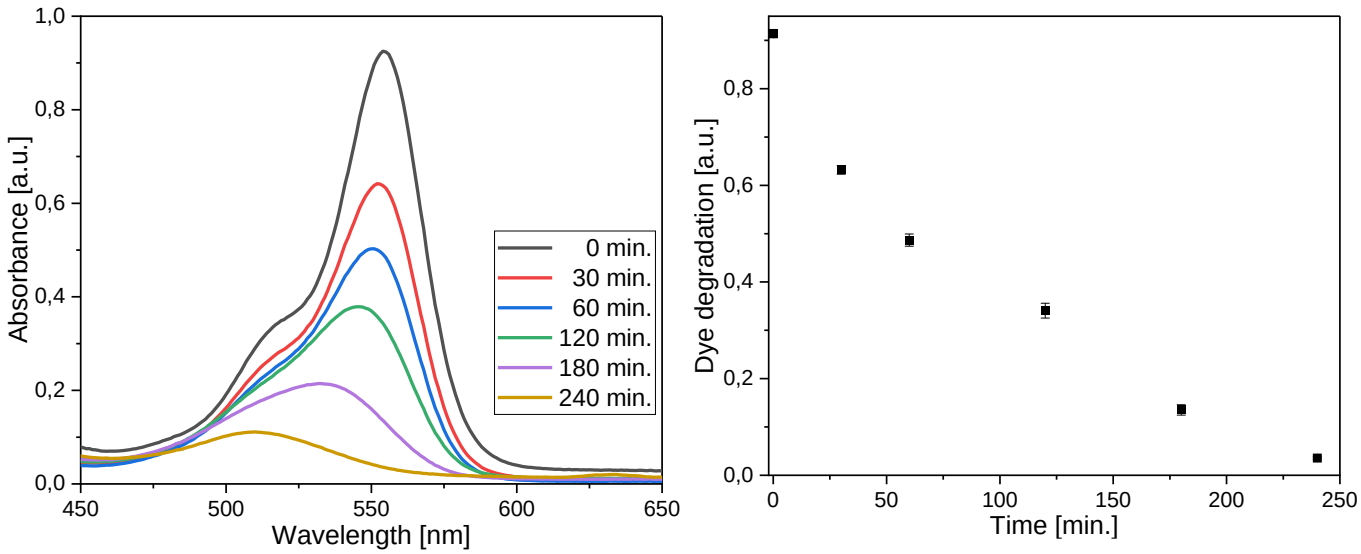

Figure 5.26 UV/Vis-spectra of time depending photodegradation of rhodamine B (left) peak intensity for the photodegradation of rhodamine B plotted against time (right).

Organic sulfur containing compounds are emerging pollutants in wastewater due to their increased presence in drug molecules.[62,330,331] As a model, methyl phenyl sulfide and its derivative were oxidized, as seen in Table 5.2. Over 99% conversion was obtained for the oxidation of methyl phenyl sulfide, with a selectivity of 98:2 towards the mono-oxidized sulfoxide. Furthermore, functional group tolerance was observed in reactions with substituted methyl phenyl sulfide molecules with only small changes in the selectivity. (Table 5.2, Figure 6.21-6.28)

All reactions could be conducted with low concentrations of photocatalyst (sulfide 30 mM, hydrogel 10 mg, 1.9 mol% photocatalyst, 1.8 µmol) and in comparison to porous classical polymer photocatalysts in the absence of oxidants.[189] Similarly Zhao *et al.* used a metal-based $Bi_4O_5Br_2$ photocatalyst (20 mg) for the photooxidation of various methyl phenyl derivatives (0.2 mmol) under blue light in water requiring up to 22 h for the oxidation of 4-chlorophenyl methyl sulfide and showcasing that under blue light irradiation, TiO_2 showed low photocatalytic activity due to its wider bandgap.[350]

Table 5.2 Photocatalytic oxidation of methyl phenyl sulfide through photocatalytic hydrogel under various condition. Sulfide (30 mM), hydrogel (10 mg, 1.8 µmol photocatalyst), 10 mL H_2O, conversion determined by GC-MS.

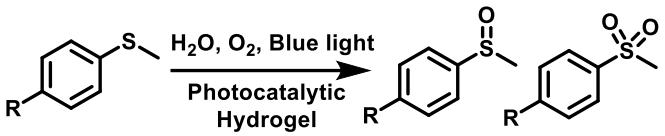

Number	Condition	Conversion
1	R=H	<99% (98:2)
2	No light	0%
3	No photocat.	0%
4	No oxygen	2% (100:0)
5	R=-Me	<99% (94:6)
6	R=-OMe	<99% (95:5)
7	R=-Cl	<99% (93:6)

Scavenger tests were undertaken to show that the oxidation observed is indeed photocatalytically driven. As expected, in the absence of light, oxygen, or photocatalyst, no conversion was detected. (Table 5.2) Benzoquinone, sodium azide, potassium iodide, isopropanol, and copper chloride were used as superoxide, singlet oxygen, vacant hole, hydroxyl radical and electron scavengers, respectively. Here, scavengers for superoxide, single oxygen, and the vacant hole species had the highest impact on conversion. In the presence of benzoquinone, a superoxide ($O_2^{\cdot-}$) scavenger, the conversion to sulfoxide was reduced by 75%, whereas the addition of a sodium azide did not decrease the conversion but led to a higher yield of the sulfone species. (Figure 5.27) Further to organic pollutants, inorganic pollutant remediation was also investigated.

Next to organic compounds, heavy metals are one of the most common pollutants in industrial wastewater.[351-353] Cr^{VI} is a non-biodegradable pollutant and can cause significant environmental damage due to its high toxicity and cancerous properties.[354,355] We have utilized the high transmittance photocatalytic hydrogels to photoreduce Cr^{VI} to Cr^{III} under aqueous conditions. Water-soluble Cr^{VI} was successfully reduced to the less toxic and water-insoluble Cr^{III}. Allowing for an easy precipitation of the pollutant and decontamination of the wastewater.

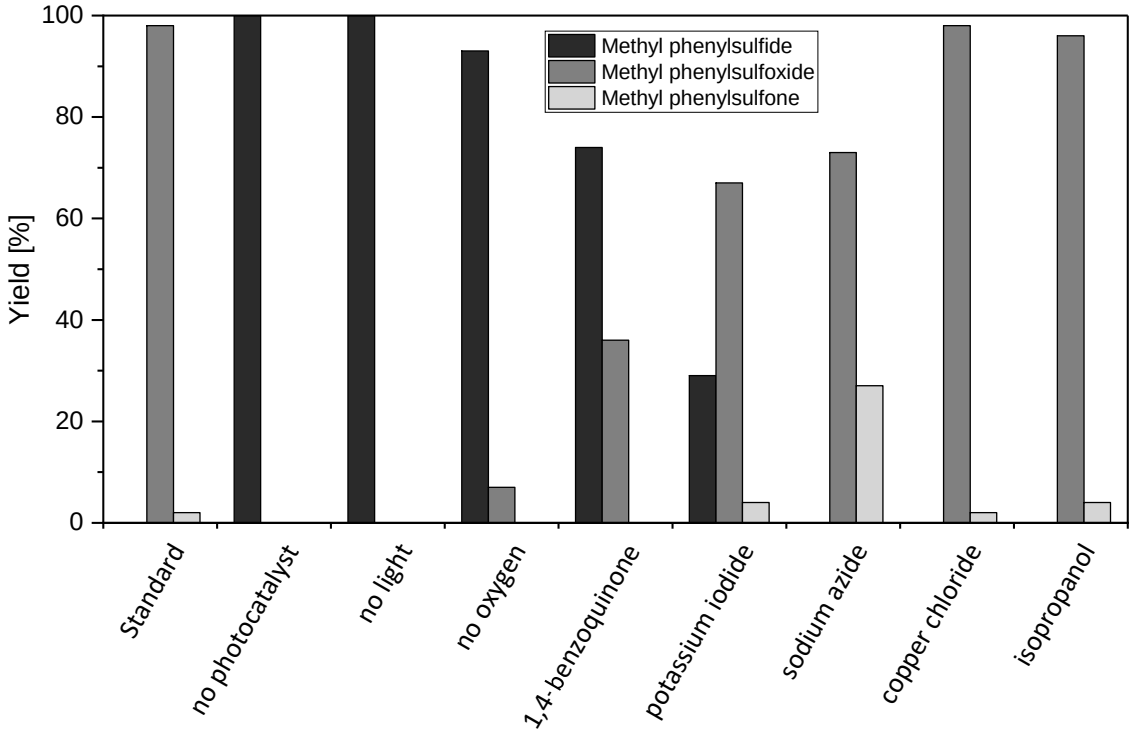

Figure 5.27: Comparison of achieved conversions and selectivity for the photooxidation of thioanisole under standard conditions, the absence of photocatalyst, light or oxygen and in the presence of quenching agents.

The Cr^{VI} photoreduction was measured by complexation of Cr^{VI} with diphenylcarbazide and monitored using UV/Vis spectroscopy. (Figure 5.28, Figure 6.29) Cr^{VI} was reduced to Cr^{III} in around 60 min under blue light irradiation with a conversion of over 92%. (Figure 5.29) In contrast, control reactions in the dark and without photocatalyst resulted in no conversion. (see Figure 6.30) Compared to previously published, water-compatible, fully conjugated microporous polyazulene photocatalysts, the photocatalytic hydrogel was found to have a higher efficiency, requiring lower amounts of photocatalytic active material.[356] Further comparison can be drawn to a donor-acceptor based benzothiadiazole covalent framework using 10 mg photoactive material paired with a xenon lamp (400 nm cutoff) for the degradation of a 10 mL Cr^{VI} solution (10 mg/L).[157]

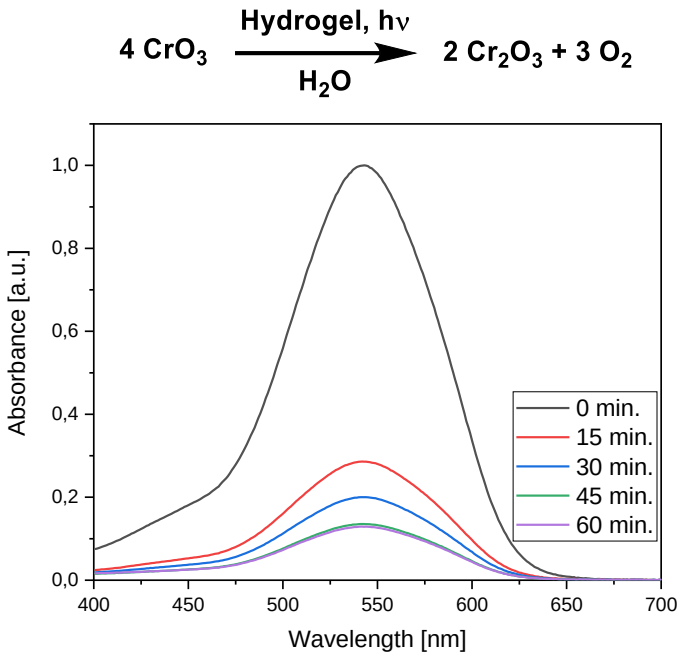

Figure 5.28: Photoreduction of chromium^{VI} is quantified through complexation of the remaining Cr^{VI} with diphenylcarbazide allowing for UV/Vis absorbance measurements at 542 nm.

The reusability of the photocatalytic hydrogel was demonstrated by conducting a recycling test for five repeating cycles. Cr^{VI} was again photoreduced in each run without significant loss in efficiency, displaying that the material is suitable as efficient and stable heterogeneous photocatalyst. (Figure 5.29, Figure 6.31)

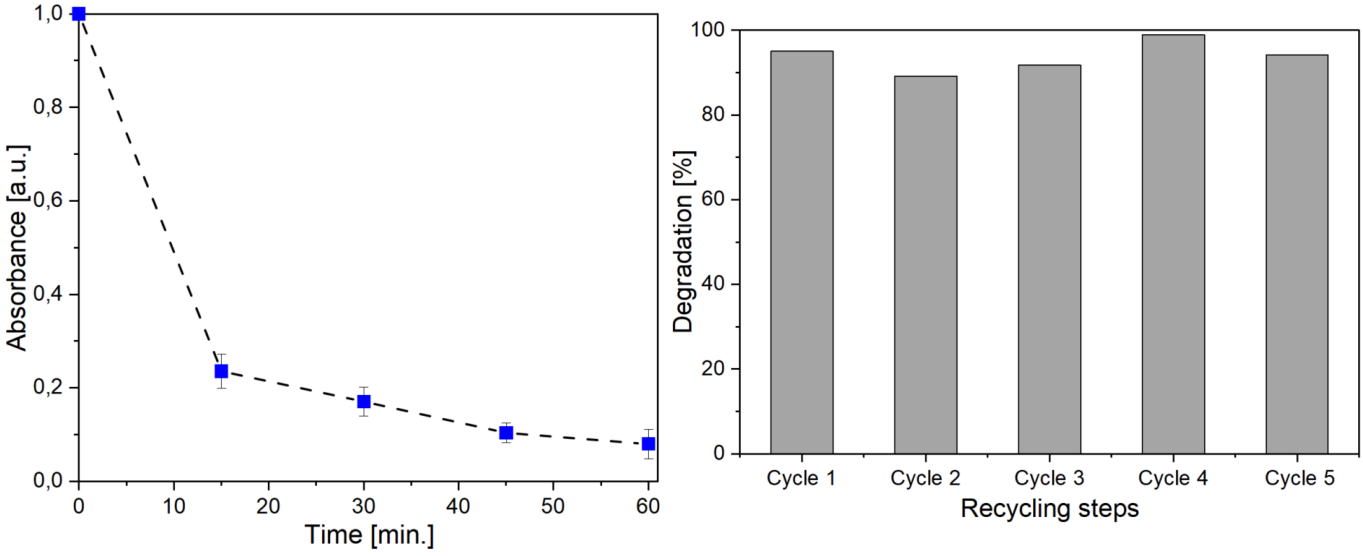

Figure 5.29 Photodegradation of chromium by photocatalytic hydrogel chromium photoreduction over time under N_2 atmosphere measured at 542 nm by complexation with diphenylcarbazide (left); 5 recycling steps for the photoreduction of Cr^{VI} to Cr^{III} using photocatalytic hydrogel under blue light irradiation (power: 0.16 W cm^{-2}, λ = 460 nm) (right).

The versatility of the high transmittance photocatalytic hydrogel for the remediation of pollutants in water was further demonstrated by investigating the photocatalytic degradation of glyphosate.

Glyphosate is a non-selective organophosphate herbicide and the most widely used herbicide globally.[357,358] Its overuse in agriculture has led to increasing concerns regarding dangerous levels of run-off into water systems such as rivers, lakes, and groundwater.[359,360] Glyphosate has been found in surface and subsurface water sources and is known to be toxic to aquatic organisms.[361-364] Therefore, it is important to produce methods that can readily degrade glyphosate in contaminated water.
Glyphosate is stable over a wide range of possible conditions and is not readily hydrolyzed in water.[365] We have demonstrated that high concentrations of glyphosate (2.5 mg/mL) can successfully be photodegraded using low amounts of the photocatalytic hydrogel (5 mg/mL, 1.9 mol% photocatalyst, 0.9 µmol) under visible light. Over 90% degradation was observed after 2.5 h under basic conditions, while no significant degradation was observed under acid or neutral conditions. The reaction progression was analyzed via 31P-NMR spectroscopy with a glyphosate shift of 16.9 ppm and the main degradation product, phosphate, emerging at 2.5 ppm, while blank measurements in the absence of photocatalyst or light showed no signs of degradation. (see Figure 6.34-6.35) NMR spectroscopy analysis further indicated the existence of an intermediate at 19.3 ppm, which is likely to be (aminomethyl)phosphonic acid.[366] (Figure 5.30, Figure 5.31)

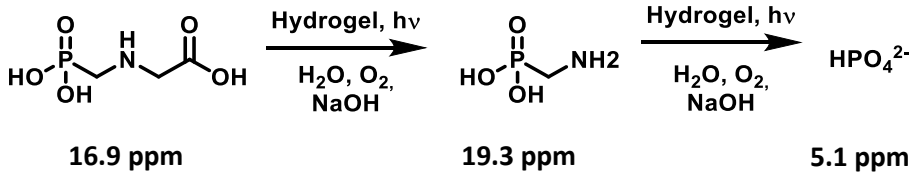

Figure 5.30: Photodegradation of glyphosate analyzed via ^{31}P-NMR spectroscopy and the observed peaks. The degradation products were assigned based on the research of Kudzin et al.[366]

The time dependent degradation was investigated by kinetic measurement. Therefore, the photodegradation of glyphosate was analyzed via ^{31}P-NMR spectroscopy, where a near-linear degradation of glyphosate was observed. (Figure 5.32 and Figure 6.32) Previously, degradation has been achieved using TiO_2-nanoparticles in a photoreactor. Here, a much larger concentration of TiO_2-nanoparticles (6 g/L) was required to achieve similar results as the hydrogel presented in this study. Furthermore, previous pure organic systems have been shown to be insufficient for photocatalytic degradation of glyphosate, where BiO_4/PDA/g-C_3N_4 hybrid systems were required.[367]

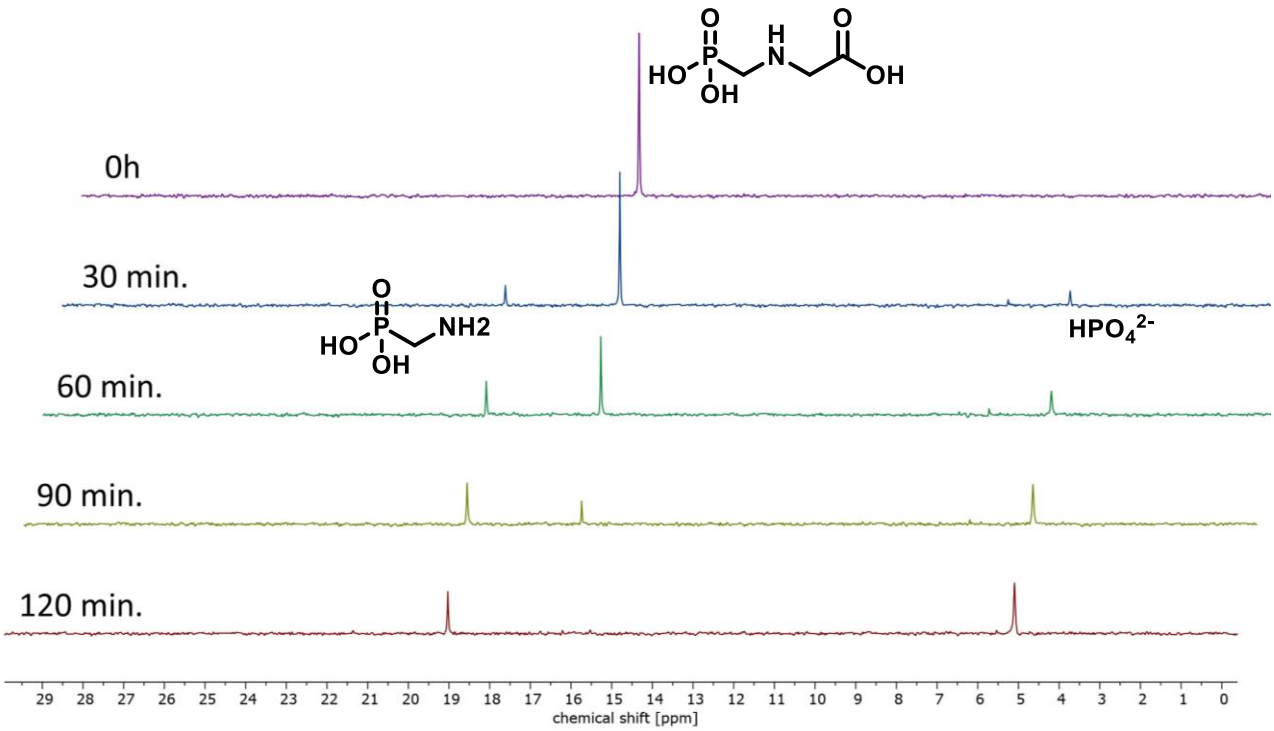

Figure 5.31: Degradation of glyphosate by linear photocatalytic PDMMA was analyzed via ^{31}P-NMR spectroscopy. The kinetic study allows a clear evidence for the complete degradation of glyphosate overtime. The degradation products were assigned based on the research of Kudzin et al.[366]

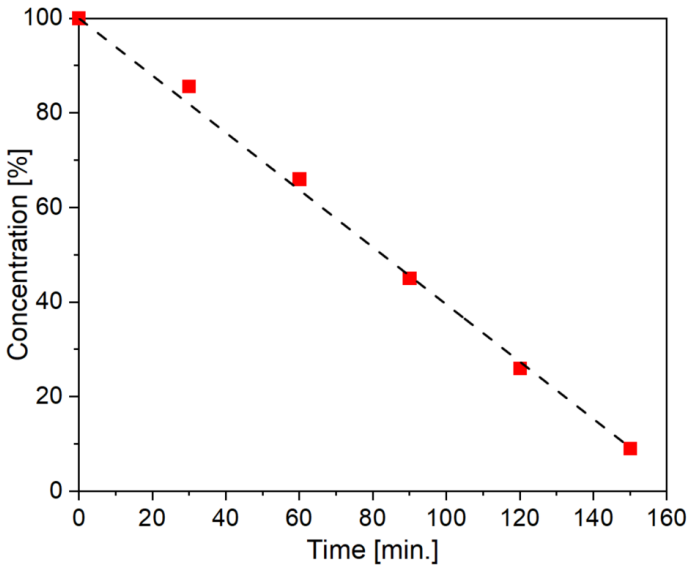

Figure 5.32 Glyphosate degradation monitored over time via ^{31}P-NMR spectroscopy.

Large-scale photocatalytic batch reactions are generally hindered by low light penetration depth and light scattering upon the heterogeneous photocatalyst, leading to low overall efficiency. The high transmittance values of the synthesized hydrogel substrate should mitigate these issues and enable large-scale photocatalysis.

In a first step, a flow-through photocatalytic column was envisioned, allowing for the efficient degradation of pollutants in flow. The assumption was that due to the swelling of the hydrogel and its high transmittance value, the material would be the ideal material. The swelling allows for a quick uptake and diffusion of pollutants into the gel, where it would be degraded, while the high transmittance would allow for a significant increase of the column's diameter, allowing for sufficient light penetration. As a test, the hydrogel was first synthesized without the photocatalytic unit within the flow-through column utilizing a heating mantel. The column possessed a glass frit and an inner diameter of around three centimeters. The polymerization was achieved using two heating blocks of 10 cm in length and a cylindrical recess for the column, leading to quick and efficient polymerization. The hydrogel was synthesized within the column and was first tested using water dyed with methylene blue. Although the synthesized gel possessed a high transmittance and allowed for the flow through of water, the polymerization in the column led to the clocking of the glass filter as well as a structural compact gel that was unable to swell. Therefore, the hydrogel possessed a low permeability, resulting in a slow water flow requiring artificial pressure. (Figure 5.32)

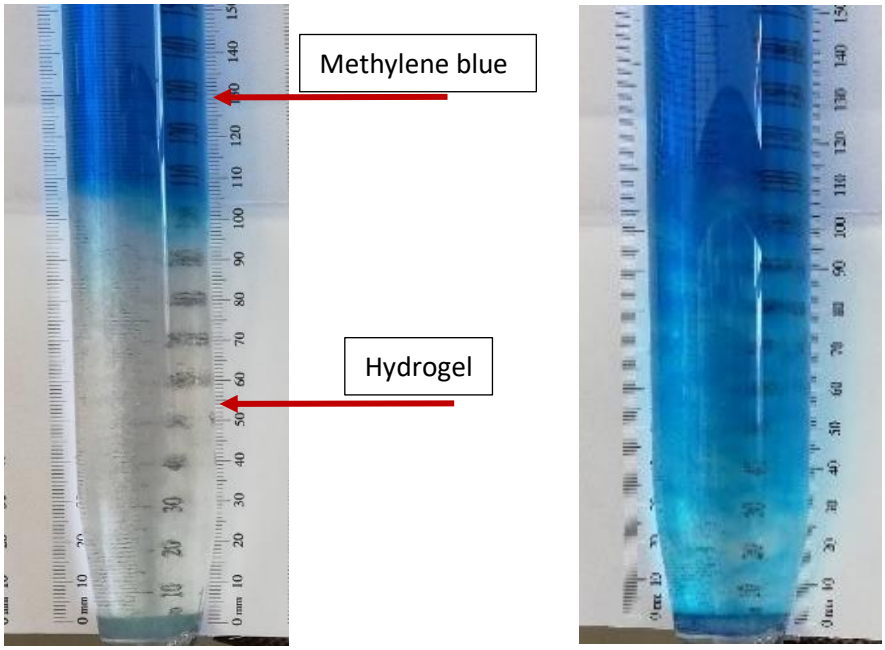

Figure 5.33: The hydrogel was polymerized inside a column to test the viability of a flow though photocatalytic column. A white paper with measurement in cm was added to visualize the column size. A methylene blue solution was used to showcase the flow of water through the gel over time (pressure 0.5 bar, 30 min.)

As the flow-through column, led to no satisfying results and did not allow for a sufficient water flow an alternative approach was used to showcase the possible large-scale application of the synthesized photocatalytic hydrogel.

A large-scale photodegradation of glyphosate was conducted in a half-liter batch reaction; 1 g glyphosate was photodegraded using the photocatalytic hydrogel, leading to 60% conversion in the first 25 h and 78% after 45 h. (Figure 5.34 and Figure 6.33) Here, we observed an initial high rate of photodegradation that slowed over time as the concentration of glyphosate decreased.

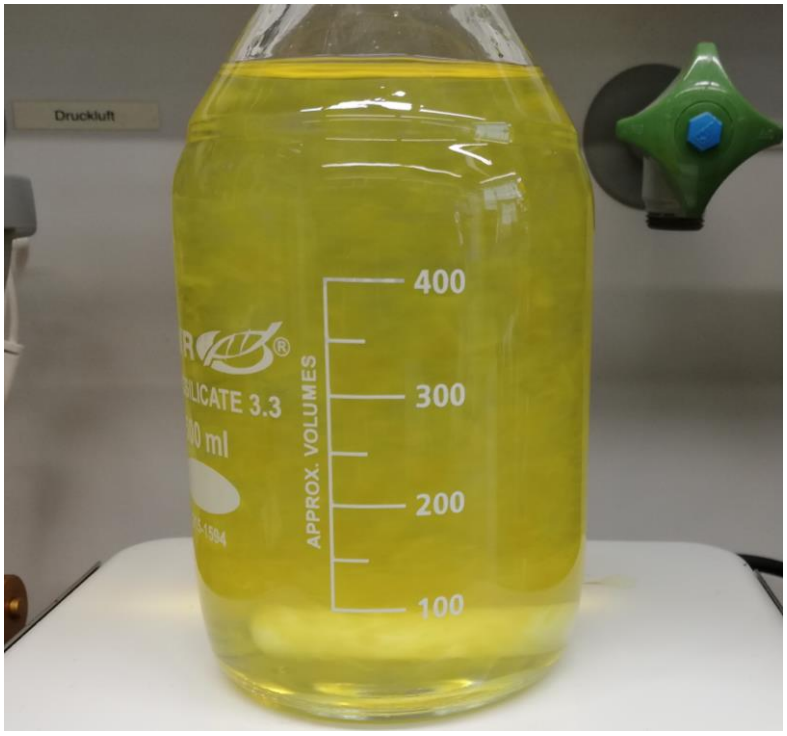

Figure 5.34 Large scale glyphosate degradation. (left) half liter scale photodegradation of 1 g of glyphosate in water.

The photocatalytic network produced in this study provides a readily recoverable heterogeneous photocatalyst. However, the gel network produced in this study requires the diffusion of reagents into the network for degradation. To investigate the effect this diffusion has on the degradation rate of glyphosate, a linear polymer was synthesized. Here, the photocatalytic monomer was copolymerized with DMAA in the same ratio as in the hydrogel without the usage of a crosslinker and was analyzed via ^{1}H-NMR spectroscopy and GPC. (see Figure 6.19, Figure 6.20) The photodegradation of glyphosate using the linear PDMAA shows a similar linear degradation, with full conversion in under 120 min. (Figure 5.35, Figure 6.36). The linear photocatalytic polymer had a slightly faster rate of degradation when compared to the polymer gel network. However, the photocatalytic polymer hydrogel is much easier to recover, making it a more favorable material for long-term use.

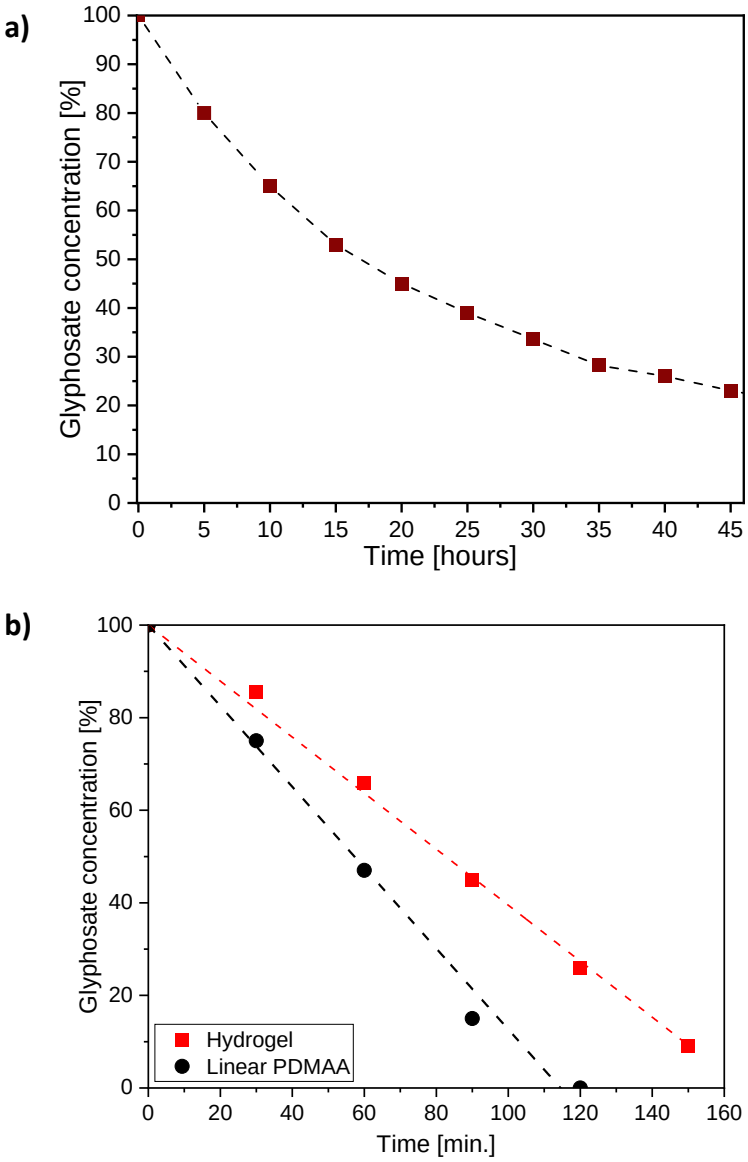

Figure 5.35: (a) Glyphosate degradation over time monitored via ^{31}P-NMR spectroscopy. (b) Glyphosate degradation monitored over time via ^{31}P-NMR spectroscopy using photocatalytic hydrogel (red) and linear photocatalytic PDMMA (right).

5.2.3 Conclusion: Novel Photocatalytic Material for Wastewater Treatment

In summary, we present the radical copolymerization of a photocatalytic monomer into a highly transparent crosslinked hydrogel used for wastewater remediation.

In the first step, three suitable monomers, DMAA, HEMA, and AA were crosslinked with PEG-DA, leading to three hydrogels with high transmittance at higher wavelength, reaching over 95% transmittance at 460 nm. Of these three polymers, PDMAA-PEG had the highest transmittance, and consequently, PDMAA was used for further optimization. It was observed that the amount of crosslinker led to a decrease in transmittance, reaching an optimal compromise between stability and transmittance at two equivalents. In the last step, PEG-DA was replaced with *N,N*-methylenebis(acrylamide), leading to a high transmittance hydrogel with over 95% transmittance over 400 nm.

In the next step, a metal-free photocatalytic moiety was synthesized and functionalized to allow for radical copolymerization. An acrylamide functionalization was chosen to allow a comparable copolymerization rate between all three compounds. The polymerization was performed in DMF instead of water due to the low solubility of the photocatalytic moiety in water. All tests to achieve a homogeneous copolymerization in water or solvent mixtures were unsuccessful.

Nevertheless, the synthesized hydrogel was easily transferred to water. The non-toxic water-compatible photocatalytic hydrogel has easily accessible photoactive centers within a high transmittance network. The transmittance of visible light to the active sites enables homogeneous photocatalysis over the whole material, as the polymer network does not interfere. This classical polymer photocatalyst was used for efficient water remediation of common pollutants in wastewater. We showcased the photoreduction CrVI, the oxidation of a model compounds in the form of organic sulfides, as well as the photodegradation of glyphosate under visible light irradiation.

Furthermore, the high transmittance hydrogels could be used on large scales, with glyphosate degradation conducted on the half-liter scale.

The usage of the hydrogel in a flow-through column was also tested but was not progressed further. Although the polymerization could be performed within the column, the resulting hydrogel was too compacted and could not expend accordingly in water, leading to a slow flow-through.

The combination of classic polymers with small molecule photocatalysts enables the production of tunable functional materials that can be used for a range of applications, including wastewater remediation. The reported material could be used for the remediation of various wastewater compounds while allowing for easy recycling of the bulky material. The created hydrogel allows for the fast uptake of wastewater pollutants and rapid remediation. The bulky material further only possesses a small amount of photocatalytically active material, allowing for easy handling and scalability.

5.3 Reactivity Tuning of Metal-Free Artificial Photoenzymes through Binding Sites Specific Bioconjugation

This chapter is based on an article "Reactivity tuning of metal-free artificial photoenzymes through binding sites specific bioconjugation" published in *Eur. J. Org. Chem.* 2023, **26**, e202201412. This work was conducted in collaboration with the University of Edinburgh under the Saltire Emerging Research Scheme. Protein expression, method development for bioconjugation, and LCMS analysis were performed by Dr. Brewster. I synthesized the photocatalytic moieties and performed protein purification, bioconjugation, characterization, and photocatalytic testing.

The design and development of artificial metal-free photoenzymes aims to combine the selectivity of enzymatic reactions with the benefits of modern synthetic photocatalysts. Removing the need for rare earth metals and allowing for milder reaction conditions, leading to a more sustainable catalytic system. Here, we present the design of a novel artificial photoenzyme by integrating an organophotocatalytic moiety based on a donor-acceptor design into a steroid carrier protein (SCP-2L). SCP-2L possesses a hydrophobic tunnel facilitating substrate binding in aqueous media. The photocatalyst was site-selectively bound to three SCP-2L variants, possessing a non-native cysteine residue strategically placed around the hydrophobic tunnel of the protein. The three modified photoenzymes were shown to be selective for the oxidation of organic sulfides, giving up to 192 turnovers.

5.3.1 Motivation: The Design of Artificial Photoenzymes

Bioengineering allows the modification and functionalization of complex biomacromolecular structures and is a highly promising approach for developing efficient and sustainable catalysts using modified proteins and enzymes.[368-371]Enzymes are highly specific and efficient catalytic systems, combining stereoselectivity, biocompatibility, and stability while having a limited substrate range. The three-dimensional nature of proteins allows for stereospecific hindrance near the active center, leading to highly selective catalytic processes, making protein scaffolds ideal platforms for the development of novel catalytic systems with the benefit of using water as a sustainable solvent. Through bioengineering, proteins can be combined with modern chemical catalysis, leading to the synthesis of novel artificial enzymes and pairing the benefits of enzymatic precision, with the substrate range and capabilities of state-of-the-art chemical catalysts.[372,373]

Unfortunately, chemical synthesis and enzymatic conditions are often incompatible due to the need for high temperature, pressure, or organic solvents, leading to the degradation of the biomaterial, making the optimization of conditions difficult.[374-376] Light is a renewable energy source and finds use in naturally occurring photoenzymes, removing the need for thermal energy.[377-379] Taking inspiration from nature, light-driven catalysis has undergone intensive research as an alternative and more

sustainable way for chemical transformations.[13,226,380] Compared to traditional catalysts, photocatalysts utilize photosensitizing molecules, allowing light absorption and energy or electron transfer via the excited state, resulting in milder reaction conditions.

Due to their versatility, fully organic metal-free photocatalysts have found widespread application in photoredox reactions.[33,381,382] Recent developments aim to modify these photocatalysts to incorporate them into support materials to increase stability and combine the material properties of the supporting material with the photocatalyst. This has led to the development of various novel photocatalytic systems, including artificial photoenzymes.[266,267,272] The incorporation of a modified photocatalytic moiety into a protein combines the advantages of a protein structure with photocatalysis, developing a biocompatible, efficient, and sustainable catalytic system.[273,383,384] To control the active site placement and structure, the catalyst is covalently bound to the protein, either through the usage of genetically encoded catalysts or site-selective bioconjugation.[272,275] Recent examples from the groups of Green and Wu incorporated genetically encoded benzophenone into a Diels-Alderase and multidrug resistance regulator LmrR, demonstrating enantioselective [2+2] cycloadditions.[270,385] Lewis and coworkers modified a prolyl oligopeptidase protein with 9-mesityl-10-methylacridinium *via* click chemistry and showed the photoenzyme was active in sulfoxidation reactions.[274] Nevertheless, the efficient incorporation of photocatalytic moieties into proteins and the overall development of bioconjugated proteins with precisely engineered catalytic centers remains a significant challenge in designing artificial enzymes.

Due to its ability to sequester substrates, the human steroid carrier protein SCP-2L is an ideal scaffold for artificial enzymes. SCP-2L possesses a single domain made from 120 amino acids, creating a hydrophobic tunnel, which allows for the uptake of apolar substrates.[386,387] The hydrophobic tunnel holds suitable positions for strategical positioning and introduction of non-native cysteine residues, while previously solved crystal structures show that no structural changes occur due to the introduction of non-native cysteine residues compared to the wild-type protein.[388]

The incorporated photocatalytic moiety is based on a well-established donor-acceptor design, allowing for better charge separation and an increased lifetime of the excited state. This photocatalytic design based on an electron-deficient benzothiadiazole unit allows control over the HOMO/LUMO level depending on the chosen donor and acceptor units.[70]

The 4,7-diphenyl-2,1,3-benzothiadiazole core has found widespread applications in conjugated frameworks,[130,136,285] homogeneous catalysis[70,73] or through incorporation into classical polymers,[185,189] catalyzing numerous light-driven photoreactions, including pollutant remediation,[301] photooxidations,[208] cycloadditions,[203] C-C coupling,[70] and bromination.[73]

Here, we report the design of novel artificial photoenzymes by integrating a photocatalytic 4,7-diphenyl-2,1,3-benzothiadiazole moiety into the protein SCP-2L, with the photocatalyst being bioconjugated at three unique cysteine residues within the protein. (Figure 5.36) The resulting

photoenzymes were analyzed via LCMS, UV/Vis, and the photocatalytic activity of all three variants was investigated by selective oxidation of thioanisole.

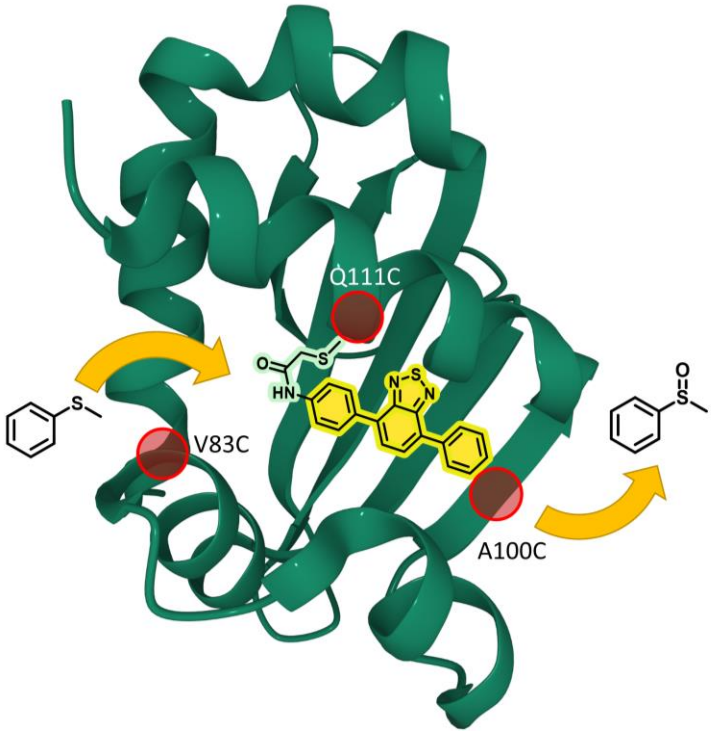

Figure 5.36 Protein scaffold with highlighted positions of non-native cysteine variants A100C, V83C, and Q111C in combination with the bioconjugated photocatalytic moiety. Image created using Mol* and 1IKT from the RCSB PDB (rcsb.org).[389,390]

5.3.2 Results and Discussion: Comparison of Three Novel Metal-Free Artificial Photoenzymes

First non-native cysteine residues were introduced into the wild-type protein, by site-directed mutagenesis to incorporate the photocatalytic unit into the protein scaffold, yielding three specific proteins: SCP-2L A100C, SCP-2L Q111C, and SCP-2L V83C (hereafter referred to as A100C, Q111C and V83C).[386,387,391] (see Figure 6.41) V83C and A100C are positioned at either end of the hydrophobic tunnel, and Q111C was chosen due to its position in the center of the tunnel.[387] (Figure 5.36)

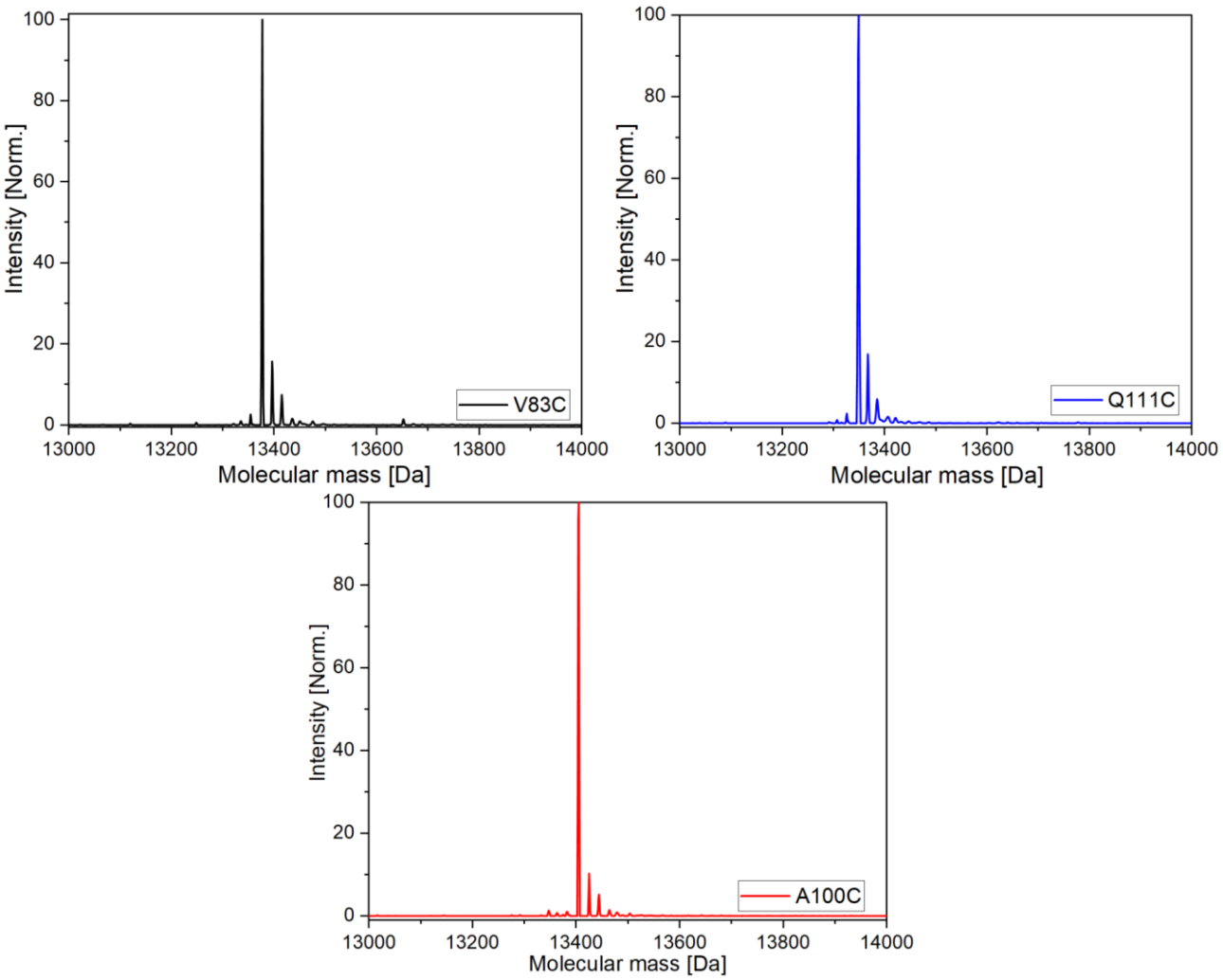

Figure 5.37: Mass spectra of A100C, Q111C and V83C, due to different replaced amino acids the three different variation possess different molecular weights: V83C (13377 Da), Q111C (13349 Da), and A100C (13405 Da).

In order to bioconjugate the 4,7-diphenyl-2,1,3-benzothiadiazole photocatalyst into the protein scaffold, a reactive handle needed to be introduced. To ensure a full bioconjugation, without any remaining non- or multiple conjugated proteins, three different functionalities for the photocatalyst with increasing reactivity were selected (Table 5.3). First, a vinyl-functionalized photocatalyst was synthesized with the goal of modifying the protein *via* a thiol-ene type coupling.[392] (Table 5.3 **Entry 1**) However, no reactivity was detected with either cysteine or V83C using blue light or radical initiator VA-044.

Acrylamides are good Michael-acceptors and are commonly used in medicinal chemistry as non-covalent inhibitors as they react selectively with cysteine.[393] A photocatalyst with an acrylamide group was synthesized and reacted with all three SCP-2L variants. (Table 5.3 **Entry 2,**Figure 5.38**,** Figure 6.42) After optimization of the bioconjugation reaction, stark differences in the incorporation yield depending on the positioning of the non-native cysteine residue were observed. V83C-2 was fully

functionalized with the photocatalytic moiety, showing no double or non-modified protein by LCMS. However, A100C-2 and Q111C-2 could not be fully bioconjugated and showed remaining non-modified protein. (Figure 6.42)

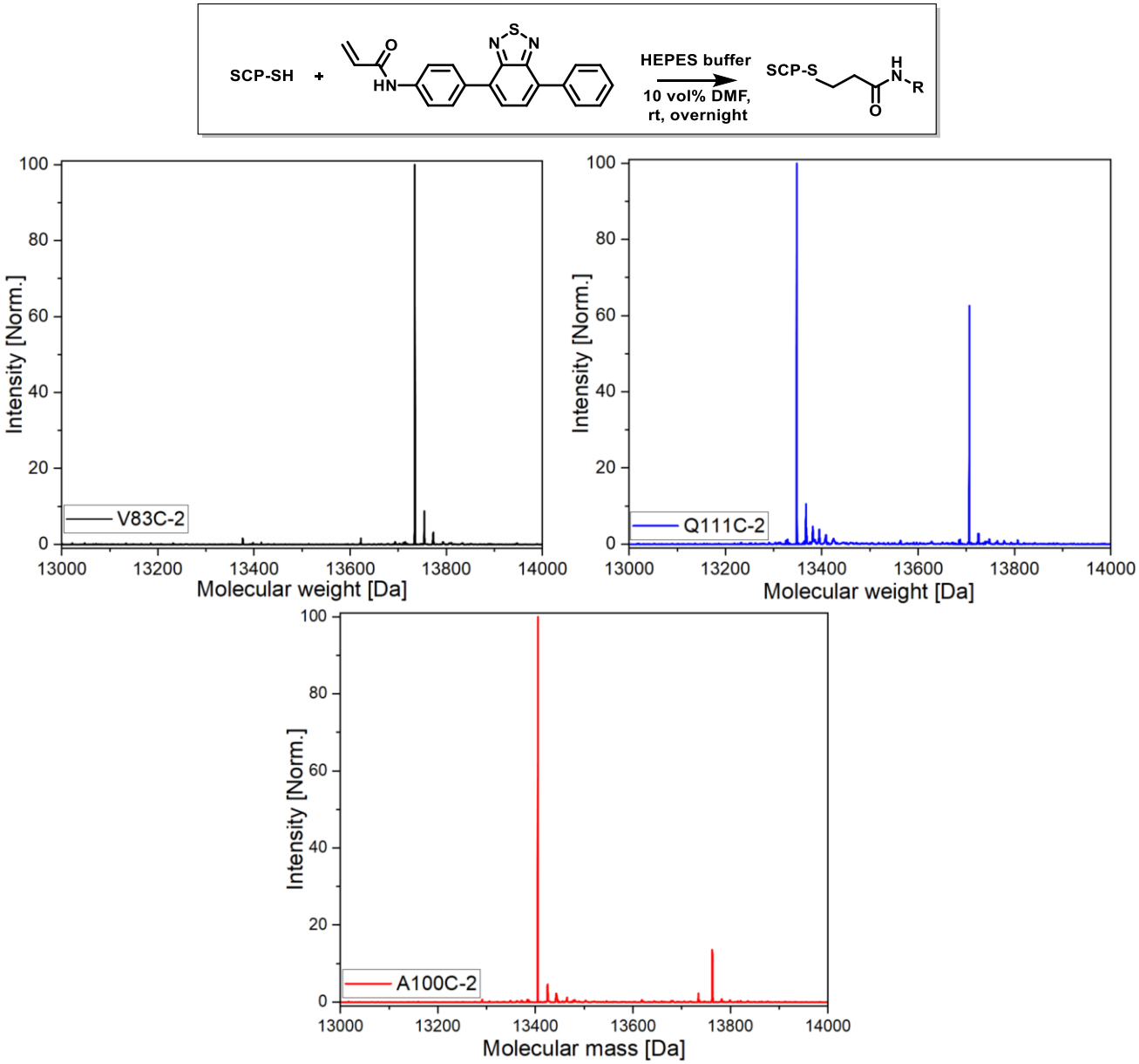

Figure 5.38: Mass spectra of V83C-2, Q111C-2 and A100C-2. The three variants were bioconjugated with acrylamide functionalized diphenyl benzothiadiazole. Q111C-2 and A100C-2 were not completely bioconjugated compared to V83C-2. 50 µM protein,1 mM photocatalyst, HEPES buffer (50 mM HEPES, 50 mM NaCl, 10% DMF) pH 8.5, 20 °C overnight

These results demonstrate site-specific preferences assumingly due to the steric hindrance of the protein scaffold surrounding the cysteine residue. Interestingly, the yield of modified Q111C-2 was higher than for A100C-2, indicating an easy uptake of the hydrophobic photocatalyst into the apolar protein tunnel. Instead of opting for harsher conditions to increase the yield of the bioconjugation, the reactivity of the functional group was increased again. A photocatalyst with an iodoacetamide group was synthesized and used for bioconjugation. (Table 5.3 **Entry 3,** Figure 5.40)

The synthesis was performed over four steps, requiring two consecutive Suzuki couplings yielding an amine functionalized 4,7-diphenyl-2,1,3-benzothiadiazole as a red solid. The product was then reacted with chloroacetyl chloride, yielding a yellow powder in quantitative yield. In a last step, a Finkelstein reaction was performed in dry acetone utilizing potassium iodide, yielding the required product, which was analyzed via NMR and mass spectra. (see Figure 6.38-6.40)

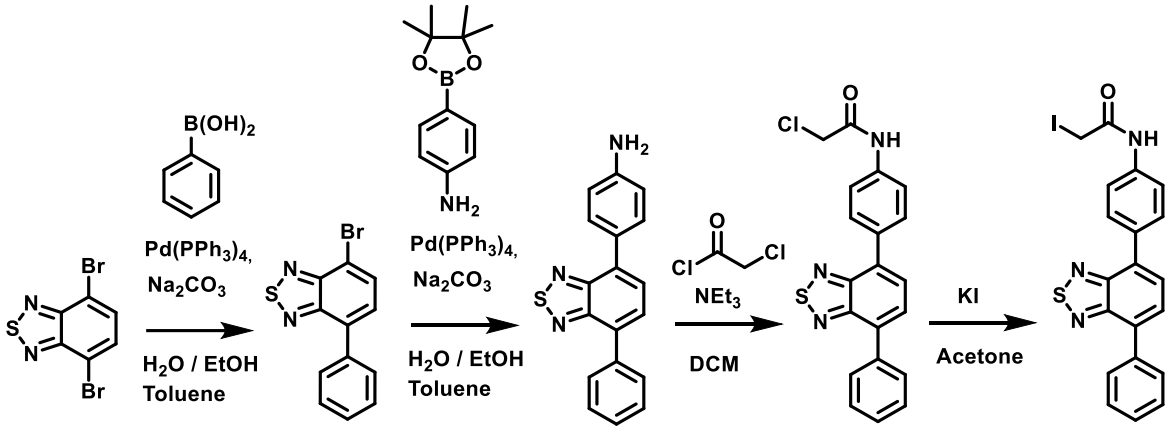

Figure 5.39: Synthesis route for iodoacetamide functionalized photocatalytic moiety. Four step synthesis due to the unavailable iodoacetyl chloride. (Synthesis Methods 6.3.2)

This modified photocatalyst was used, and a quick and efficient bioconjugation was observed leading to a complete modification of all three positions within 60 min at room temperature. Due to the replaced amino acids, all three variants possess slight differences in their mass with A100C (13405 Da), Q111C (13349 Da), and V83C (13377 Da), respectively. (Figure 5.40; Figure 6.41) The mass increases accordingly on the addition of the iodoacetamide functionalized photocatalyst by 343 Da, to give the following single modified photoenzymes A100C-3 (13748 Da), Q111C-3 (13691 Da), and V83C-3 (13720 Da). (Figure 5.40, Figure 6.43) The resulting bioconjugated proteins were analyzed via LCMS, showing no signs of non- or multiple modified proteins, and were consequentially used for analysis via UV/Vis and photocatalytic reactions and SDS. (Figure 5.41, Figure 6.44) The resulting bioconjugated photoenzymes (A100C-3, V83C-3, Q111C-3) were first analyzed using UV/Vis-absorbance and fluorescence emission spectroscopy. (Figure 5.41) Due to the different locations of the non-native cysteine residue and the bound photocatalytic moiety, slight shifts in the absorbance and emission are

due to be expected. These shifts in the absorbance and emission can be explained due to the differences in the surrounding hydrophobic structure and neighboring amino acids, creating slight differences in the protein environment. Compared to the non-conjugated protein, the bioconjugated photoenzymes showed strong visible light absorbance under 470 nm and a further peak in the UV range between 330-250 nm.

Table 5.3 Synthesized photocatalyst and yield of incorporation.

	Photocatalyst	Photoenzyme	V83C	A100C	Q111C
1	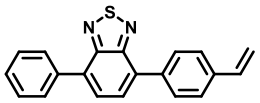	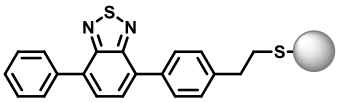	No conversion observed[a]		
2	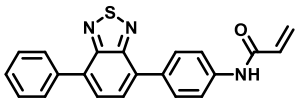	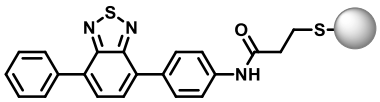	<98%[b]	<15%[b]	<49%[b]
3	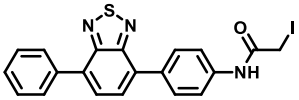	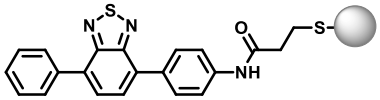	<99%[c]	<99%[c]	<99%[c]

[a] 100 µM protein 1 mM photocatalyst, blue light or VA-044, PBS (10% DMF), 37 °C, overnight [b] 50 µM protein,1 mM photocatalyst, HEPES buffer (50 mM HEPES, 50 mM NaCl, 10% DMF) pH 8.5, 20 °C overnight [c] 100 µM protein 1 mM photocatalyst, HEPES buffer (50 mM HEPES, 50 mM NaCl, 10% DMF) pH 8.5, 20 °C 1 h.

A clear absorbance peak shift was observed depending on the position of bioconjugation. For example, A100C-3 had the lowest absorbance peak at 393 nm, followed by Q111C-3 at 397 nm. Over all three proteins, the absorbance shifted by 7 nm. Similar behavior could be observed for the emission spectra, with all variants displaying a broad emission spectrum between 420-750 nm. Interestingly, the maximum emission varied largely with a shift range of 20 nm.

Q111C-3 possesses the highest emission peak and the most significant stokes-shift, while A100C-3 possesses the smallest stokes-shift paired with the lowest absorbance and emission peak. Highlighting the influence of the position of the photocatalytic moiety at the entrance or center of the hydrophobic tunnel. Further, the photophysical properties of the synthesized photocatalytic moiety bound to a free cysteine was investigated through density fluctuation theory (DFT) calculations. (Figure 5.42) The HOMO/LUMO levels (-5.87/-2.67 eV) as well as the energy of the triplet state (1.79 eV) were calculated. Highlighting the possibility for the formation of singlet oxygen in the photoenzymes.[394] Consecutive performed electron paramagnetic resonance spectroscopy (EPR) using the bioconjugated V83C-3 and 2,2,6,6-tetramethylpiperidine as singlet oxygen trapping agent confirmed the singlet oxygen formation upon irradiation, showing photoresponsive behavior and indicating the possibility to promote photocatalytic reactions. (Figure 5.43)

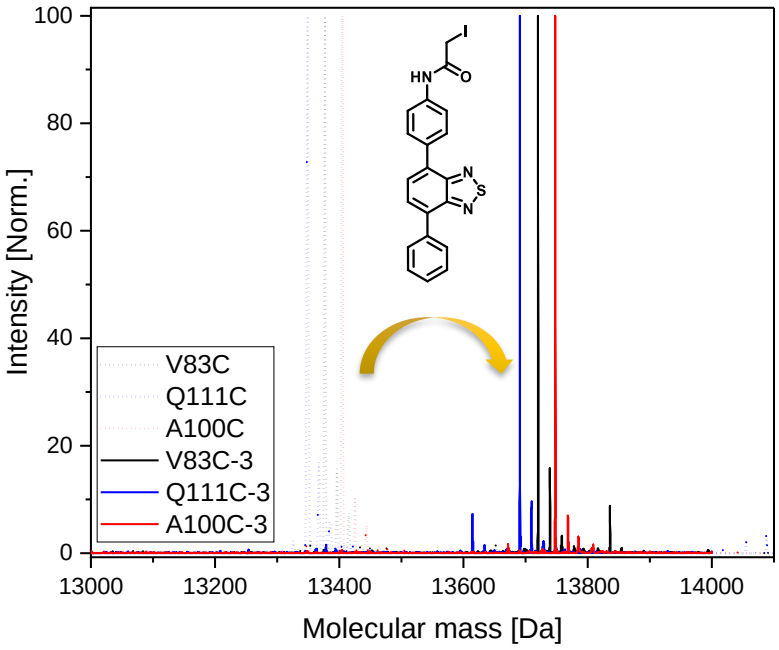

Figure 5.40 Mass spectra of all three variants A100C, V83C, and Q111C before and A100C-3, V83C-3 and Q111C-3 after bioconjugation via LC-MS.

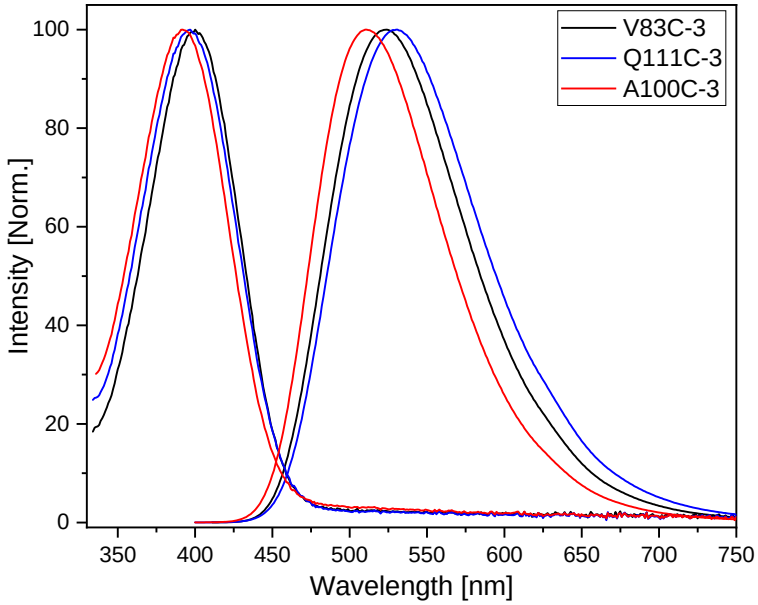

Entry	Protein	Absorbance	Emission	Stokes shift	Excitation
1	A100C-3	393	510	117	387
2	Q111C-3	397	530	133	390
3	V83C-3	400	524	124	398

Figure 5.41 Absorbance and Emission spectra of A100C-3, Q111C-3, and A100C-3, as well as their corresponding peaks.

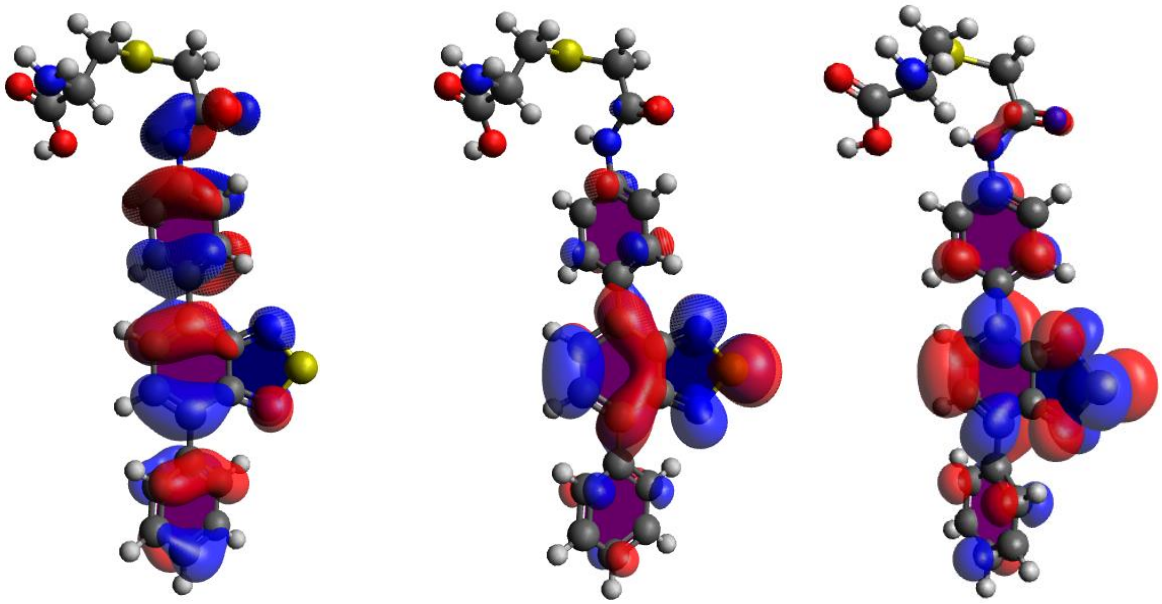

HOMO: -5,87 eV LUMO: -2,67 eV Triplet state energy: 1,79 eV

Figure 5.42: Density functional theory calculations for HOMO/LUMO levels calculated using method rb3lyp/6-31+g(d) as well as the triplet state energy calculated using method b3lyp/6-31+g(d) in Gaussian 16.

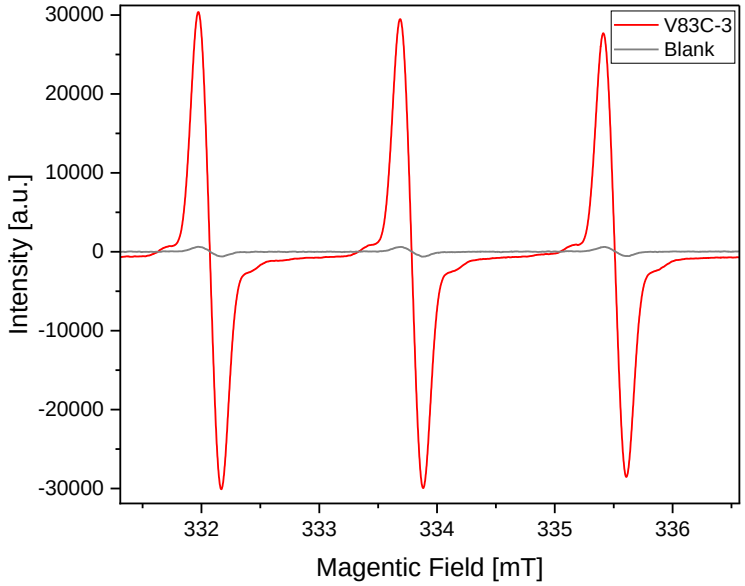

Figure 5.43: Electron paramagnetic resonance spectra of V83C-3 (red) (55 nmol) in MES buffer (20 mM MES, 50 mM NaCl, 1 mL) at pH 6 and blank measurement of MES buffer (20 mM MES, 50 mM NaCl, 1mL) at pH 6 (grey) after blue light LED irradiation in H_2O with 2,2,6,6-tetramethylpiperidine (0.1 M) as singlet oxygen trapping agent.

Sulfoxides are a common functional group in drug molecules, finding pharmaceutical application in proton-pump inhibitors or as anti-inflammatories.[395-397] The selective photocatalytic oxidation of

sulfides can be achieved in the presence of oxygen through the formation of singlet oxygen.[398] Lewis and coworkers first reported the selective oxidation of thioanisole using an artificial photoenzyme achieving modest TON of under 20.[274] Comparable results were achieved by Brustad and coworkers, who synthesized a total of twelve artificial enzymes by incorporating functionalized 9-mesityl-10-phenyl acirindium photocatalysts into three modified protein scaffolds.[266] Therefore, the catalytic activity of our artificial photoenzymes was investigated through the photooxidation of a model sulfide in water, and a kinetic study was conducted to analyze the effect of the binding site further. (Figure 5.44, Figure 6.45-6.46)

Table 5.4 Efficiency comparison of bioconjugated photoenzyme A100C-3, Q111C-3 and V83C-3.

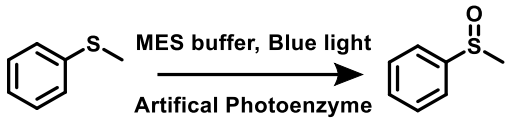

Entry	Protein	Conversion [%]	TON[a]
1	A100C-3	83	165
2	Q111C-3	95	190
3	V83C-3	96	192

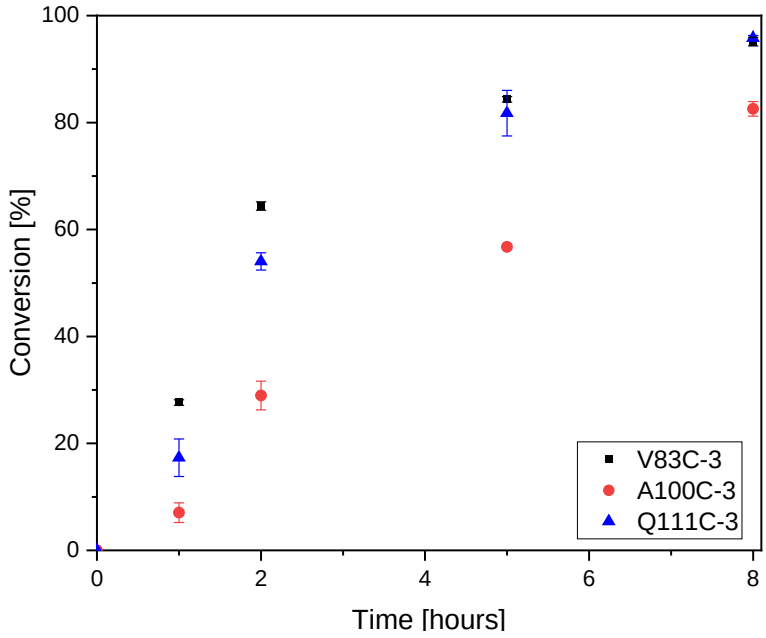

Figure 5.44 Photocatalytic oxidation of thioanisole; Conditions: Modified protein 10 µM, thioanisole 2 mM, MES buffer (MES 20 mM, 50 mM NaCl, 2% ACN) pH 6, blue light irradiation (460-465 nm) at room temperature; a) TON determination after eight hours. Conversion rate determined via GC-MS (measured in triplets).

All three variants show high selectivity, and the organic sulfide was selectively oxidized to the sulfoxide, showing no evidence for further oxidation to the sulfone, reaching conversions of up to 96%. Interestingly, it was found that the position of the photocatalytic moiety in the protein scaffold greatly affected the efficiency of the photoenzyme. (Figure 5.45) The kinetic study shows a typical decrease in the conversion rate at higher yields, leading to near completion after eight hours, with significant differences in the reaction rate. The highest conversions were achieved by Q111C-3, which is positioned in the center of the hydrophobic tunnel, and V83C-3, with 95-96%. A significantly lower conversion can be observed with A100C-3, which like V83C-3, is positioned at the entrances of the hydrophobic tunnel. (Figure 5.36)) Although V83C-3 and Q111C-3 reach near full conversions after 8 h, different reaction rates can be observed for all three modifications within the first two hours, with V83C-3 having the highest initial rate. A100C-3 has, compared to its counterparts, the lowest initial rate combined with the lowest absorbance and emission peak and the smallest stoke shift, setting it apart from V83C-3 and Q111C-3. Chiral sulfoxides are valuable pharmaceutical targets and can show differences in pharmacological activity, depending on the stereo conformation. The oxidized sulfoxide formed possesses a chiral stereo center. We therefore separated both stereoisomers via chiral HPLC but did not observe any stereoselectivity. (see Figure 6.47) This matches the previous observations by Lewis and Brustad, who also did not observe a stereoselective oxidation, presumably due to the reaction mechanism depending on the formation of singlet oxygen.[266,274]

Lastly, the stability of the created artificial photoenzymes were investigated. Six samples of V83C-3 were irradiated for up to 24 h prior to the photocatalytic reaction to analyze the photodeactivation and long-term stability of the photoenzyme. Upon long irradiation, small amount of precipitation occurred, which was removed through filtration before catalytic testing. (Figure 5.45) The photoenzyme shows a high stability, with limited decreases in conversion, only occurring after 8 h of irradiation. Even after 24 h of irradiation, a conversion of 74% and a TON of 148 is still achieved. (Figure 5.46)

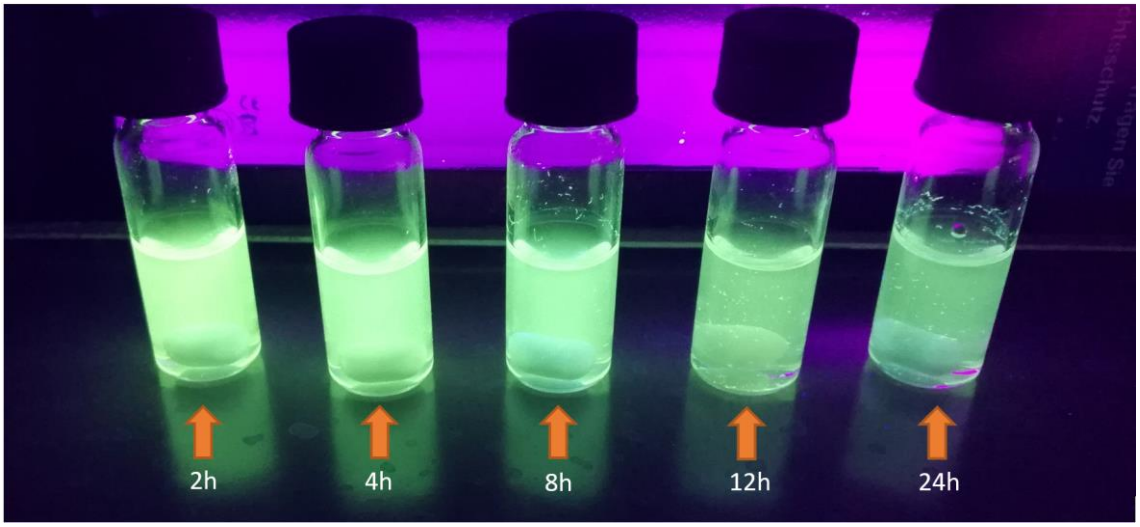

Figure 5.45: Stability test of artificial photoenzyme V83C-3. The samples were irradiated for up to 24 h under blue light and small amount of precipitation could be observed under light irradiation at 388 nm.

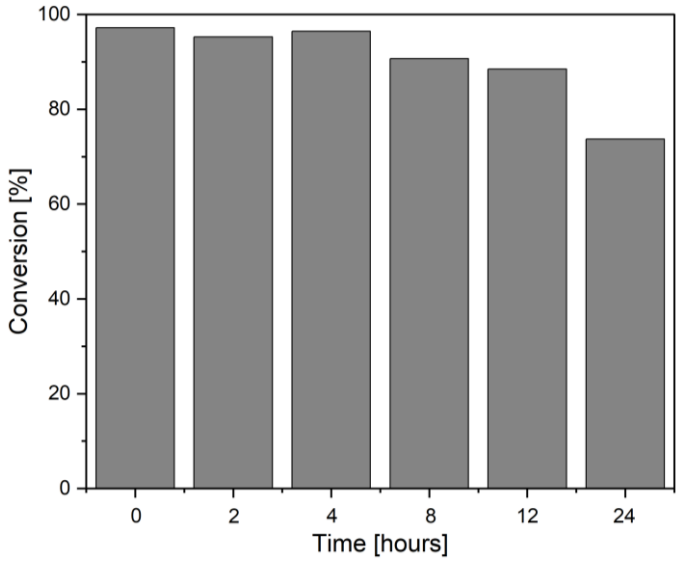

Figure 5.46: Photocatalytic conversion of thioanisole (2 µmol) using V83C-3 (10 nmol) in MES buffer (20 mM MES, 50 mM NaCl, 1 mL) after the photoenzyme was irradiated for up to 24 h under blue light before usage.

5.3.3 Conclusion: Position Depending Optical Properties and Photocatalytic Efficiency

In summary, we have produced three variants of a metal-free photoenzyme by incorporating a donor-acceptor based organophotocatalytic moiety into modified SCP-2L protein scaffolds. SCP-2L possesses a hydrophobic tunnel that we hypothesized could be an advantageous property in combination with a photocatalytic moiety, resulting in a water-soluble photocatalyst. Three distinct variants of SCP-2L with non-native cysteine residue, A100C, V83C, and Q111C, were expressed and subsequently used for bioconjugation. Three photocatalysts based on a donor-acceptor design utilizing a benzothiadiazole core were synthesized and tested. The photocatalysts were functionalized with increasingly reactive functional groups, starting with a vinyl-functionalization and acrylamide functionalization and, lastly, an iodoacetamide group. Of the three photocatalysts, only the iodoacetamide derivative of 4,7-diphenyl-2,1,3-benzothiadiazole was successfully bioconjugated with the three variants of SCP-2L, giving the corresponding photoenzymes SCP-2L A100C-3, V83C-3 and Q111C-3. The vinyl derivative of the photocatalytic moiety was unreactive. It did not react with cysteine even under addition of an initiator. In contrast, the acrylamide derivative could be used for bioconjugation but did not yield a full conversion in two of the three SCP-2L variants.

In the next step, the effect of the position of bioconjugation on the optical properties of the photocatalyst was analyzed via UV/Vis, and the efficiency of the yielded photoenzymes was determined via photocatalytic oxidation of a model sulfide under visible light irradiation. The results showed significant differences in the reaction rate depending on the cysteine position, with A100C-3 having the lowest photocatalytic activity in combination with lower absorbance and emission peaks. Q111-C3 and V83-C3 possessed comparable photophysical properties and comparable TON, with Q111-C3 being the slightly more efficient variant. The model photoreaction could, in theory, lead to a chiral product and was therefore analyzed via HPLC. However, no preference for one of the two stereoisomers was found, regardless of the used variants. Due to the assumed reaction mechanism and the proven creation of singlet oxygen via EPR, these results correlate well to literature.

Lastly, the stability of Q111C-3 was investigated by irradiation under visible light and oxygen atm. before the photocatalytic reaction, highlighting a slight decrease in reactivity assumingly due to self-oxidation and denaturation of the protein scaffold.

We believe this to be a promising start for the further development of photoenzymes based on incorporating photocatalytic moieties into SCP-2L based proteins. Combining the benefits of photocatalysis and biocatalysis, the synthesis of these novel catalytic systems eliminates the requirement for toxic materials, organic solvents, or non-degradable support material, leading to sustainable photocatalytic reactions for the synthesis of high-value chemicals.

6 Experimental section

6.1 Comonomer Effects in Photocatalytic Classical Polymers

6.1.1 Material and Characterization:

All Chemicals were bought from commercial sources ACROS Organics, Alfa Aesar, Sigma-Aldrich, or TCI. Solvents, deuterated solvents, and starting materials were used without further purification. Monomers were purified by filtration through basic Aluminium oxide to remove present inhibitors.

Methods:

^{1}H- and ^{13}C-NMR spectra were recorded with a Bruker AVIII 300 spectrometer at 400 MHz and 101 MHz, respectively, using DCM-d_2 and DMSO-d_6 and are given in ppm against TMS. NMR spectroscopy data were analyzed using MestReNova 14.2.3. Polymers were analyzed via gel permeation chromatography (GPC) using a PSS SECcurity^2 instrument with RI and UV detector at 270 nm wavelength using a PMMA standard in DMF. Fourier-transform infrared spectroscopy was performed using dry samples incorporated into potassium bromide pellets and measured with a Bruker Vertex 70. Bruker OPUS 7.8 software was used for Data analysis.

Light scattering measurements were performed using an ALV/CGS3 compact goniometer system with a He/Ne laser (632.8 nm). Measurements were performed at 20 °C at 9 angles from 30° to 150° using a solution in DMF 2 mg/mL and analyzed with ALV5000 software.

Fluorescence spectroscopy, including quantum yield, Stern Volmer Plot, and excitation spectra, were measured on a Duetta Fluorescence and Absorbance Spectrometer from Horiba using EzSpec as software for analysis and fluorescence peak integration. UV/Vis-absorption spectra were also measured on a Cary 60 UV–Vis/NIR spectrometer.

Fluorescence lifetime was measured using a Pico Quant. PDL 800-D, Pico Quant. PH 300 with an LDH-P-C-375 and analyzed using PicoHarp V 2.2.0.0 as well as FluoFit Pro. V4.4.0.1 over a time of 10 min with a degassed solution in DMF.

For cyclic voltammetry measurements, a glassy carbon electrode as the working electrode, Hg/$HgCl_2$ electrode as the reference electrode, and a platinum wire as the counter electrode were used. The measurements were performed on a Metrohm Autolab PGSTAT204 potentiostat/galvanostat using Nova 2.1 software. The measurements were performed by coating the working electrode with a polymer solution in the presence of nafion perfluorinated resin solution in an ACN solution (NH_4PCl_6 5 wt.%)

Gas chromatographic-mass spectroscopy was performed on a Shimadzu GC-2010 plus combined with a QP2010 ultra mass spectrometer using a 7HG-G010-11 Phenomenex column and helium 5.0 as the carrier. Methods were adjusted explicitly for the required separation, leading to three used temperature curves.

DFT calculations were performed using Gaussian 16. The DFTs for the HOMO/LUMO levels were calculated for optimization of local minimum using method rb3lyp/6-31+g(d) Frontier molecular orbitals pictures were produced using Avogadro. Photoreactor LEDs (Tru Components™ HighPower, 1.4 W per LED, λ = 460-470 nm.

Tauc-Plot

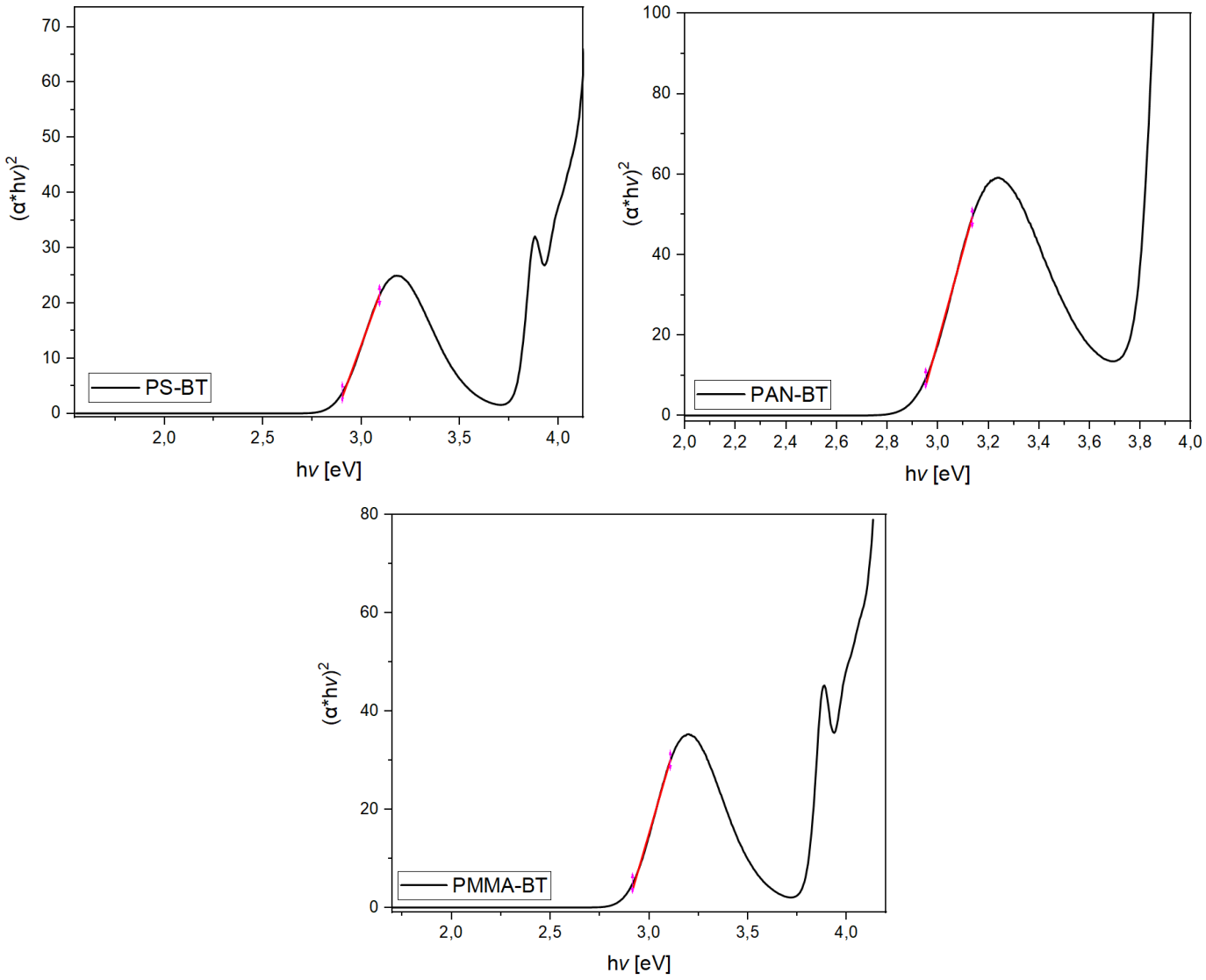

Figure 6.1: Tauc-Plot of PMMA-BT, Pan-BT and PS-BT using a model for a direct bandgap.

Dynamic Light Scattering

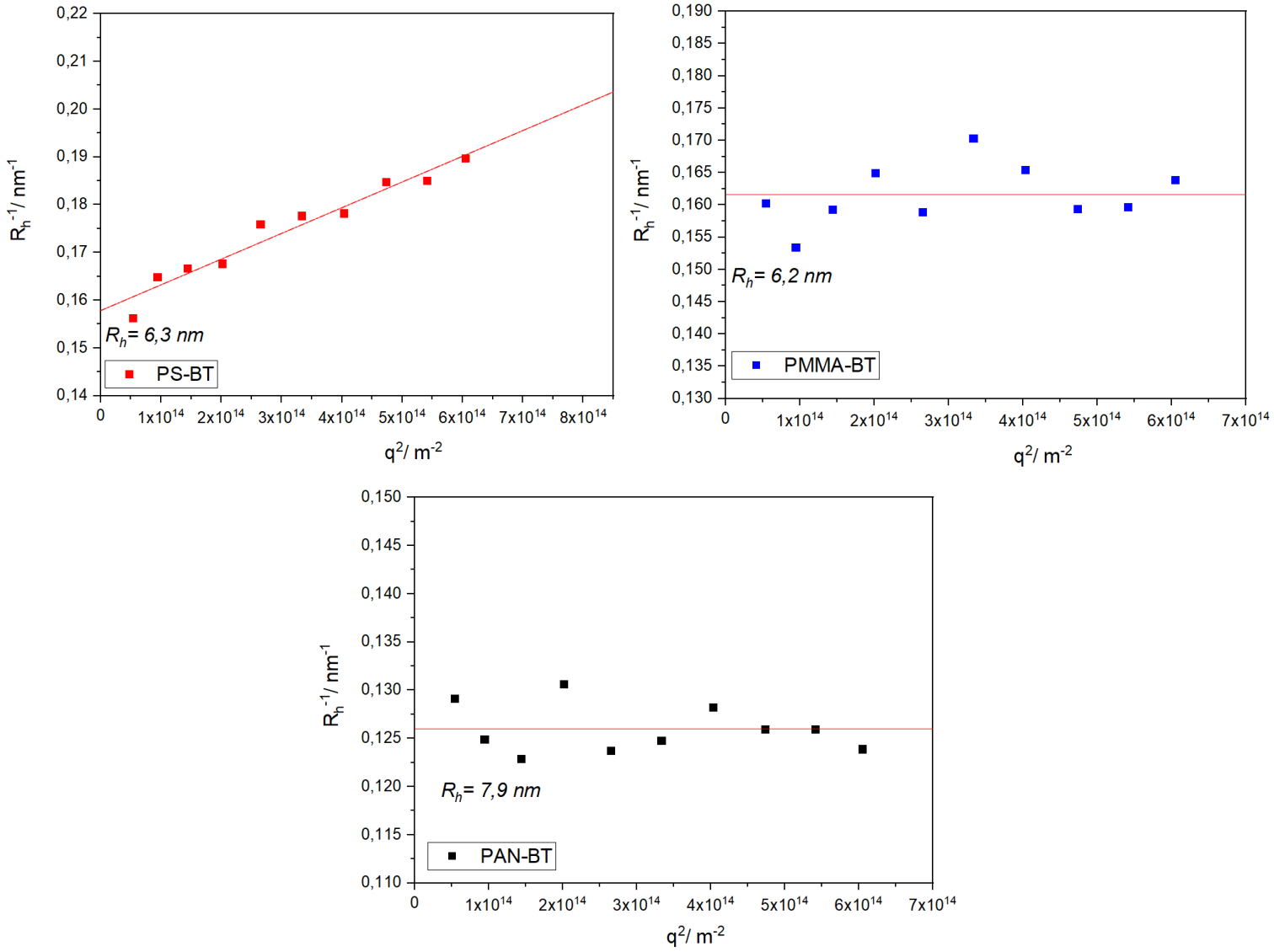

Figure 6.2: DLS measurements of PAN-BT, PS-BT and PMMA-BT and the calculated hydrodynamic radius.

Cyclic Voltammetry

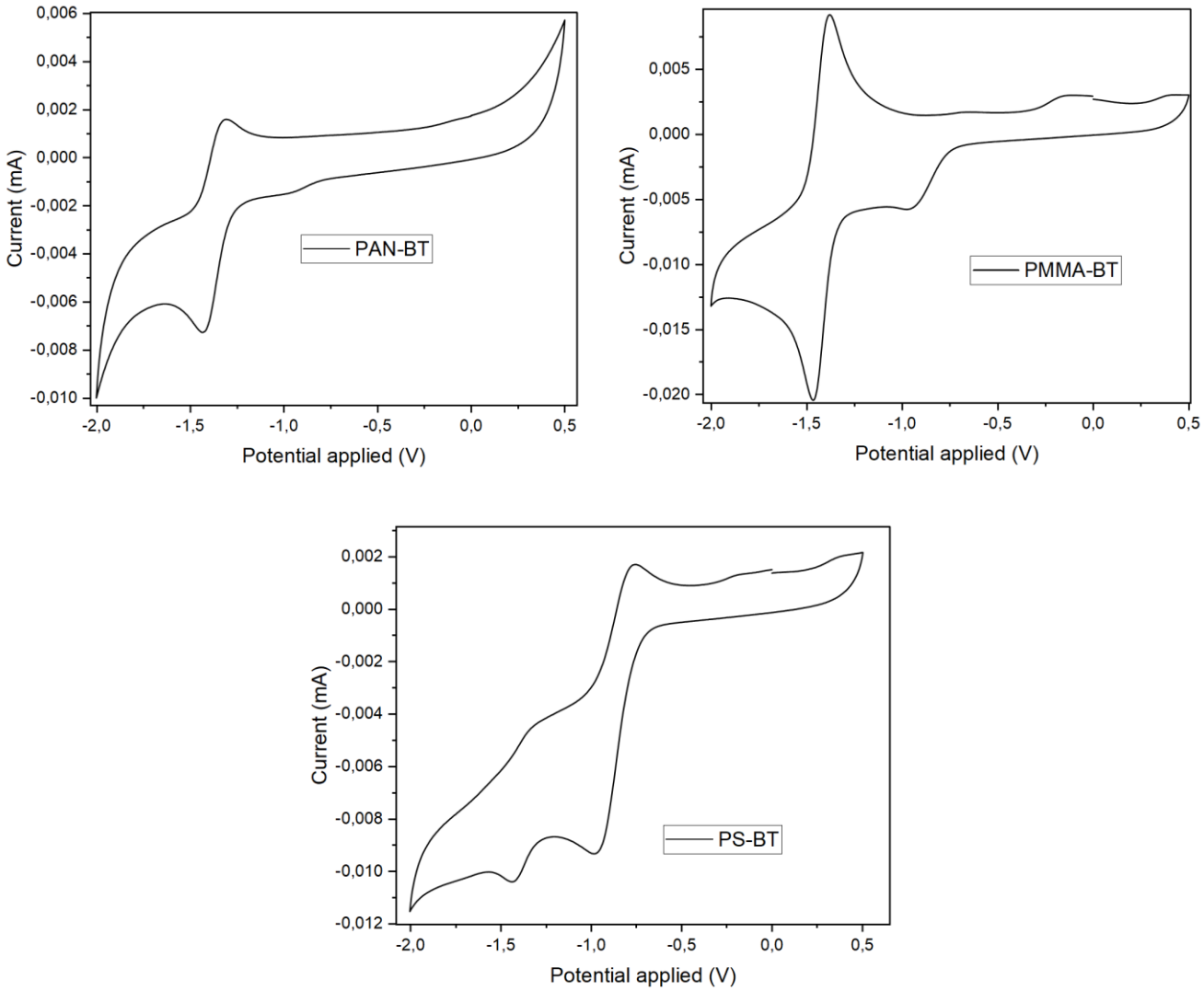

Figure 6.3: CV measurements of PAN-BT, PS-BT and PMMA-BT as membranes using Nafion in ACN (NBu_4PF_6 5.0 wt.%).

6.1.2 Synthesis Method

Polymer Synthesis:

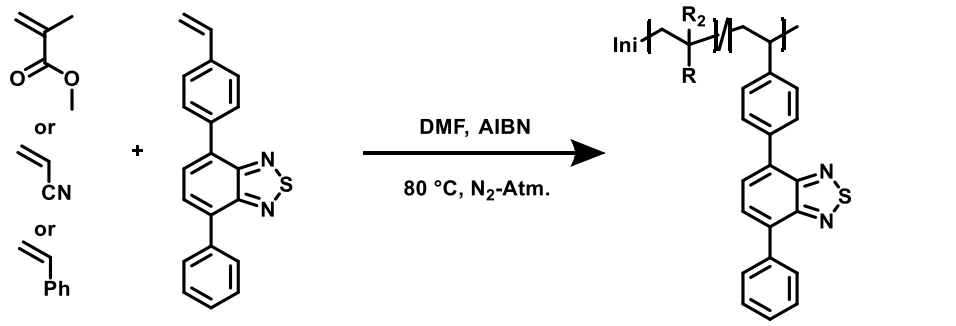

PAN-BT: R: -CN; R_2: -H
PMMA-BT: R: $-CO_2Me$; R_2: $-CH_3$
PS-BT: R: -Ph R_2: -H

The monomer was first purified by basic aluminum oxide. In a dry flask, methyl methacrylate or acrylonitrile (500 mg) was combined with 4-phenyl-7-(4-vinylphenyl)benzo[c][1,2,5]thiadiazole (5 wt.%, 25 mg) and dissolved in dry DMF (1.5 mL). The solution was degassed by N_2 bubbling for 10 min. AIBN (1 wt.%) was dissolved in DMF (0.5 mL) and degassed by N_2 bubbling. The solutions were combined and heated while stirring at 80 °C overnight. The polymers were precipitated in diethyl ether and centrifuged for 10 min. (4000 rpm. 5 °C). The supernatant was discarded, and the polymer was taken up in DMF. The precipitation and centrifugation were repeated, and the polymer was purified via Soxhlet in diethyl ether for two days. The polymer was dried under vacuum, and the concentration of incorporated photocatalyst was determined via UV/Vis-calibration.

The monomer was first purified by basic aluminum oxide. In a dry flask, methyl styrene (500 mg) was combined with 4-phenyl-7-(4-vinylphenyl)benzo[c][1,2,5]thiadiazole (5 wt.%, 25 mg) and dissolved in dry DMF (1.0 mL). The solution was degassed by N_2 bubbling for 10 min. AIBN (2 wt.%) was dissolved in DMF (0.5 mL) and degassed by N_2 bubbling. The solutions were combined and heated under stirring at 80 °C overnight. The polymers were precipitated in methanol and centrifuged for 10 min (4000 rpm, 5 °C). The supernatant was discarded and the polymer was taken up in DMF. The precipitation and centrifugation were repeated, and the polymer was purified via Soxhlet in methanol for two days. The polymer was dried under vacuum, and the concentration of incorporated photocatalyst was determined via UV/Vis-calibration.

Photocatalyst Synthesis

4-phenyl-7-(4-vinylphenyl)benzo[c][1,2,5]thiadiazole was synthesized after a previously published synthesis route.[203]

^{1}H NMR (400 MHz, DMSO-d_6) δ 8.09 – 7.93 (m, 6H), 7.67 (d, *J* = 8.2 Hz, 2H), 7.57 (dd, *J* = 8.3, 6.7 Hz, 2H), 7.52 – 7.44 (m, 1H), 6.84 (dd, *J* = 17.6, 10.9 Hz, 1H), 5.96 (d, *J* = 17.7 Hz, 1H), 5.36 (d, *J* = 11.0 Hz, 1H).

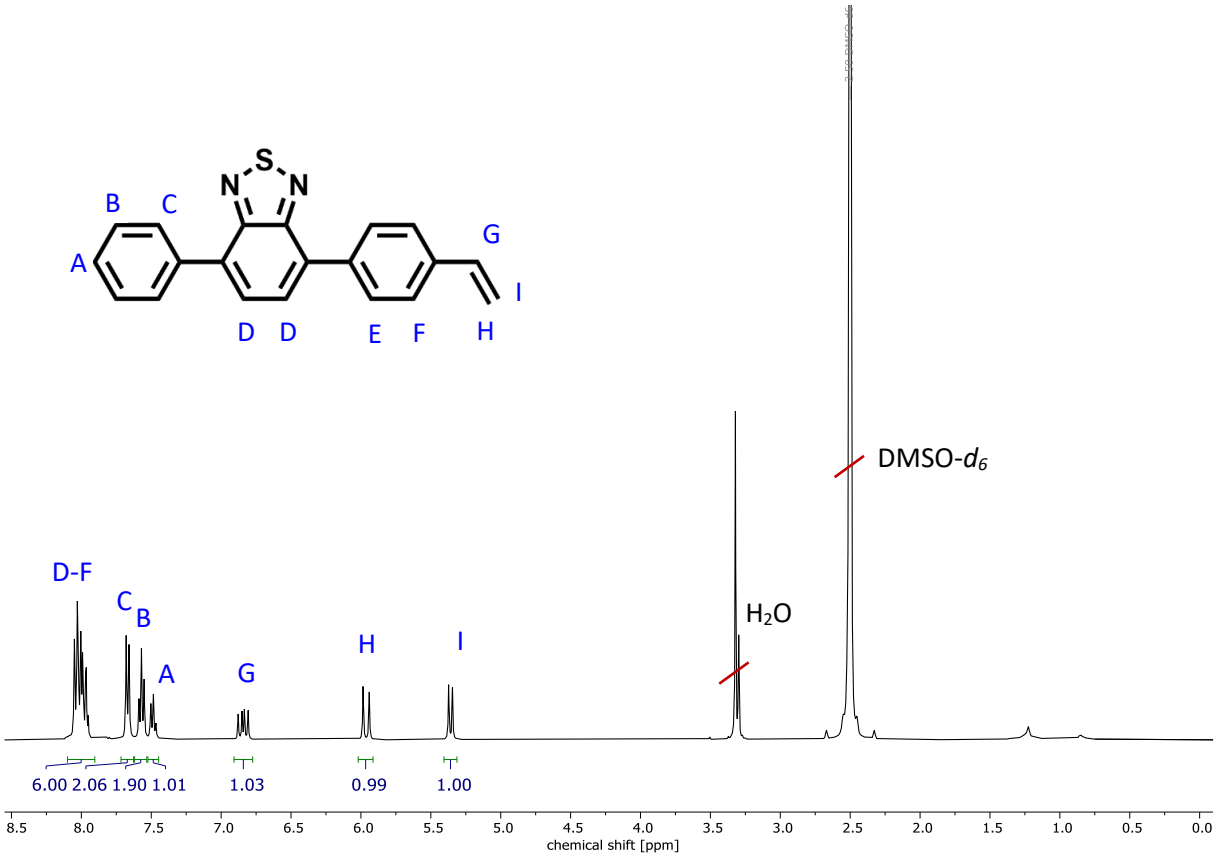

Figure 6.4: ^{1}H NMR spectrum (400 MHz, DMSO-d_6) of 4-phenyl-7-(4-vinylphenyl)benzo[c][1,2,5]thiadiazole.

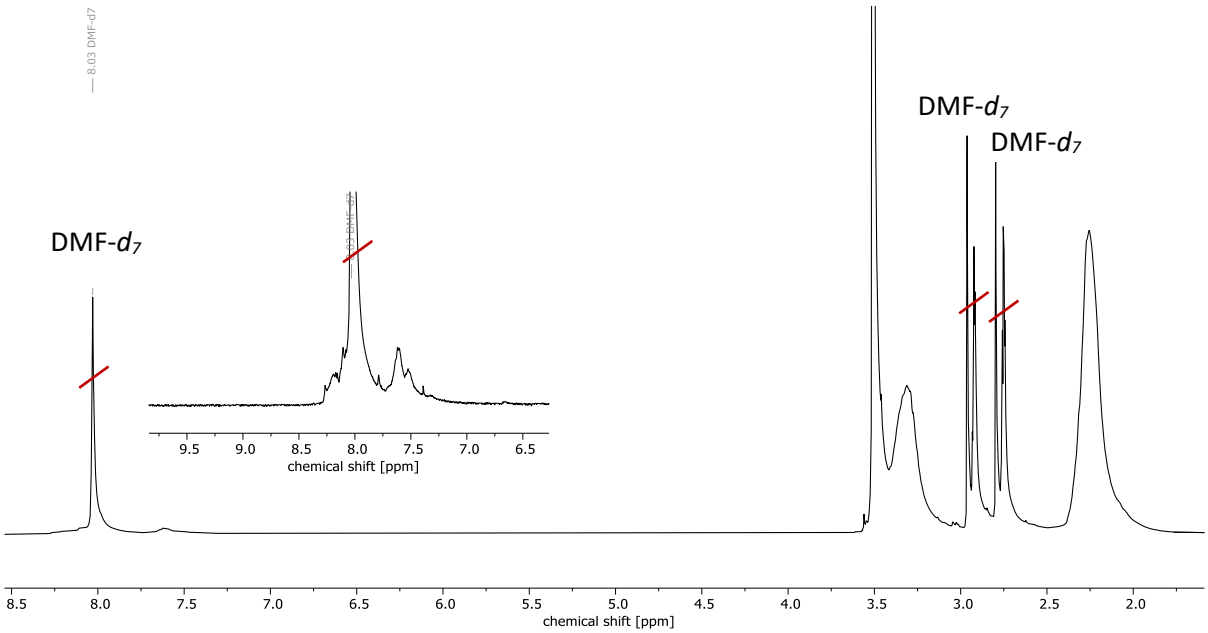

Figure 6.5: ^{1}H NMR spectrum (400 MHz, DMF-d_7) of PAN-BT.

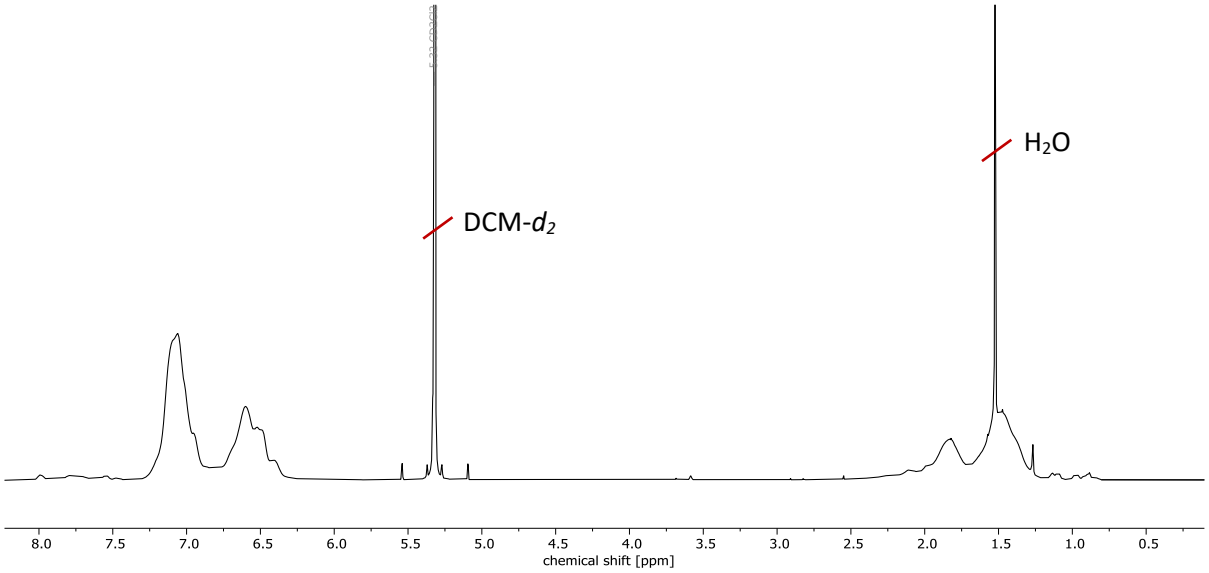

Figure 6.6: ^{1}H NMR spectrum (400 MHz, CD_2Cl_2) of PS-BT.

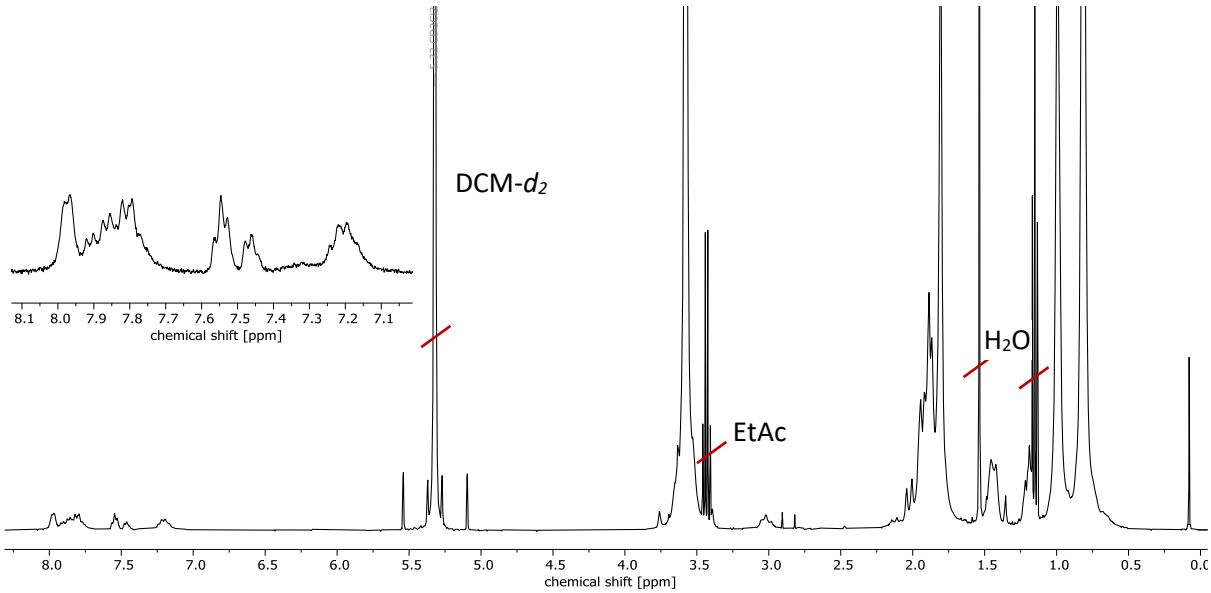

Figure 6.7: ^{1}H NMR spectrum (400 MHz, CD_2Cl_2) of PMMA-BT.

6.1.3 Photocatalytic Reactions

Diethyl 2-(3-methyl-1H-indol-2-yl)malonate (Figure 5.14, Figure 6.8-6.10)

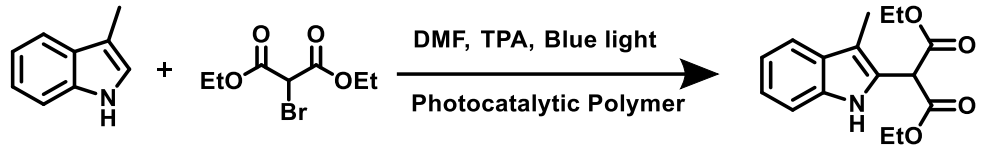

In a 2 mL flask equipped with a stir bar, 3-methyl indole (19.7 mg, 150 µmol), diethyl bromomalonate (71.7 mg, 300 µmol), and triphenylamine (73.6 mg, 300 µmol) and photocatalytic polymer (250 nmol photoactive unit) were dissolved in DMF (2 mL). The solution was degassed with Argon for 10 min, and irradiated under blue light (λ = 460-470 nm). Samples (100 µL) were taken, diluted with DCM and directly measured via GCMS. The reaction was purified via silica column chromatography DCM: PE 1:9 → EtAc: PE 8:2

^{1}H NMR (400 MHz, CD_2Cl_2) δ 8.93 (s, 1H), 7.54 (ddt, *J* = 7.9, 1.4, 0.8 Hz, 1H), 7.36 (dt, *J* = 8.1, 0.9 Hz, 1H), 7.18 (ddd, *J* = 8.2, 7.0, 1.2 Hz, 1H), 7.09 (ddd, *J* = 8.0, 7.1, 1.1 Hz, 1H), 5.00 (s, 1H), 4.35 – 4.10 (m, 4H), 2.30 (s, 3H), 1.29 (t, *J* = 7.1 Hz, 6H).

^{13}C NMR (101 MHz, CD_2Cl_2) δ 167.75, 136.19, 128.66, 125.22, 122.65, 119.55, 119.06, 111.34, 110.84, 62.71, 49.79, 14.21, 8.59.

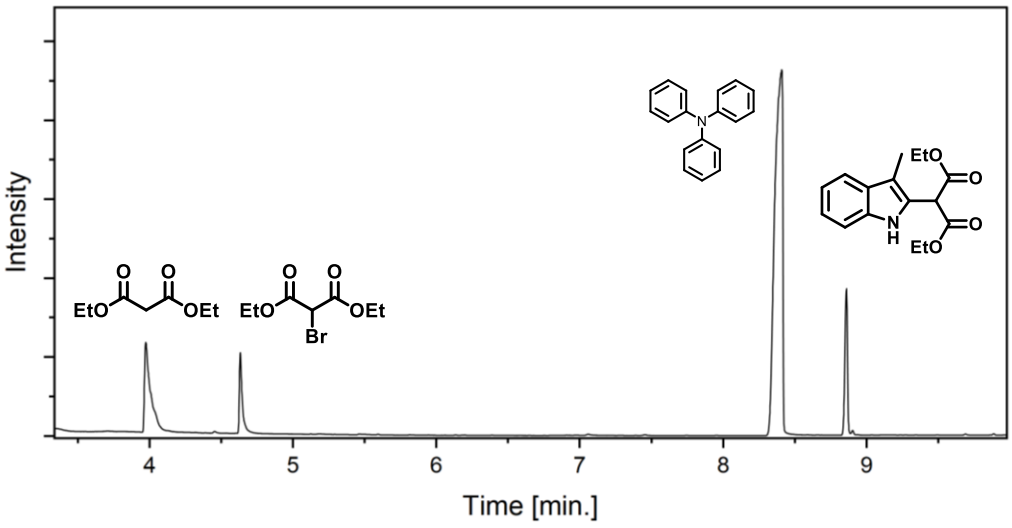

Figure 6.8: GCMS trail of Diethyl 2-(3-methyl-1H-indol-2-yl)malonate.

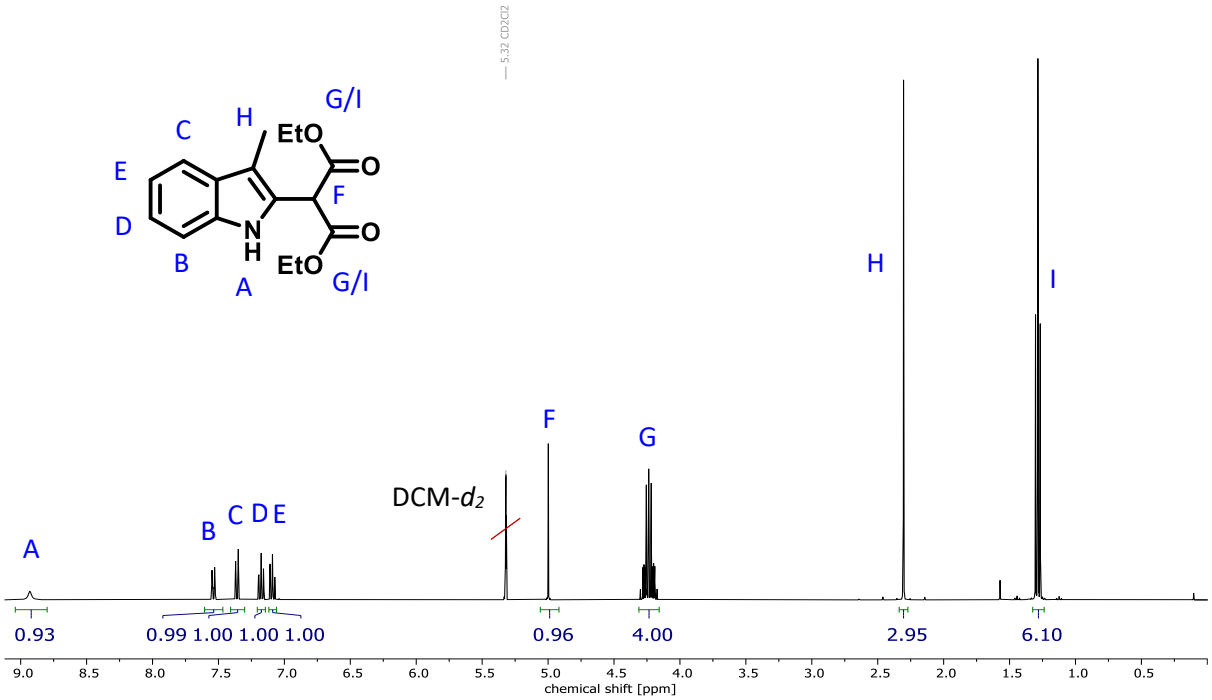

Figure 6.9: ^{1}H NMR spectrum (400 MHz, CD_2Cl_2) of Diethyl 2-(3-methyl-1H-indol-2-yl)malonate.

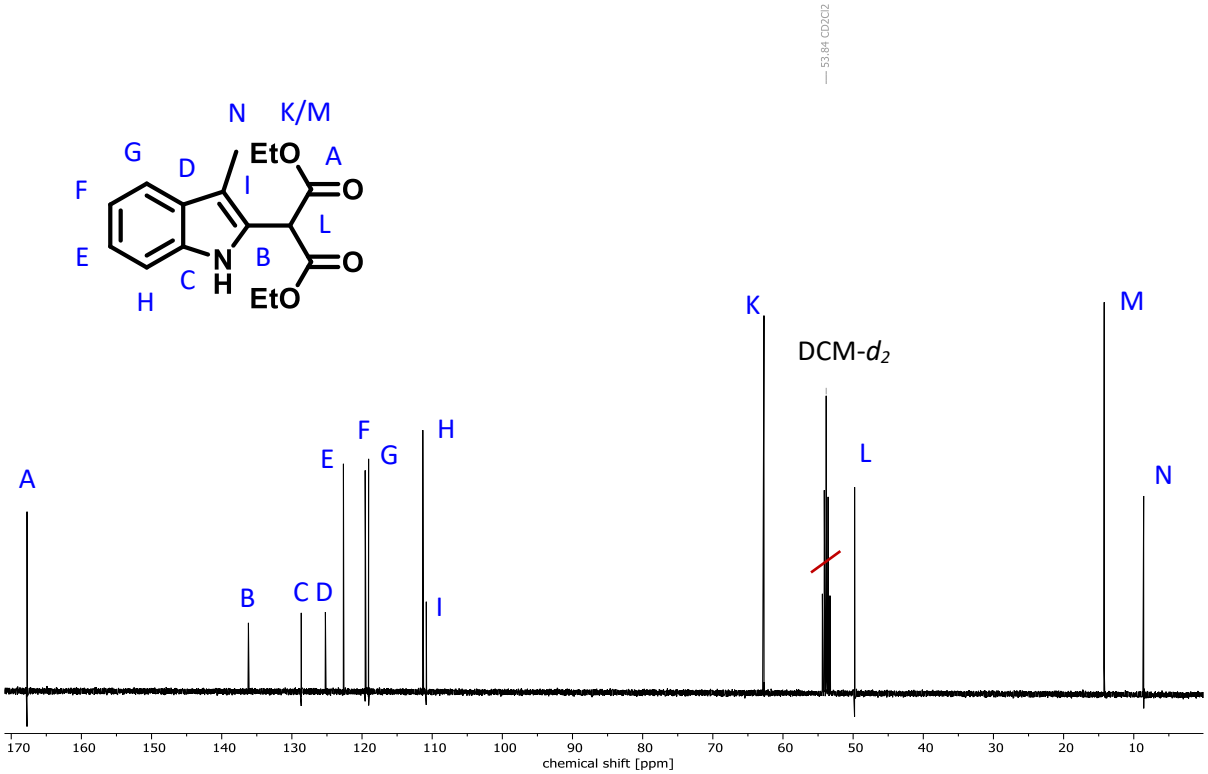

Figure 6.10: ^{13}C NMR spectrum (101 MHz, CD_2Cl_2) of diethyl 2-(3-methyl-1H-indol-2-yl)malonate.

1,2-bis(4-chlorophenyl)ethane (Figure 5.13, Figure 6.11-6.13)

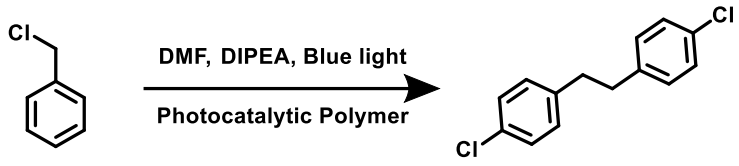

In a 2 mL flask equipped with a stir bar, 4-chlorobenzyl bromide (20.5 mg, 100 µmol) *N*,*N*-diisopropylethylamine (175 µL, 1 mmol), and photocatalytic polymer (300 nmol photocatalytic moiety) were dissolved in DMF (2 mL). The solution was degassed with argon for 10 min and irradiated under blue light (λ = 460-470 nm). Samples (100 µL) are taken, diluted with DCM, and directly measured via GCMS. The reaction was purified via silica column chromatography DCM: PE 0:10 → DCM: PE 1:9

^{1}H NMR (400 MHz, CD_2Cl_2) δ 7.28 – 7.20 (m, 1H), 7.12 – 7.04 (m, 1H), 2.87 (s, 1H).

^{13}C NMR (101 MHz, CD_2Cl_2) δ 140.4, 131.9, 130.3, 128.7, 37.3.

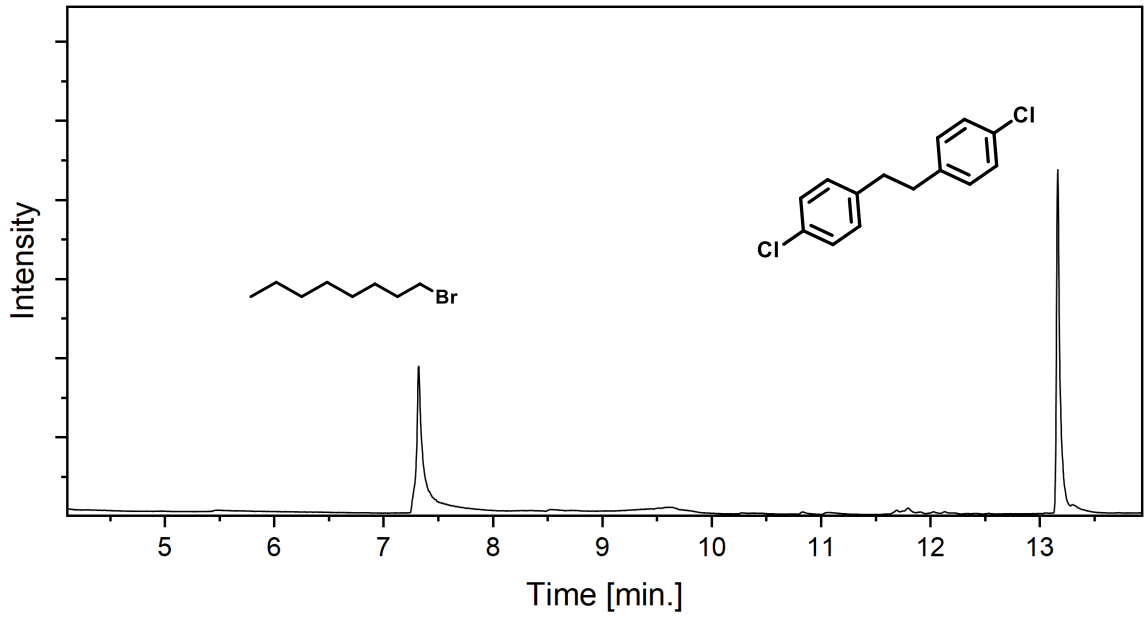

Figure 6.11: GCMS trail of 1,2-bis(4-chlorophenyl)ethane using 1-bromo-octane as standard.

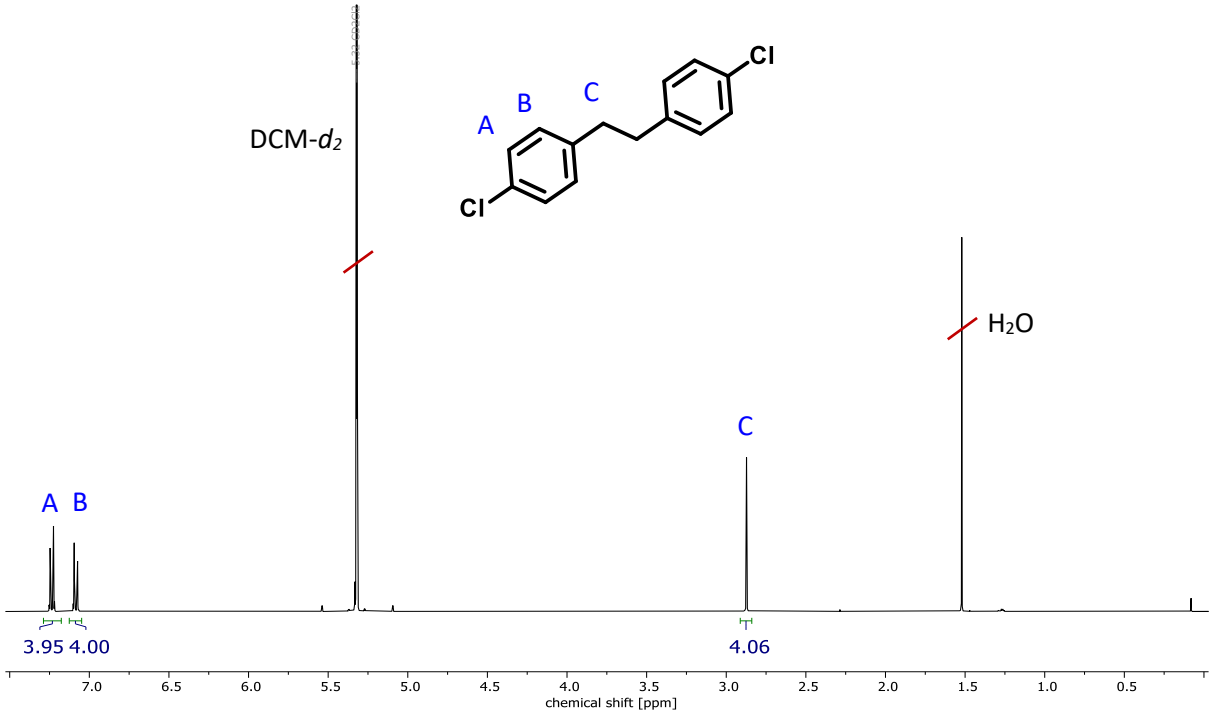

Figure 6.12: ^{1}H NMR spectrum (400 MHz, CD2Cl2) of 1,2-bis(4-chlorophenyl)ethane.

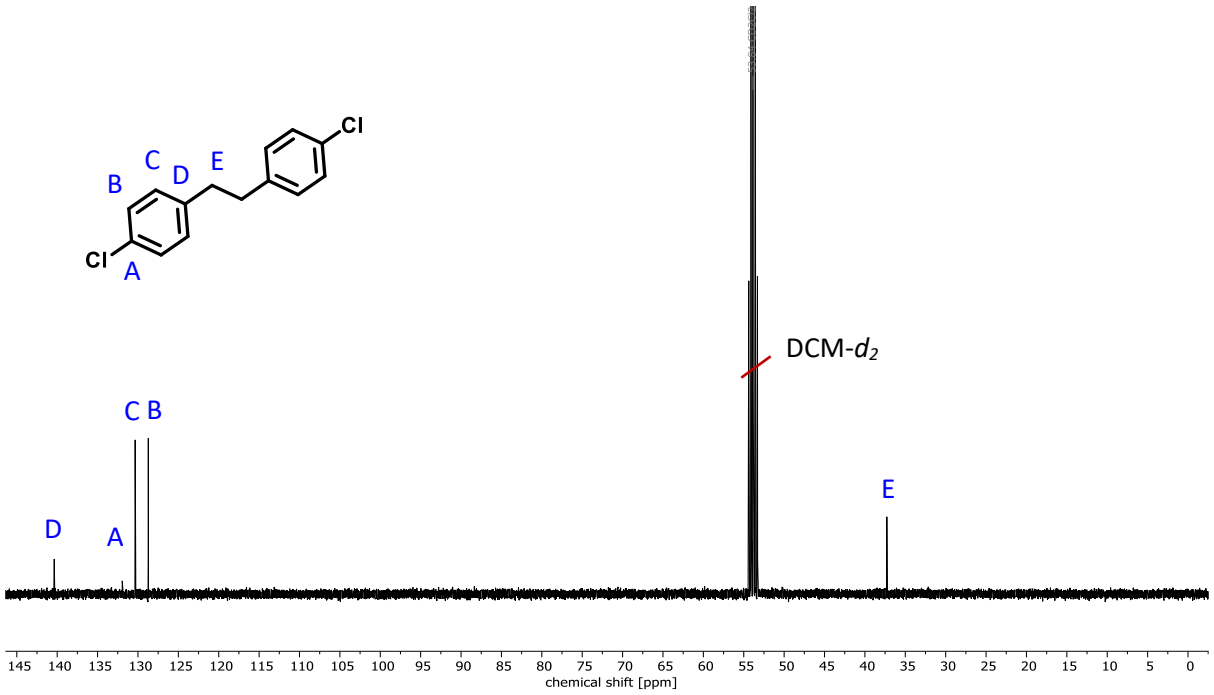

Figure 6.13: ^{13}C NMR spectrum (101 MHz, CD2Cl2) of 1,2-bis(4-chlorophenyl)ethane.

4-phenylphenol (Figure 5.11, Figure 6.12-6.15)

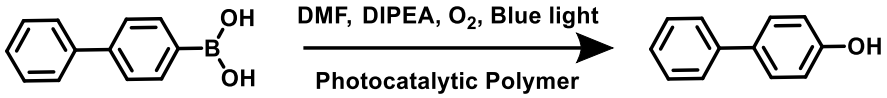

In a 2 mL flask equipped with a stir bar, 4-biphenylboronic acid (19.8 mg, 100 µmol) *N*,*N*-diisopropylethylamine (52 µL, 300 µmol), and photocatalytic polymer (100 nmol photoactive unit) were dissolved in DMF (2 mL). Oxygen was bubbled through the solution for 5 min and irradiated under blue light (λ = 460-470 nm). Samples (100 µL) were taken, diluted with DCM and directly measured via GCMS. The reaction was purified via silica column chromatography EtAc: PE 1:9 → EtAc: PE 1:0

^{1}H NMR (400 MHz, CD_2Cl_2) δ 7.58 – 7.52 (m, 1H), 7.52 – 7.46 (m, 1H), 7.45 – 7.37 (m, 1H), 7.34 – 7.24 (m, 1H), 6.94 – 6.86 (m, 1H).

^{13}C NMR (101 MHz, CH_2Cl_2) δ 155.70, 141.06, 134.18, 129.12, 128.67, 127.10, 126.97, 115.98.

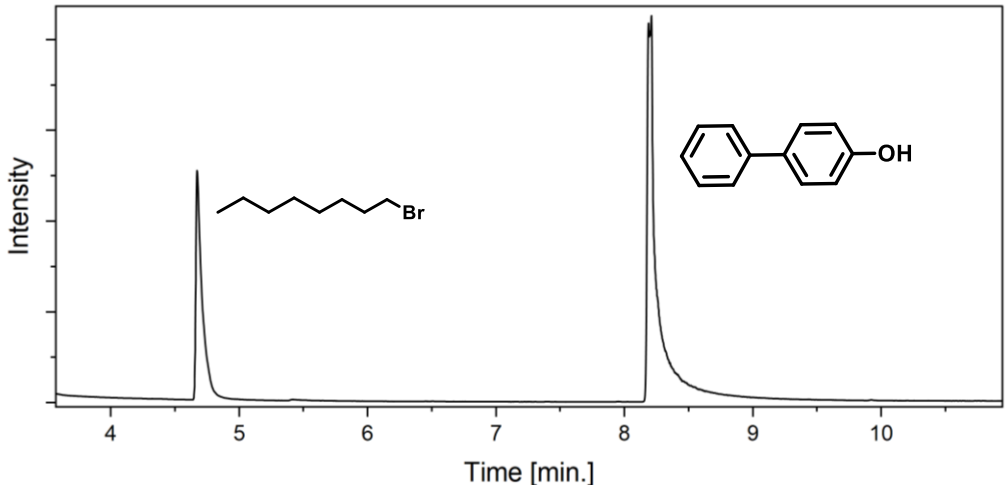

Figure 6.14: GCMS trail of 4-phenylphenol using 1-bromo-octane as standard.

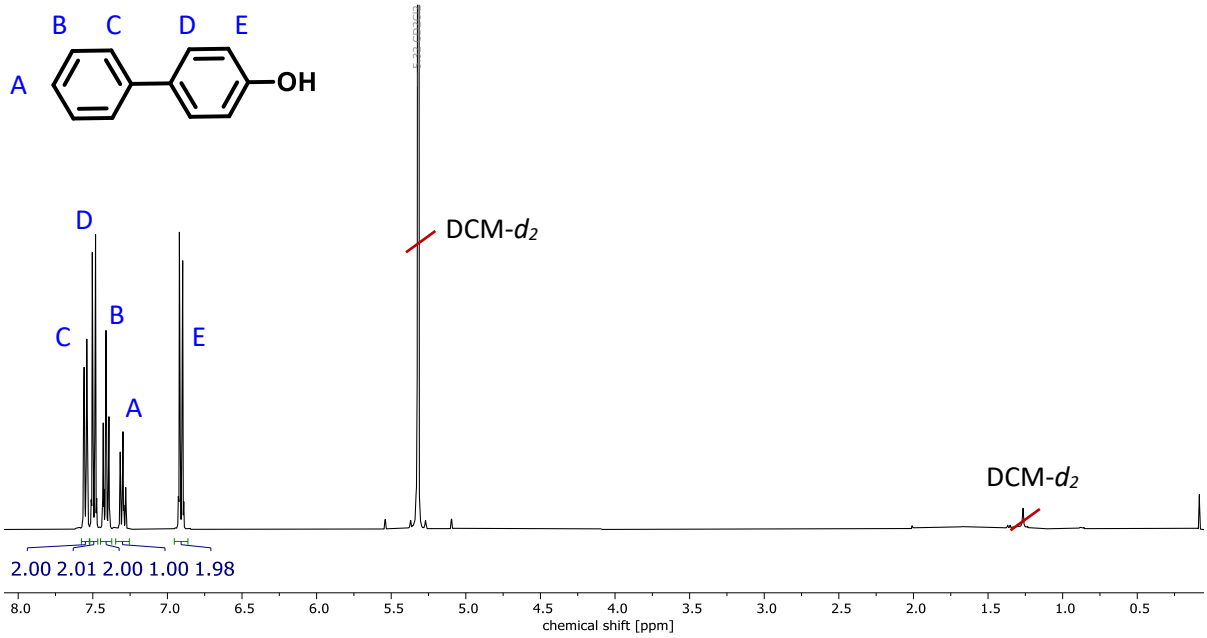

Figure 6.15: ^{1}H NMR spectrum (400 MHz, CD_2Cl_2) of 4-phenyl phenol.

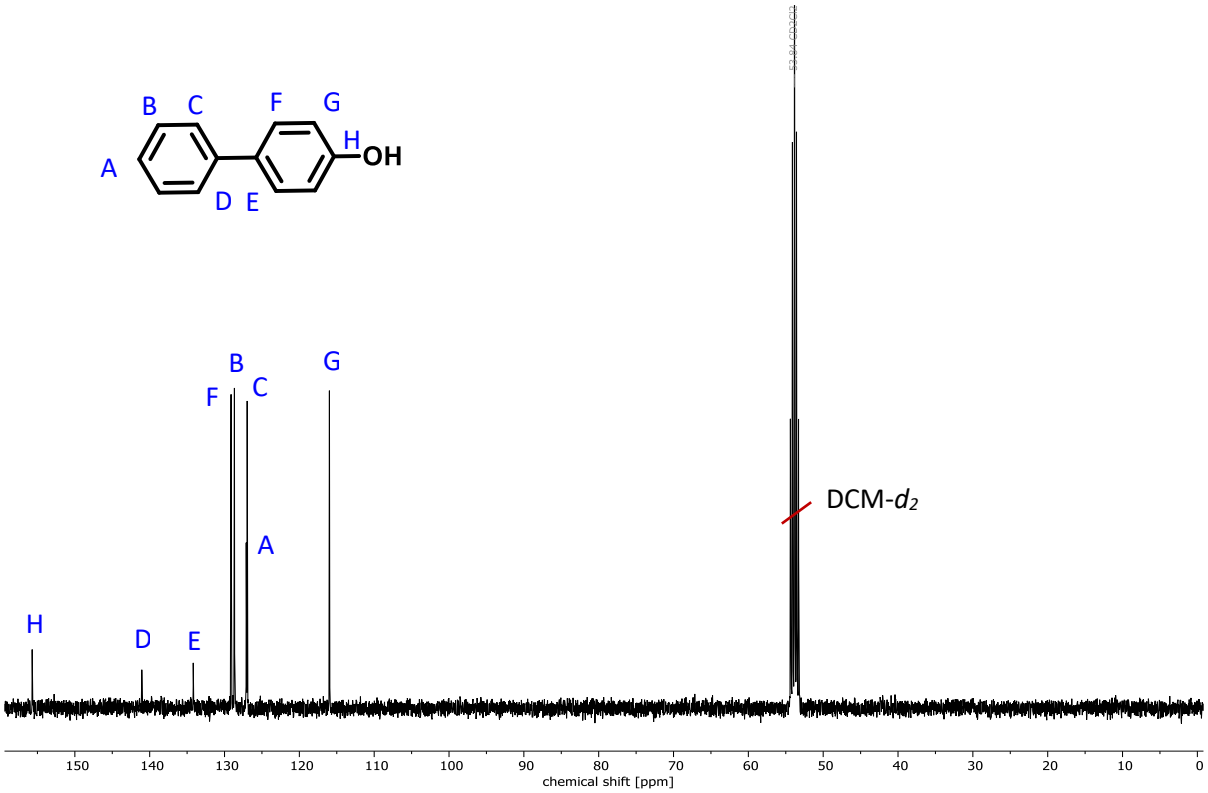

Figure 6.16: ^{13}C NMR spectrum (400 MHz, CD_2Cl_2) of 4-phenyl phenol.

6.2 Photocatalytic Hydrogels with a High Transmission Polymer Network for Pollutant Remediation

6.2.1 General Information and Methods Characterization

4,7-Dibromobenzo[c][1,2,5]thiadiazole was purchased from Combi-Blocks. Phenylboronic acid was purchased from TCI Germany. Tetrakis(triphenylphosphine)palladium(0), 4-aminophenylboronic acid pinacol ester, acryloyl chloride, rhodamine B, dimethylacrylamide, *N*,*N*'-methylenebis(acrylamide), DMSO-d_6, deuteriumoxide and 4-methoxyphenyl methylsulfide were purchased from Sigma-Aldrich. DCM-d_2 was purchased from Deutero. Methyl phenyl sulfide, 4-methylphenyl methyl sulfide, and 4-chlorophenyl methyl sulfide were purchased from Alfa Aesar. *N*-(Phosphonomethyl)glycine was purchased from Molekula and chromium trioxide from Acros Organics. All the chemicals and solvents were used without purification.

^{1}H, ^{13}C, and ^{31}P-NMR spectra were measured using a Bruker Avance 300 MHz. Solid State ^{13}C CP MAS NMR measurement was carried out using a Bruker Avance II solid-state NMR spectrometer operating at 300 MHz. FT-IR measurements were conducted with a Bruker Tensor II FTIR spectrometer. Gas chromatography was performed on a Shimadzu GC-2010 plus gas chromatograph and analyzed with a QP2010 ultra mass spectrometer. Fluorescence microscopy was performed on a Leica DMi8 inverted light microscope. UV/Vis-absorption spectra were measured on a Cary 60 UV-Vis/NIR spectrometer. For cyclic voltammetry measurements, a Metrohm Autolab PGSTAT204 potentiostat/galvanostat, with a glassy carbon electrode as the working electrode, Hg/$HgCl_2$ electrode as reference electrode, and a platinum wire as the counter electrode, was used. DFT calculations were carried out using the Gaussian 09 (rB3LYP, basis set: 6-31G).

6.2.2 Synthesis Methods

Synthesis of PDMAA-BTPh$_2$

N,N-Dimethylacrylamide (0.2 g, 2.0 mmol), *N,N'*-methylenebis(acrylamide) (6.2 mg, 40.3 µmol), *N*-(4-(7-phenylbenzo[c][1,2,5]thiadiazol-4-yl)phenyl)acrylamide (14.4 mg, 40 µmol), were dissolved in 1 mL DMF. AIBN (3.31 mg, 20 µmol) was added, and the solution was degassed using argon. The solution was heated at 80 °C overnight. The resulting polymer was excessively washed with THF and purified via dialysis against water/LiCl and pure water.

Synthesis

N-(4-(7-phenylbenzo[c][1,2,5]thiadiazol-4-yl)phenyl)acrylamide:

N-(4-(7-phenylbenzo[c][1,2,5]thiadiazol-4-yl)phenyl)acrylamide was synthesized after a previously published synthesis route.[208]

^{1}H NMR (300 MHz, DMSO) δ 10.36 (s, 1H), 8.10 – 7.94 (m, 6H), 7.86 (d, *J* = 8.4 Hz, 2H), 7.65 – 7.40 (m, 3H), 6.50 (dd, *J* = 17.0, 10.0 Hz, 1H), 6.31 (dd, *J* = 17.1, 2.1 Hz, 1H), 5.84 – 5.72 (m, 1H) ppm.

^{13}C NMR (126 MHz, DMSO) δ 163.33, 153.48, 153.37, 139.23, 136.92, 131.94, 131.85, 131.81, 129.61, 129.13, 128.58, 128.43, 128.30, 127.72, 127.19, 119.31

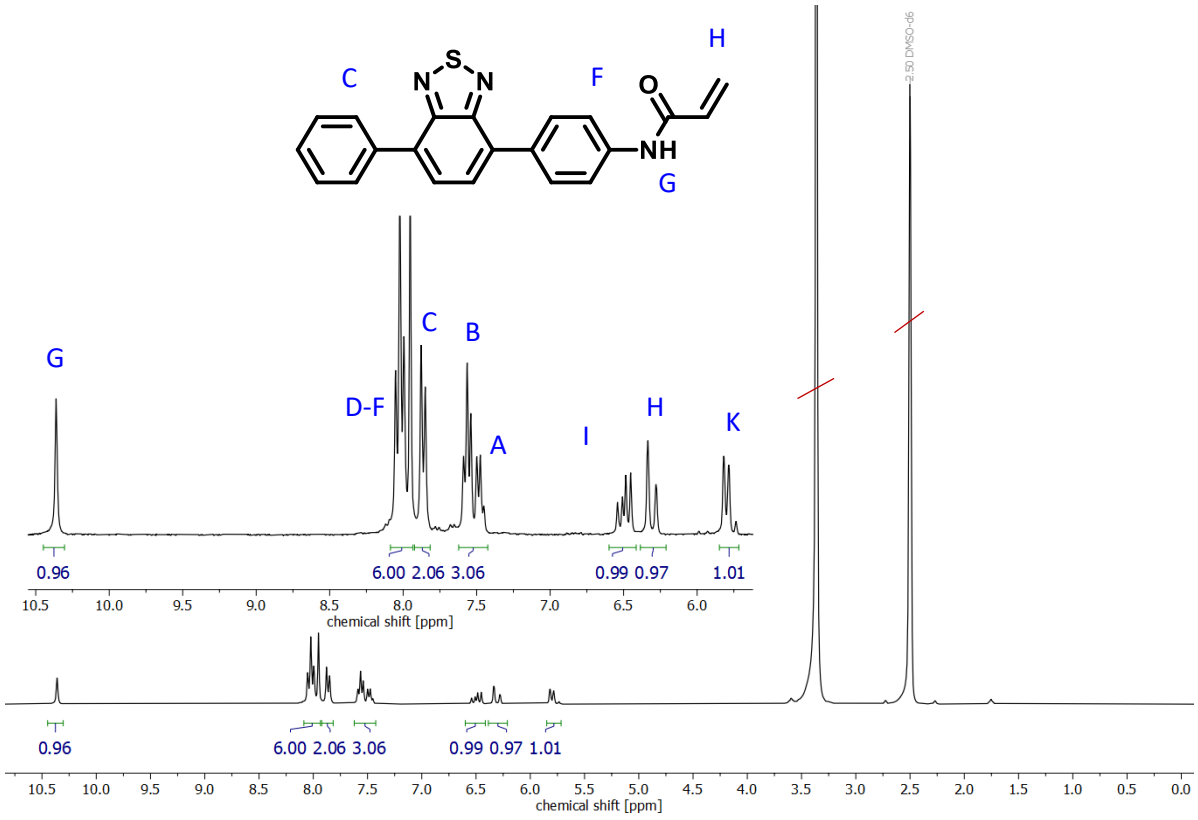

Figure 6.17: ^{1}H NMR spectrum (DMSO-d$_6$, 300 MHz): *N*-(4-(7-phenylbenzo[c][1,2,5]thiadiazol-4-yl)phenyl)acrylamide.

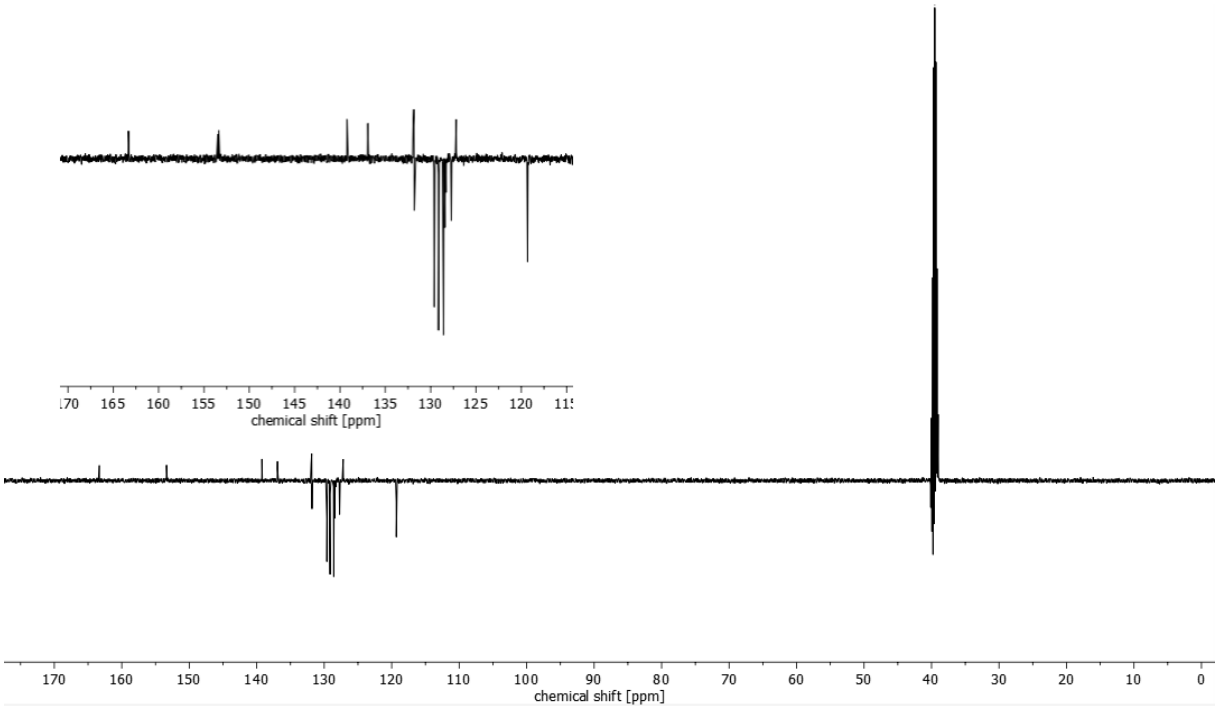

Figure 6.18: ^{13}C NMR spectrum (DMSO-d_6, 126 MHz): *N*-(4-(7-phenylbenzo[c][1,2,5]thiadiazol-4-yl)phenyl)acrylamide.

Synthesis of Linear-PDMAA-BTPh$_2$

N,N-Dimethylacrylamide (0.2 g, 2.0 mmol), *N*-(4-(7-phenylbenzo[c][1,2,5]thiadiazol-4-yl)phenyl) acrylamide (14.4 mg, 40 µmol), were dissolved in 1.5 mL DMF. AIBN (3.31 mg, 20 µmol) was added and the solutions was degassed using argon. The solution was heated at 80 °C overnight. The resulting polymer was precipitated in diethyl ether. M_n (14,403 g/mol) ***Đ*** 2.8.

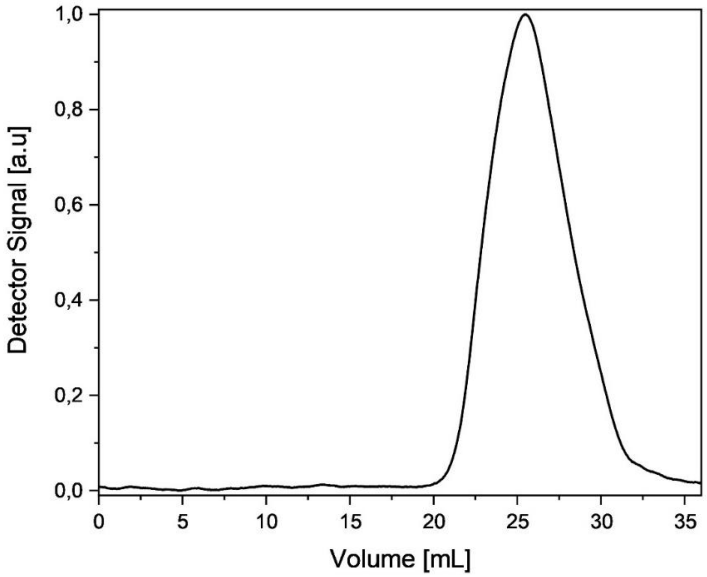

Figure 6.19: GPC analysis of the PDMAA linear photocatalytic polymer.

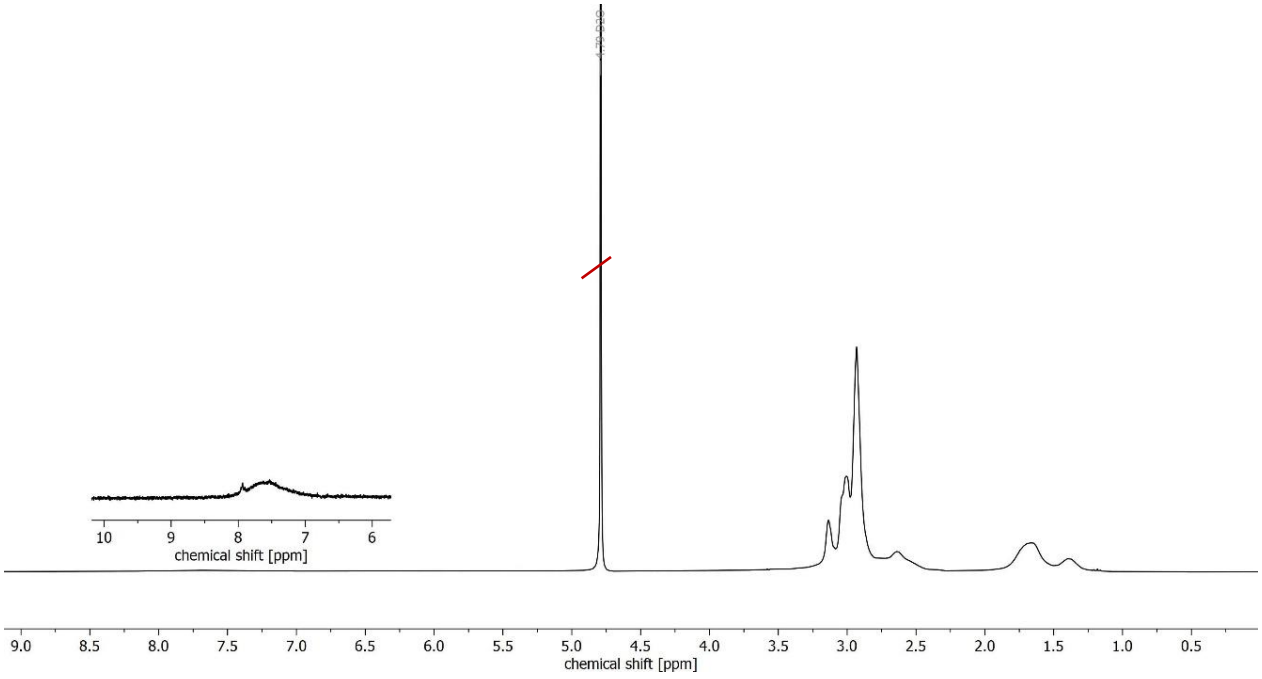

Figure 6.20: ^{1}H NMR spectrum of the PDMAA linear photocatalytic polymer.

6.2.3 Photocatalytic Reactions

Methyl phenyl sulfoxide (Table 5.2, *Figure 6.21 Figure 6.22*)

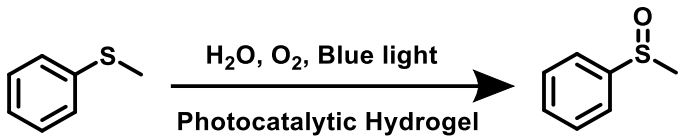

Methyl phenyl sulfide (30 mM) and photocatalytic hydrogel (10 mg, photocatalyst 1.9 mol%, 1.8 µmol photocatalyst) were dispersed in 10 mL of water. The mixture was bubbled with O_2 under stirring. The vial was irradiated with blue LED light (power: 0.16 W cm^{-2}, λ = 460 nm) for 22 h. The sample was extracted with DCM, dried over $MgSO_4$ and the conversion was determined by GC-MS. The product was purified via column chromatography (PE: EtAc = 1:1)

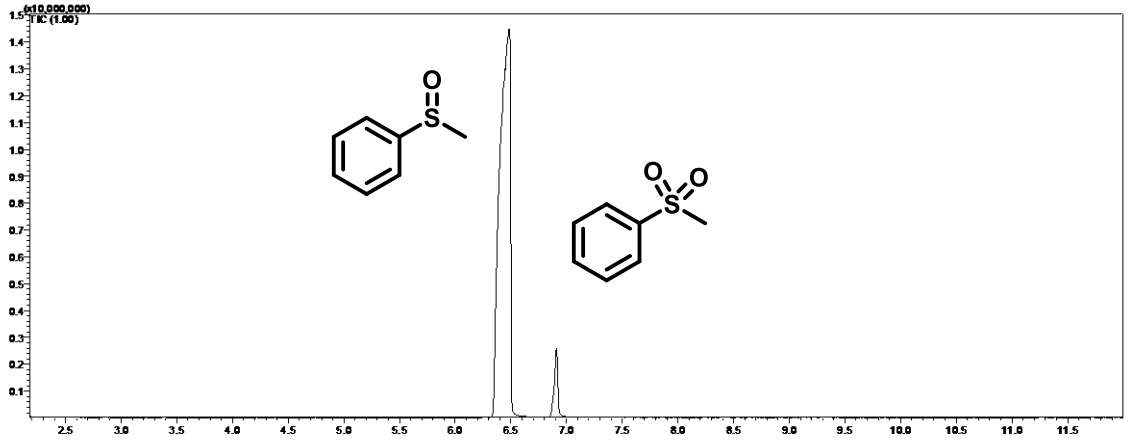

Figure 6.21: GCMS spectrum of compounds produced through thioanisole oxidation.

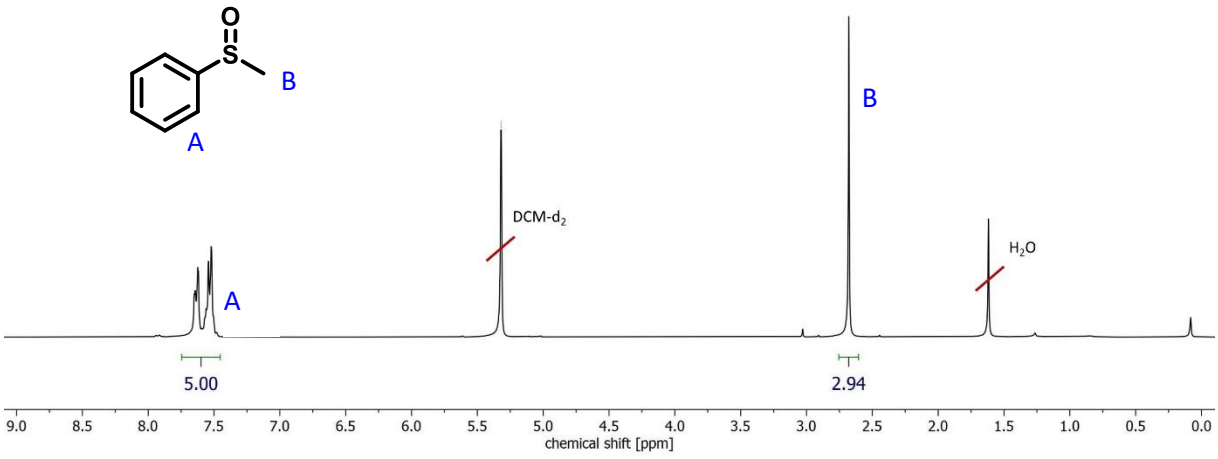

Figure 6.22: ^{1}H NMR spectrum (CD_2Cl_2, 300 MHz): phenyl methyl sulfoxide.

4-Methoxyphenyl methyl sulfoxide (Table 5.2, Figure 6.23, Figure 6.24)

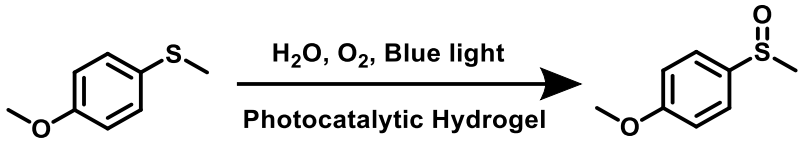

4-Methoxy methyl phenyl sulfide (30 mM) and photocatalytic hydrogel (10 mg, photocatalyst 1.9 mol%, 1.8 µmol photocatalyst) were dispersed in 10 mL of water. The mixture was bubbled with O_2 under stirring. The vial was irradiated with blue LED light (power: 0.16 W cm^{-2}, λ = 460 nm) for 22 h. The sample was extracted with DCM, dried over $MgSO_4$ and the conversion was determined by GC-MS. The product was purified via column chromatography (PE: EtAc = 1:1)

^{1}H NMR (300 MHz, CD_2Cl_2) δ 7.57 (d, J = 8.8 Hz, 1H), 7.04 (d, J = 8.8 Hz, 1H), 3.85 (s, 2H), 2.65 (s, 2H).

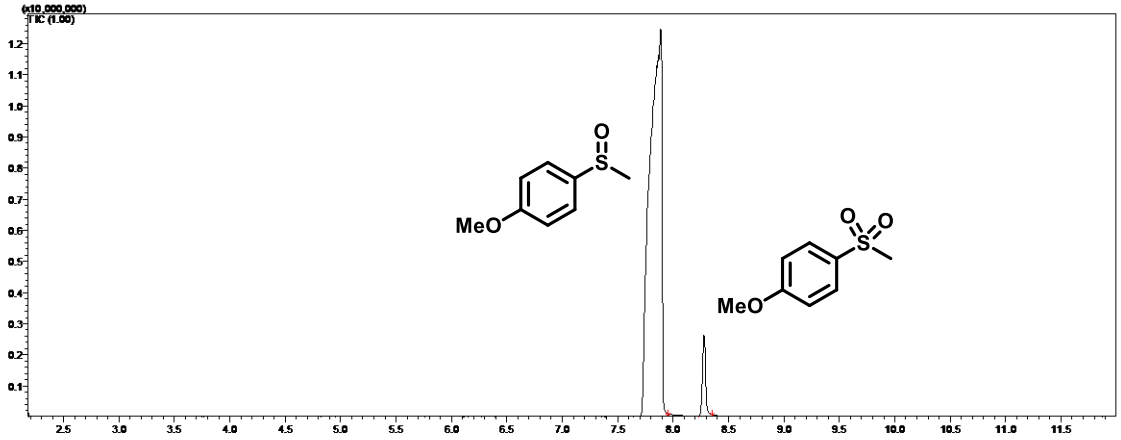

Figure 6.23: GCMS spectrum of compounds produced through 4-methoxyphenyl methyl sulfide oxidation.

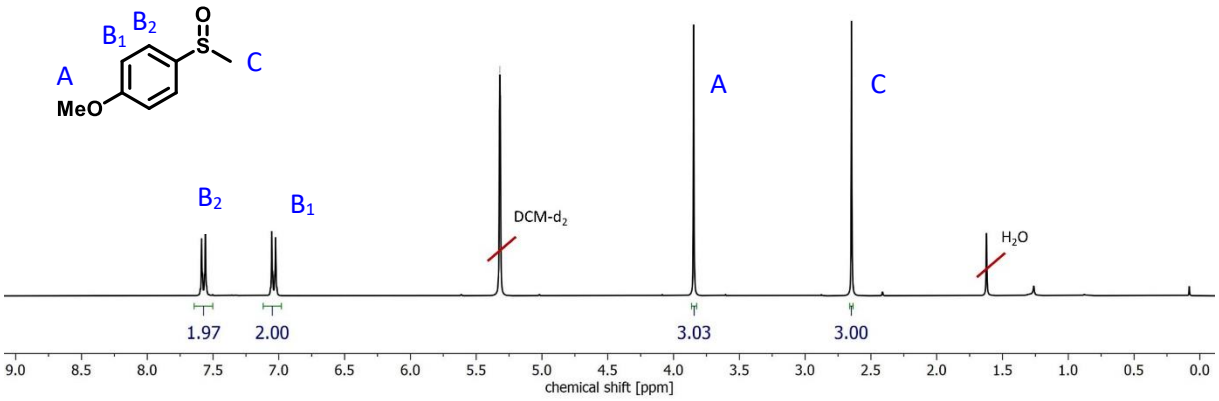

Figure 6.24: ^{1}H NMR spectrum (CD_2Cl_2, 300 MHz): 4-methoxyphenyl methyl sulfoxide.

4-Chlorophenyl methyl sulfoxide (Table 5.2, Figure 6.25, Figure 6.26)

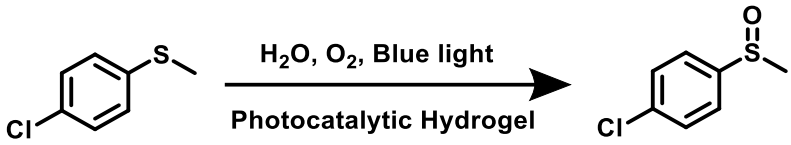

4-Chlorophenyl methyl sulfide (30 mM) and photocatalytic hydrogel (10 mg, photocatalyst 1.9 mol%, 1.8 µmol photocatalyst) were dispersed in 10 mL of water. The mixture was bubbled with O_2 under stirring. The vial was irradiated with blue LED light (power: 0.16 W cm^{-2}, λ = 460 nm) for 22 h. The sample was extracted with DCM, dried over $MgSO_4$ and the conversion was determined by GC-MS. The product was purified via column chromatography (PE: EtAc = 1:1)

^{1}H NMR (300 MHz, CD2Cl2) δ 7.62 – 7.49 (m, 1H), 2.68 (s, 1H).

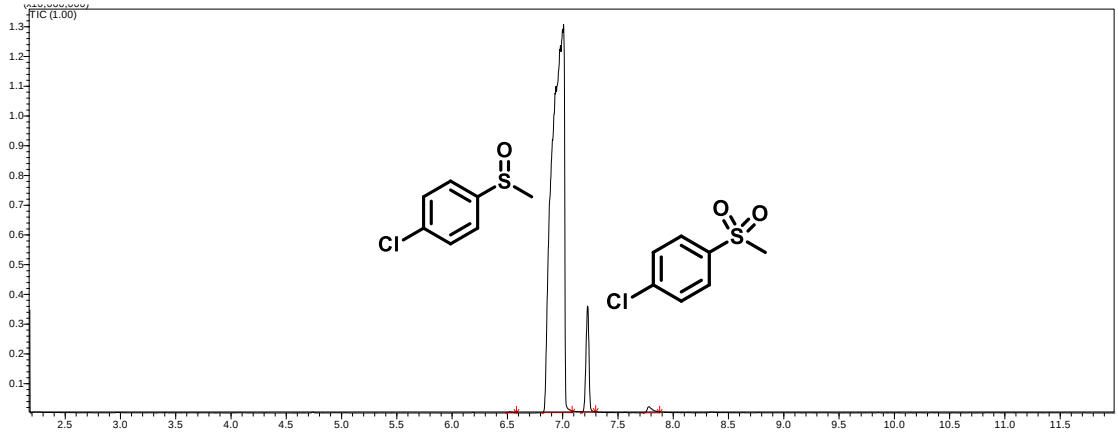

Figure 6.25: GCMS spectrum of compounds produced through 4-chlorophenyl methyl sulfide oxidation.

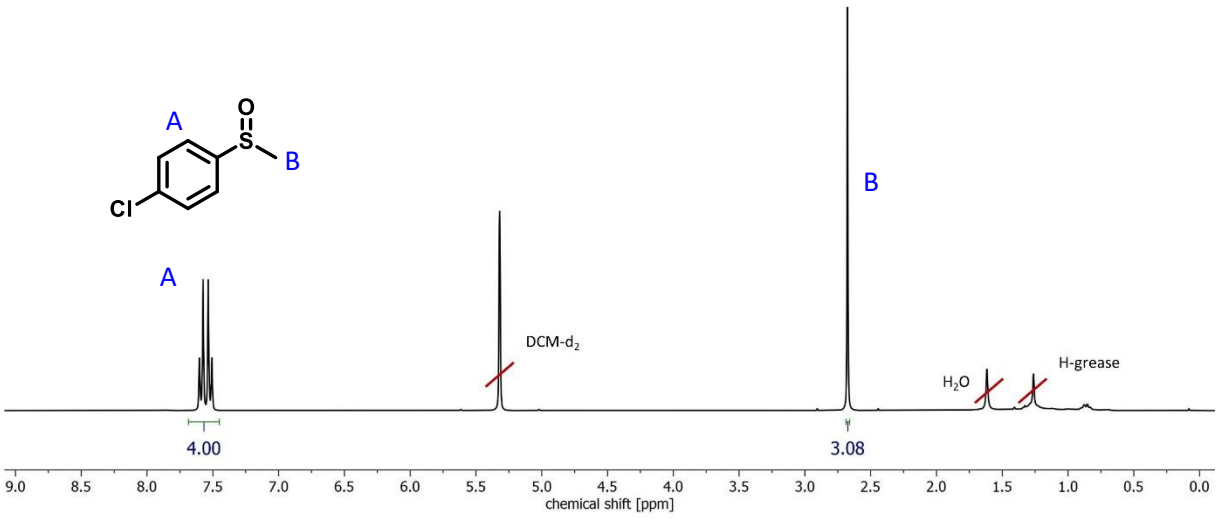

Figure 6.26: ^{1}H NMR spectrum (CD_2Cl_2, 300 MHz): 4-chlorophenyl methyl sulfoxide.

4-Methylphenyl methyl sulfoxide (Table 5.2, Figure 6.27, Figure 6.28)

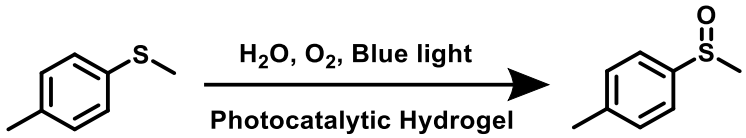

4-Methylphenyl methyl sulfide (30 mM) and photocatalytic hydrogel (10 mg, photocatalyst 1.9 mol%, 1.8 µmol photocatalyst) were dispersed in 10 mL of water. The mixture was bubbled with O_2 under stirring. The vial was irradiated with blue LED light (power: 0.16 W cm^{-2}, λ = 460 nm) for 22 h. The sample was extracted with DCM, dried over $MgSO_4$ and the conversion was determined by GC-MS. The product was purified via column chromatography (PE: EtAc = 1:1)

^{1}H NMR (300 MHz, CD_2Cl_2) δ 7.52 (d, J = 8.2 Hz, 1H), 7.34 (d, J = 8.0 Hz, 1H), 2.65 (s, 2H), 2.41 (s, 2H).

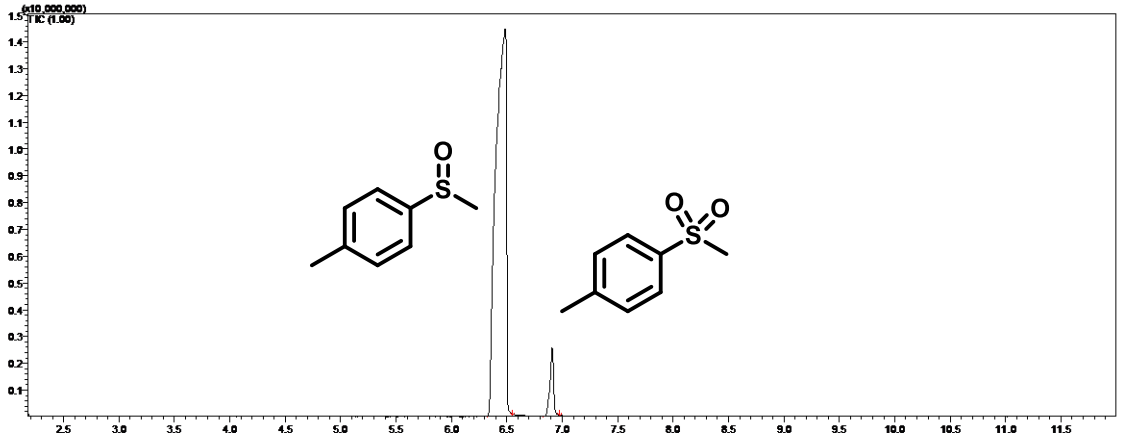

Figure 6.27: GCMS spectrum of compounds produced through 4-methylphenyl methyl sulfide oxidation.

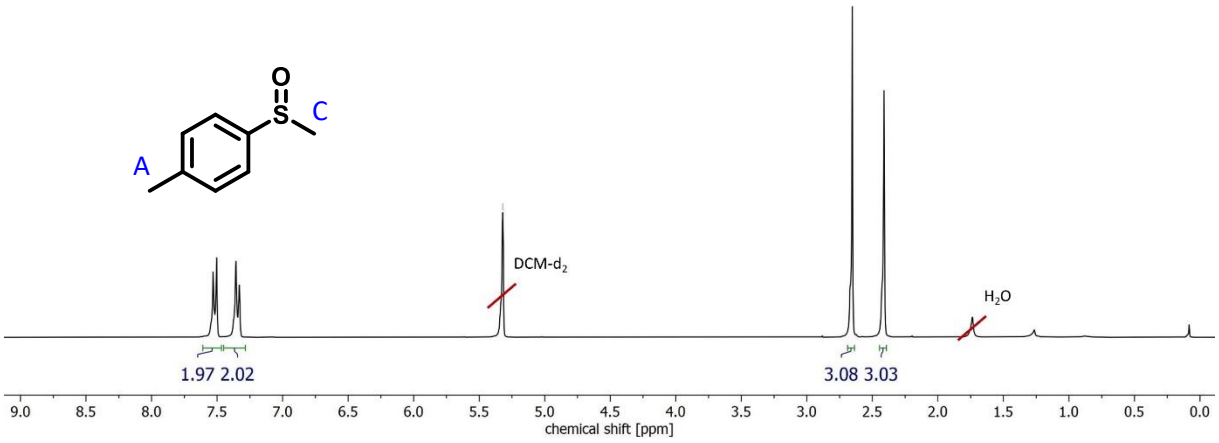

Figure 6.28: ^{1}H NMR spectrum (CD_2Cl_2, 300 MHz): 4-methlyphenyl methyl sulfoxide.

Photoreduction of Chromium Trioxide (Figure 5.28, 5.29)

To a $Cr^{VI+}O_3$ solution of a (25 mg/L, 0.125 mg, 1.25 µmol) in 5 mL water, hydrogel (15 mg, photocatalyst 1.9 mol%, 2.7 µmol) was added. The solution was degassed by nitrogen bubbling and irradiated with a blue LED light (power: 0.16 W cm^{-2}, λ = 460 nm). The Cr^{VI} concentration was determined via UV/Vis absorbance using a diphenylcarbazide solution in acetone (0.25 wt.%). Therefore, 0.5 mL of the $Cr^{VI+}O_3$ solution was centrifuged and added to 5 mL of 0.2 M H_2SO_4. Diphenylcarbazide (0.1 mL) was added and stirred for 2 min and monitored through UV/Vis spectroscopy.

Two blank measurements were performed under the same conditions. One in the absence of the photocatalytic hydrogel and one in the absence of light.

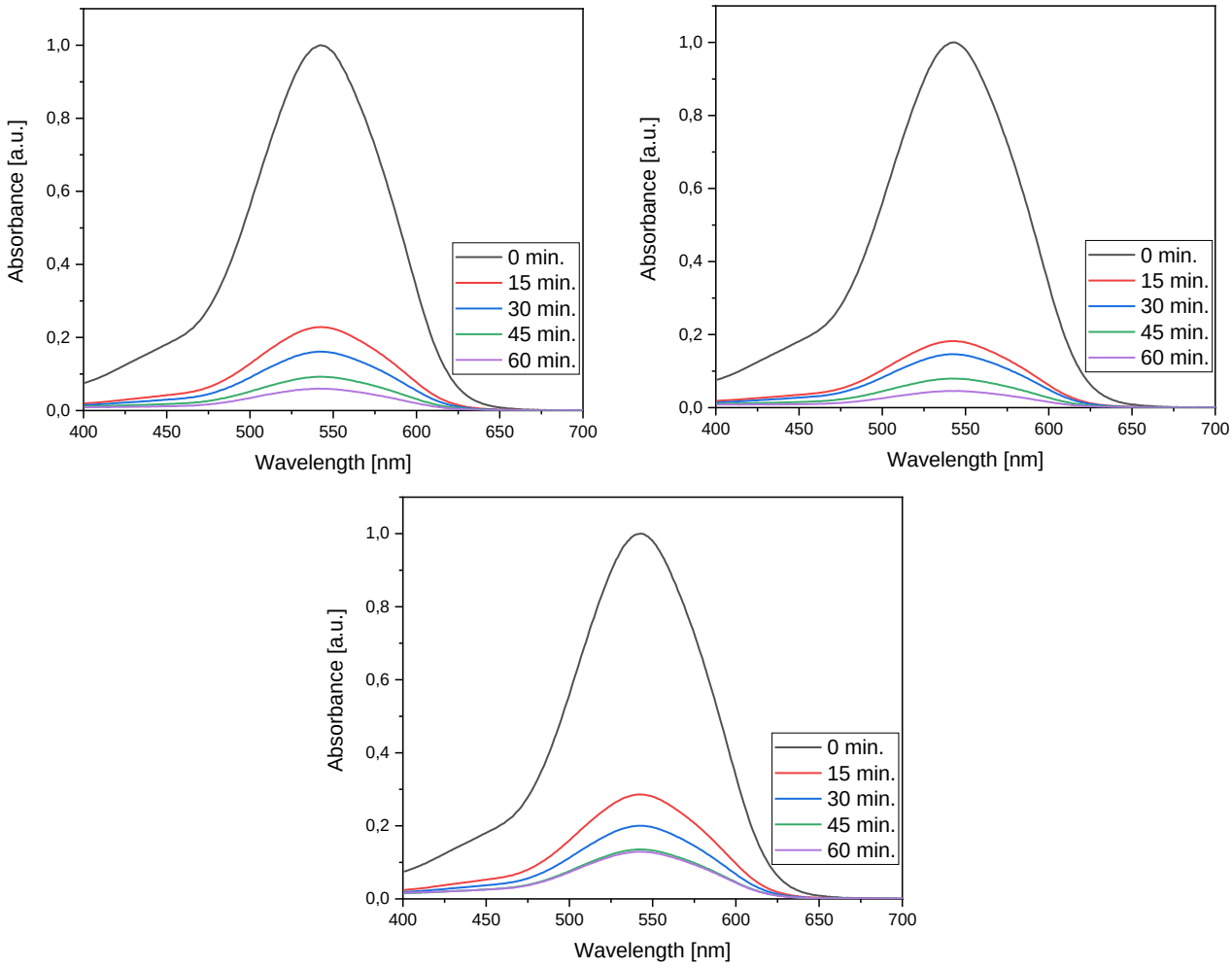

Figure 6.29: Photoreduction of Cr^{VI} to Cr^{III} using photocatalytic hydrogel under blue light irradiation (power: 0.16 W cm^{-2}, λ = 460 nm). Absorbance peak at 542 nm by complexation with diphenylcarbazide.

Chromium Blank Measurement

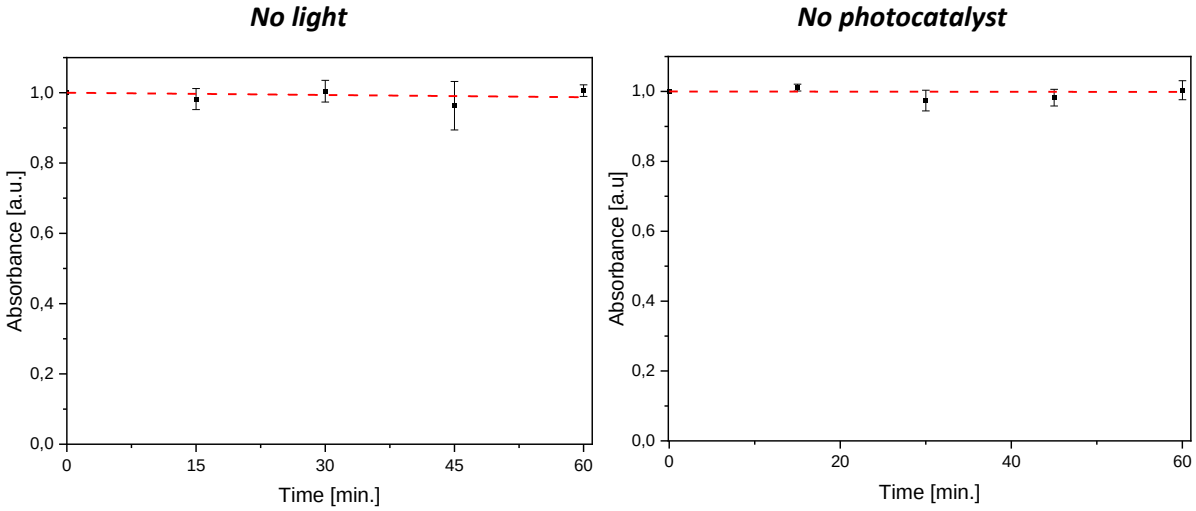

Figure 6.30: Chromium degradation performed under standard conditions in the absence of light or photocatalyst. (power: 0.16 W cm^{-2}, λ = 460 nm). Absorbance peak at 540 nm by complexation with diphenylcarbazide.

Photoreduction of Chromium Trioxide Recycle Experiment

To a $Cr^{VI+}O_3$ solution of (25 mg/L, 0.125 mg; 1.25 µmol) in 5 mL water hydrogel (15 mg photocatalyst 1.9 mol%, 2.7 µmol) was added. The solution was degassed by nitrogen bubbling and irradiated with a blue LED light (power: 0.16 W cm^{-2}, λ = 460 nm) for 2 h. The Cr^{VI} concentration was determined after 2 h as mentioned above. New $Cr^{VI+}O_3$ solution was added and the experiment repeated for 5 cycles.

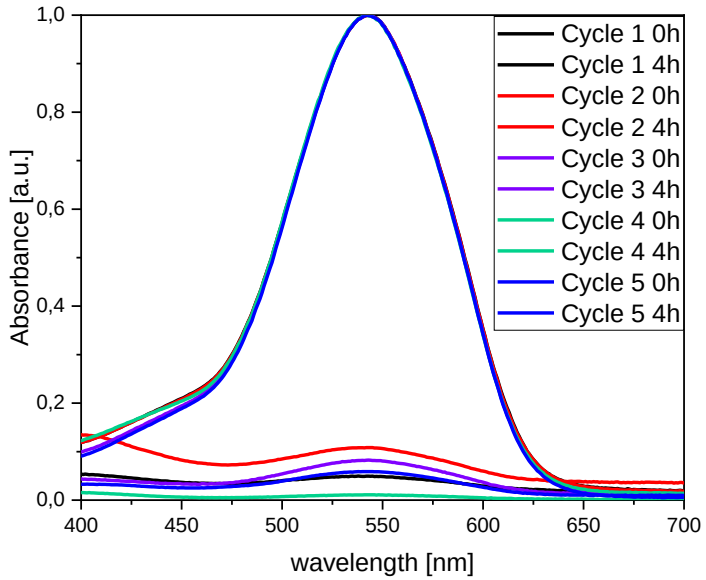

Figure 6.31: Recycling photoreduction of Cr^{VI} to Cr^{III} using photocatalytic hydrogel under blue light irradiation (power: 0.16 W cm^{-2}, λ = 460 nm). Absorbance peak at 540 nm by complexation with diphenylcarbazide.

Rhodamine B Degradation (Figure 5.26)

To a rhodamine B solution (100 mg/L) in 4 mL water hydrogel (29 mg, photocatalyst 1.9 mol%, 5.2 µmol) was added. The vial was irradiated with blue LED light (power: 0.16 W cm^{-2}, λ = 460 nm) under stirring. UV/Vis samples were taken periodically to track the degradation rates of the dye.

Scavenger test (Figure 5.27)

Methyl phenyl sulfide (30 mM), scavenger (45 mM) and photocatalytic hydrogel (10 mg, photocatalyst 1.9 mol%, 1.8 µmol photocatalyst) were dispersed in 10 mL of water. The mixture was bubbled with O_2 under stirring. The vial was irradiated with blue LED light (power: 0.16 W cm^{-2}, λ = 460 nm) for 22 h. The sample was extracted with DCM and dried over $MgSO_4$. Products and conversion were determined by GC-MS.

Photodegradation *N*-(phosphonomethyl)glycine (Figure 6.32, 6.34-6.36)

To D_2O (5 mL), *N*-(phosphonomethyl)glycine (12.5 mg; 74 µmol), NaOH (400 µL, 2M) as well as hydrogel (25 mg, 1.9 mol% photocatalyst 4.5 µmol) or linear-PDMAA-BTPh2 (25 mg) were added. The mixture was bubbled with O_2 under stirring for 5 min. The vial was then irradiated with blue LED light (power: 0.16 W cm^{-2}, λ = 460 nm) under oxygen atmosphere. The sample was centrifuged and analyzed via ^{31}P-NMR spectroscopy. Blank measurements were performed under the same conditions in the absence of photocatalyst or light.

Large Scale Photodegradation *N*-(phosphonomethyl)glycine (Figure 6.33)

To H_2O (500 mL), *N*-(phosphonomethyl)glycine (1 g, 5.9 mmol), NaOH (40 mL, 2M) as well as hydrogel (2.5 g, 1.9 mol% photocatalyst 450 µmol) were added. The mixture was bubbled with O_2 under stirring for 30 min. The flask was then irradiated with blue LED lights (power: 0.16 W cm^{-2}, λ = 460 nm) under oxygen atmosphere. Samples were taken every five hours and freeze-dried. The residue was taken up in 1 mL D_2O centrifuged and analyzed via ^{31}P-NMR spectroscopy.

Glyphosate Kinetic Measurement

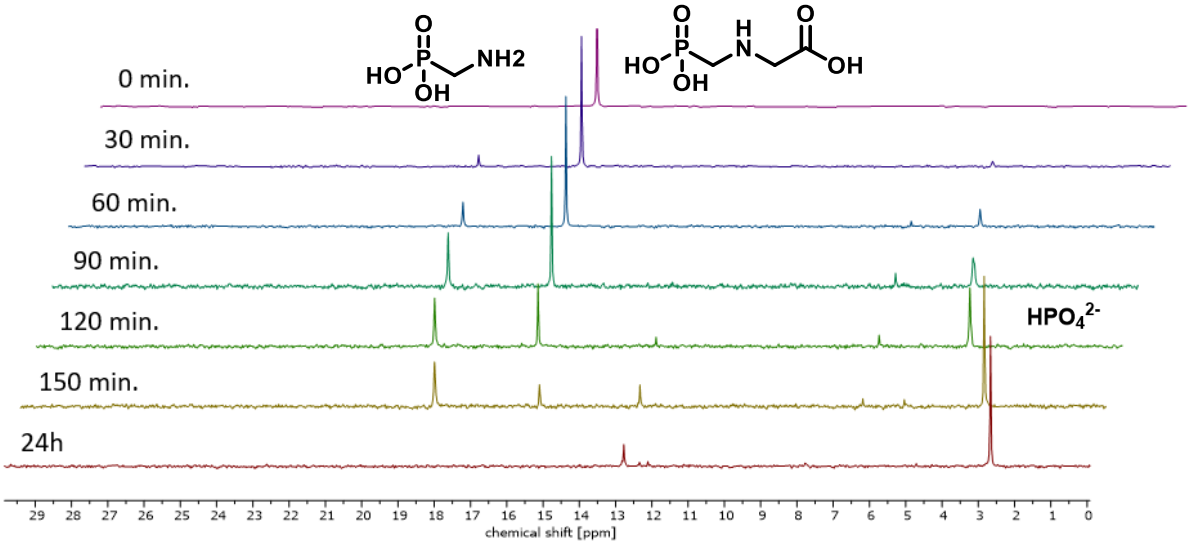

Figure 6.32: ^{31}P NMR spectra (D_2O, 300 MHz): stacked kinetic measurement of photodegradation of glyphosate.

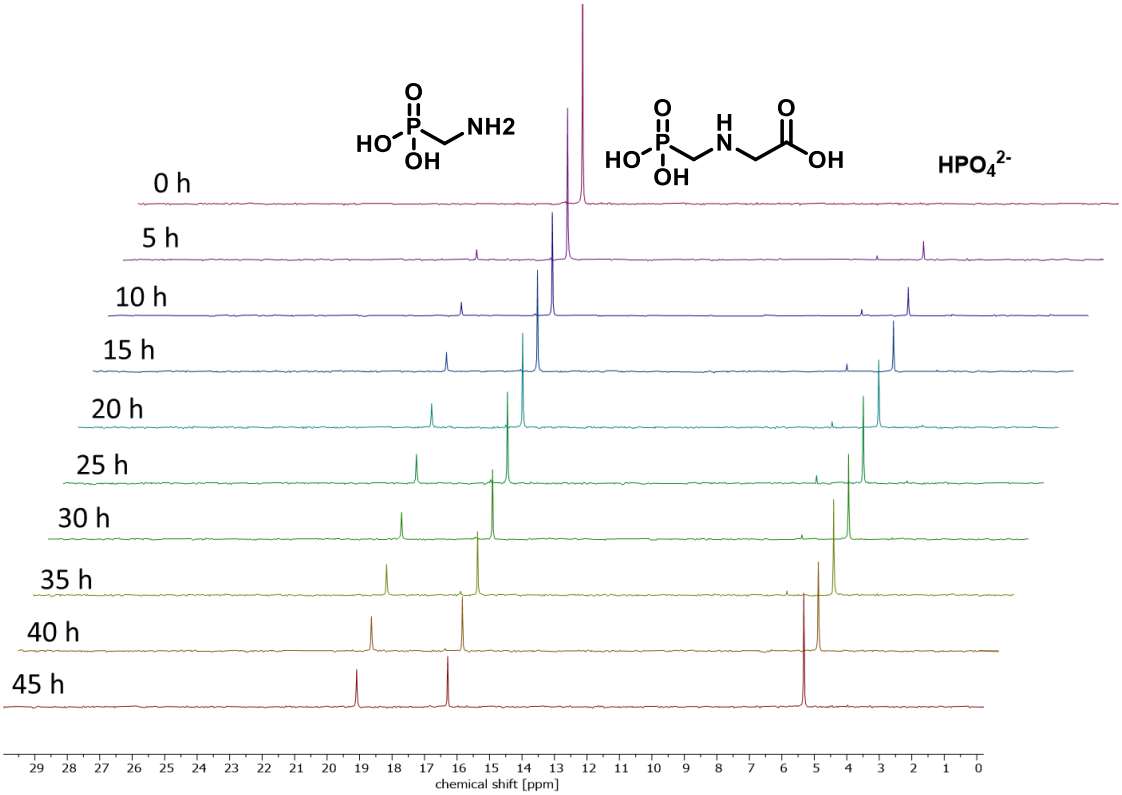

Figure 6.33: ^{31}P NMR spectra (D_2O, 300 MHz): stacked kinetic measurement of large scale photodegradation of glyphosate.

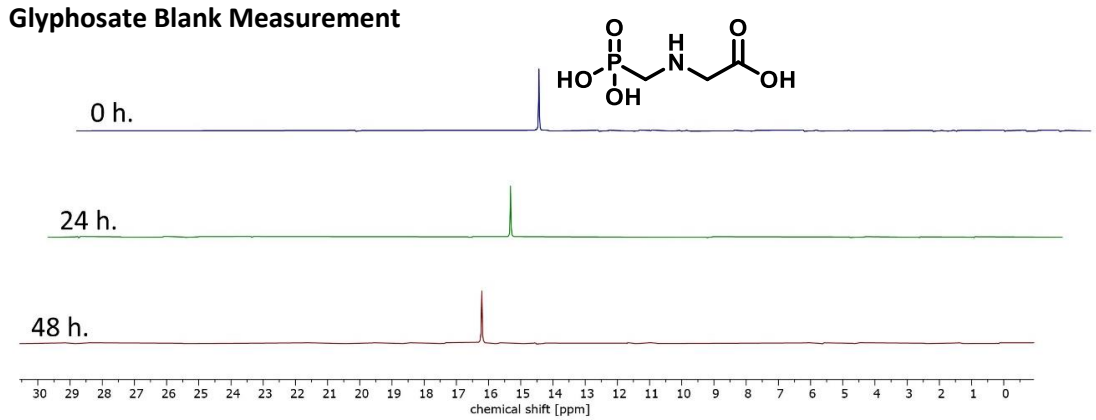

Figure 6.34: ^{31}P NMR spectra (D_2O, 300 MHz): stacked blank measurement of glyphosate without photocatalyst.

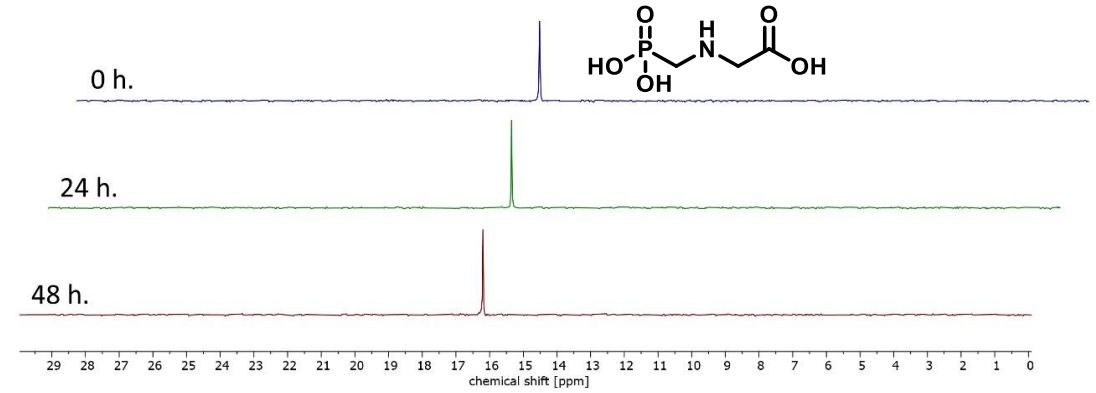

Figure 6.35: ^{31}P NMR spectra (D_2O, 300 MHz): stacked blank measurement of glyphosate without light.

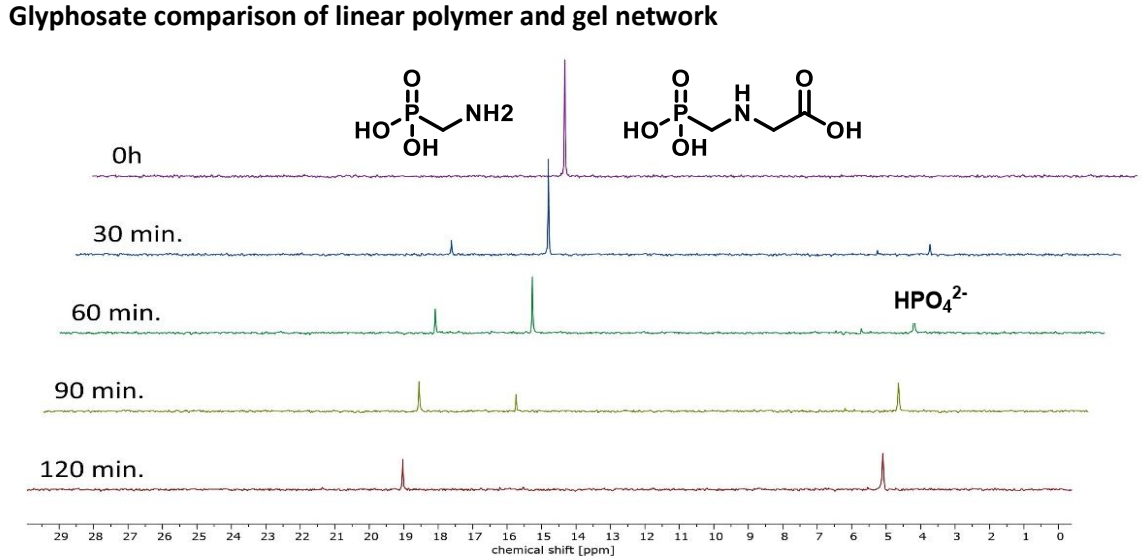

Figure 6.36: ^{31}P NMR spectra (D_2O, 300 MHz): stacked glyphosate degradation with linear polymer photocatalyst.

6.3 Reactivity Tuning of Metal-Free Artificial Photoenzyme through Binding Sites Specific Bioconjugation

6.3.1 General Information and Characterization:

All chemicals were purchased from commercial sources and used without further purification. Analysis of proteins and modified proteins was performed via LC-MS(ES+) on a Waters Acquity I-Class UPLC coupled to a Waters Synapt G2 HDMS, and the results were analyzed via MassLynx V. 4.0. Yield for incorporation of N-(4-(7-phenyl benzo[c][1,2,5]thiadiazol-4-yl)phenyl)acrylamide was calculated by mass peak count ratio (±1 Da). UV/Vis absorbance spectroscopy was measured on a Cary 50 UV−Vis/NIR spectrometer, and fluorescence emission was measured on a RF-6000 – Shimadzu using LabSolutions RF. ^{1}H and ^{13}C-NMR spectra were measured using a Bruker Pro 500 operating at 500 MHz or 126 MHz, respectively, and analyzed via MestReNova. Gas chromatography was performed on a Shimadzu GC-2010 plus gas chromatograph and analyzed with a QP2010 ultra mass spectrometer, using a ZB-5MS column with helium as carrier gas. Integration of starting material and product peak is used to determine the conversion ratio while using anisole as a reference. Chiral HPLC was measured on an Agilent Series 1200 using a Daicel Chiralpak IE 250mm/4.6mm/5µm column in THF/n-hexane 20/80. Mass spectroscopy was measured on an Advion Expression LCMS using (APCI) and was analyzed using Advion data express. DFT calculations were performed using Gaussian 16. The DFTs for the HOMO/LUMO levels were calculated for optimization of the local minimum using method rb3lyp/6-31+g(d) the triplet state energy was calculated for optimization of the local minimum using method b3lyp/6-31+g(d). Frontier molecular orbital pictures were produced using Avogadro. Electron Paramagnetic Resonance spectroscopy was performed on a Magnettech Miniscope MS200 spectrometer at room temperature, microwave frequency: 9.391 GHz, scan time: 60 seconds. Photocatalytic reactions were performed using 24V super bright LED tape, blue 460-465 nm, 18W, from Ultra LEDs. All graphs and figures were created using OriginPro 2019b. Chemical structures were drawn in ChemDraw 20.1.

6.3.2 Synthesis Methods

Synthesis:

4-phenyl-7-(4-vinylphenyl)benzo[c][1,2,5]thiadiazole **(**Table 5.3 **Entry 1)** and *N*-(4-(7-phenyl benzo[c][1,2,5]thiadiazol-4-yl)phenyl)acryl amide **(**Table 5.3 **Entry 2)** were performed and purified after previously published procedures.[203,208]

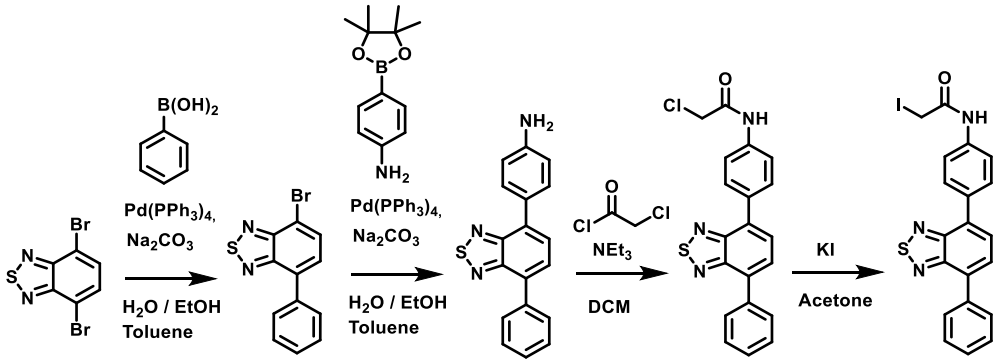

Figure 6.37: Synthesis method of 2-iodo-N-(4-(7-phenylbenzo[c][1,2,5]thiadiazol-4-yl)phenyl)acetamide.

Synthesis of 2-iodo-*N*-(4-(7-phenylbenzo[c][1,2,5]thiadiazol-4-yl) phenyl)acetamide:

Phenylboronic acid (553 mg, 4.54 mmol, 1.00 eq.), 4,7-dibromobenzo[c][1,2,5]thiadiazole (2 g, 6.80 mmol, 1.50 eq.), $Pd(PPh_3)_4$ (157 mg, 136 µmol, 0.03 eq.), Na_2CO_3 (1.7g, 15.96 mmol) were added to a Schlenk tube and evacuated. Toluene (18 mL), ethanol (8 mL), and water (8 mL) were degassed via nitrogen bubbling for 20 min. The Schlenk tube was filled with nitrogen, the solvents were added, and the solution was vigorously stirred (90 °C, 24 h). After reaching room temperature, the solution was extracted with dichloromethane, and the combined organic phases were washed with brine and dried over anhydrous $MgSO_4$. Concentrated, and the catalyst was removed over silica column chromatography (PE/DCM gradient 4:1→0:1).

Step 2: The crude product from step 1 (330 mg), 4-(4,4,5,5-tetramethyl-1 ,3,2-dioxaborolan-2-yl)aniline (270 mg, 1.29 mmol, 1.10 eq.), $Pd(PPh_3)_4$ (99 mg, 85.9 µmol, 0.05 eq.), Na_2CO_3 (0.63 g, 5.95 mmol) were transferred into a Schlenk tube and evacuated. 1,4-Dioxane (7.5 mL) and H_2O (3 mL) were degassed using nitrogen over 20 min. The Schlenk tube was backfilled with nitrogen, and the solvents were added. The solution was stirred at 100 °C overnight. The resulting mixture was extracted with dichloromethane, and the combined organic phases were washed with brine (50 mL), dried over anhydrous $MgSO_4$, and concentrated using a rotary evaporator. The crude product was then purified by column chromatography on silica gel (PE/DCM gradient 2:1 → 0:1). The column was further pretreated with DCM / 5 vol.% TEA). The product was yielded as red crystals. (191 mg, 0.63 mmol, 56% yield) In good reference to previous reported results.[208]

^{1}H NMR (300 MHz, CD2Cl2) δ 8.02 – 7.92 (m, 2H), 7.84 (d, 2H), 7.75 (q, 2H), 7.53 (t, 2H), 7.44 (t, 1H), 6.84 (d, 2H), 3.95 (s, 2H).

Step 3: To a dried Schlenk tube 4-(7-phenyl-benzo[c][1,2,5]thiadiazol-4-yl)aniline (100 mg, 330 µmol, 1.00 eq.), triethylamine (69 µL, 494 µmol, 1.5 eq.) and dry THF (2 mL) were added. The solution was stirred at room temperature for 10 min before being cooled to 0 °C. A stock solution of chloroacetyl chloride (39.5 µL, 494 µmol, 1.50 eq.) in dry THF (2 mL) was prepared and slowly added over time. The solution slowly changed color from red to yellow/brown. The solution was stirred at room temperature overnight and was then quenched with water and extracted with DCM. The combined organic fractions were washed with water and dried over $MgSO_4$. The solvent was evaporated, and the product was washed with n-Hexane and used without further purification.

Step 4: The starting materials 2-chloro-N-(4-(7-phenylbenzo[c][1,2,5]thiadiazol-4-yl)phenyl)acetamide (113 mg, 297 µmol) and KI (74 mg, 446 µmol) were transferred into a flame dried flask and dispersed in dry benzene. The solution was then freeze-dried. Around 80 mL of dry acetone were added, and the flask was refluxed overnight. The solvent was evaporated, and the solid was taken up in DCM and washed with water. The water phase was extracted with DCM and the organic phases were combined. The solvent was evaporated, and the product was washed with n-hexane. Yielding the product as an orange powder (65 mg, 138 µmol = 41% yield over two steps)

^{1}H NMR (500 MHz, DMSO) δ 10.52 (s, 1H), 8.07 – 7.98 (m, 4H), 7.94 (s, 2H), 7.80 – 7.71 (m, 2H), 7.60 – 7.52 (m, 2H), 7.51 – 7.44 (m, 1H), 3.89 (s, 2H).

^{13}C NMR (126 MHz, DMSO) δ 167, 153, 153, 139, 137, 132, 132, 130, 129, 129, 128, 128, 128, 119, 2.

MS m/z: 268.9, 301.0, 304.0, 345.0, 346.1, 347.0 471.9 [*M*+H]$^{+}$, 473.7, 475.7

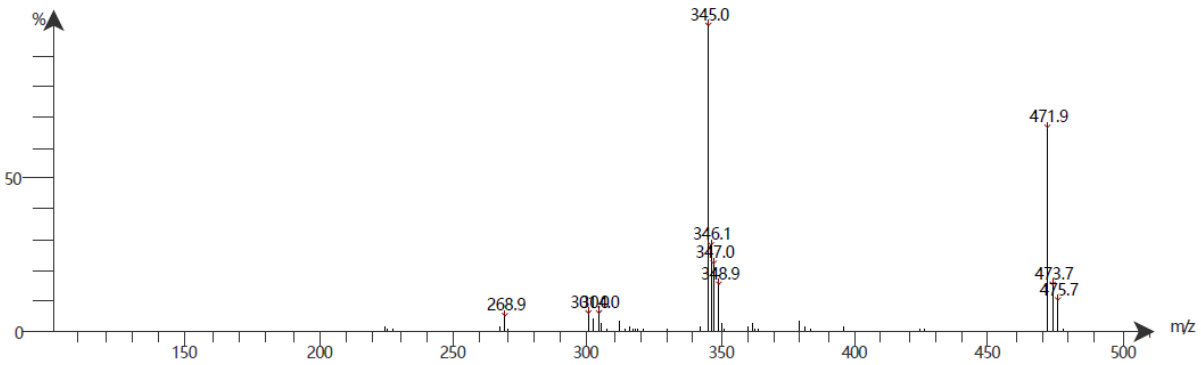

Figure 6.38: Mass spectrum of 2-iodo-N-(4-(7-phenylbenzo[c][1,2,5]thiadiazol-4-yl)phenyl)acetamide.

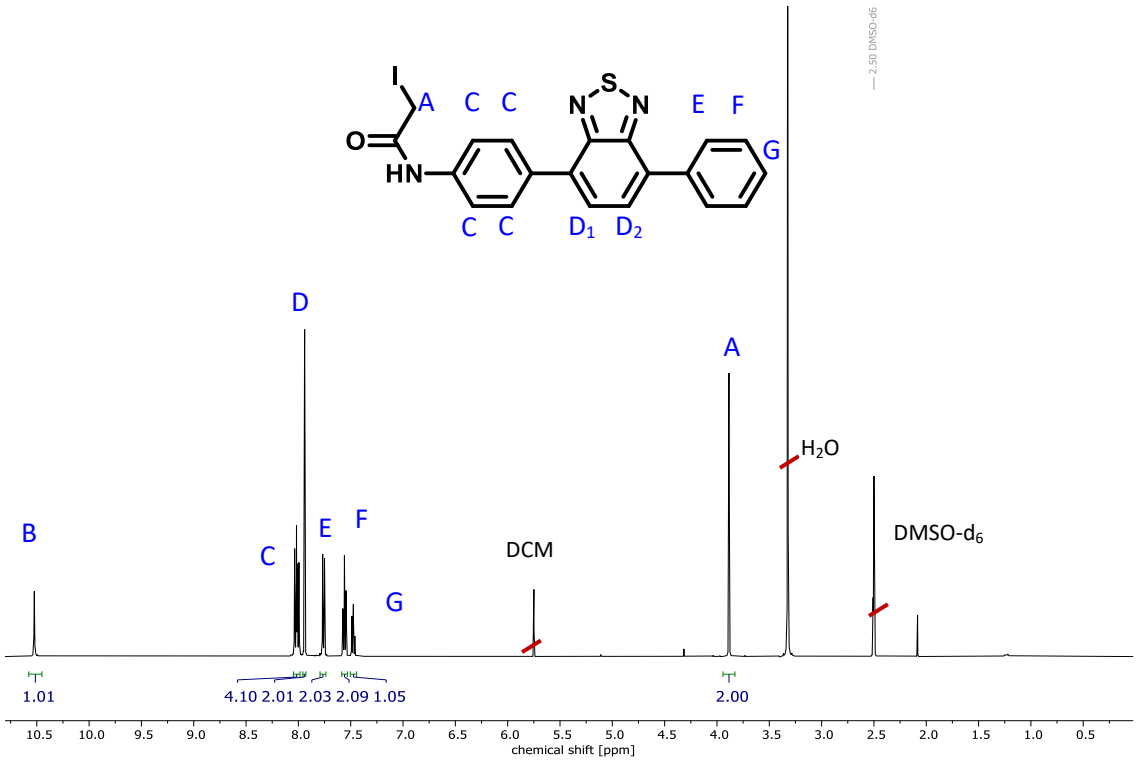

Figure 6.39 ^{1}H NMR spectrum (500 MHz, DMSO) of 2-iodo-*N*-(4-(7-phenylbenzo[c][1,2,5]thiadiazol-4-yl)phenyl)acetamide.

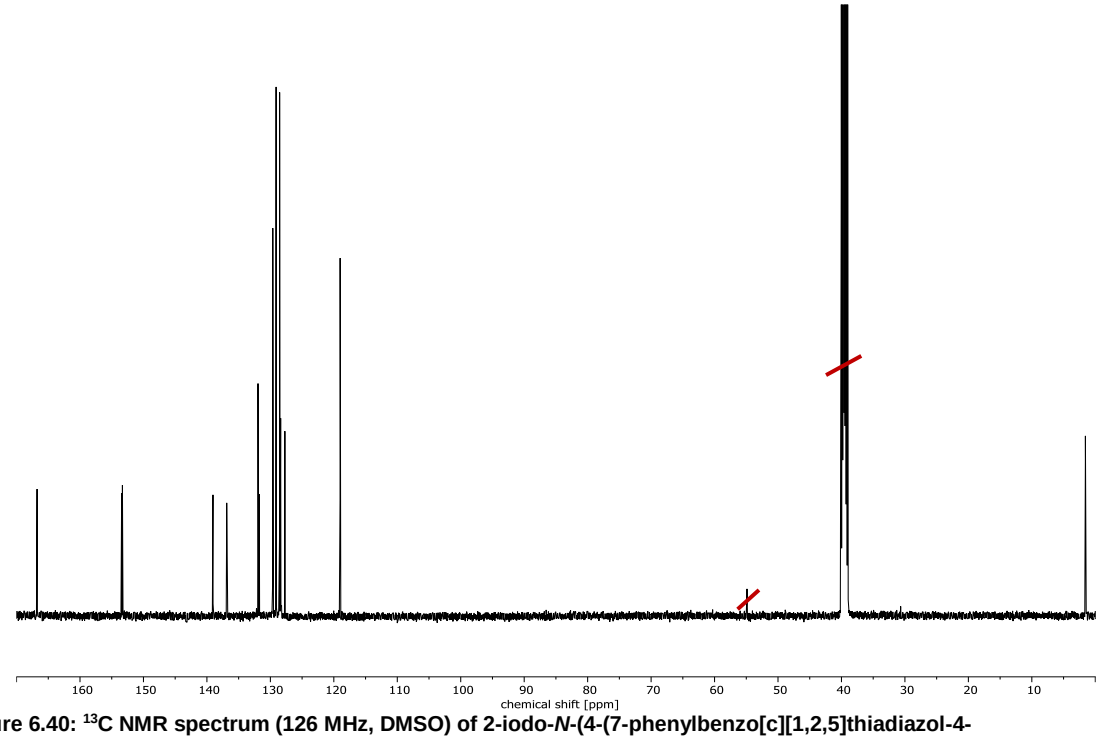

Figure 6.40: ^{13}C NMR spectrum (126 MHz, DMSO) of 2-iodo-*N*-(4-(7-phenylbenzo[c][1,2,5]thiadiazol-4-yl)phenyl)acetamide.

Protein Purification and Expression:

The mutagenesis, expression, and purification of the protein variants were carried out as previously reported.[386,387,391]

General Method for Bioconjugation:

All protein variants were modified after the same procedure. Purified protein was defrosted and taken up in HEPES buffer (50 mM HEPES, 50 mM NaCl, 8.5 pH) to a concentration of 100 µM. 10 equivalents of 2-iodo-*N*-(4-(7-phenylbenzo[c][1,2,5]thiadiazol-4-yl)phenyl)acetamide (stock solution: 10 mM in DMF) were added. The solution was incubated in a thermoshaker (20 °C, 1 h, 300 rpm). The Eppendorf was then centrifuged (12k, rt, 5 min.) twice and each time the precipitate was discarded. The supernatant was filtered, centrifuged again and then purified over a PD-10 desalting column (MES buffer 20 mM, 50 mM NaCl, 6 pH). If the solution volume exceeded the recommended volume of the desalting column, a centrifugation filter (10 kDa cut-off, Amicon) was used to concentrate the solution and diluted again afterward. The final concentration was determined via a Bradford assay.[399]

Example Conditions for Attempted Thiol-ene Conjugation of Vinyl Photocatalyst 1:

To SCP-2L V83C (100 µM, 100 µL) in PBS or MES buffer was added photocatalyst 1 (10 µL of 1 mM stock in DMF) in a clear PCR tube. The reaction was irradiated with light (254, 365, or 460 nm) for 1-8 h at room temperature. The results were analyzed by SDS page gel and LCMS showing no protein conjugation.

VA-044 activation: To SCP-2L V83C (100 µM, 100 µL) in PBS or MES buffer was added photocatalyst 1 (10 µL of 1 mM stock in DMF) in a PCR tube. VA-044 (1 µL; 10 mM solution in H_2O) was added, and the solution was heated at 40 °C in a heat block for 24 h. The results were analyzed by SDS page gel and LCMS, showing no protein conjugation.

Characterization of the Unmodified Protein

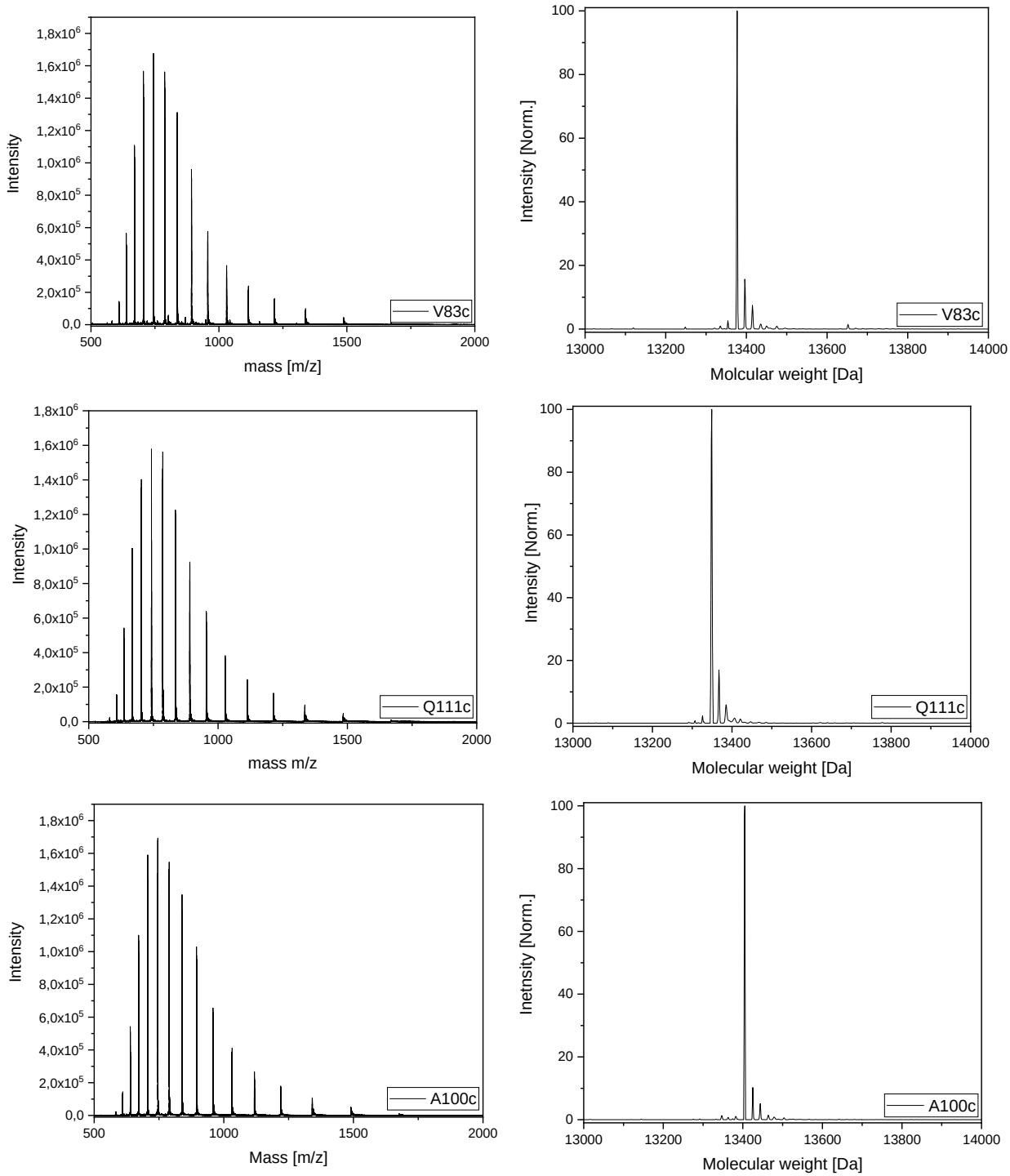

Figure 6.41: Mass spectra of purified SCP-2L V83C, Q111C and A100C before bioconjugation. Raw mass spectrum (left) and the deconvoluted mass-spectrum (right) obtained by LC-MS (ES+).

Characterization of the Modified Protein

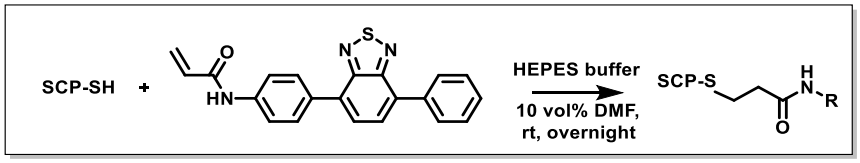

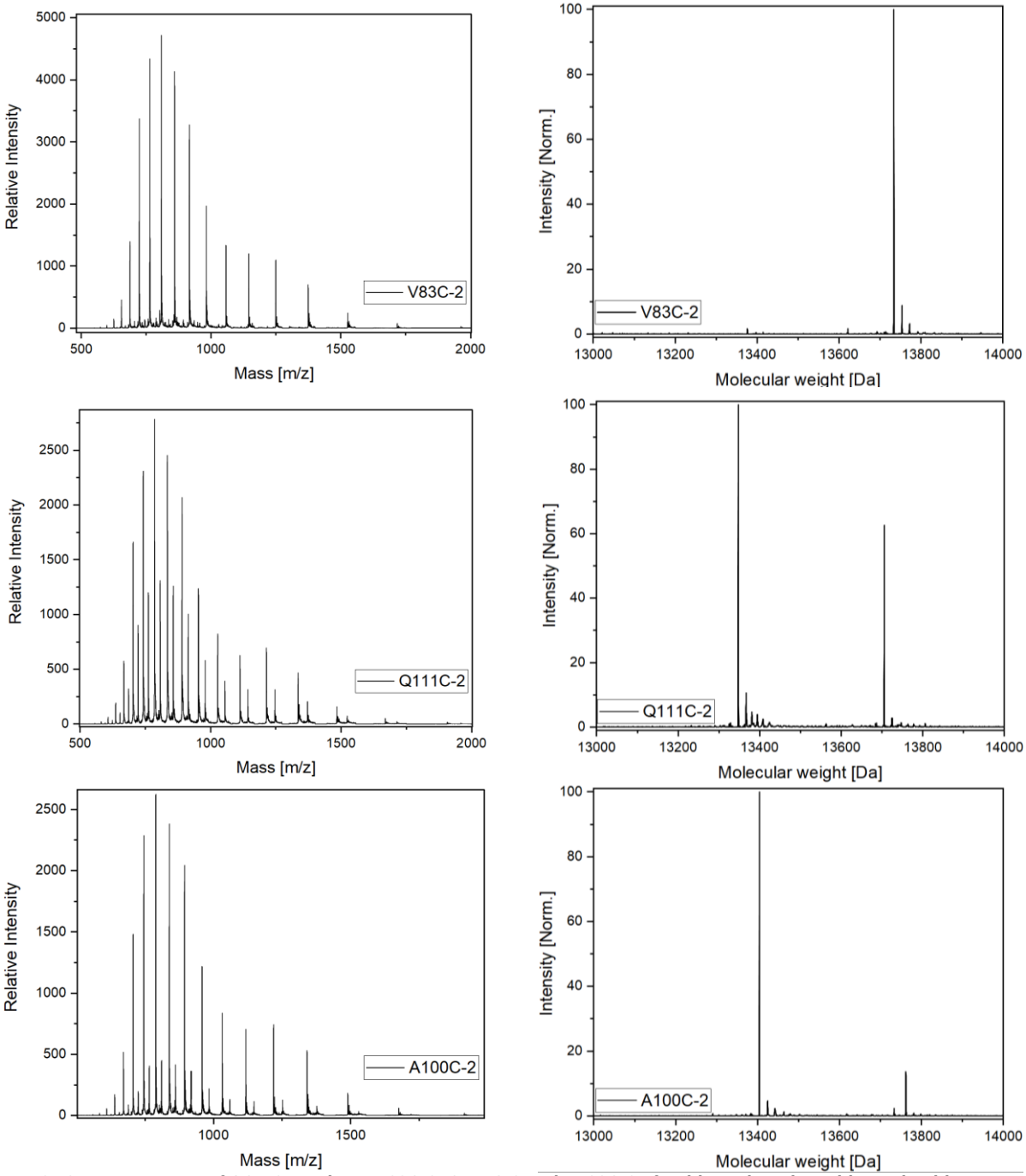

Figure 6.42: Mass spectra of SCP-2L variants V83C-2, Q111C-2 and A100C-2 after bioconjugation with acrylamide functionalized photocatalytic moiety. Raw mass spectrum (left) and the deconvoluted mass-spectrum (right) obtained by LC-MS (ES+).

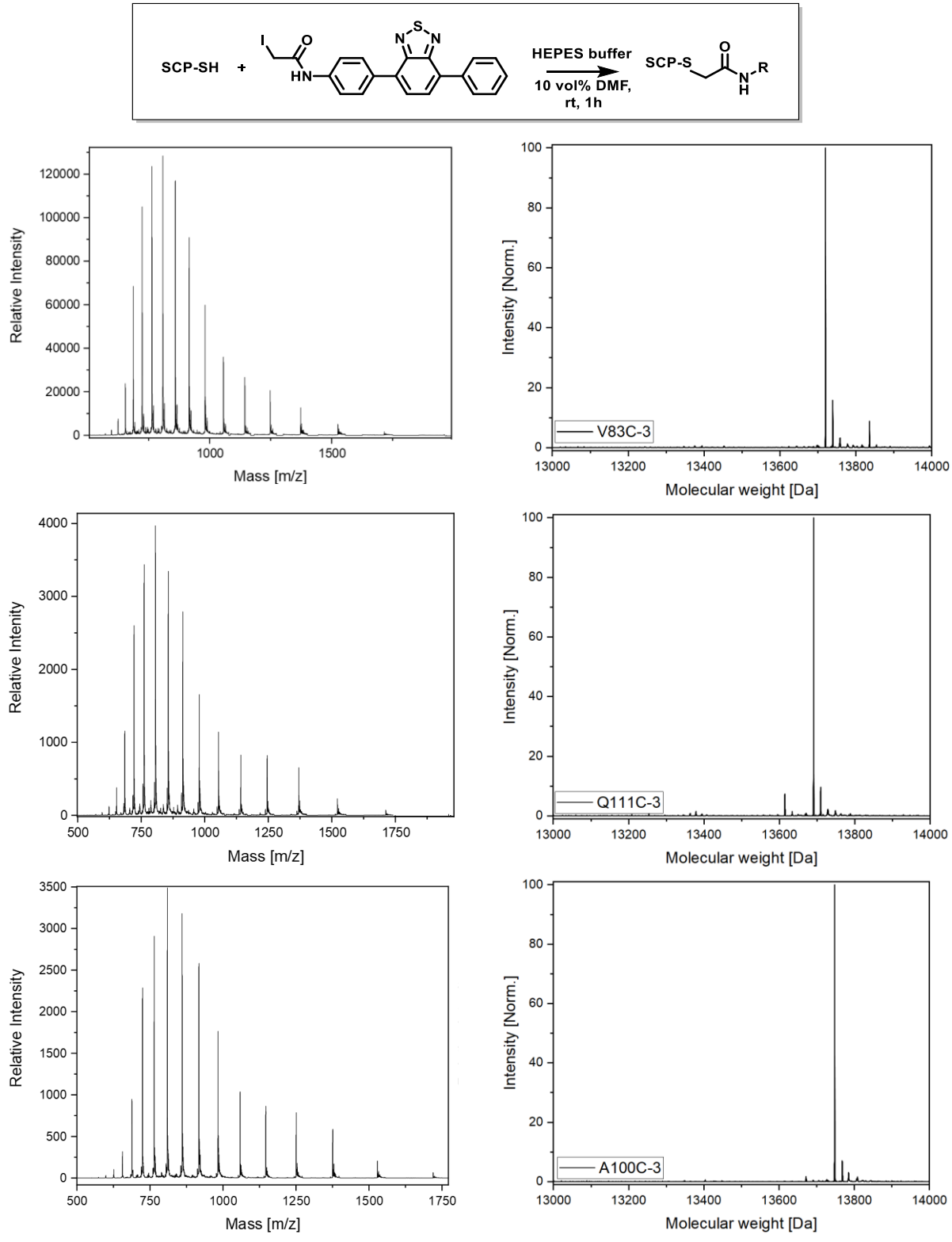

Figure 6.43: Mass spectra of SCP-2L variants V83C-3, Q111C-3 and A100C-3 after bioconjugation with iodoacetamide functionalized photocatalytic moiety. Raw mass spectrum (left) and the deconvoluted mass-spectrum (right) obtained by LC-MS (ES+).

Table 6.1: Calculated and observed masses of SCP-2L A100C, Q111C, V83C before and after bioconjugation.

Entry	SCP-2L	Photocatalyst	Theoretical Mass [Da]	Observed Mass [Da]
1	A100C	-	13404.66	13405
2	Q111C	-	13347.61	13349
3	V83C	-	13376.61	13377
4	A100C-2	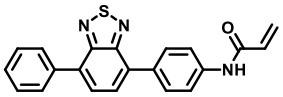	13761.75	13405+13762
5	Q111C-2	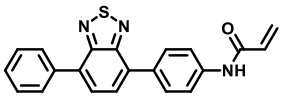	13704.70	13348+13706
6	V83C-2	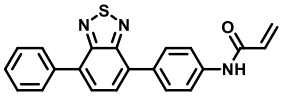	13733.70	13734
7	A100C-3	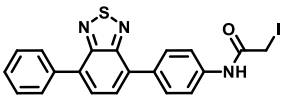	13747.74	13748
8	Q111C-3	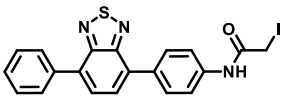	13690.69	13691
9	V83C-3	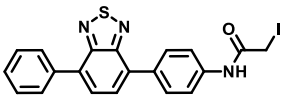	13719.69	13720

SDS-Page

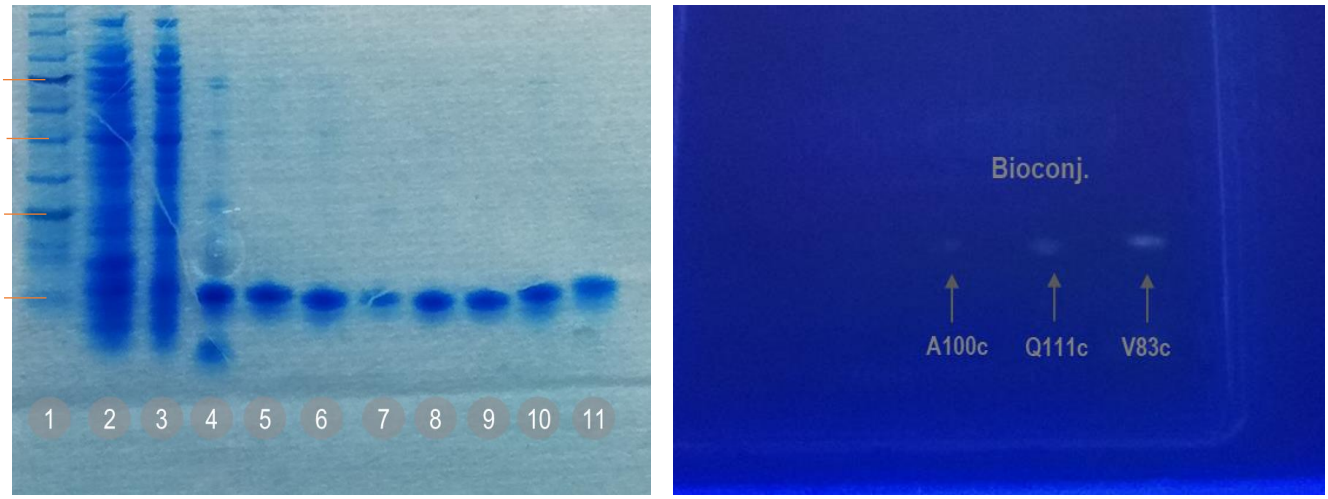

Figure 6.44 SDS-page (Nupage™ 4-12% Bis-Tris gel) of standard purification method and all 3 variants before and after bioconjugation b) SDS-page under UV/Vis lamp irradiated at 388 nm; Ladder: Prestained Protein Ladder – Broad molecular weight (10-245 kDa) ab116028.

1:	Protein ladder	8:	Pure Q111C
2:	Purification of V83C: Pre purification	9:	Pure Q111C-3
3:	Purification of V83C: Flow through	10:	Pure V83C
4:	Purification of V83C: HIS-Tag cleavage	11:	Pure V83C-3
5:	Purification of V83C: Purified V83c	A100C-3:	irradiated at 388 nm
6:	Pure A100C	Q111C-3:	irradiated at 388 nm
7:	Pure A100C-3	V83C-3:	irradiated at 388 nm

6.3.3 Photocatalytic Reaction

Methyl phenyl sulfoxide:

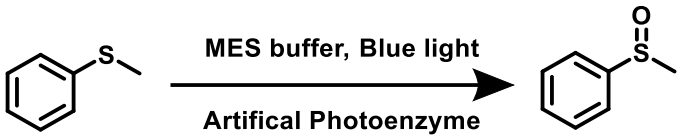

Modified SCP-2L protein (10 nmol) in MES buffer (20 mM MES, 50 mM NaCl, 1 mL) at pH 6 is added to a glass vial. The organic sulfide was dissolved in acetonitrile (100 mM), and 20 µL (2 µmol) were added to the vial. The vial was capped and placed in the photoreactor. The samples were irradiated with blue LED light (460-465 nm, 18 W) for a set time period. After irradiation, the solution was extracted three times with DCM, dried over $MgSO_4$ and analyzed via GC/MS.

Photostability Test:

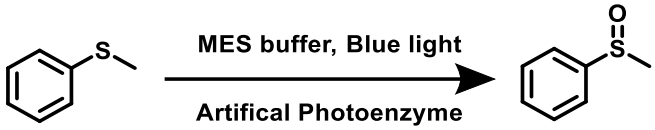

Modified SCP-2L protein (20 nmol) in MES buffer (20 mM MES, 50 mM NaCl, 2 mL) at pH 6 is added to a glass vial and irradiated with blue light for up to 24 h under room temperature. The samples are filtered and 1 mL (SCP-2L 10 nmol) is used for photocatalytic testing. The organic sulfide was dissolved in acetonitrile (100 mM) and 20 µL (2 µmol) are added to the vial. The vial was capped and placed in the photoreactor. The samples were irradiated for 8 h under blue light, extracted three times with DCM dried over $MgSO_4$, and analyzed via GC/MS.

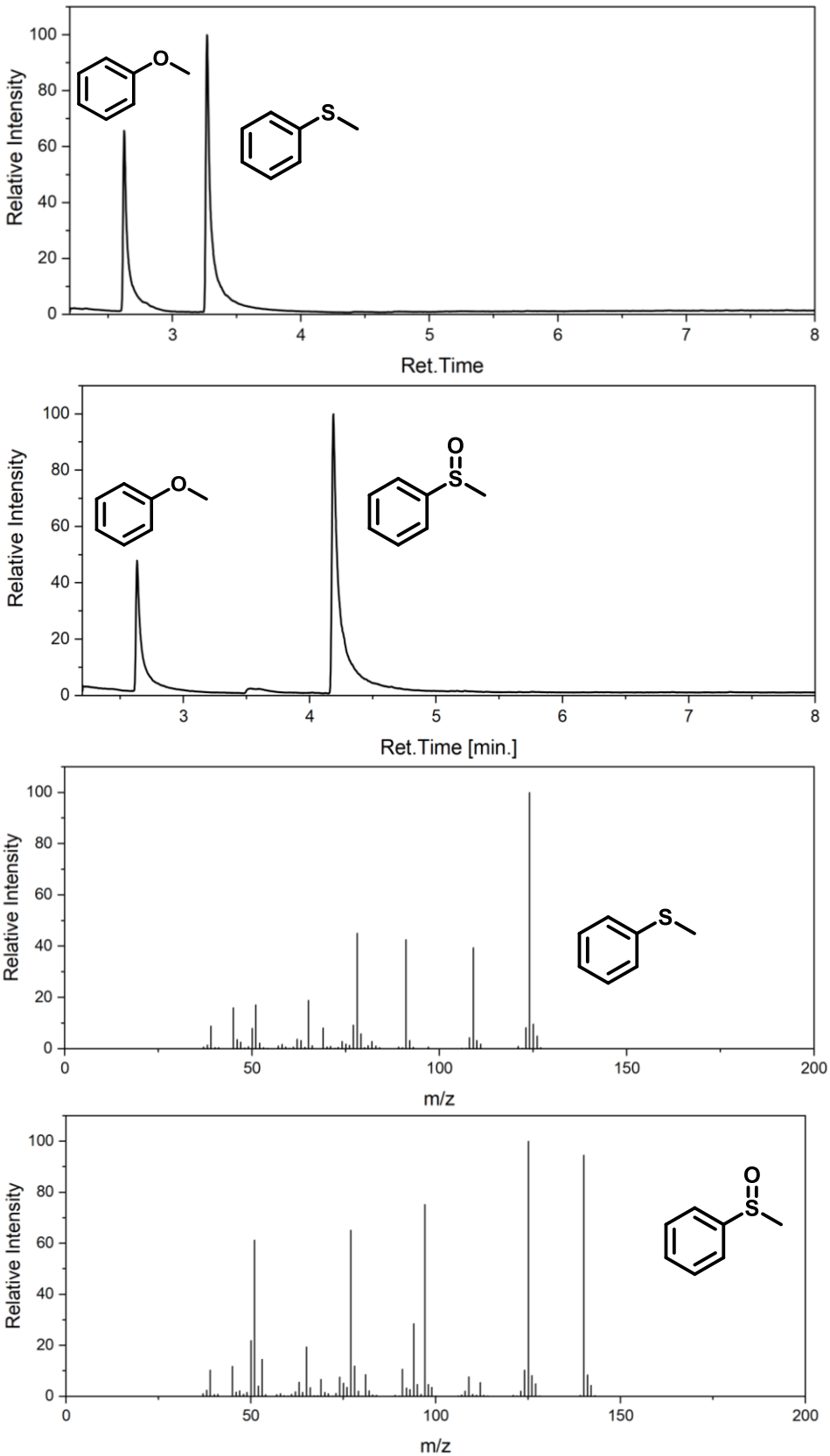

Figure 6.45: a) GC-MS temperature curve; column temp. 50 °C, heating rate 50 °C/min, inject. temp. 310 °C b) measured retention times of anisole, thioanisole and methyl phenyl sulfoxide. GC-MS ion source 250 °C, interface temp. 310 °C; measured mass spectra for thioanisole and methyl phenyl sulfoxide.

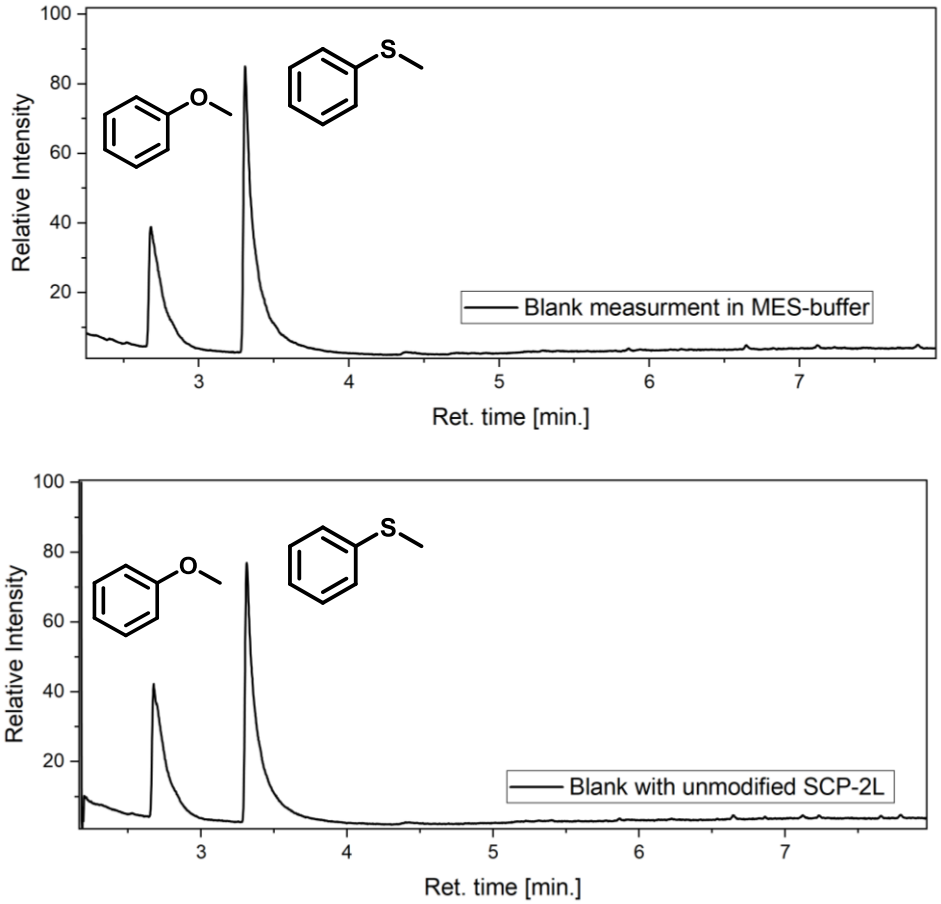

Figure 6.46: Blank measurements; Conditions: thioanisole 2 mM, MES buffer (MES 20 mM, 50 mM NaCl, 2% ACN) pH 6, blue light irradiation (460nm) at room temperature (up); Unmodified V83C 10 µM, thioanisole 2 mM, MES buffer (MES 20 mM, 50 mM NaCl, 2% ACN) pH 6, blue light irradiation (460-465 nm) at room temperature (down); anisole as reference.

Chiral HPLC Data

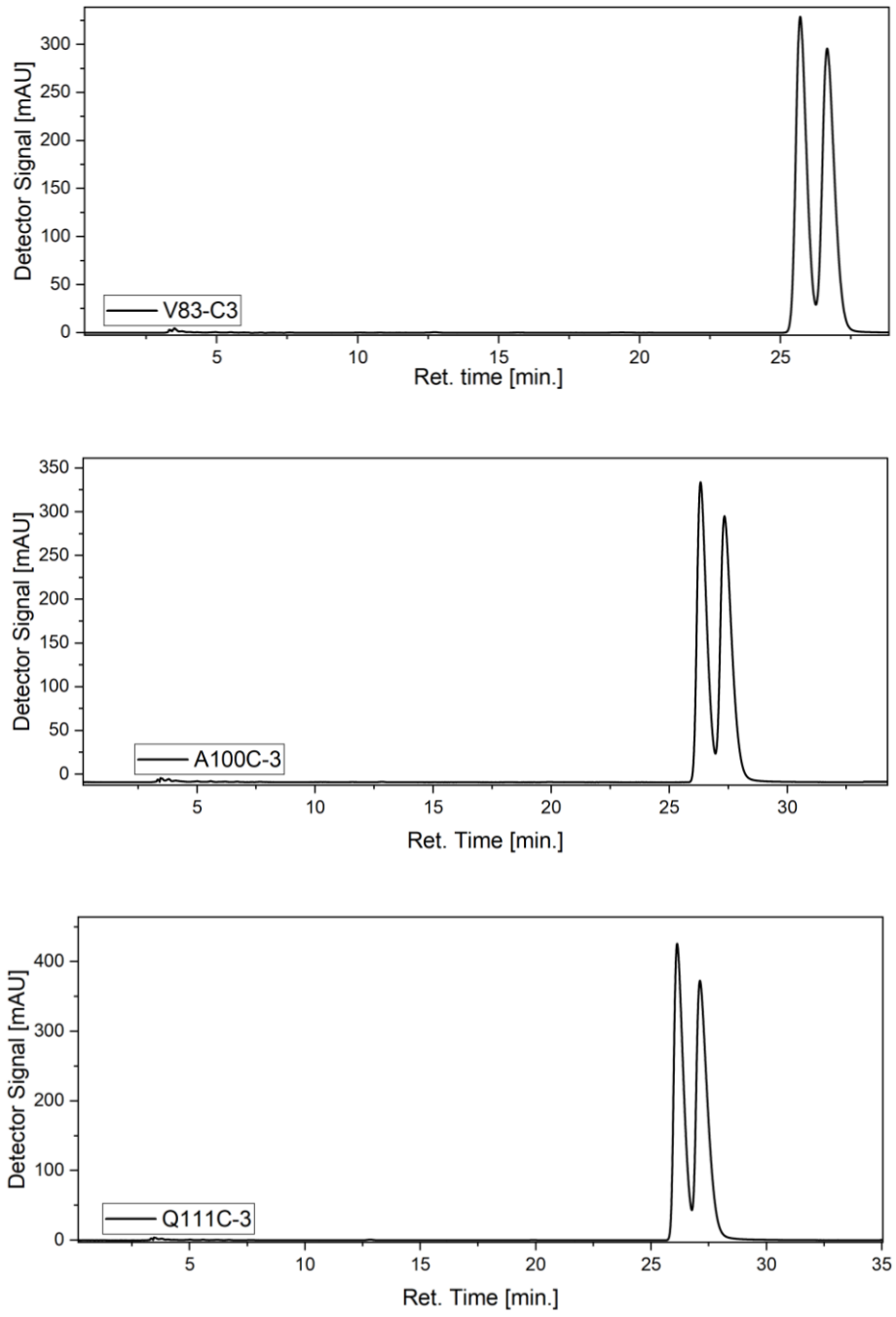

Figure 6.47: Chiral HPLC measurement of methyl phenyl sulfoxide separating both stereoisomers.

7 Summary and Outlook

In this thesis, metal-free benzothiadiazole-based photocatalysts were incorporated into various support materials to combine beneficial material properties with photocatalytic prowess. Creating new photocatalytic material and analyzing the effect of the support on the photocatalyst.

In the initial project, a vinyl-functionalized benzothiadiazole was copolymerized with three monomers: styrene, methyl methacrylate, and acrylonitrile. The project aimed to analyze the effect of different commoners on the efficiency of the photocatalytic moiety. Therefore, the photophysical properties and photocatalytic capabilities were analyzed. It was observed that the chosen comonomer affects the optical properties, including UV/Vis-absorbance, fluorescence lifetime, and quantum yield. Three reactions, including C-C couplings and hydroxylation of boronic acid, were performed to investigate the effect on the photocatalytic efficiency. Again, changes in the efficiency could be observed depending on the chosen copolymer, indicating that the comonomers have a more significant effect than expected.

In the second project, an acrylamide functionalized photocatalyst was copolymerized with *N,N*-dimethylacrylamide, and *N,N*'-methylenebis(acrylamide), creating a high transmittance hydrogel that readily swelled in water. The hydrogel allows for easy substrate diffusion and substrate-photocatalyst interaction, while the high transmittance value enables light penetration into the support material. The material was intended for application in wastewater purification, and four photocatalytic reactions were performed for pollutant remediation, including the reduction of toxic chromium (VI) and the photodegradation of glyphosate, a known herbicide. The benefits of the transmittance hydrogel were proven by performing a scaled-up 1 g photodegradation.

Lastly, in cooperation with the group of Amanda Jarvis at the University of Edinburgh, artificial photoenzymes were created. An iodoacetamide functionalized photocatalytic moiety was bioconjugated with three steroid carrier protein (SCP-2L) variants possessing non-native cysteine residues. The created artificial photoenzymes were used for the photocatalytic oxidation of an organic sulfide compound. The effect of photocatalytic moiety positioning within the protein scaffold was analyzed via fluorescence and kinetic measurements. Highlighting a significant difference in the performance of the artificial photoenzyme depending on the position. Further EPR measurements and long-term stability tests were performed, proofing the longevity of the artificial photoenzyme. The project is another step towards analyzing and profiting from the beneficial merging of protein scaffolds with photocatalysis.

In conclusion, in this thesis, single photocatalytic moieties based on π-extended benzothiadiazole were functionalized and incorporated into different macromolecular structures to investigate possible beneficial synergies and analyze the effect of the support. As a result, these materials highlight a promising alternative to conventional homogeneous or heterogeneous photocatalysts by combining advantageous material properties with the photocatalyst's capabilities.

8 References

1. Schultz, D. M.; Yoon, T. P. Solar synthesis: prospects in visible light photocatalysis. *Science* **2014,** *343*, 1239176.
2. Kopp, G.; Lean, J. L. A new, lower value of total solar irradiance: Evidence and climate significance. *Geophysical Research Letters* **2011,** *38*, L01706.
3. IEA *CO_2 Emissions in 2022*; IEA: Paris, 2023.
4. Coronado, J. M., A Historical Introduction to Photocatalysis. In *Design of Advanced Photocatalytic Materials for Energy and Environmental Applications*, Coronado, J. M.; Fresno, F.; Hernández-Alonso, M. D.; Portela, R., Eds. Springer London: London, 2013; pp 1-4.
5. Ciamician, G. The Photochemistry of the Future. *Science* **1912,** *36*, 385-394.
6. Ciamician, G.; Silber, P. Chemische Lichtwirkungen. *Ber. Dtsch. Chem. Ges.* **1901,** *34*, 2040-2046.
7. Fujishima, A.; Honda, K. Electrochemical Photolysis of Water at a Semiconductor Electrode. *Nature* **1972,** *238*, 37-38.
8. Nicewicz, D. A.; MacMillan, D. W. C. Merging Photoredox Catalysis with Organocatalysis: The Direct Asymmetric Alkylation of Aldehydes. *Science* **2008,** *322*, 77-80.
9. Prier, C. K.; Rankic, D. A.; MacMillan, D. W. Visible light photoredox catalysis with transition metal complexes: applications in organic synthesis. *Chem. Rev.* **2013,** *113*, 5322-63.
10. Gisbertz, S.; Pieber, B. Heterogeneous Photocatalysis in Organic Synthesis. *ChemPhotoChem* **2020,** *4*, 456-475.
11. Zhou, Q. Q.; Zou, Y. Q.; Lu, L. Q.; Xiao, W. J. Visible-Light-Induced Organic Photochemical Reactions through Energy-Transfer Pathways. *Angew. Chem. Int. Ed.* **2019,** *58*, 1586-1604.
12. Strieth-Kalthoff, F.; James, M. J.; Teders, M.; Pitzer, L.; Glorius, F. Energy transfer catalysis mediated by visible light: principles, applications, directions. *Chem. Soc. Rev.* **2018,** *47*, 7190-7202.
13. Shaw, M. H.; Twilton, J.; MacMillan, D. W. Photoredox Catalysis in Organic Chemistry. *J. Org. Chem.* **2016,** *81*, 6898-926.
14. Arias-Rotondo, D. M.; McCusker, J. K., An Overview of the Physical and Photophysical Properties of $[Ru(bpy)_3]^{2+}$. In *Visible Light Photocatalysis in Organic Chemistry*, Stephenson, C.; Yoon, T.; MacMillan, D. W., Eds. Wiley-VCH Verlag GmbH & Co: Weinheim, Germany, 2018; pp 1-24.
15. Burstall, F. H. 34. Optical activity dependent on co-ordinated bivalent ruthenium. *J. Chem. Soc.* **1936**, 173-175.
16. Hedstrand, D. M.; Kruizinga, W. H.; Kellogg, R. M. Light induced and dye accelerated reductions of phenacyl onium salts by 1,4-dihydropyridines. *Tetrahedron Lett.* **1978,** *19*, 1255-1258.
17. Van Bergen, T. J.; Hedstrand, D. M.; Kruizinga, W. H.; Kellogg, R. M. Chemistry of dihydropyridines. 9. Hydride transfer from 1,4-dihydropyridines to sp^3-hybridized carbon in sulfonium salts and activated halides. Studies with NAD(P)H models. *J. Org. Chem.* **1979,** *44*, 4953-4962.
18. Cano-Yelo, H.; Deronzier, A. Photocatalysis of the pschorr reaction by $Ru(bpy)_3^{2+}$. *J. Photochem.* **1987,** *37*, 315-321.
19. Ischay, M. A.; Anzovino, M. E.; Du, J.; Yoon, T. P. Efficient Visible Light Photocatalysis of [2+2] Enone Cycloadditions. *J. Am. Chem. Soc.* **2008,** *130*, 12886-12887.
20. Zou, Y. Q.; Chen, J. R.; Liu, X. P.; Lu, L. Q.; Davis, R. L.; Jorgensen, K. A.; Xiao, W. J. Highly efficient aerobic oxidative hydroxylation of arylboronic acids: photoredox catalysis using visible light. *Angew. Chem. Int. Ed.* **2012,** *51*, 784-8.
21. Jiang, M.; Yang, H.; Fu, H. Visible-Light Photoredox Borylation of Aryl Halides and Subsequent Aerobic Oxidative Hydroxylation. *Org. Lett.* **2016,** *18*, 5248-5251.

22. Liang, Z.; Lv, K.; Zhou, S.; Zhu, C.; Bao, X. Visible-light photocatalytic preparation of alkenyl thioethers from 1,2,3-thiadiazoles and Hantzsch esters: synthetic and mechanistic investigations. *Org. Chem. Front.* **2021,** *8*, 6499-6507.
23. Zhang, L.; Hu, X. Room temperature C(sp^2)-H oxidative chlorination via photoredox catalysis. *Chem. Sci.* **2017,** *8*, 7009-7013.
24. Shi, P.; Tu, Y.; Wang, C.; Ma, D.; Bolm, C. Visible Light-Promoted Synthesis of beta-Keto Sulfoximines from N-Tosyl-Protected Sulfoximidoyl Chlorides. *J. Org. Chem.* **2022,** *87*, 3817-3824.
25. Trieu, P.; Filkin, W. H.; Pinarci, A.; Tobias, E. M.; Madiu, R.; Dellosso, B.; Roldan, J.; Das, P.; Austin, B. E.; Moura-Letts, G. Synthesis of Isoxazolidines from Substituted Vinylnitrones and Conjugated Carbonyls via Visible-Light Photocatalysis. *ChemPhotoChem* **2022,** *7*.
26. Sutin, N.; Creutz, C. Light induced electron transfer reactions of metal complexes. *Pure Appl. Chem.* **1980,** *52*, 2717-2738.
27. Juris, A.; Balzani, V.; Barigelletti, F.; Campagna, S.; Belser, P.; von Zelewsky, A. Ru(II) polypyridine complexes: photophysics, photochemistry, eletrochemistry, and chemiluminescence. *Coord. Chem. Rev.* **1988,** *84*, 85-277.
28. Flamigni, L.; Barbieri, A.; Sabatini, C.; Ventura, B.; Barigelletti, F., Photochemistry and Photophysics of Coordination Compounds: Iridium. In *Photochemistry and Photophysics of Coordination Compounds II*, Balzani, V.; Campagna, S., Eds. Springer Berlin Heidelberg: Berlin, Heidelberg, 2007; pp 143-203.
29. Sutin, N.; Creutz, C., Properties and Reactivities of the Luminescent Excited States of Polypyridine Complexes of Ruthenium(II) and Osmium(II). In *Inorganic and Organometallic Photochemistry*, Wrighton, M. S., Ed. American Chemical Society: Washington, DC, 1978; Vol. 168, pp 1-27.
30. Damrauer, N. H.; Cerullo, G.; Yeh, A.; Boussie, T. R.; Shank, C. V.; McCusker, J. K. Femtosecond Dynamics of Excited-State Evolution in $[Ru(bpy)_3]^{2+}$. *Science* **1997,** *275*, 54-57.
31. Lin, C. T.; Boettcher, W.; Chou, M.; Creutz, C.; Sutin, N. Mechanism of the quenching of the emission of substituted polypyridineruthenium(II) complexes by iron(III), chromium(III), and europium(III) ions. *J. Am. Chem. Soc.* **1976,** *98*, 6536-6544.
32. Demas, J. N.; Diemente, D.; Harris, E. W. Oxygen quenching of charge-transfer excited states of ruthenium(II) complexes. Evidence for singlet oxygen production. *J. Am. Chem. Soc.* **1973,** *95*, 6864-6865.
33. Romero, N. A.; Nicewicz, D. A. Organic Photoredox Catalysis. *Chem. Rev.* **2016,** *116*, 10075-166.
34. Zeitler, K., Metal-Free Photo(redox) Catalysis. In *Visible Light Photocatalysis in Organic Chemistry*, Stephenson, C.; Yoon, T.; MacMillan, D. W., Eds. Wiley-VCH Verlag GmbH & Co: Weinheim, Germany, 2018; pp 159-232.
35. Singh, M.; Yadav, A. K.; Yadav, L. D. S.; Singh, R. K. P. Visible light photocatalysis with benzophenone for radical thiol-ene reactions. *Tetrahedron Lett.* **2017,** *58*, 2206-2208.
36. Dondi, D.; Protti, S.; Albini, A.; Carpio, S. M.; Fagnoni, M. Synthesis of γ-lactols, γ-lactones and 1,4-monoprotected succinaldehydes under moderately concentrated sunlight. *Green Chem.* **2009,** *11*, 1653-1659.
37. Luridiana, A.; Mazzarella, D.; Capaldo, L.; Rincón, J. A.; García-Losada, P.; Mateos, C.; Frederick, M. O.; Nuño, M.; Jan Buma, W.; Noël, T. The Merger of Benzophenone HAT Photocatalysis and Silyl Radical-Induced XAT Enables Both Nickel-Catalyzed Cross-Electrophile Coupling and 1,2-Dicarbofunctionalization of Olefins. *ACS Catal.* **2022,** *12*, 11216-11225.
38. Xiang, M.; Xin, Z. K.; Chen, B.; Tung, C. H.; Wu, L. Z. Exploring the Reducing Ability of Organic Dye (Acr(+)-Mes) for Fluorination and Oxidation of Benzylic C(sp(3))-H Bonds under Visible Light Irradiation. *Org. Lett.* **2017,** *19*, 3009-3012.

39. Tlili, A.; Lakhdar, S. Acridinium Salts and Cyanoarenes as Powerful Photocatalysts: Opportunities in Organic Synthesis. *Angew. Chem. Int. Ed.* **2021,** *60*, 19526-19549.
40. Ohkubo, K.; Mizushima, K.; Fukuzumi, S. Oxygenation and chlorination of aromatic hydrocarbons with hydrochloric acid photosensitized by 9-mesityl-10-methylacridinium under visible light irradiation. *Res. Chem. Intermed.* **2012,** *39*, 205-220.
41. Pitre, S. P.; McTiernan, C. D.; Ismaili, H.; Scaiano, J. C. Metal-Free Photocatalytic Radical Trifluoromethylation Utilizing Methylene Blue and Visible Light Irradiation. *ACS Catal.* **2014,** *4*, 2530-2535.
42. Pitre, S. P.; McTiernan, C. D.; Ismaili, H.; Scaiano, J. C. Mechanistic Insights and Kinetic Analysis for the Oxidative Hydroxylation of Arylboronic Acids by Visible Light Photoredox Catalysis: A Metal-Free Alternative. *J. Am. Chem. Soc.* **2013,** *135*, 13286-13289.
43. Jiang, H.; Mao, G.; Wu, H.; An, Q.; Zuo, M.; Guo, W.; Xu, C.; Sun, Z.; Chu, W. Synthesis of dibenzocycloketones by acyl radical cyclization from aromatic carboxylic acids using methylene blue as a photocatalyst. *Green Chem.* **2019,** *21*, 5368-5373.
44. Neckers, D. C.; Valdes-Aguilera, O. M., Photochemistry of the Xanthene Dyes. In *Advances in Photochemistry*, Volman, D. H.; Hammond, G. S.; Neckers, D. C., Eds. John Wiley & Sons, Inc.: New York, 1993; pp 315-394.
45. Sharma, S.; Sharma, A. Recent advances in photocatalytic manipulations of Rose Bengal in organic synthesis. *Org. Biomol. Chem.* **2019,** *17*, 4384-4405.
46. Vila, C.; Lau, J.; Rueping, M. Visible-light photoredox catalyzed synthesis of pyrroloisoquinolines via organocatalytic oxidation/[3 + 2] cycloaddition/oxidative aromatization reaction cascade with Rose Bengal. *Beilstein J. Org. Chem.* **2014,** *10*, 1233-8.
47. Kee, C. W.; Chan, K. M.; Wong, M. W.; Tan, C.-H. Selective Bromination of sp^3 C-H Bonds by Organophotoredox Catalysis. *Asian J. Org. Chem.* **2014,** *3*, 536-544.
48. Slyusareva, E. A.; Gerasimova, M. A. pH-Dependence of the Absorption and Fluorescent Properties of Fluorone Dyes in Aqueous Solutions. *Russian Physics Journal* **2014,** *56*, 1370-1377.
49. Majek, M.; Filace, F.; von Wangelin, A. J. On the mechanism of photocatalytic reactions with eosin Y. *Beilstein J. Org. Chem.* **2014,** *10*, 981-9.
50. Penzkofer, A.; Beidoun, A.; Daiber, M. Intersystem-Crossing and Excited-State Absorption in Eosin Y Solutions Determined by Picosecond Double Pulse Transient Absorption Measurements. *J. Lumin.* **1992,** *51*, 297-314.
51. Fleming, G. R.; Knight, A. W. E.; Morris, J. M.; Morrison, R. J. S.; Robinson, G. W. Picosecond fluorescence studies of xanthene dyes. *J. Am. Chem. Soc.* **1977,** *99*, 4306-4311.
52. Shen, T.; Zhao, Z.-G.; Yu, Q.; Xu, H.-J. Photosensitized reduction of benzil by heteroatom-containing anthracene dyes. *J. Photochem. Photobiol. A.* **1989,** *47*, 203-212.
53. Yoon, J.; Jung, Y. J.; Yoon, J. B.; Damodar, K.; Kim, H.; Shin, M.; Seo, M.; Cho, D. W.; Lee, J. T.; Lee, J. K. The heavy-atom effect on xanthene dyes for photopolymerization by visible light. *Polym. Chem.* **2019,** *10*, 5737-5742.
54. Zhang, X. F.; Zhang, I.; Liu, L. Photophysics of halogenated fluoresceins: involvement of both intramolecular electron transfer and heavy atom effect in the deactivation of excited states. *Photochem. Photobiol.* **2010,** *86*, 492-8.
55. Redmond, R. W.; Gamlin, J. N. A Compilation of Singlet Oxygen Yields from Biologically Relevant Molecules. *Photochem. Photobiol.* **1999,** *70*, 391-475.
56. Murasecco-Suardi, P.; Gassmann, E.; Braun, A. M.; Oliveros, E. Determination of the Quantum Yield of Intersystem Crossing of Rose Bengal. *Helv. Chim. Acta* **1987,** *70*, 1760-1773.

57. Liu, Q.; Li, Y. N.; Zhang, H. H.; Chen, B.; Tung, C. H.; Wu, L. Z. Reactivity and mechanistic insight into visible-light-induced aerobic cross-dehydrogenative coupling reaction by organophotocatalysts. *Chemistry* **2012,** *18*, 620-7.
58. Kasche, V.; Lindqvist, L. TRANSIENT SPECIES IN THE PHOTOCHEMISTRY OF EOSIN*. *Photochem. Photobiol.* **1965,** *4*, 923-933.
59. Wintgens, V.; Scaiano, J. C.; Linden, S. M.; Neckers, D. C. Transient phenomena in the laser flash photolysis of Rose Bengal C-2' ethyl ester C-6 sodium salt. *J. Org. Chem.* **1989,** *54*, 5242-5246.
60. Lambert, C. R.; Kochevar, I. E. Electron transfer quenching of the rose bengal triplet state. *Photochem. Photobiol.* **1997,** *66*, 15-25.
61. Hari, D. P.; Konig, B. Synthetic applications of eosin Y in photoredox catalysis. *Chem. Commun.* **2014,** *50*, 6688-99.
62. Marin, M. L.; Santos-Juanes, L.; Arques, A.; Amat, A. M.; Miranda, M. A. Organic photocatalysts for the oxidation of pollutants and model compounds. *Chem. Rev.* **2012,** *112*, 1710-50.
63. Latour, V.; Pigot, T.; Simon, M.; Cardy, H.; Lacombe, S. Photo-oxidation of di-n-butylsulfide by various electron transfer sensitizers in oxygenated acetonitrile. *Photochem. Photobiol. Sci.* **2005,** *4*, 221-9.
64. Rueping, M.; Zhu, S.; Koenigs, R. M. Photoredox catalyzed C-P bond forming reactions-visible light mediated oxidative phosphonylations of amines. *Chem. Commun.* **2011,** *47*, 8679-81.
65. Noble, A.; Anderson, J. C. Nitro-Mannich reaction. *Chem. Rev.* **2013,** *113*, 2887-939.
66. Pan, Y.; Kee, C. W.; Chen, L.; Tan, C.-H. Dehydrogenative coupling reactions catalysed by Rose Bengal using visible light irradiation. *Green Chem.* **2011,** *13*.
67. Neumann, M.; Zeitler, K. A cooperative hydrogen-bond-promoted organophotoredox catalysis strategy for highly diastereoselective, reductive enone cyclization. *Chemistry* **2013,** *19*, 6950-5.
68. Yang, X.-J.; Chen, B.; Zheng, L.-Q.; Wu, L.-Z.; Tung, C.-H. Highly efficient and selective photocatalytic hydrogenation of functionalized nitrobenzenes. *Green Chem.* **2014,** *16*, 1082-1086.
69. Hari, D. P.; Hering, T.; König, B. Visible Light Photocatalytic Synthesis of Benzothiophenes. *Org. Lett.* **2012,** *14*, 5334-5337.
70. Wang, L.; Huang, W.; Li, R.; Gehrig, D.; Blom, P. W.; Landfester, K.; Zhang, K. A. Structural Design Principle of Small-Molecule Organic Semiconductors for Metal-Free, Visible-Light-Promoted Photocatalysis. *Angew. Chem. Int. Ed.* **2016,** *55*, 9783-7.
71. Wang, L.; Rörich, I.; Ramanan, C.; Blom, P. W. M.; Huang, W.; Li, R.; Zhang, K. A. I. Electron donor-free photoredox catalysis via an electron transfer cascade by cooperative organic photocatalysts. *Catal. Sci. Technol.* **2018,** *8*, 3539-3547.
72. DaSilveira Neto, B. A.; Lopes, A. S. A.; Ebeling, G.; Gonçalves, R. S.; Costa, V. E. U.; Quina, F. H.; Dupont, J. Photophysical and electrochemical properties of π-extended molecular 2,1,3-benzothiadiazoles. *Tetrahedron* **2005,** *61*, 10975-10982.
73. Li, R.; Gehrig, D. W.; Ramanan, C.; Blom, P. W. M.; Kohl, F. F.; Wagner, M.; Landfester, K.; Zhang, K. A. I. Visible Light-Mediated Conversion of Alcohols to Bromides by a Benzothiadiazole-Containing Organic Photocatalyst. *Adv. Synth. Catal.* **2019,** *361*, 3852-3859.
74. Wang, L.; Byun, J.; Li, R.; Huang, W.; Zhang, K. A. I. Molecular Design of Donor-Acceptor-Type Organic Photocatalysts for Metal-free Aromatic C−C Bond Formations under Visible Light. *Adv. Synth. Catal.* **2018,** *360*, 4312-4318.
75. Wang, L.; Li, R.; Zhang, K. A. I. Atom Transfer Radical Polymerization (ATRP) Catalyzed by Visible Light-Absorbed Small Molecule Organic Semiconductors. *Macromol. Rapid Commun.* **2018,** *39*, e1800466.
76. Wang, J.; Zhou, S.; Li, B.; Liu, X.; Chen, H.; Wang, H. Improving the Photostability of $[Ru(bpy)_3]^{2+}$ by Embedment in Silica. *ChemPhotoChem* **2022,** *6*.

77. Herculano, L. S.; Malacarne, L. C.; Zanuto, V. S.; Lukasievicz, G. V. B.; Capeloto, O. A.; Astrath, N. G. C. Investigation of the Photobleaching Process of Eosin Y in Aqueous Solution by Thermal Lens Spectroscopy. *J. Phys. Chem. B.* **2013,** *117*, 1932-1937.
78. Demchenko, A. P. Photobleaching of organic fluorophores: quantitative characterization, mechanisms, protection. *Methods Appl. Fluoresc.* **2020,** *8*, 022001.
79. Savateev, A.; Antonietti, M. Heterogeneous Organocatalysis for Photoredox Chemistry. *ACS Catal.* **2018,** *8*, 9790-9808.
80. Salaneck, W. R.; Brédas, J. L. Electronic band structure of conjugated polymers. *Synth. Met.* **1994,** *67*, 15-22.
81. Peng, Y.-K.; Tsang, S. C. E. Facet-dependent photocatalysis of nanosize semiconductive metal oxides and progress of their characterization. *Nano Today* **2018,** *18*, 15-34.
82. Xiao, M.; Luo, B.; Wang, S.; Wang, L. Solar energy conversion on g-C_3N_4 photocatalyst: Light harvesting, charge separation, and surface kinetics. *J. Energy Chem.* **2018,** *27*, 1111-1123.
83. Peng, X.; Manna, L.; Yang, W.; Wickham, J.; Scher, E.; Kadavanich, A.; Alivisatos, A. P. Shape control of CdSe nanocrystals. *Nature* **2000,** *404*, 59-61.
84. Talapin, D. V.; Shevchenko, E. V.; Murray, C. B.; Kornowski, A.; Förster, S.; Weller, H. CdSe and CdSe/CdS Nanorod Solids. *J. Am. Chem. Soc.* **2004,** *126*, 12984-12988.
85. Hu, J.; Li, L.-s.; Yang, W.; Manna, L.; Wang, L.-w.; Alivisatos, A. P. Linearly Polarized Emission from Colloidal Semiconductor Quantum Rods. *Science* **2001,** *292*, 2060-2063.
86. Banerjee, T.; Lotsch, B. V. The wetter the better. *Nature Chemistry* **2018,** *10*, 1175-1177.
87. Cheng, H.; Xu, W. Recent advances in modified TiO_2 for photo-induced organic synthesis. *Org. Biomol. Chem.* **2019,** *17*, 9977-9989.
88. Hosseini-Sarvari, M.; Koohgard, M.; Firoozi, S.; Mohajeri, A.; Tavakolian, H. Alizarin red S–TiO_2-catalyzed cascade C(sp^3)–H to C(sp^2)–H bond formation/cyclization reactions toward tetrahydroquinoline derivatives under visible light irradiation. *New J. Chem.* **2018,** *42*, 6880-6888.
89. Ren, L.; Yang, M.-M.; Tung, C.-H.; Wu, L.-Z.; Cong, H. Visible-Light Photocatalysis Employing Dye-Sensitized Semiconductor: Selective Aerobic Oxidation of Benzyl Ethers. *ACS Catal.* **2017,** *7*, 8134-8138.
90. Riente, P.; Noël, T. Application of metal oxide semiconductors in light-driven organic transformations. *Catal. Sci. Technol.* **2019,** *9*, 5186-5232.
91. Buglioni, L.; Riente, P.; Palomares, E.; Pericàs, M. A. Visible-Light-Promoted Arylation Reactions Photocatalyzed by Bismuth(III) Oxide. *Eur. J. Org. Chem.* **2017,** *2017*, 6986-6990.
92. Fadeyi, O. O.; Mousseau, J. J.; Feng, Y.; Allais, C.; Nuhant, P.; Chen, M. Z.; Pierce, B.; Robinson, R. Visible-Light-Driven Photocatalytic Initiation of Radical Thiol-Ene Reactions Using Bismuth Oxide. *Org. Lett.* **2015,** *17*, 5756-9.
93. Jiang, H.-Y.; Liu, J.; Cheng, K.; Sun, W.; Lin, J. Enhanced Visible Light Photocatalysis of Bi_2O_3 upon Fluorination. *J. Phys. Chem. C* . **2013,** *117*, 20029-20036.
94. Enright, M. J.; Gilbert-Bass, K.; Sarsito, H.; Cossairt, B. M. Photolytic C–O Bond Cleavage with Quantum Dots. *Chem. Mater.* **2019,** *31*, 2677-2682.
95. Jiang, Y.; Wang, C.; Rogers, C. R.; Kodaimati, M. S.; Weiss, E. A. Regio- and diastereoselective intermolecular [2+2] cycloadditions photocatalysed by quantum dots. *Nat. Chem.* **2019,** *11*, 1034-1040.
96. Liu, C.; Chen, Z.; Su, C.; Zhao, X.; Gao, Q.; Ning, G. H.; Zhu, H.; Tang, W.; Leng, K.; Fu, W.; Tian, B.; Peng, X.; Li, J.; Xu, Q. H.; Zhou, W.; Loh, K. P. Controllable deuteration of halogenated compounds by photocatalytic D_2O splitting. *Nat. Commun.* **2018,** *9*, 80.

97. Pal, A.; Ghosh, I.; Sapra, S.; König, B. Quantum Dots in Visible-Light Photoredox Catalysis: Reductive Dehalogenations and C–H Arylation Reactions Using Aryl Bromides. *Chem. Mater.* **2017,** *29*, 5225-5231.
98. Wu, W.-B.; Wong, Y.-C.; Tan, Z.-K.; Wu, J. Photo-induced thiol coupling and C–H activation using nanocrystalline lead-halide perovskite catalysts. *Catal. Sci. Technol.* **2018,** *8*, 4257-4263.
99. Zhu, X.; Lin, Y.; San Martin, J.; Sun, Y.; Zhu, D.; Yan, Y. Lead halide perovskites for photocatalytic organic synthesis. *Nat. Commun.* **2019,** *10*, 2843.
100. Zhu, X.; Lin, Y.; Sun, Y.; Beard, M. C.; Yan, Y. Lead-Halide Perovskites for Photocatalytic alpha-Alkylation of Aldehydes. *J. Am. Chem. Soc.* **2019,** *141*, 733-738.
101. Li, H.; Yang, Y.; He, C.; Zeng, L.; Duan, C. Mixed-Ligand Metal–Organic Framework for Two-Photon Responsive Photocatalytic C–N and C–C Coupling Reactions. *ACS Catal.* **2018,** *9*, 422-430.
102. Xu, C.; Liu, H.; Li, D.; Su, J. H.; Jiang, H. L. Direct evidence of charge separation in a metal-organic framework: efficient and selective photocatalytic oxidative coupling of amines via charge and energy transfer. *Chem. Sci.* **2018,** *9*, 3152-3158.
103. Zhu, Y. Y.; Lan, G.; Fan, Y.; Veroneau, S. S.; Song, Y.; Micheroni, D.; Lin, W. Merging Photoredox and Organometallic Catalysts in a Metal-Organic Framework Significantly Boosts Photocatalytic Activities. *Angew. Chem. Int. Ed.* **2018,** *57*, 14090-14094.
104. Zeng, L.; Guo, X.; He, C.; Duan, C. Metal–Organic Frameworks: Versatile Materials for Heterogeneous Photocatalysis. *ACS Catal.* **2016,** *6*, 7935-7947.
105. Chen, Z.; Wang, J.; Hao, M.; Xie, Y.; Liu, X.; Yang, H.; Waterhouse, G. I. N.; Wang, X.; Ma, S. Tuning excited state electronic structure and charge transport in covalent organic frameworks for enhanced photocatalytic performance. *Nat. Commun.* **2023,** *14*, 1106.
106. Calik, M.; Auras, F.; Salonen, L. M.; Bader, K.; Grill, I.; Handloser, M.; Medina, D. D.; Dogru, M.; Löbermann, F.; Trauner, D.; Hartschuh, A.; Bein, T. Extraction of Photogenerated Electrons and Holes from a Covalent Organic Framework Integrated Heterojunction. *J. Am. Chem. Soc.* **2014,** *136*, 17802-17807.
107. Liu, Q.; Tang, Z.; Wu, M.; Zhou, Z. Design, preparation and application of conjugated microporous polymers. *Polym. Int.* **2014,** *63*, 381-392.
108. Wang, H.; Wang, H.; Wang, Z.; Tang, L.; Zeng, G.; Xu, P.; Chen, M.; Xiong, T.; Zhou, C.; Li, X.; Huang, D.; Zhu, Y.; Wang, Z.; Tang, J. Covalent organic framework photocatalysts: structures and applications. *Chem. Soc. Rev.* **2020,** *49*, 4135-4165.
109. Jiang, J. X.; Su, F.; Trewin, A.; Wood, C. D.; Campbell, N. L.; Niu, H.; Dickinson, C.; Ganin, A. Y.; Rosseinsky, M. J.; Khimyak, Y. Z.; Cooper, A. I. Conjugated microporous poly(aryleneethynylene) networks. *Angew. Chem. Int. Ed.* **2007,** *46*, 8574-8.
110. Monterde, C.; Pintado-Sierra, M.; Navarro, R.; Sanchez, F.; Iglesias, M. Effective Approach toward Conjugated Porous Organic Frameworks Based on Phenanthrene Building Blocks: Metal-Free Heterogeneous Photocatalysts. *ACS Appl. Mater. Interfaces* **2020,** *12*, 15108-15114.
111. Jiang, J.-X.; Li, Y.; Wu, X.; Xiao, J.; Adams, D. J.; Cooper, A. I. Conjugated Microporous Polymers with Rose Bengal Dye for Highly Efficient Heterogeneous Organo-Photocatalysis. *Macromolecules* **2013,** *46*, 8779-8783.
112. Wang, Z. J.; Ghasimi, S.; Landfester, K.; Zhang, K. A. I. Bandgap Engineering of Conjugated Nanoporous Poly-benzobisthiadiazolesviaCopolymerization for Enhanced Photocatalytic 1,2,3,4-Tetrahydroquinoline Synthesis under Visible Light. *Adv. Synth. Catal.* **2016,** *358*, 2576-2582.
113. Xu, Y.; Mao, N.; Feng, S.; Zhang, C.; Wang, F.; Chen, Y.; Zeng, J.; Jiang, J.-X. Perylene-Containing Conjugated Microporous Polymers for Photocatalytic Hydrogen Evolution. *Macromol. Chem. Phys.* **2017,** *218*.

114. Wang, Z.; Yang, X.; Yang, T.; Zhao, Y.; Wang, F.; Chen, Y.; Zeng, J. H.; Yan, C.; Huang, F.; Jiang, J.-X. Dibenzothiophene Dioxide Based Conjugated Microporous Polymers for Visible-Light-Driven Hydrogen Production. *ACS Catal.* **2018,** *8*, 8590-8596.
115. Sun, L.; Liang, Z.; Yu, J.; Xu, R. Luminescent microporous organic polymers containing the 1,3,5-tri(4-ethenylphenyl)benzene unit constructed by Heck coupling reaction. *Polym. Chem.* **2013,** *4*.
116. Wang, L.; Wan, Y.; Ding, Y.; Wu, S.; Zhang, Y.; Zhang, X.; Zhang, G.; Xiong, Y.; Wu, X.; Yang, J.; Xu, H. Conjugated Microporous Polymer Nanosheets for Overall Water Splitting Using Visible Light. *Adv. Mater.* **2017,** *29*.
117. Huang, X.; Wu, Z.; Zheng, H.; Dong, W.; Wang, G. A sustainable method toward melamine-based conjugated polymer semiconductors for efficient photocatalytic hydrogen production under visible light. *Green Chem.* **2018,** *20*, 664-670.
118. Schwab, M. G.; Hamburger, M.; Feng, X.; Shu, J.; Spiess, H. W.; Wang, X.; Antonietti, M.; Mullen, K. Photocatalytic hydrogen evolution through fully conjugated poly(azomethine) networks. *Chem. Commun.* **2010,** *46*, 8932-4.
119. Chen, Q.; Luo, M.; Hammershoj, P.; Zhou, D.; Han, Y.; Laursen, B. W.; Yan, C. G.; Han, B. H. Microporous polycarbazole with high specific surface area for gas storage and separation. *J. Am. Chem. Soc.* **2012,** *134*, 6084-7.
120. Sprick, R. S.; Jiang, J. X.; Bonillo, B.; Ren, S.; Ratvijitvech, T.; Guiglion, P.; Zwijnenburg, M. A.; Adams, D. J.; Cooper, A. I. Tunable organic photocatalysts for visible-light-driven hydrogen evolution. *J. Am. Chem. Soc.* **2015,** *137*, 3265-70.
121. Chen, Y.; Ji, G.; Guo, S.; Yu, B.; Zhao, Y.; Wu, Y.; Zhang, H.; Liu, Z.; Han, B.; Liu, Z. Visible-light-driven conversion of CO_2 from air to CO using an ionic liquid and a conjugated polymer. *Green Chem.* **2017,** *19*, 5777-5781.
122. Yu, X.; Yang, Z.; Qiu, B.; Guo, S.; Yang, P.; Yu, B.; Zhang, H.; Zhao, Y.; Yang, X.; Han, B.; Liu, Z. Eosin Y-Functionalized Conjugated Organic Polymers for Visible-Light-Driven CO_2 Reduction with H_2O to CO with High Efficiency. *Angew. Chem. Int. Ed.* **2019,** *58*, 632-636.
123. Wang, Z. J.; Garth, K.; Ghasimi, S.; Landfester, K.; Zhang, K. A. Conjugated Microporous Poly(Benzochalcogenadiazole)s for Photocatalytic Oxidative Coupling of Amines under Visible Light. *ChemSusChem* **2015,** *8*, 3459-64.
124. Su, C.; Tandiana, R.; Tian, B.; Sengupta, A.; Tang, W.; Su, J.; Loh, K. P. Visible-Light Photocatalysis of Aerobic Oxidation Reactions Using Carbazolic Conjugated Microporous Polymers. *ACS Catal.* **2016,** *6*, 3594-3599.
125. Liras, M.; Iglesias, M.; Sánchez, F. Conjugated Microporous Polymers Incorporating BODIPY Moieties as Light-Emitting Materials and Recyclable Visible-Light Photocatalysts. *Macromolecules* **2016,** *49*, 1666-1673.
126. Wang, Z. J.; Ghasimi, S.; Landfester, K.; Zhang, K. A. Highly porous conjugated polymers for selective oxidation of organic sulfides under visible light. *Chem. Commun.* **2014,** *50*, 8177-80.
127. Luo, J.; Zhang, X.; Zhang, J. Carbazolic Porous Organic Framework as an Efficient, Metal-Free Visible-Light Photocatalyst for Organic Synthesis. *ACS Catal.* **2015,** *5*, 2250-2254.
128. Zhi, Y.; Ma, S.; Xia, H.; Zhang, Y.; Shi, Z.; Mu, Y.; Liu, X. Construction of donor-acceptor type conjugated microporous polymers: A fascinating strategy for the development of efficient heterogeneous photocatalysts in organic synthesis. *Appl. Catal. B: Environ.* **2019,** *244*, 36-44.
129. Wang, Z. J.; Ghasimi, S.; Landfester, K.; Zhang, K. A. I. A conjugated porous poly-benzobisthiadiazole network for a visible light-driven photoredox reaction. *J. Mater. Chem. A* **2014,** *2*, 18720-18724.

130. Ayed, C.; Caire da Silva, L.; Wang, D.; Zhang, K. A. I. Designing conjugated microporous polymers for visible light-promoted photocatalytic carbon–carbon double bond cleavage in aqueous medium. *J. Mater. Chem. A* **2018,** *6*, 22145-22151.
131. Huang, W.; Ma, B. C.; Wang, D.; Wang, Z. J.; Li, R.; Wang, L.; Landfester, K.; Zhang, K. A. I. A fixed-bed photoreactor using conjugated nanoporous polymer-coated glass fibers for visible light-promoted continuous photoredox reactions. *J. Mater. Chem. A* **2017,** *5*, 3792-3797.
132. Ghasimi, S.; Bretschneider, S. A.; Huang, W.; Landfester, K.; Zhang, K. A. I. A Conjugated Microporous Polymer for Palladium-Free, Visible Light-Promoted Photocatalytic Stille-Type Coupling Reactions. *Adv. Sci.* **2017,** *4*, 1700101.
133. Zhang, W.; Tang, J.; Yu, W.; Huang, Q.; Fu, Y.; Kuang, G.; Pan, C.; Yu, G. Visible Light-Driven C-3 Functionalization of Indoles over Conjugated Microporous Polymers. *ACS Catal.* **2018,** *8*, 8084-8091.
134. Ghosh, S.; Kouame, N. A.; Ramos, L.; Remita, S.; Dazzi, A.; Deniset-Besseau, A.; Beaunier, P.; Goubard, F.; Aubert, P. H.; Remita, H. Conducting polymer nanostructures for photocatalysis under visible light. *Nat. Mater.* **2015,** *14*, 505-11.
135. Wang, J.; Yang, H.; Jiang, L.; Liu, S.; Hao, Z.; Cheng, J.; Ouyang, G. Highly efficient removal of organic pollutants by ultrahigh-surface-area-ethynylbenzene-based conjugated microporous polymers via adsorption–photocatalysis synergy. *Catal. Sci. Technol.* **2018,** *8*, 5024-5033.
136. Li, R.; Ma, B. C.; Huang, W.; Wang, L.; Wang, D.; Lu, H.; Landfester, K.; Zhang, K. A. I. Photocatalytic Regioselective and Stereoselective [2 + 2] Cycloaddition of Styrene Derivatives Using a Heterogeneous Organic Photocatalyst. *ACS Catal.* **2017,** *7*, 3097-3101.
137. Diercks, C. S.; Yaghi, O. M. The atom, the molecule, and the covalent organic framework. *Science* **2017,** *355*.
138. Feng, X.; Ding, X.; Jiang, D. Covalent organic frameworks. *Chem. Soc. Rev.* **2012,** *41*, 6010-22.
139. Côté, A. P.; Benin, A. I.; Ockwig, N. W.; O'Keeffe, M.; Matzger, A. J.; Yaghi, O. M. Porous, Crystalline, Covalent Organic Frameworks. *Science* **2005,** *310*, 1166-1170.
140. Blanchard, P.; Raimundo, J. M.; Roncali, J. New synthetic strategies towards conjugated NLO-phores and fluorophores. *Synth. Met.* **2001,** *119*, 527-528.
141. Zhi, Y.; Li, Z.; Feng, X.; Xia, H.; Zhang, Y.; Shi, Z.; Mu, Y.; Liu, X. Covalent organic frameworks as metal-free heterogeneous photocatalysts for organic transformations. *J. Mater. Chem. A* **2017,** *5*, 22933-22938.
142. Li, Z.; Feng, X.; Zou, Y.; Zhang, Y.; Xia, H.; Liu, X.; Mu, Y. A 2D azine-linked covalent organic framework for gas storage applications. *Chem. Commun.* **2014,** *50*, 13825-8.
143. Vyas, V. S.; Haase, F.; Stegbauer, L.; Savasci, G.; Podjaski, F.; Ochsenfeld, C.; Lotsch, B. V. A tunable azine covalent organic framework platform for visible light-induced hydrogen generation. *Nat. Commun.* **2015,** *6*, 8508.
144. Kailasam, K.; Mesch, M. B.; Möhlmann, L.; Baar, M.; Blechert, S.; Schwarze, M.; Schröder, M.; Schomäcker, R.; Senker, J.; Thomas, A. Donor-Acceptor-Type Heptazine-Based Polymer Networks for Photocatalytic Hydrogen Evolution. *Energy Technology* **2016,** *4*, 744-750.
145. Huang, N.; Zhai, L.; Coupry, D. E.; Addicoat, M. A.; Okushita, K.; Nishimura, K.; Heine, T.; Jiang, D. Multiple-component covalent organic frameworks. *Nat. Commun.* **2016,** *7*, 12325.
146. Dienstmaier, J. F.; Medina, D. D.; Dogru, M.; Knochel, P.; Bein, T.; Heckl, W. M.; Lackinger, M. Isoreticular Two-Dimensional Covalent Organic Frameworks Synthesized by On-Surface Condensation of Diboronic Acids. *ACS Nano* **2012,** *6*, 7234-7242.
147. Nagai, A.; Chen, X.; Feng, X.; Ding, X.; Guo, Z.; Jiang, D. A squaraine-linked mesoporous covalent organic framework. *Angew. Chem. Int. Ed.* **2013,** *52*, 3770-4.

148. Chen, R.; Shi, J. L.; Ma, Y.; Lin, G.; Lang, X.; Wang, C. Designed Synthesis of a 2D Porphyrin-Based sp^2 Carbon-Conjugated Covalent Organic Framework for Heterogeneous Photocatalysis. *Angew. Chem. Int. Ed.* **2019,** *58*, 6430-6434.
149. Bi, S.; Yang, C.; Zhang, W.; Xu, J.; Liu, L.; Wu, D.; Wang, X.; Han, Y.; Liang, Q.; Zhang, F. Two-dimensional semiconducting covalent organic frameworks via condensation at arylmethyl carbon atoms. *Nat. Commun.* **2019,** *10*, 2467.
150. Wei, P. F.; Qi, M. Z.; Wang, Z. P.; Ding, S. Y.; Yu, W.; Liu, Q.; Wang, L. K.; Wang, H. Z.; An, W. K.; Wang, W. Benzoxazole-Linked Ultrastable Covalent Organic Frameworks for Photocatalysis. *J. Am. Chem. Soc.* **2018,** *140*, 4623-4631.
151. Mendoza-Cortes, J. L.; Pascal, T. A.; Goddard, W. A., 3rd Design of covalent organic frameworks for methane storage. *J. Phys. Chem. A* **2011,** *115*, 13852-7.
152. Luo, B.; Liu, G.; Wang, L. Recent advances in 2D materials for photocatalysis. *Nanoscale* **2016,** *8*, 6904-20.
153. Liu, X.; Pang, H.; Liu, X.; Li, Q.; Zhang, N.; Mao, L.; Qiu, M.; Hu, B.; Yang, H.; Wang, X. Orderly Porous Covalent Organic Frameworks-based Materials: Superior Adsorbents for Pollutants Removal from Aqueous Solutions. *Innovation* **2021,** *2*, 100076.
154. Li, W.-T.; Zhuang, Y.-T.; Wang, J.-Y.; Yang, T.; Yu, Y.-L.; Chen, M.-L.; Wang, J.-H. A Three-Dimensional Porous Organic Framework for Highly Selective Capture of Mercury and Copper Ions. *ACS Appl. Polym. Mater.* **2019,** *1*, 2797-2806.
155. Lan, J.; Cao, D.; Wang, W. High uptakes of methane in Li-doped 3D covalent organic frameworks. *Langmuir* **2010,** *26*, 220-6.
156. Feng, X.; Liu, L.; Honsho, Y.; Saeki, A.; Seki, S.; Irle, S.; Dong, Y.; Nagai, A.; Jiang, D. High-rate charge-carrier transport in porphyrin covalent organic frameworks: switching from hole to electron to ambipolar conduction. *Angew. Chem. Int. Ed.* **2012,** *51*, 2618-22.
157. Chen, W.; Yang, Z.; Xie, Z.; Li, Y.; Yu, X.; Lu, F.; Chen, L. Benzothiadiazole functionalized D–A type covalent organic frameworks for effective photocatalytic reduction of aqueous chromium(vi). *J. Mater. Chem. A* **2019,** *7*, 998-1004.
158. Lv, H.; Zhao, X.; Niu, H.; He, S.; Tang, Z.; Wu, F.; Giesy, J. P. Ball milling synthesis of covalent organic framework as a highly active photocatalyst for degradation of organic contaminants. *J. Hazard. Mater.* **2019,** *369*, 494-502.
159. Liu, R.; Tan, K. T.; Gong, Y.; Chen, Y.; Li, Z.; Xie, S.; He, T.; Lu, Z.; Yang, H.; Jiang, D. Covalent organic frameworks: an ideal platform for designing ordered materials and advanced applications. *Chem. Soc. Rev.* **2021,** *50*, 120-242.
160. Lin, S.; Diercks, C. S.; Zhang, Y.-B.; Kornienko, N.; Nichols, E. M.; Zhao, Y.; Paris, A. R.; Kim, D.; Yang, P.; Yaghi, O. M.; Chang, C. J. Covalent organic frameworks comprising cobalt porphyrins for catalytic CO_2 reduction in water. *Science* **2015,** *349*, 1208-1213.
161. Stegbauer, L.; Schwinghammer, K.; Lotsch, B. V. A hydrazone-based covalent organic framework for photocatalytic hydrogen production. *Chem. Sci.* **2014,** *5*, 2789-2793.
162. Kuhn, P.; Antonietti, M.; Thomas, A. Porous, covalent triazine-based frameworks prepared by ionothermal synthesis. *Angew. Chem. Int. Ed.* **2008,** *47*, 3450-3.
163. Wang, K.; Yang, L. M.; Wang, X.; Guo, L.; Cheng, G.; Zhang, C.; Jin, S.; Tan, B.; Cooper, A. Covalent Triazine Frameworks via a Low-Temperature Polycondensation Approach. *Angew. Chem. Int. Ed.* **2017,** *56*, 14149-14153.
164. Liu, M.; Guo, L.; Jin, S.; Tan, B. Covalent triazine frameworks: synthesis and applications. *J. Mater. Chem. A* **2019,** *7*, 5153-5172.

165. Ren, S.; Bojdys, M. J.; Dawson, R.; Laybourn, A.; Khimyak, Y. Z.; Adams, D. J.; Cooper, A. I. Porous, fluorescent, covalent triazine-based frameworks via room-temperature and microwave-assisted synthesis. *Adv. Mater.* **2012,** *24*, 2357-61.
166. Troschke, E.; Gratz, S.; Lubken, T.; Borchardt, L. Mechanochemical Friedel-Crafts Alkylation-A Sustainable Pathway Towards Porous Organic Polymers. *Angew. Chem. Int. Ed.* **2017,** *56*, 6859-6863.
167. Guo, L.; Niu, Y.; Razzaque, S.; Tan, B.; Jin, S. Design of D–A1–A2 Covalent Triazine Frameworks via Copolymerization for Photocatalytic Hydrogen Evolution. *ACS Catal.* **2019,** *9*, 9438-9445.
168. Meier, C. B.; Clowes, R.; Berardo, E.; Jelfs, K. E.; Zwijnenburg, M. A.; Sprick, R. S.; Cooper, A. I. Structurally Diverse Covalent Triazine-Based Framework Materials for Photocatalytic Hydrogen Evolution from Water. *Chem. Mater.* **2019,** *31*, 8830-8838.
169. Schwinghammer, K.; Hug, S.; Mesch, M. B.; Senker, J.; Lotsch, B. V. Phenyl-triazine oligomers for light-driven hydrogen evolution. *Energy Environ. Sci.* **2015,** *8*, 3345-3353.
170. Lan, Z. A.; Fang, Y.; Zhang, Y.; Wang, X. Photocatalytic Oxygen Evolution from Functional Triazine-Based Polymers with Tunable Band Structures. *Angew. Chem. Int. Ed.* **2018,** *57*, 470-474.
171. Huang, W.; He, Q.; Hu, Y.; Li, Y. Molecular Heterostructures of Covalent Triazine Frameworks for Enhanced Photocatalytic Hydrogen Production. *Angew. Chem. Int. Ed.* **2019,** *58*, 8676-8680.
172. Gu, S.; Guo, J.; Huang, Q.; He, J.; Fu, Y.; Kuang, G.; Pan, C.; Yu, G. 1,3,5-Triazine-Based Microporous Polymers with Tunable Porosities for CO_2 Capture and Fluorescent Sensing. *Macromolecules* **2017,** *50*, 8512-8520.
173. Roeser, J.; Kailasam, K.; Thomas, A. Covalent triazine frameworks as heterogeneous catalysts for the synthesis of cyclic and linear carbonates from carbon dioxide and epoxides. *ChemSusChem* **2012,** *5*, 1793-9.
174. Bloh, J. Z. Intensification of Heterogeneous Photocatalytic Reactions Without Efficiency Losses: The Importance of Surface Catalysis. *Catal. Lett.* **2021,** *151*, 3105-3113.
175. Huang, W.; Ma, B. C.; Lu, H.; Li, R.; Wang, L.; Landfester, K.; Zhang, K. A. I. Visible-Light-Promoted Selective Oxidation of Alcohols Using a Covalent Triazine Framework. *ACS Catal.* **2017,** *7*, 5438-5442.
176. Wang, N.; Cheng, G.; Guo, L.; Tan, B.; Jin, S. Hollow Covalent Triazine Frameworks with Variable Shell Thickness and Morphology. *Adv. Funct. Mater.* **2019,** *29*.
177. Huang, W.; Wang, Z. J.; Ma, B. C.; Ghasimi, S.; Gehrig, D.; Laquai, F.; Landfester, K.; Zhang, K. A. I. Hollow nanoporous covalent triazine frameworks via acid vapor-assisted solid phase synthesis for enhanced visible light photoactivity. *J. Mater. Chem. A* **2016,** *4*, 7555-7559.
178. Huang, W.; Huber, N.; Jiang, S.; Landfester, K.; Zhang, K. A. I. Covalent Triazine Framework Nanoparticles via Size-Controllable Confinement Synthesis for Enhanced Visible-Light Photoredox Catalysis. *Angew. Chem. Int. Ed.* **2020,** *59*, 18368-18373.
179. Yadav, R. K.; Kumar, A.; Park, N.-J.; Kong, K.-J.; Baeg, J.-O. A highly efficient covalent organic framework film photocatalyst for selective solar fuel production from CO_2. *J. Mater. Chem. A* **2016,** *4*, 9413-9418.
180. Smith, B. J.; Parent, L. R.; Overholts, A. C.; Beaucage, P. A.; Bisbey, R. P.; Chavez, A. D.; Hwang, N.; Park, C.; Evans, A. M.; Gianneschi, N. C.; Dichtel, W. R. Colloidal Covalent Organic Frameworks. *ACS Cent. Sci.* **2017,** *3*, 58-65.
181. Yang, C. X.; Liu, C.; Cao, Y. M.; Yan, X. P. Facile room-temperature solution-phase synthesis of a spherical covalent organic framework for high-resolution chromatographic separation. *Chem. Commun.* **2015,** *51*, 12254-7.
182. Pachfule, P.; Kandmabeth, S.; Mallick, A.; Banerjee, R. Hollow tubular porous covalent organic framework (COF) nanostructures. *Chem. Commun.* **2015,** *51*, 11717-20.

183. Huang, W.; Jiang, Y.; Li, X.; Li, X.; Wang, J.; Wu, Q.; Liu, X. Solvothermal synthesis of microporous, crystalline covalent organic framework nanofibers and their colorimetric nanohybrid structures. *ACS Appl. Mater. Interfaces* **2013,** *5*, 8845-9.
184. Kim, S.; Landfester, K.; Ferguson, C. T. J. Hairy Conjugated Microporous Polymer Nanoparticles Facilitate Heterogeneous Photoredox Catalysis with Solvent-Specific Dispersibility. *ACS Nano* **2022,** *16*, 17041-17048.
185. Ferguson, C. T. J.; Zhang, K. A. I. Classical Polymers as Highly Tunable and Designable Heterogeneous Photocatalysts. *ACS Catal.* **2021,** *11*, 9547-9560.
186. Heuer, J.; Ferguson, C. T. J. Photocatalytic polymer nanomaterials for the production of high value compounds. *Nanoscale* **2022,** *14*, 1646-1652.
187. Zhang, K.; Kopetzki, D.; Seeberger, P. H.; Antonietti, M.; Vilela, F. Surface area control and photocatalytic activity of conjugated microporous poly(benzothiadiazole) networks. *Angew. Chem. Int. Ed.* **2013,** *52*, 1432-6.
188. Petrizza, L.; Le Bechec, M.; Decompte, E.; El Hadri, H.; Lacombe, S.; Save, M. Tuning photosensitized singlet oxygen production from microgels synthesized by polymerization in aqueous dispersed media. *Polym. Chem.* **2019,** *10*, 3170-3179.
189. Ferguson, C. T. J.; Huber, N.; Kuckhoff, T.; Zhang, K. A. I.; Landfester, K. Dispersible porous classical polymer photocatalysts for visible light-mediated production of pharmaceutically relevant compounds in multiple solvents. *J. Mater. Chem. A* **2020,** *8*, 1072-1076.
190. Ribeiro, S.; Serra, A. C.; A. Rocha Gonsalves, A. M. d. Efficient Solar Photooxygenation with Supported Porphyrins as Catalysts. *ChemCatChem* **2013,** *5*, 134-137.
191. Ballestri, M.; Caruso, E.; Guerrini, A.; Ferroni, C.; Banfi, S.; Gariboldi, M.; Monti, E.; Sotgiu, G.; Varchi, G. Core–shell poly-methyl methacrylate nanoparticles covalently functionalized with a non-symmetric porphyrin for anticancer photodynamic therapy. *J. Photochem. Photobiol. B, Biol.* **2018,** *186*, 169-177.
192. Yoo, W.-J.; Kobayashi, S. Efficient visible light-mediated cross-dehydrogenative coupling reactions of tertiary amines catalyzed by a polymer-immobilized iridium-based photocatalyst. *Green Chem.* **2014,** *16*, 2438-2442.
193. Schaap, A. P.; Thayer, A. L.; Blossey, E. C.; Neckers, D. C. Polymer-based sensitizers for photooxidations. II. *J. Am. Chem. Soc.* **1975,** *97*, 3741-3745.
194. Tobin, J. M.; McCabe, T. J. D.; Prentice, A. W.; Holzer, S.; Lloyd, G. O.; Paterson, M. J.; Arrighi, V.; Cormack, P. A. G.; Vilela, F. Polymer-Supported Photosensitizers for Oxidative Organic Transformations in Flow and under Visible Light Irradiation. *ACS Catal.* **2017,** *7*, 4602-4612.
195. Shiraishi, Y.; Kimata, Y.; Koizumi, H.; Hirai, T. Temperature-Controlled Photooxygenation with Polymer Nanocapsules Encapsulating an Organic Photosensitizer. *Langmuir* **2008,** *24*, 9832-9836.
196. Guerra, J.; Cantillo, D.; Kappe, C. O. Visible-light photoredox catalysis using a macromolecular ruthenium complex: reactivity and recovery by size-exclusion nanofiltration in continuous flow. *Catal. Sci. Technol.* **2016,** *6*, 4695-4699.
197. Chavan, S. A.; Maes, W.; Gevers, L. E.; Wahlen, J.; Vankelecom, I. F.; Jacobs, P. A.; Dehaen, W.; De Vos, D. E. Porphyrin-functionalized dendrimers: synthesis and application as recyclable photocatalysts in a nanofiltration membrane reactor. *Chem. Eur. J.* **2005,** *11*, 6754-62.
198. Shimakoshi, H.; Nishi, M.; Tanaka, A.; Chikama, K.; Hisaeda, Y. Photocatalytic function of a polymer-supported B12 complex with a ruthenium trisbipyridine photosensitizer. *Chem. Commun.* **2011,** *47*, 6548-50.
199. Zhang, W.; Shimakoshi, H.; Houfuku, N.; Song, X. M.; Hisaeda, Y. A polymerized ionic liquid-supported B12 catalyst with a ruthenium trisbipyridine photosensitizer for photocatalytic dechlorination in ionic liquids. *Dalton Trans* **2014,** *43*, 13972-8.

200. Widawski, G.; Rawiso, M.; François, B. Self-organized honeycomb morphology of star-polymer polystyrene films. *Nature* **1994,** *369*, 387-389.
201. Boussiron, C.; Le Bechec, M.; Petrizza, L.; Sabalot, J.; Lacombe, S.; Save, M. Synthesis of Film-Forming Photoactive Latex Particles by Emulsion Polymerization-Induced Self-Assembly to Produce Singlet Oxygen. *Macromol. Rapid Commun.* **2019,** *40*, e1800329.
202. Ibrahimova, V.; Denisov, S. A.; Vanvarenberg, K.; Verwilst, P.; Preat, V.; Guigner, J. M.; McClenaghan, N. D.; Lecommandoux, S.; Fustin, C. A. Photosensitizer localization in amphiphilic block copolymers controls photodynamic therapy efficacy. *Nanoscale* **2017,** *9*, 11180-11186.
203. Huber, N.; Li, R.; Ferguson, C. T. J.; Gehrig, D. W.; Ramanan, C.; Blom, P. W. M.; Landfester, K.; Zhang, K. A. I. A PMMA-based heterogeneous photocatalyst for visible light-promoted [4 + 2] cycloaddition. *Catal. Sci. Technol.* **2020,** *10*, 2092-2099.
204. Zhi, P.; Xi, Z.-W.; Wang, D.-Y.; Wang, W.; Liang, X.-Z.; Tao, F.-F.; Shen, R.-P.; Shen, Y.-M. Vilsmeier–Haack reagent mediated synthetic transformations with an immobilized iridium complex photoredox catalyst. *New J. Chem.* **2019,** *43*, 709-717.
205. Peng, F.; Zhi, P.; Ji, H.; Zhao, H.; Kong, F.-Y.; Liang, X.-Z.; Shen, Y.-M. Visible light mediated cyclization of tertiary anilines with maleimides using a supported iridium complex catalyst. *RSC Adv.* **2017,** *7*, 19948-19953.
206. Li, W.; Li, L.; Cui, G.; Bai, Y.; Xiao, X.; Li, Y.; Yan, L. HIPE Polymerization Materials Functionalized with Iodic-BODIPY on the Surface as Porous Heterogeneous Visible-Light Photocatalysts. *Chem. Asian J.* **2017,** *12*, 392-396.
207. Li, X.; Li, Y.; Huang, Y.; Zhang, T.; Liu, Y.; Yang, B.; He, C.; Zhou, X.; Zhang, J. Organic sponge photocatalysis. *Green Chem.* **2017,** *19*, 2925-2930.
208. Ferguson, C. T. J.; Huber, N.; Landfester, K.; Zhang, K. A. I. Dual-Responsive Photocatalytic Polymer Nanogels. *Angew. Chem. Int. Ed.* **2019,** *58*, 10567-10571.
209. Li, R.; Heuer, J.; Kuckhoff, T.; Landfester, K.; Ferguson, C. pH-triggered Recovery of Organic Polymer Photocatalytic Particles for the Production of High Value Compounds and Enhanced Recyclability. *Angew. Chem. Int. Ed.* **2023**, e202217652.
210. Lü, W.; Sun, C.; Lu, Q.; Li, N.; Wu, D.; Yao, Y.; Chen, W. Synthesis and photoactivity of pH-responsive amphiphilic block polymer photosensitizer bonded zinc phthalocyanine. *Sci. China Chem.* **2012,** *55*, 1108-1114.
211. Li, R.; Landfester, K.; Ferguson, C. T. J. Temperature- and pH-Responsive Polymeric Photocatalysts for Enhanced Control and Recovery. *Angew. Chem. Int. Ed.* **2022,** *61*, e202211132.
212. Gao, Z.; Liang, J.; Tao, X.; Cui, Y.; Satoh, T.; Kakuchi, T.; Duan, Q. Synthesis of star-shaped poly(N-isopropylacrylamide) via atom transfer radical polymerization and its photocatalytic oxidation of Rhodamine B. *Macromol. Res.* **2012,** *20*, 508-514.
213. Qiu, N.; Li, Y.; Han, S.; Cui, G.; Satoh, T.; Kakuchi, T.; Duan, Q. Synthesis of star poly(N-isopropylacrylamide) with end-group of zinc-porphyrin via ATRP and its photocatalytic activity under visible light. *J. Photochem. Photobiol. A.* **2014,** *283*, 38-44.
214. Ruan, Y.; Gao, B.; Lv, S.; Duan, Q. The synthesis of star-shaped poly(N-isopropylacrylamide) with two zinc porphyrins as the core and end groups via ATRP and "CLICK" chemistry and a photocatalytic performance study. *New J. Chem.* **2020,** *44*, 2781-2787.
215. Zuo, Q.; Feng, K.; Zhong, J.; Mai, Y.; Zhou, Y. Single-Metal-Atom Polymeric Unimolecular Micelles for Switchable Photocatalytic H_2 Evolution. *CCS Chemistry* **2021,** *3*, 1963-1971.
216. Priyadarshani, N.; Liang, Y.; Suriboot, J.; Bazzi, H. S.; Bergbreiter, D. E. Recoverable Reusable Polyisobutylene (PIB)-Bound Ruthenium Bipyridine ($Ru(PIB\text{-}bpy)_3Cl_2$) Photoredox Polymerization Catalysts. *ACS Macro Lett.* **2013,** *2*, 571-574.

217. Rackl, D.; Kreitmeier, P.; Reiser, O. Synthesis of a polyisobutylene-tagged fac-Ir(ppy)$_3$ complex and its application as recyclable visible-light photocatalyst in a continuous flow process. *Green Chem.* **2016,** *18*, 214-219.
218. Pessoni, L.; Lacombe, S.; Billon, L.; Brown, R.; Save, M. Photoactive, porous honeycomb films prepared from Rose Bengal-grafted polystyrene. *Langmuir* **2013,** *29*, 10264-71.
219. Boussiron, C.; Le Bechec, M.; Sabalot, J.; Lacombe, S.; Save, M. Photoactive rose bengal-based latex via RAFT emulsion polymerization-induced self-assembly. *Polym. Chem.* **2021,** *12*, 134-147.
220. Korpusik, A. B.; Tan, Y.; Garrison, J. B.; Tan, W.; Sumerlin, B. S. Aptamer-Conjugated Micelles for Targeted Photodynamic Therapy Via Photoinitiated Polymerization-Induced Self-Assembly. *Macromolecules* **2021,** *54*, 7354-7363.
221. Heuer, J.; Kuckhoff, T.; Li, R.; Landfester, K.; Ferguson, C. T. J. Tunable Photocatalytic Selectivity by Altering the Active Center Microenvironment of an Organic Polymer Photocatalyst. *ACS Appl. Mater. Interfaces* **2023,** *15*, 2891-2900.
222. Radjagobalou, R.; Blanco, J.-F.; Petrizza, L.; Le Bechec, M.; Dechy-Cabaret, O.; Lacombe, S.; Save, M.; Loubiere, K. Efficient Photooxygenation Process of Biosourced α-Terpinene by Combining Controlled LED-Driven Flow Photochemistry and Rose Bengal-Anchored Polymer Colloids. *ACS Sustain. Chem. Eng.* **2020,** *8*, 18568-18576.
223. Lessard, J. J.; Scheutz, G. M.; Korpusik, A. B.; Olson, R. A.; Figg, C. A.; Sumerlin, B. S. Self-catalyzing photoredox polymerization for recyclable polymer catalysts. *Polym. Chem.* **2021,** *12*, 2205-2209.
224. Li, W.; Zhang, W.; Dong, X.; Yan, L.; Qi, R.; Wang, W.; Xie, Z.; Jing, X. Porous heterogeneous organic photocatalyst prepared by HIPE polymerization for oxidation of sulfides under visible light. *J. Mater. Chem.* **2012,** *22*.
225. Petzold, D.; Giedyk, M.; Chatterjee, A.; König, B. A Retrosynthetic Approach for Photocatalysis. *Eur. J. Org. Chem.* **2020,** *2020*, 1193-1244.
226. Genzink, M. J.; Kidd, J. B.; Swords, W. B.; Yoon, T. P. Chiral Photocatalyst Structures in Asymmetric Photochemical Synthesis. *Chem. Rev.* **2022,** *122*, 1654-1716.
227. Cieśla, P.; Kocot, P.; Mytych, P.; Stasicka, Z. Homogeneous photocatalysis by transition metal complexes in the environment. *J. Mol. Catal. A: Chem.* **2004,** *224*, 17-33.
228. Burguete, M. I.; Gavara, R.; Galindo, F.; Luis, S. V. New polymer-supported photocatalyst with improved compatibility with polar solvents. Synthetic application using solar light as energy source. *Catal. Commun.* **2010,** *11*, 1081-1084.
229. Patel, P.; Patel, V.; Patel, P. M. Synthetic strategy of dendrimers: A review. *J. Indian Chem. Soc.* **2022,** *99*, 100514.
230. Najafi, F.; Salami-Kalajahi, M.; Roghani-Mamaqani, H. A review on synthesis and applications of dendrimers. *J. Iran. Chem. Soc.* **2020,** *18*, 503-517.
231. Choi, S.-J.; Kwon, T.-H.; Im, H.; Moon, D.-I.; Baek, D. J.; Seol, M.-L.; Duarte, J. P.; Choi, Y.-K. A Polydimethylsiloxane (PDMS) Sponge for the Selective Absorption of Oil from Water. *ACS Applied Materials & Interfaces* **2011,** *3*, 4552-4556.
232. Huber, N.; Sirim, M.; Qian, Z.; Ferguson, C. T. J.; Wei, W.; Zhang, K. A. I. Water-Compatible Poly(methyl methacrylate) Networks for Visible Light-Driven Photocatalytic Pollutant Remediation in Aqueous Medium. *ACS Appl. Polym. Mater.* **2022,** *4*, 5728-5736.
233. Frese, M.; Sewald, N. Enzymatic halogenation of tryptophan on a gram scale. *Angew. Chem. Int. Ed.* **2015,** *54*, 298-301.
234. Barker, R. D.; Yu, Y.; De Maria, L.; Johannissen, L. O.; Scrutton, N. S. Mechanism of Action of Flavin-Dependent Halogenases. *ACS Catal.* **2022,** *12*, 15352-15360.

235. McGovern, P. E.; Zhang, J.; Tang, J.; Zhang, Z.; Hall, G. R.; Moreau, R. A.; Nuñez, A.; Butrym, E. D.; Richards, M. P.; Wang, C.-s.; Cheng, G.; Zhao, Z.; Wang, C. Fermented beverages of pre- and proto-historic China. *Proc. Natl. Acad. Sci. U.S.A.* **2004,** *101*, 17593-17598.
236. Armstrong, E. F. Enzymes: A Discovery and its Consequences. *Nature* **1933,** *131*, 535-537.
237. Heckmann, C. M.; Paradisi, F. Looking Back: A Short History of the Discovery of Enzymes and How They Became Powerful Chemical Tools. *ChemCatChem* **2020,** *12*, 6082-6102.
238. Fischer, E. Einfluss der Configuration auf die Wirkung der Enzyme. *Ber. Dtsch. Chem. Ges.* **2006,** *27*, 2985-2993.
239. Hutchison, C. A.; Phillips, S.; Edgell, M. H.; Gillam, S.; Jahnke, P.; Smith, M. Mutagenesis at a specific position in a DNA sequence. *J. Biol. Chem.* **1978,** *253*, 6551-6560.
240. Chen, K.; Arnold, F. H. Tuning the activity of an enzyme for unusual environments: sequential random mutagenesis of subtilisin E for catalysis in dimethylformamide. *Proc. Natl. Acad. Sci. U.S.A.* **1993,** *90*, 5618-5622.
241. Arnold, F. H. Directed Evolution: Bringing New Chemistry to Life. *Angew. Chem. Int. Ed.* **2018,** *57*, 4143-4148.
242. Arnold, F. H. The nature of chemical innovation: new enzymes by evolution. *Q. Rev. Biophys.* **2015,** *48*, 404-10.
243. Davids, T.; Schmidt, M.; Bottcher, D.; Bornscheuer, U. T. Strategies for the discovery and engineering of enzymes for biocatalysis. *Curr. Opin. Chem. Biol.* **2013,** *17*, 215-20.
244. Jacques, P.; Bechet, M.; Bigan, M.; Caly, D.; Chataigne, G.; Coutte, F.; Flahaut, C.; Heuson, E.; Leclere, V.; Lecouturier, D.; Phalip, V.; Ravallec, R.; Dhulster, P.; Froidevaux, R. High-throughput strategies for the discovery and engineering of enzymes for biocatalysis. *Bioprocess Biosyst. Eng.* **2017,** *40*, 161-180.
245. Woodley, J. M. Protein engineering of enzymes for process applications. *Curr. Opin. Chem. Biol.* **2013,** *17*, 310-6.
246. Romero-Rivera, A.; Garcia-Borras, M.; Osuna, S. Computational tools for the evaluation of laboratory-engineered biocatalysts. *Chem. Commun.* **2016,** *53*, 284-297.
247. Turner, N. J.; Truppo, M. D. Biocatalysis enters a new era. *Curr. Opin. Chem. Biol.* **2013,** *17*, 212-4.
248. Bornscheuer, U. T.; Huisman, G. W.; Kazlauskas, R. J.; Lutz, S.; Moore, J. C.; Robins, K. Engineering the third wave of biocatalysis. *Nature* **2012,** *485*, 185-94.
249. Reetz, M. T. Biocatalysis in organic chemistry and biotechnology: past, present, and future. *J. Am. Chem. Soc.* **2013,** *135*, 12480-96.
250. Alonso, E.; Field, F. R.; Kirchain, R. E. In *A case study of the availability of platinum group metals for electronics manufacturers*, 2008 IEEE International Symposium on Electronics and the Environment, San Francisco, CA, USA 19-22 May 2008; IEEE: San Francisco, CA, USA 2008; pp 1-6.
251. Liu, G.; Zhang, J.; Bao, J. Cost evaluation of cellulase enzyme for industrial-scale cellulosic ethanol production based on rigorous Aspen Plus modeling. *Bioprocess Biosyst. Eng.* **2016,** *39*, 133-40.
252. Klein-Marcuschamer, D.; Oleskowicz-Popiel, P.; Simmons, B. A.; Blanch, H. W. The challenge of enzyme cost in the production of lignocellulosic biofuels. *Biotechnol. Bioeng.* **2012,** *109*, 1083-7.
253. Porter, J. L.; Rusli, R. A.; Ollis, D. L. Directed Evolution of Enzymes for Industrial Biocatalysis. *ChemBioChem* **2016,** *17*, 197-203.
254. Mesbah, N. M. Industrial Biotechnology Based on Enzymes From Extreme Environments. *Front Bioeng Biotechnol* **2022,** *10*, 870083.
255. Seel, C. J.; Gulder, T. Biocatalysis Fueled by Light: On the Versatile Combination of Photocatalysis and Enzymes. *ChemBioChem* **2019,** *20*, 1871-1897.

256. Brown, K. A.; Wilker, M. B.; Boehm, M.; Hamby, H.; Dukovic, G.; King, P. W. Photocatalytic Regeneration of Nicotinamide Cofactors by Quantum Dot–Enzyme Biohybrid Complexes. *ACS Catal.* **2016,** *6*, 2201-2204.
257. Wei, W.; Mazzotta, F.; Lieberwirth, I.; Landfester, K.; Ferguson, C. T. J.; Zhang, K. A. I. Aerobic Photobiocatalysis Enabled by Combining Core-Shell Nanophotoreactors and Native Enzymes. *J. Am. Chem. Soc.* **2022,** *144*, 7320-7326.
258. Peers, M. K.; Toogood, H. S.; Heyes, D. J.; Mansell, D.; Coe, B. J.; Scrutton, N. S. Light-driven biocatalytic reduction of alpha,beta-unsaturated compounds by ene reductases employing transition metal complexes as photosensitizers. *Catal. Sci. Technol.* **2016,** *6*, 169-177.
259. Lee, S. H.; Choi, D. S.; Pesic, M.; Lee, Y. W.; Paul, C. E.; Hollmann, F.; Park, C. B. Cofactor-Free, Direct Photoactivation of Enoate Reductases for the Asymmetric Reduction of C=C Bonds. *Angew. Chem. Int. Ed.* **2017,** *56*, 8681-8685.
260. Seel, C. J.; Králík, A.; Hacker, M.; Frank, A.; König, B.; Gulder, T. Atom-Economic Electron Donors for Photobiocatalytic Halogenations. *ChemCatChem* **2018,** *10*, 3960-3963.
261. Schroeder, L.; Frese, M.; Müller, C.; Sewald, N.; Kottke, T. Photochemically Driven Biocatalysis of Halogenases for the Green Production of Chlorinated Compounds. *ChemCatChem* **2018,** *10*, 3336-3341.
262. Eggeling, C.; Widengren, J.; Rigler, R.; Seidel, C. A. M. Photobleaching of Fluorescent Dyes under Conditions Used for Single-Molecule Detection: Evidence of Two-Step Photolysis. *Anal. Chem.* **1998,** *70*, 2651-2659.
263. Gonçalves, L. C. P.; Mansouri, H. R.; PourMehdi, S.; Abdellah, M.; Fadiga, B. S.; Bastos, E. L.; Sá, J.; Mihovilovic, M. D.; Rudroff, F. Boosting photobioredox catalysis by morpholine electron donors under aerobic conditions. *Catal. Sci. Technol.* **2019,** *9*, 2682-2688.
264. Kim, J.; Lee, S. H.; Tieves, F.; Choi, D. S.; Hollmann, F.; Paul, C. E.; Park, C. B. Biocatalytic C=C Bond Reduction through Carbon Nanodot-Sensitized Regeneration of NADH Analogues. *Angew. Chem. Int. Ed.* **2018,** *57*, 13825-13828.
265. Choudhury, S.; Baeg, J. O.; Park, N. J.; Yadav, R. K. A photocatalyst/enzyme couple that uses solar energy in the asymmetric reduction of acetophenones. *Angew. Chem. Int. Ed.* **2012,** *51*, 11624-8.
266. Schwochert, T. D.; Cruz, C. L.; Watters, J. W.; Reynolds, E. W.; Nicewicz, D. A.; Brustad, E. M. Design and Evaluation of Artificial Hybrid Photoredox Biocatalysts. *ChemBioChem* **2020,** *21*, 3146-3150.
267. Tran, N. H.; Nguyen, D.; Dwaraknath, S.; Mahadevan, S.; Chavez, G.; Nguyen, A.; Dao, T.; Mullen, S.; Nguyen, T. A.; Cheruzel, L. E. An efficient light-driven P450 BM3 biocatalyst. *J. Am. Chem. Soc.* **2013,** *135*, 14484-7.
268. Ener, M. E.; Lee, Y. T.; Winkler, J. R.; Gray, H. B.; Cheruzel, L. Photooxidation of cytochrome P450-BM3. *Proc. Natl. Acad. Sci. USA* **2010,** *107*, 18783-6.
269. Trimble, J. S.; Crawshaw, R.; Hardy, F. J.; Levy, C. W.; Brown, M. J. B.; Fuerst, D. E.; Heyes, D. J.; Obexer, R.; Green, A. P. A designed photoenzyme for enantioselective [2+2] cycloadditions. *Nature* **2022,** *611*, 709-714.
270. Sun, N.; Huang, J.; Qian, J.; Zhou, T. P.; Guo, J.; Tang, L.; Zhang, W.; Deng, Y.; Zhao, W.; Wu, G.; Liao, R. Z.; Chen, X.; Zhong, F.; Wu, Y. Enantioselective [2+2]-cycloadditions with triplet photoenzymes. *Nature* **2022,** *611*, 715-720.
271. Tran, N. H.; Huynh, N.; Bui, T.; Nguyen, Y.; Huynh, P.; Cooper, M. E.; Cheruzel, L. E. Light-initiated hydroxylation of lauric acid using hybrid P450 BM3 enzymes. *Chem. Commun.* **2011,** *47*, 11936-8.
272. Liu, X.; Kang, F.; Hu, C.; Wang, L.; Xu, Z.; Zheng, D.; Gong, W.; Lu, Y.; Ma, Y.; Wang, J. A genetically encoded photosensitizer protein facilitates the rational design of a miniature photocatalytic CO_2-reducing enzyme. *Nat. Chem.* **2018,** *10*, 1201-1206.

273. Fu, Y.; Huang, J.; Wu, Y.; Liu, X.; Zhong, F.; Wang, J. Biocatalytic Cross-Coupling of Aryl Halides with a Genetically Engineered Photosensitizer Artificial Dehalogenase. *J. Am. Chem. Soc.* **2021,** *143*, 617-622.
274. Gu, Y.; Ellis-Guardiola, K.; Srivastava, P.; Lewis, J. C. Preparation, Characterization, and Oxygenase Activity of a Photocatalytic Artificial Enzyme. *ChemBioChem* **2015,** *16*, 1880-1883.
275. Zubi, Y. S.; Liu, B.; Gu, Y.; Sahoo, D.; Lewis, J. C. Controlling the optical and catalytic properties of artificial metalloenzyme photocatalysts using chemogenetic engineering. *Chem. Sci.* **2022,** *13*, 1459-1468.
276. Elgrishi, N.; Rountree, K. J.; McCarthy, B. D.; Rountree, E. S.; Eisenhart, T. T.; Dempsey, J. L. A Practical Beginner's Guide to Cyclic Voltammetry. *J. Chem. Educ.* **2017,** *95*, 197-206.
277. Harris, R. K.; Becker, E. D.; Menezes, S. M. C. d.; Goodfellow, R.; Granger, P. NMR nomenclature. Nuclear spin properties and conventions for chemical shifts(IUPAC Recommendations 2001). *Pure Appl. Chem.* **2001,** *73*, 1795-1818.
278. Rosso, C.; Filippini, G.; Criado, A.; Melchionna, M.; Fornasiero, P.; Prato, M. Metal-Free Photocatalysis: Two-Dimensional Nanomaterial Connection toward Advanced Organic Synthesis. *ACS Nano* **2021,** *15*, 3621-3630.
279. Zhi, Y.; Wang, Z.; Zhang, H. L.; Zhang, Q. Recent Progress in Metal-Free Covalent Organic Frameworks as Heterogeneous Catalysts. *Small* **2020,** *16*, e2001070.
280. Marzo, L.; Pagire, S. K.; Reiser, O.; Konig, B. Visible-Light Photocatalysis: Does It Make a Difference in Organic Synthesis? *Angew. Chem. Int. Ed.* **2018,** *57*, 10034-10072.
281. Twilton, J.; Le, C.; Zhang, P.; Shaw, M. H.; Evans, R. W.; MacMillan, D. W. C. The merger of transition metal and photocatalysis. *Nat. Rev. Chem.* **2017,** *1*.
282. Xuan, J.; Xiao, W. J. Visible-light photoredox catalysis. *Angew. Chem. Int. Ed.* **2012,** *51*, 6828-38.
283. Tucker, J. W.; Stephenson, C. R. J. Shining Light on Photoredox Catalysis: Theory and Synthetic Applications. *J. Org. Chem.* **2012,** *77*, 1617-1622.
284. Chen, H.; Jena, H. S.; Feng, X.; Leus, K.; Van Der Voort, P. Engineering Covalent Organic Frameworks as Heterogeneous Photocatalysts for Organic Transformations. *Angew. Chem. Int. Ed.* **2022,** *61*, e202204938.
285. Li, R.; Byun, J.; Huang, W.; Ayed, C.; Wang, L.; Zhang, K. A. I. Poly(benzothiadiazoles) and Their Derivatives as Heterogeneous Photocatalysts for Visible-Light-Driven Chemical Transformations. *ACS Catal.* **2018,** *8*, 4735-4750.
286. Wang, T.-X.; Liang, H.-P.; Anito, D. A.; Ding, X.; Han, B.-H. Emerging applications of porous organic polymers in visible-light photocatalysis. *J. Mater. Chem. A* **2020,** *8*, 7003-7034.
287. Liu, Z.; Su, Q.; Ju, P.; Li, X.; Li, G.; Wu, Q.; Yang, B. A hydrophilic covalent organic framework for photocatalytic oxidation of benzylamine in water. *Chem. Commun.* **2020,** *56*, 766-769.
288. Marinho, B. A.; Cristovao, R. O.; Djellabi, R.; Caseiro, A.; Miranda, S. M.; Loureiro, J. M.; Boaventura, R. A. R.; Dias, M. M.; Lopes, J. C. B.; Vilar, V. J. P. Strategies to reduce mass and photons transfer limitations in heterogeneous photocatalytic processes: Hexavalent chromium reduction studies. *J. Environ. Manage.* **2018,** *217*, 555-564.
289. Ballari, M. d. l. M.; Brandi, R.; Alfano, O.; Cassano, A. Mass transfer limitations in photocatalytic reactors employing titanium dioxide suspensions. *Chem. Eng. J.* **2008,** *136*, 242-255.
290. Chaudhuri, A.; Zondag, S. D. A.; Schuurmans, J. H. A.; van der Schaaf, J.; Noel, T. Scale-Up of a Heterogeneous Photocatalytic Degradation Using a Photochemical Rotor-Stator Spinning Disk Reactor. *Org. Process Res. Dev.* **2022,** *26*, 1279-1288.
291. Kuckhoff, T.; Brewster, R.; Ferguson, C.; Jarvis, A. Reactivity Tuning of Metal-Free Artificial Photoenzymes through Binding Site Specific Bioconjugation. *Eur. J. Org. Chem. 26*, e202201412.

292. Cai, W.; Xu, D.; Qian, L.; Wei, J.; Xiao, C.; Qian, L.; Lu, Z. Y.; Cui, S. Force-Induced Transition of pi-pi Stacking in a Single Polystyrene Chain. *J. Am. Chem. Soc.* **2019,** *141*, 9500-9503.
293. Delgado-Gonzalez, A.; Garcia-Fernandez, E.; Valero, T.; Cano-Cortes, M. V.; Ruedas-Rama, M. J.; Unciti-Broceta, A.; Sanchez-Martin, R. M.; Diaz-Mochon, J. J.; Orte, A. Metallofluorescent Nanoparticles for Multimodal Applications. *ACS Omega* **2018,** *3*, 144-153.
294. Wu, Q. Y.; Chen, X. N.; Wan, L. S.; Xu, Z. K. Interactions between polyacrylonitrile and solvents: density functional theory study and two-dimensional infrared correlation analysis. *J. Phys. Chem. B* **2012,** *116*, 8321-30.
295. Bao, Z.; Lu, C.; Qin, C.; Tang, S.; Dai, L.; Chen, G.; Mei, F. Preparation of fluorescent polyacrylonitrile nanofiber membrane based on polymerizable 1,8-naphthalimide fluorescent disperse dye. *Fibers Polym.* **2017,** *18*, 1017-1024.
296. Grabolle, M.; Spieles, M.; Lesnyak, V.; Gaponik, N.; Eychmüller, A.; Resch-Genger, U. Determination of the Fluorescence Quantum Yield of Quantum Dots: Suitable Procedures and Achievable Uncertainties. *Anal. Chem.* **2009,** *81*, 6285-6294.
297. Becke, A. D. Density-functional thermochemistry. III. The role of exact exchange. *J. Chem. Phys.* **1993,** *98*, 5648-5652.
298. Stephens, P. J.; Devlin, F. J.; Chabalowski, C. F.; Frisch, M. J. Ab Initio Calculation of Vibrational Absorption and Circular Dichroism Spectra Using Density Functional Force Fields. *J. Phys. Chem.* **1994,** *98*, 11623-11627.
299. Petersson, G. A.; Al-Laham, M. A. A complete basis set model chemistry. II. Open-shell systems and the total energies of the first-row atoms. *J. Chem. Phys.* **1991,** *94*, 6081-6090.
300. Petersson, G. A.; Bennett, A.; Tensfeldt, T. G.; Al-Laham, M. A.; Shirley, W. A.; Mantzaris, J. A complete basis set model chemistry. I. The total energies of closed-shell atoms and hydrides of the first-row elements. *J. Chem. Phys.* **1988,** *89*, 2193-2218.
301. Kuckhoff, T.; Landfester, K.; Zhang, K. A. I.; Ferguson, C. T. J. Photocatalytic Hydrogels with a High Transmission Polymer Network for Pollutant Remediation. *Chem. Mater.* **2021,** *33*, 9131-9138.
302. Makula, P.; Pacia, M.; Macyk, W. How To Correctly Determine the Band Gap Energy of Modified Semiconductor Photocatalysts Based on UV-Vis Spectra. *J. Phys. Chem. Lett.* **2018,** *9*, 6814-6817.
303. Tauc, J.; Grigorovici, R.; Vancu, A. Optical Properties and Electronic Structure of Amorphous Germanium. *Phys. Status Solidi B* **1966,** *15*, 627-637.
304. Gehlen, M. H. The centenary of the Stern-Volmer equation of fluorescence quenching: From the single line plot to the SV quenching map. *J. Photochem. Photobiol. C: Photochem. Rev.* **2020,** *42*, 100338.
305. Pitre, S. P.; McTiernan, C. D.; Ismaili, H.; Scaiano, J. C. Mechanistic insights and kinetic analysis for the oxidative hydroxylation of arylboronic acids by visible light photoredox catalysis: a metal-free alternative. *J. Am. Chem. Soc.* **2013,** *135*, 13286-9.
306. Li, R. Visible light-induced organic transformations using benzothiadiazole derivates as highly efficient photocatalysts. phd, Johannes Gutenberg-Universität, Mainz, 2017.
307. Li, Y.; Ren, P.; Zhang, D.; Qiao, W.; Wang, D.; Yang, X.; Wen, X.; Rummeli, M. H.; Niemantsverdriet, H.; Lewis, J. P.; Besenbacher, F.; Xiang, H.; Li, Y.; Su, R. Rationally Designed Metal Cocatalyst for Selective Photosynthesis of Bibenzyls via Dehalogenative C–C Homocoupling. *ACS Catal.* **2021,** *11*, 4338-4348.
308. Rahman, M. Z.; Kibria, M. G.; Mullins, C. B. Metal-free photocatalysts for hydrogen evolution. *Chem. Soc. Rev.* **2020,** *49*, 1887-1931.

309. Rahman, M. Z.; Davey, K.; Qiao, S.-Z. Carbon, nitrogen and phosphorus containing metal-free photocatalysts for hydrogen production: progress and challenges. *J. Mater. Chem. A* **2018,** *6*, 1305-1322.
310. Bi, S.; Lan, Z.-A.; Paasch, S.; Zhang, W.; He, Y.; Zhang, C.; Liu, F.; Wu, D.; Zhuang, X.; Brunner, E.; Wang, X.; Zhang, F. Substantial Cyano-Substituted Fully sp2-Carbon-Linked Framework: Metal-Free Approach and Visible-Light-Driven Hydrogen Evolution. *Adv. Funct. Mater.* **2017,** *27*, 1703146.
311. Chen, W.; Wang, L.; Mo, D.; He, F.; Wen, Z.; Wu, X.; Xu, H.; Chen, L. Modulating Benzothiadiazole-Based Covalent Organic Frameworks via Halogenation for Enhanced Photocatalytic Water Splitting. *Angew. Chem. Int. Ed.* **2020,** *59*, 16902-16909.
312. Wang, Z.; Li, C.; Domen, K. Recent developments in heterogeneous photocatalysts for solar-driven overall water splitting. *Chem. Soc. Rev.* **2019,** *48*, 2109-2125.
313. Wang, X.; Maeda, K.; Thomas, A.; Takanabe, K.; Xin, G.; Carlsson, J. M.; Domen, K.; Antonietti, M. A metal-free polymeric photocatalyst for hydrogen production from water under visible light. *Nat. Mater.* **2009,** *8*, 76-80.
314. Liu, J.; Liu, Y.; Liu, N.; Han, Y.; Zhang, X.; Huang, H.; Lifshitz, Y.; Lee, S.-T.; Zhong, J.; Kang, Z. Metal-free efficient photocatalyst for stable visible water splitting via a two-electron pathway. *Science* **2015,** *347*, 970-974.
315. Su, F.; Mathew, S. C.; Mohlmann, L.; Antonietti, M.; Wang, X.; Blechert, S. Aerobic oxidative coupling of amines by carbon nitride photocatalysis with visible light. *Angew. Chem. Int. Ed.* **2011,** *50*, 657-60.
316. Huang, W.; Byun, J.; Rorich, I.; Ramanan, C.; Blom, P. W. M.; Lu, H.; Wang, D.; Caire da Silva, L.; Li, R.; Wang, L.; Landfester, K.; Zhang, K. A. I. Asymmetric Covalent Triazine Framework for Enhanced Visible-Light Photoredox Catalysis via Energy Transfer Cascade. *Angew. Chem. Int. Ed.* **2018,** *57*, 8316-8320.
317. Zhao, G.; Huang, X.; Wang, X.; Wang, X. Progress in catalyst exploration for heterogeneous CO_2 reduction and utilization: a critical review. *J. Mater. Chem. A* **2017,** *5*, 21625-21649.
318. Cao, S.; Low, J.; Yu, J.; Jaroniec, M. Polymeric photocatalysts based on graphitic carbon nitride. *Adv. Mater.* **2015,** *27*, 2150-76.
319. Habisreutinger, S. N.; Schmidt-Mende, L.; Stolarczyk, J. K. Photocatalytic reduction of CO_2 on TiO_2 and other semiconductors. *Angew. Chem. Int. Ed.* **2013,** *52*, 7372-408.
320. Fu, Y.; Zhu, X.; Huang, L.; Zhang, X.; Zhang, F.; Zhu, W. Azine-based covalent organic frameworks as metal-free visible light photocatalysts for CO_2 reduction with H_2O. *Appl. Catal. B* **2018,** *239*, 46-51.
321. Konan, Y. N.; Gurny, R.; Allémann, E. State of the art in the delivery of photosensitizers for photodynamic therapy. *J. Photochem. Photobiol. B* **2002,** *66*, 89-106.
322. Zhu, C.; Liu, L.; Yang, Q.; Lv, F.; Wang, S. Water-soluble conjugated polymers for imaging, diagnosis, and therapy. *Chem. Rev.* **2012,** *112*, 4687-735.
323. He, C.; Duan, X.; Guo, N.; Chan, C.; Poon, C.; Weichselbaum, R. R.; Lin, W. Core-shell nanoscale coordination polymers combine chemotherapy and photodynamic therapy to potentiate checkpoint blockade cancer immunotherapy. *Nat. Commun.* **2016,** *7*, 12499.
324. Lucky, S. S.; Soo, K. C.; Zhang, Y. Nanoparticles in photodynamic therapy. *Chem. Rev.* **2015,** *115*, 1990-2042.
325. Ahmed, S. N.; Haider, W. Heterogeneous photocatalysis and its potential applications in water and wastewater treatment: a review. *Nanotechnology* **2018,** *29*.
326. Byun, J.; Landfester, K.; Zhang, K. A. I. Conjugated Polymer Hydrogel Photocatalysts with Expandable Photoactive Sites in Water. *Chem. Mater.* **2019,** *31*, 3381-3387.

327. Ahmed, S.; Rasul, M. G.; Martens, W. N.; Brown, R.; Hashib, M. A. Heterogeneous photocatalytic degradation of phenols in wastewater: A review on current status and developments. *Desalination* **2010,** *261*, 3-18.
328. Zheng, Q.; Durkin, D. P.; Elenewski, J. E.; Sun, Y.; Banek, N. A.; Hua, L.; Chen, H.; Wagner, M. J.; Zhang, W.; Shuai, D. Visible-Light-Responsive Graphitic Carbon Nitride: Rational Design and Photocatalytic Applications for Water Treatment. *Environ. Sci. Technol.* **2016,** *50*, 12938-12948.
329. Andreozzi, R.; Raffaele, M.; Nicklas, P. Pharmaceuticals in STP effluents and their solar photodegradation in aquatic environment. *Chemosphere* **2003,** *50*, 1319-1330.
330. Petrie, B.; Barden, R.; Kasprzyk-Hordern, B. A review on emerging contaminants in wastewaters and the environment: current knowledge, understudied areas and recommendations for future monitoring. *Water Res.* **2015,** *72*, 3-27.
331. Shen, J.; Steinbach, R.; Tobin, J. M.; Mouro Nakata, M.; Bower, M.; McCoustra, M. R. S.; Bridle, H.; Arrighi, V.; Vilela, F. Photoactive and metal-free polyamide-based polymers for water and wastewater treatment under visible light irradiation. *Appl. Catal. B* **2016,** *193*, 226-233.
332. Chen, S.; Liu, Y. Study on the photocatalytic degradation of glyphosate by TiO_2 photocatalyst. *Chemosphere* **2007,** *67*, 1010-7.
333. Koe, W. S.; Lee, J. W.; Chong, W. C.; Pang, Y. L.; Sim, L. C. An overview of photocatalytic degradation: photocatalysts, mechanisms, and development of photocatalytic membrane. *Environ. Sci. Pollut. Res. Int.* **2020,** *27*, 2522-2565.
334. He, X.; Wu, Z.; Xue, Y.; Gao, Z.; Yang, X. Fabrication of interlayer β-CD/g-C_3N_4@MoS_2 for highly enhanced photodegradation of glyphosate under simulated sunlight irradiation. *RSC Adv.* **2019,** *9*, 4635-4643.
335. Manassero, A.; Satuf, M. L.; Alfano, O. M. Photocatalytic reactors with suspended and immobilized TiO_2: Comparative efficiency evaluation. *Chem. Eng. J.* **2017,** *326*, 29-36.
336. Yang, C.; Li, R.; Zhang, K. A. I.; Lin, W.; Landfester, K.; Wang, X. Heterogeneous photoredox flow chemistry for the scalable organosynthesis of fine chemicals. *Nat. Commun.* **2020,** *11*, 1239.
337. Sivagami, K.; Vikraman, B.; Krishna, R. R.; Swaminathan, T. Chlorpyrifos and Endosulfan degradation studies in an annular slurry photo reactor. *Ecotoxicol. Environ. Saf.* **2016,** *134*, 327-331.
338. Berberidou, C.; Kitsiou, V.; Kazala, E.; Lambropoulou, D. A.; Kouras, A.; Kosma, C. I.; Albanis, T. A.; Poulios, I. Study of the decomposition and detoxification of the herbicide bentazon by heterogeneous photocatalysis: Kinetics, intermediates and transformation pathways. *Appl. Catal. B* **2017,** *200*, 150-163.
339. Ghasimi, S.; Prescher, S.; Wang, Z. J.; Landfester, K.; Yuan, J.; Zhang, K. A. Heterophase Photocatalysts from Water-Soluble Conjugated Polyelectrolytes: An Example of Self-Initiation under Visible Light. *Angew. Chem. Int. Ed.* **2015,** *54*, 14549-53.
340. Wang, X.; Liang, Y.; An, W.; Hu, J.; Zhu, Y.; Cui, W. Removal of chromium (VI) by a self-regenerating and metal free g-C3N4/graphene hydrogel system via the synergy of adsorption and photo-catalysis under visible light. *Appl. Catal. B* **2017,** *219*, 53-62.
341. Yun, J.; Im, J. S.; Oh, A.; Jin, D.-H.; Bae, T.-S.; Lee, Y.-S.; Kim, H.-I. pH-sensitive photocatalytic activities of TiO_2/poly(vinyl alcohol)/poly(acrylic acid) composite hydrogels. *Materials Science and Engineering: B* **2011,** *176*, 276-281.
342. Yang, J.; Gao, J.; Wang, X.; Mei, S.; Zhao, R.; Hao, C.; Wu, Y.; Zhai, X.; Liu, Y. Polyacrylamide hydrogel as a template in situ synthesis of CdS nanoparticles with high photocatalytic activity and photostability. *J. Nanopart. Res.* **2017,** *19*, 350.
343. Nuhn, L.; Hirsch, M.; Krieg, B.; Koynov, K.; Fischer, K.; Schmidt, M.; Helm, M.; Zentel, R. Cationic Nanohydrogel Particles as Potential siRNA Carriers for Cellular Delivery. *ACS Nano* **2012,** *6*, 2198-2214.

344. Kopeček, J. Hydrogels from Soft Contact Lenses and Implants to Self-Assembled Nanomaterials. *J. Polym. Sci. A Polym. Chem.* **2009,** *47*, 5929-5946.
345. Burdick, J. A.; Murphy, W. L. Moving from static to dynamic complexity in hydrogel design. *Nat. Commun.* **2012,** *3*, 1269.
346. Peng, C. C.; Kim, J.; Chauhan, A. Extended delivery of hydrophilic drugs from silicone-hydrogel contact lenses containing vitamin E diffusion barriers. *Biomaterials* **2010,** *31*, 4032-47.
347. Xinming, L.; Yingde, C.; Lloyd, A. W.; Mikhalovsky, S. V.; Sandeman, S. R.; Howel, C. A.; Liewen, L. Polymeric hydrogels for novel contact lens-based ophthalmic drug delivery systems: a review. *Cont. Lens Anterior Eye* **2008,** *31*, 57-64.
348. Qi, X.; Wei, W.; Su, T.; Zhang, J.; Dong, W. Fabrication of a new polysaccharide-based adsorbent for water purification. *Carbohydr. Polym.* **2018,** *195*, 368-377.
349. Bekiari, V.; Lianos, P. Ureasil Gels as a Highly Efficient Adsorbent for Water Purification. *Chem. Mater.* **2006,** *18*, 4142-4146.
350. Zhao, W.; Yang, C.; Huang, J.; Jin, X.; Deng, Y.; Wang, L.; Su, F.; Xie, H.; Wong, P. K.; Ye, L. Selective aerobic oxidation of sulfides to sulfoxides in water under blue light irradiation over $Bi_4O_5Br_2$. *Green Chem.* **2020,** *22*, 4884-4889.
351. Akpor, O. B.; G. O. Ohiobor; Olaolu, T. D. Heavy Metal Pollutants in Wastewater Effluents: Sources, Effects and Remediation. *Adv. Biosci. Bioeng.* **2014,** *2*, 37-43.
352. Barakat, M. A. New trends in removing heavy metals from industrial wastewater. *Arab. J. Chem.* **2011,** *4*, 361-377.
353. Kieber, R. J.; Willey, J. D.; Zvalaren, S. D. Chromium Speciation in Rainwater: Temporal Variability and Atmospheric Deposition. *Environ. Sci. & Technol.* **2002,** *36*, 5321-5327.
354. Shanker, A. K.; Cervantes, C.; Loza-Tavera, H.; Avudainayagam, S. Chromium toxicity in plants. *Environ. Int.* **2005,** *31*, 739-53.
355. Zhitkovich, A. Chromium in Drinking Water: Sources, Metabolism, and Cancer Risks. *Chem. Res. Toxicol.* **2011,** *24*, 1617-1629.
356. Ghasimi, S.; Landfester, K.; Zhang, K. A. I. Water Compatible Conjugated Microporous Polyazulene Networks as Visible-Light Photocatalysts in Aqueous Medium. *ChemCatChem* **2016,** *8*, 694-698.
357. Woodburn, A. T. Glyphosate: production, pricing and use worldwide. *Pest Manag. Sci.* **2000,** *56*, 309-312.
358. Baylis, A. D. Why glyphosate is a global herbicide: strengths, weaknesses and prospects. *Pest Management Science* **2000,** *56*, 299-308.
359. Hébert, M.-P.; Fugère, V.; Gonzalez, A. The overlooked impact of rising glyphosate use on phosphorus loading in agricultural watersheds. *Front. Ecol. Enviro.* **2019,** *17*, 48-56.
360. Battaglin, W. A.; Kolpin, D. W.; Scribner, E. A.; Kuivila, K. M.; Sandstrom, M. W. GLYPHOSATE, OTHER HERBICIDES, AND TRANSFORMATION PRODUCTS IN MIDWESTERN STREAMS, 20021. *J. Am. Water Resour. Assoc.* **2005,** *41*, 323-332.
361. Poiger, T.; Buerge, I. J.; Bachli, A.; Muller, M. D.; Balmer, M. E. Occurrence of the herbicide glyphosate and its metabolite AMPA in surface waters in Switzerland determined with on-line solid phase extraction LC-MS/MS. *Environ. Sci. Pollut. Res. Int.* **2017,** *24*, 1588-1596.
362. Toss, V.; Leito, I.; Yurchenko, S.; Freiberg, R.; Kruve, A. Determination of glyphosate in surface water with high organic matter content. *Environ. Sci. Pollut. Res. Int.* **2017,** *24*, 7880-7888.
363. Tsui, M. T. K.; Chu, L. M. Aquatic toxicity of glyphosate-based formulations: comparison between different organisms and the effects of environmental factors. *Chemosphere* **2003,** *52*, 1189-1197.

364. Annett, R.; Habibi, H. R.; Hontela, A. Impact of glyphosate and glyphosate-based herbicides on the freshwater environment. *J. Appl. Toxicol.* **2014,** *34*, 458-479.
365. Lund-HØie, K.; Friestad, H. O. Photodegradation of the Herbicide Glyphosate in Water. *Bull. Environ. Contam. Toxicol* **1986**, 723-729.
366. Kudzin, M.; Żyłła, R.; Mrozińska, Z.; Urbaniak, P. 31P NMR Investigations on Roundup Degradation by AOP Procedures. *Water* **2019,** *11*, 331.
367. Huo, R.; Yang, X.-L.; Yang, J.-Y.; Yang, S.-Y.; Xu, Y.-H. Self-assembly synthesis of $BiVO_4$/Polydopamine/g-C_3N_4 with enhanced visible light photocatalytic performance. *Mater. Res. Bull.* **2018,** *98*, 225-230.
368. Brewster, R. C.; Klemencic, E.; Jarvis, A. G. Palladium in biological media: Can the synthetic chemist's most versatile transition metal become a powerful biological tool? *J. Inorg. Biochem.* **2021,** *215*, 111317.
369. Chen, K.; Arnold, F. H. Engineering new catalytic activities in enzymes. *Nat. Catal.* **2020,** *3*, 203-213.
370. Schwizer, F.; Okamoto, Y.; Heinisch, T.; Gu, Y.; Pellizzoni, M. M.; Lebrun, V.; Reuter, R.; Kohler, V.; Lewis, J. C.; Ward, T. R. Artificial Metalloenzymes: Reaction Scope and Optimization Strategies. *Chem. Rev.* **2018,** *118*, 142-231.
371. Jarvis, A. G. Designer metalloenzymes for synthetic biology: Enzyme hybrids for catalysis. *Curr. Opin. Chem. Biol.* **2020,** *58*, 63-71.
372. Davis, H. J.; Ward, T. R. Artificial Metalloenzymes: Challenges and Opportunities. *ACS Cent. Sci.* **2019,** *5*, 1120-1136.
373. Matsuo, T.; Hirota, S. Artificial enzymes with protein scaffolds: structural design and modification. *Bioorg. Med. Chem.* **2014,** *22*, 5638-56.
374. Polizzi, K. M.; Bommarius, A. S.; Broering, J. M.; Chaparro-Riggers, J. F. Stability of biocatalysts. *Curr. Opin. Chem. Biol.* **2007,** *11*, 220-5.
375. Kristjánsson, M. M.; Kinsella, J. E., Protein and Enzyme Stability: Structural, Thermodynamic, and Experimental Aspects. In *Advances in Food and Nutrition Research*, Kinsella, J. E., Ed. Academic Press: 1991; Vol. 35, pp 237-316.
376. Patil, P. D.; Nadar, S. S.; Marghade, D. T., Photo-Enzymatic Green Synthesis: The Potential of Combining Photo-Catalysis and Enzymes. In *Advances in Green Synthesis: Avenues and Sustainability*, Inamuddin; Boddula, R.; Ahamed, M. I.; Khan, A., Eds. Springer International Publishing: Cham, 2021; pp 173-189.
377. Brettel, K.; Byrdin, M. Reaction mechanisms of DNA photolyase. *Curr. Opin. Struct. Biol.* **2010,** *20*, 693-701.
378. Gabruk, M.; Mysliwa-Kurdziel, B. Light-Dependent Protochlorophyllide Oxidoreductase: Phylogeny, Regulation, and Catalytic Properties. *Biochem.* **2015,** *54*, 5255-62.
379. Sorigué, D.; Légeret, B.; Cuiné, S.; Blangy, S.; Moulin, S.; Billon, E.; Richaud, P.; Brugière, S.; Couté, Y.; Nurizzo, D.; Müller, P.; Brettel, K.; Pignol, D.; Arnoux, P.; Li-Beisson, Y.; Peltier, G.; Beisson, F. An algal photoenzyme converts fatty acids to hydrocarbons. *Science* **2017,** *357*, 903-907.
380. Li, P.; Terrett, J. A.; Zbieg, J. R. Visible-Light Photocatalysis as an Enabling Technology for Drug Discovery: A Paradigm Shift for Chemical Reactivity. *ACS Med. Chem. Lett.* **2020,** *11*, 2120-2130.
381. Srivastava, V.; Singh, P. P. Eosin Y catalysed photoredox synthesis: a review. *RSC Adv.* **2017,** *7*, 31377-31392.
382. Fukuzumi, S.; Ohkubo, K. Selective photocatalytic reactions with organic photocatalysts. *Chem. Sci.* **2013,** *4*, 561-574.

383. Mejias, S. H.; Roelfes, G.; Browne, W. R. Impact of binding to the multidrug resistance regulator protein LmrR on the photo-physics and -chemistry of photosensitizers. *Phys. Chem. Chem. Phys.* **2020,** *22*, 12228-12238.
384. Cesana, P. T.; Li, B. X.; Shepard, S. G.; Ting, S. I.; Hart, S. M.; Olson, C. M.; Martinez Alvarado, J. I.; Son, M.; Steiman, T. J.; Castellano, F. N.; Doyle, A. G.; MacMillan, D. W. C.; Schlau-Cohen, G. S. A biohybrid strategy for enabling photoredox catalysis with low-energy light. *Chem* **2022,** *8*, 174-185.
385. Trimble, J. S.; Crawshaw, R.; Hardy, F. J.; Levy, C. W.; Brown, M. J. B.; Fuerst, D. E.; Heyes, D. J.; Obexer, R.; Green, A. P. A Designed Photoenzyme for Enantioselective [2+2]-Cycloadditions. *Nature* **2022,** *611*, 709-714.
386. Jarvis, A. G.; Obrecht, L.; Deuss, P. J.; Laan, W.; Gibson, E. K.; Wells, P. P.; Kamer, P. C. J. Enzyme Activity by Design: An Artificial Rhodium Hydroformylase for Linear Aldehydes. *Angew. Chem. Int. Ed.* **2017,** *56*, 13596-13600.
387. Imam, H. T.; Jarvis, A. G.; Celorrio, V.; Baig, I.; Allen, C. C. R.; Marr, A. C.; Kamer, P. C. J. Catalytic and biophysical investigation of rhodium hydroformylase. *Catal. Sci. Technol.* **2019,** *9*, 6428-6437.
388. Doble, M. V.; Obrecht, L.; Joosten, H.-J.; Lee, M.; Rozeboom, H. J.; Branigan, E.; Naismith, J. H.; Janssen, D. B.; Jarvis, A. G.; Kamer, P. C. J. Engineering Thermostability in Artificial Metalloenzymes to Increase Catalytic Activity. *ACS Catal.* **2021,** *11*, 3620-3627.
389. Haapalainen, A. M.; van Aalten, D. M.; Merilainen, G.; Jalonen, J. E.; Pirila, P.; Wierenga, R. K.; Hiltunen, J. K.; Glumoff, T. Crystal structure of the liganded SCP-2-like domain of human peroxisomal multifunctional enzyme type 2 at 1.75 A resolution. *J. Mol. Biol.* **2001,** *313*, 1127-38.
390. Sehnal, D.; Bittrich, S.; Deshpande, M.; Svobodová, R.; Berka, K.; Bazgier, V.; Velankar, S.; Burley, S. K.; Koča, J.; Rose, A. S. Mol* Viewer: modern web app for 3D visualization and analysis of large biomolecular structures. *Nucleic Acids Res.* **2021,** *49*, W431-w437.
391. Deuss, P. J.; Popa, G.; Botting, C. H.; Laan, W.; Kamer, P. C. Highly efficient and site-selective phosphane modification of proteins through hydrazone linkage: development of artificial metalloenzymes. *Angew. Chem. Int. Ed.* **2010,** *49*, 5315-7.
392. Sinha, A. K.; Equbal, D. Thiol−Ene Reaction: Synthetic Aspects and Mechanistic Studies of an Anti-Markovnikov-Selective Hydrothiolation of Olefins. *Asian J. Org. Chem.* **2019,** *8*, 32-47.
393. Martin, J. S.; MacKenzie, C. J.; Fletcher, D.; Gilbert, I. H. Characterising covalent warhead reactivity. *Bioorg. Med. Chem.* **2019,** *27*, 2066-2074.
394. Schweitzer, C.; Schmidt, R. Physical Mechanisms of Generation and Deactivation of Singlet Oxygen. *Chem. Rev.* **2003,** *103*, 1685-1758.
395. Bentley, R. Role of sulfur chirality in the chemical processes of biology. *Chem. Soc. Rev.* **2005,** *34*, 609-24.
396. Surur, A. S.; Schulig, L.; Link, A. Interconnection of sulfides and sulfoxides in medicinal chemistry. *Arch. Pharm.* **2019,** *352*, e1800248.
397. Xiong, F.; Yang, B. B.; Zhang, J.; Li, L. Enantioseparation, Stereochemical Assignment and Chiral Recognition Mechanism of Sulfoxide-Containing Drugs. *Molecules* **2018,** *23*, 2680.
398. Skolia, E.; Gkizis, P. L.; Kokotos, C. G. Aerobic Photocatalysis: Oxidation of Sulfides to Sulfoxides. *ChemPlusChem* **2022,** *87*, e202200008.
399. Bradford, M. M. A rapid and sensitive method for the quantitation of microgram quantities of protein utilizing the principle of protein-dye binding. *Anal. Biochem.* **1976,** *72*, 248-254.

9 List of Figures

Figure 1.1 Number of publications between 1980 and 2022. Search term “photocatalysis” CAS SciFinder^{n}. www.scifinder-n.cas.org. Accessed 22 May, 2023. 9
Figure 2.1 Depiction of the photocatalytic mechanism involving an oxidative or reductive quenching cycle. Reproduced with permission of the author.[10] (CC BY 4.0) 14
Figure 3.1: Depiction of molecular orbitals of $[Ru(bpy)_3]^{2+}$ and the creation of an electron-hole pair upon irradiation. Followed by the possible SET in an oxidative or reductive quenching process.[9] Reproduced with permission of ACS Copyright © 2013. 16
Figure 3.2 Common fully organic dyes used as photocatalysts based on acridinium, fluorescein, rhodamine thiazine. 17
Figure 3.3 π-extended benzothiadiazole investigated by DaSilveira Neto *et al.*[72] (left). Calculated molecular orbitals of the HOMO/LUMO-level of diphenyl benzothiadiazole (1) indicating a shift in electron density upon irradiation.[73] (right) Reproduced with permission of Wiley-VCH Copyright © 2019. 19
Figure 3.4: Formation of the band structure in heterogeneous photocatalyst, based on molecular orbital of a small molecular photocatalyst. Depictured mechanism of heterogeneous photocatalysis through light absorption followed by electron transfer from the photocatalyst towards an electron acceptor (A) or from an electron donor (D) into the valence band. 20
Figure 3.5: Methods utilized in coupling reactions to synthesis conjugated mesoporous polymers. .. 21
Figure 3.6 Small molecular photocatalyst incorporated into classical polymers. 24
Figure 3.7 Schematic aggregation of pH-responsive RAFT-PISA photocatalytic nanoparticle[210] Reproduced with permission of the author. (CC BY 4.0) 26
Figure 3.8 Synthesis route for encapsulated homogeneous methylene blue in thermoresponsive crosslinked PNIPAM shell.[196] Reproduced with permission of the American Chemical Society Copyright © 2008 27
Figure 3.9 Schematic miniemulsion polymerization for the synthesis of photocatalytic microgels.[189] Reproduced with permission from the Royal Society of Chemistry. 28
Figure 3.10: Working mechanism of pH-responsive star-shaped polymer with hydrophobic porphyrin core.[216] Reproduced with permission of the Chinese Chemical Society © 2020. 29
Figure 3.11 Synthesis route for photocatalytic dendrimer. Based on second generation PAMAM dendrimer.[197] Reproduced with permissions from the Royal Society of Chemistry. 30
Figure 3.12: Non-covalent surface modification of a heterogeneous PDMS sponge with rose bengal.[208] Reproduced with permission from the Royal Society of Chemistry. 32
Figure 3.13 Synthesis of the heterogeneous support via HIPE followed by surface modification through azide-alkyne cycloaddition.[207] Reproduced with permission of Wiley-VCH © 2017. 33

Figure 3.14. Comparison of the natural redox reaction and the pathway using the artificial photoenzyme. (top) Detailed interaction between the photocatalyst and the active center.[268] Reproduced with permission from the American Chemical Society Copyright © 2013. 37
Figure 3.15 Reaction scope for the hydroxylation of aryl halides using the synthesized artificial photoenzyme.[274] Reproduced with permission from the American Chemical Society Copyright © 2021. 38
Figure 3.16 Synthesis of artificial photoenzyme through bioconjugation using azide-alkyne cycloaddition.[275] Reproduced with permission of WILEY-VCH © 2015. 39
Figure 3.17 Functionalized Mes-Acr$^+$ photocatalytic moieties (left) and the protein scaffolds for the bioconjugation (right) used for the photooxidation of thioanisole derivatives.[267] Reproduced with permission of WILEY-VCH © 2020. 40
Figure 4.1: GCMS set up consisting of the injector and preheater, oven with column as well as the mass-spectrometer. 43
Figure 4.2 UV/Vis-spectrometer. Consisting of a light source, monochromator, cuvette and detector. 44
Figure 4.3: Fluorescence spectrometer setup (left); Jablonski-Diagram with absorbance and possible radiative transitions fluorescence, and phosphorescence (right). 45
Figure 4.4 Depicturing of an electrochemical cell.[277] Reproduced with permission of The American Chemical Society and Division of Chemical Education, Copyright © 2017. 47
Figure 4.5 Energy splitting of a nucleus in an applied magnetic field with a spin of ½. 48
Figure 5.1: Photocatalytic moiety is copolymerized with three distinct monomers, styrene, methyl methacrylate and acrylonitrile to investigate the effect of the comonomer on the photocatalytic efficiency and photophysical properties. 52
Figure 5.2: The chosen functionality effects the absorbance of the diphenyl benzothiadiazole core based on the ± inductive and mesomeric effect of the functionality. Measurement performed in DMF. 54
Figure 5.3: Used monomers for the copolymerization with the photocatalytic moiety. Methyl methacrylate, styrene and acrylonitrile were chosen for further analysis. 55
Figure 5.4: Influence of different solvents on the absorbance of the photocatalytic moiety. (left) Influence of comonomer choice on the absorbance of the photocatalytic moiety. Measurements were performed in DMF. PDMAEMA measured in water. (right) 55
Figure 5.5: GPC of PAN-BT, PS-BT and PMMA-BT in DMF against a PMMA standard (left). FTIR spectra of PAN-BT, PS-BT and PMMA-BT as dry powder in KBr pellets (right). 56
Figure 5.6: Absorbance spectra (left) of PMMA-BT, PAN-BT and PS-BT in DMF indicating a change in absorbance depending on the comonomer. Fluorescence spectra (right) of PAN-BT, PMMA-BT and PS-BT showing a blue shift in PAN-BT indicating the influence of the comonomer. 57

Figure 5.7: Normalized average of three fluorescence lifetime measurements of PAN-BT, PMMA-BT, PS-BT. 58
Figure 5.8: Quantum yield calculation of PAN-BT, PMMA-BT and PS-BT using 4,7-diphenyl-2,1,3-benzothiadiazole at 366 nm in ACN as reference. 59
Figure 5.9: Three copolymers were analyzed via excitation spectra (left) and DFT calculations (right). The copolymers show a blue shift from PS-BT to polar PAN-BT. DFT calculations confirm a higher bandgap for PAN-BT, while PMMA-BT and PS-BT lie closer together. 60
Figure 5.10: HOMO (left) and LUMO (right) of PAN-BT, PS-BT and PMMA-BT Indicating electron density shift in excited state compared to ground state. 62
Figure 5.11: Photocatalytic hydroxylation of 4-biphenyl boronic acid measured over time using PS-BT, PMMA-BT and PAN-BT. 4-biphenylboronic acid (19.8 mg, 100 µmol) *N*,*N*-diisopropylethylamine (52 µL, 300 µmol) and photocatalytic polymer (100 nmol photoactive unit) in DMF (2mL), O_2-Atm. blue light irradiation. 63
Figure 5.12: Stern-Volmer Plot of PAN-BT, PS-BT and PMMA-BT using DIPEA (left) and TPA (right) as quenching agent. 64
Figure 5.13: Photocatalytic C-C coupling of 4-Chlorobenzylbromide over eight hours using PS-BT, PMMA-BT and PAN-BT indicating a comonomer on the overall efficiency. 4-chlorobenzyl bromide (20.5 mg, 100 µmol) *N*,*N*-diisopropylethylamine (175 µL, 1 mmol) and photocatalytic polymer (300 nmol photocatalytic moiety) in DMF (2 mL), N_2-Atm. blue light irradiation. 65
Figure 5.14: Kinetic investigation of the C-C coupling of 3-methyl indole measured over 80 min showing full conversion for PS-BT. 3-methyl indole (19.7 mg, 150 µmol), diethyl bromomalonate (71.7 mg, 300 µmol) and triphenylamine (73.6 mg, 300 µmol) and photocatalytic polymer (250 nmol photoactive unit) in DMF (2 mL) Ar-Atm. blue light irradiation. 66
Figure 5.15 High transmittance photocatalytic hydrogels allow for easy light penetration into the photocatalytic system for efficient water remediation. Light is not reflected or absorbed by the polymer network and is, therefore, available for photocatalytic reactions. 71
Figure 5.16: Analyzed monomers and used crosslinker to synthesis a highly transmittance hydrogel. Highlighted are *N,N*-dimethylacrylamide and *N*,*N*'-methylenebis(acrylamide) which were chosen for the hydrogel. 72
Figure 5.17: Transmittance values of PDMA, PAA and PHEMA crosslinked with PEG. PDMA possesses the highest transmittance compared to the other monomers. (left) Influence of crosslinker concentration on the transmittance of the synthesized hydrogel. (right) 73
Figure 5.18 High transmittance hydrogel (a) molecular structure of designed hydrogel, (b) synthesized high transmittance hydrogel, (c) molecular structure of designed photocatalytic hydrogel, (d) synthesized photocatalytic. 74
Figure 5.19 Transmittance spectra of the hydrogel without photocatalyst (red), absorbance spectra of the photocatalyst (black). 74

Figure 5.20 (left) DFT-Calculated electron structure and HOMO/LUMO-level of *N*-(4-(7-phenylbenzo[c][1,2,5]thiadiazol-4-yl)phenyl)acrylamide vs SCE. (right) Cyclic voltammetry of photocatalytic hydrogel (100 mV/S). 75
Figure 5.21: Solid state NMR spectroscopy: ^{13}C-CP-MAS NMR spectrum of photocatalytic hydrogel. 76
Figure 5.22 FTIR of photocatalytic hydrogel (red) and the synthesized photocatalytic monomer (black). 76
Figure 5.23 a) UV/Vis-Absorbance spectra of dried photocatalytic hydrogel. b) Photocurrent measurements under blue light (power: 0.16 W cm^2, λ = 460 nm) with 20 sec. irradiation intervals. 77
Figure 5.24 Swelling behavior of the photocatalytic hydrogel. Dry hydrogel in the absence of water. (a and c) Photocatalytic hydrogel after 30 sec. in the presence of water (b and d). 78
Figure 5.25 Reversible swelling and drying of the photocatalytic polymer hydrogel (left); weight gain during swelling circle (right). 78
Figure 5.26 UV/Vis-spectra of time depending photodegradation of rhodamine B (left) peak intensity for the photodegradation of rhodamine B plotted against time (right). 79
Figure 5.27: Comparison of achieved conversions and selectivity for the photooxidation of thioanisole under standard conditions, the absence of photocatalyst, light or oxygen and in the presence of quenching agents. 81
Figure 5.28: Photoreduction of chromium^{VI} is quantified through complexation of the remaining Cr^{VI} with diphenylcarbazide allowing for UV/Vis absorbance measurements at 542 nm. 82
Figure 5.29 Photodegradation of chromium by photocatalytic hydrogel chromium photoreduction over time under N_2 atmosphere measured at 542 nm by complexation with diphenylcarbazide (left); 5 recycling steps for the photoreduction of Cr^{VI} to Cr^{III} using photocatalytic hydrogel under blue light irradiation (power: 0.16 W cm^{-2}, λ = 460 nm) (right). 82
Figure 5.30: Photodegradation of glyphosate analyzed via ^{31}P-NMR spectroscopy and the observed peaks. The degradation products were assigned based on the research of Kudzin et al.[367] 83
Figure 5.31: Degradation of glyphosate by linear photocatalytic PDMMA was analyzed via ^{31}P-NMR spectroscopy. The kinetic study allows a clear evidence for the complete degradation of glyphosate overtime. The degradation products were assigned based on the research of Kudzin et al.[367] 84
Figure 5.32 Glyphosate degradation monitored over time via ^{31}P-NMR spectroscopy. 84
Figure 5.33: The hydrogel was polymerized inside a column to test the viability of a flow though photocatalytic column. A white paper with measurement in cm was added to visualize the column size. A methylene blue solution was used to showcase the flow of water through the gel over time (pressure 0.5 bar, 30 min.) 85
Figure 5.34 Large scale glyphosate degradation. (left) half liter scale photodegradation of 1 g of glyphosate in water. 86

Figure 5.35: (a) Glyphosate degradation over time monitored via ^{31}P-NMR spectroscopy. (b) Glyphosate degradation monitored over time via ^{31}P-NMR spectroscopy using photocatalytic hydrogel (red) and linear photocatalytic PDMMA (right). 87
Figure 5.36 Protein scaffold with highlighted positions of non-native cysteine variants A100C, V83C, and Q111C in combination with the bioconjugated photocatalytic moiety. Image created using Mol* and 1IKT from the RCSB PDB (rcsb.org).[390,391] 91
Figure 5.37: Mass spectra of A100C, Q111C and V83C, due to different replaced amino acids the three different variation possess different molecular weights: V83C (13377 Da), Q111C (13349 Da), and A100C (13405 Da). 92
Figure 5.38: Mass spectra of V83C-2, Q111C-2 and A100C-2. The three variants were bioconjugated with acrylamide functionalized diphenyl benzothiadiazole. Q111C-2 and A100C-2 were not completely bioconjugated compared to V83C-2. 50 µM protein,1 mM photocatalyst, HEPES buffer (50 mM HEPES, 50 mM NaCl, 10% DMF) pH 8.5, 20 °C overnight 93
Figure 5.39: Synthesis route for iodoacetamide functionalized photocatalytic moiety. Four step synthesis due to the unavailable iodoacetyl chloride. (Synthesis Methods 6.3.2) 94
Figure 5.40 Mass spectra of all three variants A100C, V83C, and Q111C before and A100C-3, V83C-3 and Q111C-3 after bioconjugation via LC-MS. 96
Figure 5.41 Absorbance and Emission spectra of A100C-3, Q111C-3, and A100C-3, as well as their corresponding peaks. 96
Figure 5.42: Density functional theory calculations for HOMO/LUMO levels calculated using method rb3lyp/6-31+g(d) as well as the triplet state energy calculated using method b3lyp/6-31+g(d) in Gaussian 16. 97
Figure 5.43: Electron paramagnetic resonance spectra of V83C-3 (red) (55 nmol) in MES buffer (20 mM MES, 50 mM NaCl, 1 mL) at pH 6 and blank measurement of MES buffer (20 mM MES, 50 mM NaCl, 1mL) at pH 6 (grey) after blue light LED irradiation in H_2O with 2,2,6,6-tetramethylpiperidine (0.1 M) as singlet oxygen trapping agent. 97
Figure 5.44 Photocatalytic oxidation of thioanisole; Conditions: Modified protein 10 µM, thioanisole 2 mM, MES buffer (MES 20 mM, 50 mM NaCl, 2% ACN) pH 6, blue light irradiation (460-465 nm) at room temperature; a) TON determination after eight hours. Conversion rate determined via GC-MS (measured in triplets). 98
Figure 5.45: Stability test of artificial photoenzyme V83C-3. The samples were irradiated for up to 24 h under blue light and small amount of precipitation could be observed under light irradiation at 388 nm. 100
Figure 5.46: Photocatalytic conversion of thioanisole (2 µmol) using V83C-3 (10 nmol) in MES buffer (20 mM MES, 50 mM NaCl, 1 mL) after the photoenzyme was irradiated for up to 24 h under blue light before usage. 100
Figure 6.1: Tauc-Plot of PMMA-BT, Pan-BT and PS-BT using a model for a direct bandgap. 104

Figure 6.2: DLS measurements of PAN-BT, PS-BT and PMMA-BT and the calculated hydrodynamic radius. 105
Figure 6.3: CV measurements of PAN-BT, PS-BT and PMMA-BT as membranes using Nafion in ACN (NBu_4PF_6 5.0 wt.%). 106
Figure 6.4: ^1H NMR spectrum (400 MHz, DMSO-d_6) of 4-phenyl-7-(4-vinylphenyl)benzo[c][1,2,5]thiadiazole. 108
Figure 6.5: ^1H NMR spectrum (400 MHz, DMF-d_7) of PAN-BT. 108
Figure 6.6: ^1H NMR spectrum (400 MHz, CD_2Cl_2) of PS-BT. 109
Figure 6.7: ^1H NMR spectrum (400 MHz, CD_2Cl_2) of PMMA-BT. 109
Figure 6.8: GCMS trail of Diethyl 2-(3-methyl-1H-indol-2-yl)malonate. 110
Figure 6.9: ^1H NMR spectrum (400 MHz, CD_2Cl_2) of Diethyl 2-(3-methyl-1H-indol-2-yl)malonate. 111
Figure 6.10: ^{13}C NMR spectrum (101 MHz, CD_2Cl_2) of diethyl 2-(3-methyl-1H-indol-2-yl)malonate. . 111
Figure 6.11: GCMS trail of 1,2-bis(4-chlorophenyl)ethane using 1-bromo-octane as standard. 112
Figure 6.12: ^1H NMR spectrum (400 MHz, CD2Cl2) of 1,2-bis(4-chlorophenyl)ethane. 113
Figure 6.13: ^{13}C NMR spectrum (101 MHz, CD2Cl2) of 1,2-bis(4-chlorophenyl)ethane 113
Figure 6.14: GCMS trail of 4-phenylphenol using 1-bromo-octane as standard 114
Figure 6.15: ^1H NMR spectrum (400 MHz, CD_2Cl_2) of 4-phenyl phenol. 115
Figure 6.16: ^{13}C NMR spectrum (400 MHz, CD_2Cl_2) of 4-phenyl phenol. 115
Figure 6.17: ^1H NMR spectrum (DMSO-d_6, 300 MHz): *N*-(4-(7-phenylbenzo[c][1,2,5]thiadiazol-4-yl)phenyl)acrylamide. 117
Figure 6.18: ^{13}C NMR spectrum (DMSO-d_6, 126 MHz): *N*-(4-(7-phenylbenzo[c][1,2,5]thiadiazol-4-yl)phenyl)acrylamide. 118
Figure 6.19: GPC analysis of the PDMAA linear photocatalytic polymer. 119
Figure 6.20: ^1H NMR spectrum of the PDMAA linear photocatalytic polymer. 119
Figure 6.21: GCMS spectrum of compounds produced through thioanisole oxidation. 120
Figure 6.22: ^1H NMR spectrum (CD_2Cl_2, 300 MHz): phenyl methyl sulfoxide. 120
Figure 6.23: GCMS spectrum of compounds produced through 4-methoxyphenyl methyl sulfide oxidation 121
Figure 6.24: ^1H NMR spectrum (CD_2Cl_2, 300 MHz): 4-methoxyphenyl methyl sulfoxide. 121
Figure 6.25: GCMS spectrum of compounds produced through 4-chlorophenyl methyl sulfide oxidation 122
Figure 6.26: ^1H NMR spectrum (CD_2Cl_2, 300 MHz): 4-chlorophenyl methyl sulfoxide. 122
Figure 6.27: GCMS spectrum of compounds produced through 4-methylphenyl methyl sulfide oxidation 123
Figure 6.28: ^1H NMR spectrum (CD_2Cl_2, 300 MHz): 4-methlyphenyl methyl sulfoxide. 123

Figure 6.29: Photoreduction of Cr^{VI} to Cr^{III} using photocatalytic hydrogel under blue light irradiation (power: 0.16 W cm^{-2}, λ = 460 nm). Absorbance peak at 542 nm by complexation with diphenylcarbazide. 124
Figure 6.30: Chromium degradation performed under standard conditions in the absence of light or photocatalyst. (power: 0.16 W cm^{-2}, λ = 460 nm). Absorbance peak at 540 nm by complexation with diphenylcarbazide. 125
Figure 6.31: Recycling photoreduction of Cr^{VI} to Cr^{III} using photocatalytic hydrogel under blue light irradiation (power: 0.16 W cm^{-2}, λ = 460 nm). Absorbance peak at 540 nm by complexation with diphenylcarbazide. 125
Figure 6.32: ^{31}P NMR spectra (D_2O, 300 MHz): stacked kinetic measurement of photodegradation of glyphosate. 127
Figure 6.33: ^{31}P NMR spectra (D_2O, 300 MHz): stacked kinetic measurement of large scale photodegradation of glyphosate. 127
Figure 6.34: ^{31}P NMR spectra (D_2O, 300 MHz): stacked blank measurement of glyphosate without photocatalyst. 128
Figure 6.35: ^{31}P NMR spectra (D_2O, 300 MHz): stacked blank measurement of glyphosate without light. 128
Figure 6.36: ^{31}P NMR spectra (D_2O, 300 MHz): stacked glyphosate degradation with linear polymer photocatalyst. 128
Figure 6.37: Synthesis method of 2-iodo-N-(4-(7-phenylbenzo[c][1,2,5]thiadiazol-4-yl)phenyl)acetamide. 130
Figure 6.38: Mass spectrum of 2-iodo-N-(4-(7-phenylbenzo[c][1,2,5]thiadiazol-4-yl)phenyl)acetamide. 131
Figure 6.39 ^{1}H NMR spectrum (500 MHz, DMSO) of 2-iodo-*N*-(4-(7-phenylbenzo[c][1,2,5]thiadiazol-4-yl)phenyl)acetamide. 132
Figure 6.40: ^{13}C NMR spectrum (126 MHz, DMSO) of 2-iodo-*N*-(4-(7-phenylbenzo[c][1,2,5]thiadiazol-4-yl)phenyl)acetamide. 132
Figure 6.41: Mass spectra of purified SCP-2L V83C, Q111C and A100C before bioconjugation. Raw mass spectrum (left) and the deconvoluted mass-spectrum (right) obtained by LC-MS (ES+). 134
Figure 6.42: Mass spectra of SCP-2L variants V83C-2, Q111C-2 and A100C-2 after bioconjugation with acrylamide functionalized photocatalytic moiety. Raw mass spectrum (left) and the deconvoluted mass-spectrum (right) obtained by LC-MS (ES+). 135
Figure 6.43: Mass spectra of SCP-2L variants V83C-3, Q111C-3 and A100C-3 after bioconjugation with iodoacetamide functionalized photocatalytic moiety. Raw mass spectrum (left) and the deconvoluted mass-spectrum (right) obtained by LC-MS (ES+). 136

Figure 6.44 SDS-page (Nupage™ 4-12% Bis-Tris gel) of standard purification method and all 3 variants before and after bioconjugation b) SDS-page under UV/Vis lamp irradiated at 388 nm; Ladder: Prestained Protein Ladder – Broad molecular weight (10-245 kDa) ab116028. 138
Figure 6.45: a) GC-MS temperature curve; column temp. 50 °C, heating rate 50 °C/min, inject. temp. 310 °C b) measured retention times of anisole, thioanisole and methyl phenyl sulfoxide. GC-MS ion source 250 °C, interface temp. 310 °C; measured mass spectra for thioanisole and methyl phenyl sulfoxide. 140
Figure 6.46: Blank measurements; Conditions: thioanisole 2 mM, MES buffer (MES 20 mM, 50 mM NaCl, 2% ACN) pH 6, blue light irradiation (460nm) at room temperature (up); Unmodified V83C 10 µM, thioanisole 2 mM, MES buffer (MES 20 mM, 50 mM NaCl, 2% ACN) pH 6, blue light irradiation (460-465 nm) at room temperature (down); anisole as reference..... 141
Figure 6.47: Chiral HPLC measurement of methyl phenyl sulfoxide separating both stereoisomers. 142

10 List of Tables

Table 4.1: Isotopes and their intrinsic properties.[278]
Table 5.1: Measured and calculated values for PMMA-BT, PAN-BT and PAN-BT. Absorbance, Emission, Excitation maxima and fluorescence lifetime were measured in DMF. Quantum yield measured in DMF against 4,7-Diphenyl-2,1,3-benzothiadiazol in ACN at 366 nm. DFT calculations performed using B3LYP 6-31+g(d). Optical bandgap calculation based on UV/Vis-measurements in DMF.
Table 5.2 Photocatalytic oxidation of methyl phenyl sulfide through photocatalytic hydrogel under various condition. Sulfide (30 mM), hydrogel (10 mg, 1.8 µmol photocatalyst), 10 mL H_2O, conversion determined by GC-MS.
Table 5.3 Synthesized photocatalyst and yield of incorporation.
Table 5.4 Efficiency comparison of bioconjugated photoenzyme A100C-3, Q111C-3 and V83C-3.
Table 6.1: Calculated and observed masses of SCP-2L A100C, Q111C, V83C before and after bioconjugation.

11 List of Acronyms

ACN	Acetonitrile
AN	Acrylonitrile
ATRP	Atom transfer radical polymerization
BMA	Benzyl methacrylate
CP-MAS	Cross polarization angle spinning
CB	Conduction band
CT	Charge transfer
CV	Cyclic voltammetry
DFT	Density functional theory
DIPEA	Diisopropylethyl amine
DMAEMA	*N,N*-dimethylaminoethyl methacrylateDMAA
DMAA	*N,N*-Dimethyl acrylamide
DCM	Dichloromethane
DMF	*N,N*-Dimethylformamide
DMSO	Dimethyl sulfoxide
E_{ox}	Oxidative Potential
E_{red}	Reductive Potential
EnT	Energy transfer
ET	Electron transfer
EtAc	Ethyl acetate
FTIR	Fourier transform infrared
GCMS	Gas chromatography mass spectroscopy
GPC	Gel permeation chromatography
HEMA	hydroxyethyl methacrylate
HEPES	(4-(2-hydroxyethyl)-1-piperazineethanesulfonic acid)
HIS-Tag	Polyhistidine-tag
HOMO	Highest occupied molecule orbital
HPLC	High-performance liquid chromatography
ISC	Inter system crossing
LCMS	Liquid chromatography–mass spectrometry
LED	Light-emitting diode
LUMO	Lowest unoccupied molecule orbital
MES	2-(N-morpholino)ethanesulfonic acid
MLCT	Metal-ligand charge transfer

MMA	Methyl methacrylate
NIR	Near infrared
NMR	Nuclear magnetic resonance
PAA	Polyacrylic acid
PAN	Poly(acrylonitrile)
PDA	Polydiacetylenes
PDB	Protein Data Bank
PDMAA	Poly(N,N-dimethyl acrylamide)
PE	Petrol ether
PHEMA	Poly(hydroxyethyl methacrylate)
PMMA	Poly(methyl methacrylate)
PNIPA	Poly(*N*-isopropyl acrylamide)
PS	Polystyrene
RAFT	Reversible addition−fragmentation chain-transfer
rt	Room temperature
SCE	Saturated calomel electrode
SCP	Steroid carrier protein
SDS	Sodium dodecyl sulfate
SET	Single electron transfer
ssNMR	Solid state nuclear magnetic resonance
TEA	Triethylamine
THF	Tetrahydrofuran
TON	Turnover number
UV	Ultraviolet
VB	Valence band
Vis	Visible

12 **Scientific Contribution**

Kuckhoff, T.; Brewster, R.; Ferguson, C.; Jarvis, A. Reactivity Tuning of Metal-Free Artificial Photoenzymes through Binding Site Specific Bioconjugation. *Eur. J. Org. Chem.* 2023, **26**, e202201412.

Kuckhoff, T.; Landfester, K.; Zhang, K. A. I.; Ferguson, C. T. J. Photocatalytic Hydrogels with a High Transmission Polymer Network for Pollutant Remediation. *Chem. Mater.* 2021, **33**, 9131-9138.

Kuckhoff, T. Heuer, J. Li, R. Landfester, K.; Ferguson, C. T. J. Comonomer effects in photocatalytic classical polymers. (in preparation)

Heuer, J.; Kuckhoff, T.; Li, R.; Landfester, K.; Ferguson, C. T. J. Tunable Photocatalytic Selectivity by Altering the Active Center Microenvironment of an Organic Polymer Photocatalyst. *ACS Applied Materials & Interfaces* 2023, *15*, 2891-2900.

Li, R.; Heuer, J.; Kuckhoff, T.; Landfester, K.; Ferguson, C. pH-triggered Recovery of Organic Polymer Photocatalytic Particles for the Production of High Value Compounds and Enhanced Recyclability. *Angew. Chem. Int. Ed*. 2023, e202217652.

Ferguson, C. T. J.; Huber, N.; Kuckhoff, T.; Zhang, K. A. I.; Landfester, K. Dispersible porous classical polymer photocatalysts for visible light-mediated production of pharmaceutically relevant compounds in multiple solvents. *J. Mater. Chem. A* 2020, **8**, 1072-1076.

Markwart, J. C.; Battig, A.; Kuckhoff, T.; Schartel, B.; Wurm, F. R. First phosphorus AB2 monomer for flame-retardant hyperbranched polyphosphoesters: AB2 vs. A2 + B3. Polymer Chemistry 2019, 10, 5920-5930.

Conferences:

Poster presentation: Kuckhoff, T.; Landfester, K.; Zhang, K. A. I.; Ferguson, C. T. J. Photocatalytic Hydrogels with a High Transmission Polymer Network for Pollutant Remediation. at Bordeaux Polymer Conference June 13-16, 2022.

Curriculum Vitae

Thomas Kuckhoff

Anschreiben:	Thomas Kuckhoff Mozartstraße 15 84539 Ampfing
Mobil:	+49 (0)176/76625497
Post:	T.Kuckhoff@gmx.de
Geboren:	14. Juli 1990 in Koblenz
Familienstand:	ledig
Staatsangehörigkeit:	Deutsch

Berufliche Laufbahn

07/2019 - 07/2023 Max-Planck-Institut für Polymerforschung, Mainz
Doktorand Chemie, Thema der Dissertation (Englisch):
“Designing photocatalytic materials by merging macromolecules with small molecular photocatalysts”

- Umfassende Kenntnisse in Polymerchemie und Materialwissenschaft
- Design und Synthese von makromolekularen Photokatalysatoren
- Fachkenntnisse in Polymeranalyse und Polymerisationarten
- Synthese von organischen Halbleitern
- Eigenständiges Projektmanagement
- Arbeit in internationalen Kooperationen

Stipendium

04/2022 - 07/2022 Scholarship: Saltire Emerging Researcher Scheme
School of Chemistry, University of Edinburgh

- Herstellung künstlicher Enzyme
- Entwicklung und Handhabung von künstlichen Photoenzymen
- Biokonjugation von Katalysatoren in modifizierte Proteine

Studie

2015 - 2019 Chemie, Johannes Gutenberg-Universität, Mainz
Hochschulabschluss: Master of Science Chemie (M.Sc.)

Projektarbeit in Solarzellentechnik

- Design und Herstellung von mehrschichtigen Perowskit-Solarzellen unter Glovebox-Bedingungen

Projektarbeit in Flammschutzentwicklung

- Entwurf und Synthese von hyperverzweigten Polyphosphoestern

Masterarbeit (Englisch):
In Zusammenarbeit mit Evonik am Max-Planck-Institut für Polymerforschung:
“From lipophilic to hydrophilic: a library of soluble polyaziridines”

- Design und Synthese von öllöslichen Polymeren als Anwendung in Oberflächenbeschichtungen, Dispergiermittel, Emulgatoren
- Anionische Polymerisation von Epoxiden und Aziridinen
- Untersuchung von Copolymerisationen

2011 - 2015 Chemie, Johannes Gutenberg-Universität, Mainz
Studienabschluss: Bachelor of Science Chemie (B.Sc.)

Internationaler Aufenthalt

01/2011-03/2011 Sprachreisen USA, Kalifornien

Verantwortung

2020 - 2023 Beaufsichtigung:

- Gaschromatograph/Massenspektrometer (GC/MS)
- Automatischer Säulenchromatograph
- Laboreinführung und Schulung neuer Kollegen

2021 - 2023 Laborleitung:

- Sicherheitskontrollen
- Wartung der Ausrüstung
- Lagerung von Chemikalien

2020 - 2021 Lehre:

Seminar der Johannes Gutenberg-Universität:

- "Allgemeine und analytische Chemie von anorganischen Arzneimitteln, Hilfsstoffen und Schadstoffen"

Max-Planck-Institut für Polymerforschung:

- "Short Newcomer Introduction Program "

Wissenschaftliche Beiträge

Präsentationen: Kuckhoff, T.; Landfester, K.; Zhang, K. A. I.; Ferguson, C. T. J. Photocatalytic Hydrogels with a High Transmission Polymer Network for Pollutant Remediation at Bordeaux Polymer Conference June 13- 16, 2022

Veröffentlichungen: Kuckhoff, T.; Brewster, R.; Ferguson, C.; Jarvis, A. Reactivity Tuning of Metal-Free Artificial Photoenzymes through Binding Site Specific Bioconjugation. *Eur. J. Org. Chem*. **2023**, *26*, e202201412.

Kuckhoff, T.; Landfester, K.; Zhang, K. A. I.; Ferguson, C. T. J. Photocatalytic hydrogels with a high transmission polymer network for pollutant remediation. *Chem. Mater.* **2021,** *33*, 9131-9138.

Heuer, J.; Kuckhoff, T.; Li, R.; Landfester, K.; Ferguson, C. T. J. Tunable Photocatalytic Selectivity by Altering the Active Center Microenvironment of an Organic Polymer Photocatalyst. *ACS Applied Materials & Interfaces* **2023,** *15*, 2891-2900.

Ferguson, C. T. J.; Huber, N.; Kuckhoff, T.; Zhang, K. A. I.; Landfester, K. Dispersible porous classical polymer photocatalysts for visible light-mediated production of pharmaceutically relevant compounds in multiple solvents. *J. Mater. Chem. A* **2020,** *8*, 1072-1076.

Markwart, J. C.; Battig, A.; Kuckhoff, T.; Schartel, B.; Wurm, F. R. First phosphorus AB_2 monomer for flame-retardant hyperbranched polyphosphoesters: AB_2 vs. $A_2 + B_3$. *Polymer Chemistry* **2019,** *10*, 5920-5930.

Kuckhoff, T.; Heuer, J.; Li, R.; Landfester, K.; Ferguson, C. T. J; Comonomer effects in photocatalytic classical polymers. **2023** (in preparation)